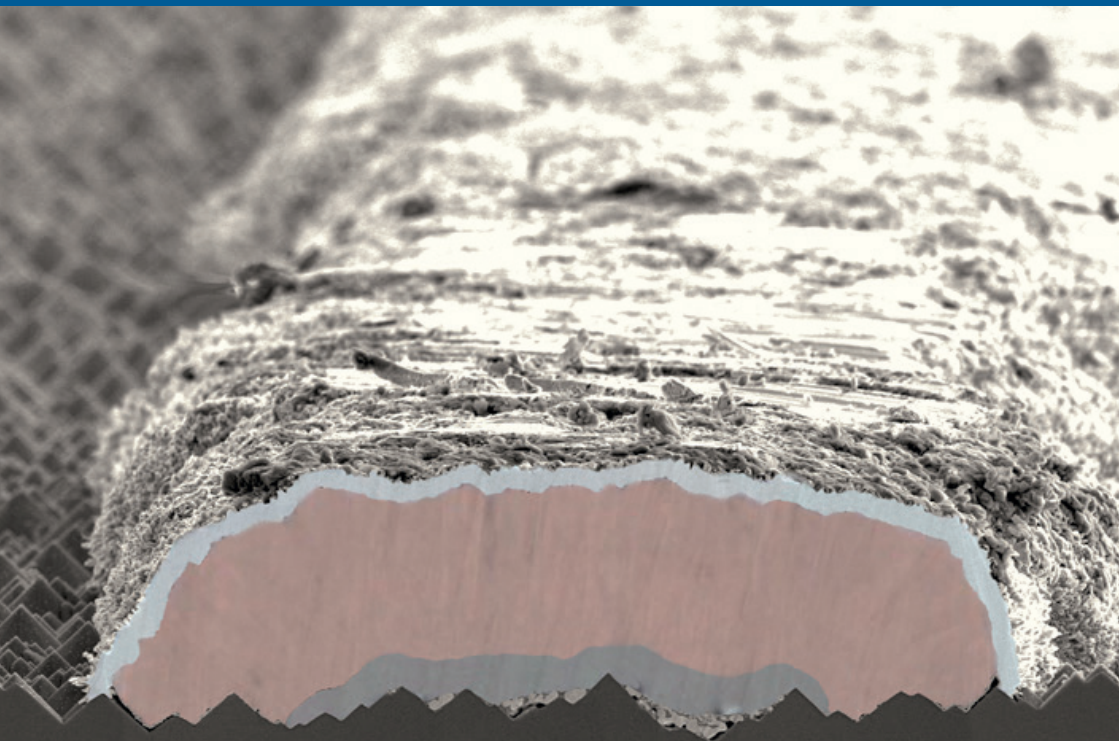


Achim Kraft

PLATED COPPER FRONT SIDE METALLIZATION ON PRINTED SEED-LAYERS FOR SILICON SOLAR CELLS



Fraunhofer Institute for Solar Energy Systems ISE

SOLARE ENERGIE- UND SYSTEMFORSCHUNG /
SOLAR ENERGY AND SYSTEMS RESEARCH

Plated Copper Front Side Metallization on Printed Seed-Layers for Silicon Solar Cells

Achim Kraft

FRAUNHOFER VERLAG

Contact:

Fraunhofer Institute for Solar Energy Systems ISE
Heidenhofstrasse 2
79110 Freiburg
Phone +49 761/4588-5150
Fax +49 761/4588-9342
E-Mail info@ise.fraunhofer.de
URL www.ise.fraunhofer.de

Bibliographic information published by Die Deutsche Bibliothek

Die Deutsche Bibliothek lists this publication in the Deutsche Nationalbibliografie;
detailed bibliographic data is available in the Internet at <<http://dnb.d-nb.de>>.

D 25

Zugl.: Freiburg, Univ., Diss., 2015

Book Series: »Solare Energie- und Systemforschung / Solar Energy and Systems Research«

Printing and Bindery:

Mediendienstleistungen des
Fraunhofer-Informationszentrum Raum und Bau IRB, Stuttgart

Printed on acid-free and chlorine-free bleached paper.

All rights reserved; no part of this publication may be translated, reproduced, stored in a retrieval system, or transmitted in any form or by any means, electronic, mechanical, photocopying, recording or otherwise, without the written permission of the publisher.

Many of the designations used by manufacturers and sellers to distinguish their products are claimed as trademarks. The quotation of those designations in whatever way does not imply the conclusion that the use of those designations is legal without the consent of the owner of the trademark.

© by **Fraunhofer Verlag**, 2015, ISBN 978-3-8396-0939-2

Fraunhofer Information-Centre for Regional Planning and Building Construction IRB
P.O. Box 80 04 69, D-70504 Stuttgart
Nobelstrasse 12, D-70569 Stuttgart
Phone +49 (0) 7 11/9 70-25 00
Fax +49 (0) 7 11/9 70-25 07
E-Mail: verlag@fraunhofer.de
URL www.verlag.fraunhofer.de

Plated Copper Front Side Metallization on Printed Seed-Layers for Silicon Solar Cells

Dissertation

zur Erlangung des akademischen Grades eines
Doktors der Ingenieurwissenschaften (Dr. Ing.)

an der Fakultät für Angewandte Wissenschaften
der Albert-Ludwigs-Universität Freiburg im Breisgau

vorgelegt von

M. Sc. Achim Kraft
aus Karlsruhe

Fraunhofer Institut für Solare Energiesysteme
Freiburg im Breisgau 2015

Dekan: Prof. Dr. Georg Lausen
Referent: Prof. Dr. Holger Reinecke
Korreferent: Prof. Dr. Eicke R. Weber
Datum der mündlichen Prüfung: 19.06.2015

To Friederike and Sophia

Table of contents

Abstract	xi
1 Introduction	13
1.1 Thesis motivation	13
1.2 Aim of the thesis.....	15
1.3 Thesis outline	17
2 Theoretical background	19
2.1 Crystalline silicon solar cells.....	19
2.1.1 Structure and operation principle of crystalline silicon solar cells	19
2.1.2 Current-voltage curve.....	20
2.1.3 Loss mechanisms in silicon solar cells	24
2.1.4 Industrial realization of silicon solar cells	32
2.2 Electrochemical deposition of metals	34
2.3 Light induced plating of solar cells	38
2.4 Copper diffusion into silicon	40
3 State of the art of front side metallization for silicon solar cells and novel approaches.....	44
3.1 Requirements for solar cell front side metallization	44
3.1.1 Contact geometry and silver consumption	44
3.1.2 Contact adhesion	47
3.1.3 Long term stability	47
3.1.4 Electrical conductivity and contact resistance	49
3.2 Screen-printed silver front side metallization	50
3.2.1 Screen-printing of the front side metallization	50
3.2.2 Contact formation in the firing furnace	53
3.3 Ni-Cu front side metallization on printed seed-layers	56
3.3.1 Process route	57
3.3.2 State of the art	57

3.3.3	Challenges	58
3.4	Alternative seed-layer printing technologies	59
3.4.1	Aerosol jet printing	60
3.4.2	Ink jet printing	61
3.4.3	Flexographic printing.....	62
3.5	Ni-Cu front side metallization by direct plating	64
4	Characterization methods for solar cells and solar cell contacts	66
4.1	Optical characterization of solar cell contacts	66
4.1.1	Confocal laser scanning microscopy.....	66
4.1.2	Cross-section preparation.....	67
4.1.3	Scanning electron microscopy and energy dispersive X-ray spectroscopy	69
4.1.4	Scanning transmission electron microscopy	70
4.2	Mechanical characterization of solar cell contacts	71
4.2.1	Peel-force-test	71
4.2.2	Contact failure mechanisms	72
4.2.3	Dependence of the peeling angle	74
4.2.4	Atomic force microscopy.....	75
4.3	Electrical characterization of solar cells and lifetime samples	76
4.3.1	Suns Voc measurement.....	76
4.3.2	Photoluminescence imaging	77
4.3.3	Electroluminescence imaging	78
4.3.4	Quasi steady-state photo conductance measurement	79
4.4	Chemical and electrochemical material characterization	80
4.4.1	Inductively coupled plasma optical emission spectroscopy	80
4.4.2	Cyclic voltammetry.....	81
4.4.3	Powder X-ray-diffraction measurement.....	83
4.5	Rheological characterization of silver pastes	84
4.5.1	Controlled shear stress test.....	85
4.5.2	Evaluation of the yield stress	86

5	Experimental setups and procedures	88
5.1	Electrochemical Ni-Cu-Ag deposition – electrolytes and tools	88
5.1.1	Lab scale tank setup	88
5.1.2	Inline tool for electrochemical metal deposition	91
5.1.3	Used electrolytes for metal deposition	92
5.2	Exposure procedure for adhesion evaluation of solar cell contacts	93
5.2.1	Solar cell contact precursors for exposure experiments	94
5.2.2	Contact exposure without applied voltage.....	94
5.2.3	Contact exposure with applied voltage.....	95
5.3	Soldering procedures for solar cell contacts	96
5.4	Fast degradation of plated solar cells at elevated temperature	98
5.5	Solar cell precursors for experimental research.....	100
6	Printed silver seed-layers for copper front side metallization.....	101
6.1	Influence of paste rheology on screen-printed seed-layers	101
6.1.1	Influence of the paste viscosity	104
6.1.2	Influence of the particle size	105
6.1.3	Influence of the yield stress.....	107
6.2	Evaluation of printed seed-layers	110
6.2.1	Solar cells with plated copper metallization on ink-jet printed seed-layer ...	111
6.2.2	Solar cells with plated copper metallization on aerosol-jet printed seed-layer.....	114
6.2.3	Solar cells with plated copper metallization on flexographic-printed seed-layer.....	116
6.2.4	Solar cells with plated copper metallization on screen-printed seed-layer ...	118
6.2.5	Comparison and classification with fully screen-printed solar cells.....	120
6.3	Chapter summary	124
7	Corrosion mechanism of the screen-printed silver seed-layer	126
7.1	Contact adhesion after Ni-Cu-Ag plating	126

7.2	Interaction between plating chemicals and screen-printed Ag-contacts	129
7.3	Microstructure analysis of the Watts-type nickel electrolyte impact on screen-printed contacts	136
7.3.1	SEM analysis of the contact microstructure.....	136
7.3.2	TEM analysis of the glass-silver interface	143
7.3.3	AFM analysis of the gap formation at the glass silver interface	146
7.4	Chemical interaction between Watts-type nickel electrolyte and printed Ag-contacts	149
7.4.1	Contact adhesion after Watts-type nickel electrolyte exposure.....	149
7.4.2	Material changes in the solid contact compounds	153
7.5	Influence of the plating process on contact adhesion	157
7.5.1	Impact of an applied voltage to the contact microstructure.....	157
7.5.2	Impact of an applied voltage on contact adhesion	158
7.5.3	Influence of the reduction potential on contact adhesion	159
7.6	Model of the solar cell contact corrosion by electrolyte solutions	163
7.7	Strategies to reach sufficient contact adhesion.....	166
7.8	Chapter summary	169
8	Long term stability of plated copper front side metallization based on screen-printed seed-layers.....	171
8.1	Copper diffusion behaviour in silicon solar cells	171
8.2	Silicon nitride as diffusion barrier.....	177
8.3	Effectiveness of the nickel diffusion barrier.....	182
8.3.1	Degradation of cells at elevated temperatures.....	183
8.3.2	Degradation of modules in the climate chamber.....	187
8.3.3	Comparison of cell and module degradation.....	190
8.4	Influencing parameters for cell degradation.....	191
8.4.1	Influence of the used seed-layer.....	191
8.4.2	Influence of the firing temperature	193
8.5	Challenges for nickel plating on screen-printed silver seed-layers.....	198
8.5.1	Distribution of plated nickel on screen-printed silver contacts	198

8.5.2	Plating at the edge zones of screen-printed silver contacts.....	202
8.6	Homogeneity of the plated nickel diffusion barrier	204
8.7	Improvement of the nickel homogeneity	209
8.8	Chapter summary	213
9	Acetic acid corrosion impact on printed solar cell contacts	215
9.1	Introduction into damp heat induced degradation.....	215
9.2	Corrosion of screen-printed silver contacts due to the interaction with acetic acid	216
9.3	SEM cross-section analysis	219
9.4	Chemical trace analysis	220
9.5	Cyclic voltammetry measurements.....	222
9.6	Incubation experiment with ethylene-vinyl acetate	226
9.7	Pourbaix diagrams	226
9.8	Model of the solar cell contact corrosion by acetic acid	229
9.9	Chapter summary	232
10	Cost effects of solar cell front side metallization	234
11	Summary and outlook	239
	Deutsche Zusammenfassung	247
	Appendix A	252
A.1	Pourbaix diagrams of silver in aqueous solution.....	252
A.2	Pourbaix diagrams of lead in aqueous solution	254
	Appendix B	256
B.1	Diffractograms of powder XRD measurements	256
	List of Publications	264
	Abbreviations and symbols	268
	Danksagung	274
	Bibliography	277

Abstract

In the present work, a novel front side metallization architecture for silicon solar cells based on a fine printed silver seed-layer, plated with nickel, copper and silver, is investigated. Practical challenges with this type of metallization motivated associated research, and scientific insights into different aspects of this metallization approach and beyond were obtained. The work focuses on the printing of fine seed-layers with low silver consumption using screen-printing, the corrosion of the printed seed-layers by the interaction with electrolyte solutions and the encapsulation material on module level and on the long term stability of the cells due to copper migration.

To realize fine contact structures and simultaneously low silver consumption by screen-printing a high yield stress of >400 Pa for the silver pastes were shown to be beneficial. Fine contact fingers with a width of $30\text{ }\mu\text{m}$ were reproducibly printed. Seed-layers printed with ink-jet, aerosol-jet, screen-printing and flexographic printing were used to produce industrial scale $156 \times 156\text{ mm}^2$ solar cells. A total silver consumption for the front side metallization of less than 15 mg/cell was achieved with screen-printed seed-layers. This represents a reduction of the silver consumption of at least 80% compared to solar cells with fully screen-printed silver front side contacts.

The analysis of the contact corrosion due to interaction with the electrolyte solutions revealed that a site specific dissolution of the glass layer inside the fired contacts is responsible for the observed contact adhesion loss. A model of the underlying reaction mechanism was developed which explains the experimental results and provides profound understanding of the interaction between solar cell contacts and electrolyte solutions. It was found that lead glass is dissolved within the acidic aqueous systems. Several factors were identified to shift this equilibrium in favour of pronounced glass dissolution, especially the presence of complexation or precipitation agents, low pH and a cathodic potential. The acceleration of the contact corrosion by a cathodic voltage was found to depend on the nobility of further ions in the system. If noble ions like silver or copper are present, the reduction of these species at the silver contact is preferred compared to the reduction of the dissolved lead, whereas ions similarly or less noble than lead, like nickel, enable the reduction of the dissolved species, which shifts the equilibrium of the dissolution reaction strongly towards further dissolution and leads to quick and significant loss of contact adhesion. The

described mechanism explains the observed fast gap expansion specifically at the glass silver interface in the contact. Strategies to avoid critical adhesion loss in practical application have been derived from these findings.

The results regarding contact corrosion were successfully transferred to improve the understanding of a phenomenon which occurs on module level and is often described in literature. Damp heat induced degradation is known to be caused by acetic acid, released from the module encapsulation material ethylene-vinyl acetate in presence of humidity and heat. With the methods developed in this work, close analogies to electrolyte corrosion could be demonstrated. It was shown that the observed loss of electrical contact between front side metallization and emitter originates from the corrosion of the glass layer inside the contacts by acidic acid, accelerated considerably by applied negative voltages. The reduction of dissolved lead was demonstrated to be the reason behind this effect. The developed model and the combined detailed understanding of the corrosion mechanism offer the possibility of considerable lifetime extension for PV-modules irrespective if cells with seed- and plate or fully printed contacts are used.

The investigations of the copper migration revealed that silicon nitride anti reflection coatings deposited by industrial inline plasma enhanced chemical vapour deposition and sputtering prevent copper diffusion into the underlying silicon wafer even after a pre-treatment with hydro-fluoric acid or the mechanical load induced by screen-printing. The effectiveness of the plated nickel diffusion barrier was evaluated with cells featuring different nickel diffusion barrier thicknesses. It was shown that 20 mg plated nickel per cell, which represents a layer thickness of at least 0.2 μm , is sufficient to avoid long term stability issues due to copper migration during a module lifetime on the tested screen-printed seed-layer.

1 Introduction

1.1 Thesis motivation

Renewable energies offer the possibility to transform the quasi-unlimited energy offered by sun, wind and water into electrical energy to satisfy the growing world-wide energy demand. The use of renewable energies, which all trace back directly or indirectly to the energy provided by the sun, represents a fundamental change in the electrical energy consumption behaviour of mankind. The exploitation of the limited fossil energy resources coal, oil and gas enabled the industrial revolution. In the last century the use of nuclear power, which also represents a limited resource, extended the used energy mix. The use of these energy sources enabled rapid economic progress and came with the price of nuclear radiation risks combined with the open question of ultimate disposal of the nuclear waste and increasing carbon dioxide emissions. The worldwide annual carbon dioxide emissions by fuel increased sharply from ~15.6 Mt in 1973 to ~31.7 Mt in 2012 [1] which represents a doubling in 41 years. The emissions accelerate the process of global warming and started the first man caused intervention in the world climate [2]. According to the Intergovernmental Panel on Climate Change (IPCC) the years between 1983 and 2012 represent the warmest 30-year period in the last 1500 years in the northern hemisphere [2]. The consequences and challenges future generations will have to face to handle this massive environmental change are not conclusively conceivable and cannot be determined monetarily. In the same time the worldwide energy demand grows. According to the International Energy Agency (IEA) the annual worldwide energy demand is predicted to be 33% higher in 2035 than 2012 [1]. Regarding the limited fossil resources this will inevitably lead to an increase of energy prices because the intensification of coal, gas and oil production will not be able to balance the massive increase in demand at today's production costs on the long term view. The transition to the use of renewable energies offers the possibility of ongoing increased production of electrical energy with a simultaneous decrease of the carbon dioxide emissions. The life cycle greenhouse gas emissions of PV systems are ~45 g CO₂ eq./kWh [3]. This is considerably lower than the fossil options which cause greenhouse gas emissions of ~1000 g CO₂ eq./kWh for coal or ~469 g CO₂ eq./kWh for natural gas [4]. Additionally the sun offers outside the atmosphere an energy amount

of $5.36 \cdot 10^{24}$ J/a [5]. With the conservative estimate that ~70% of the irradiation reaches the earth's surface, an energy amount of $\sim 3.75 \cdot 10^{24}$ J/a is available. The total worldwide energy demand in 2012 was $\sim 3.76 \cdot 10^{20}$ J [1]. This means, the sun offers, as long as it keeps burning, an energy amount, which is nearly 10.000 times higher than the world-wide demand.

The modification of the world-wide energy production away from the exclusive use of fossil sources toward the direct use of the inexhaustible sun energy has started in the last years and can mark the starting point of a revolution in energy production during this century. Since 2009 the rate of new built photovoltaic capacity raised from 7 GW/a in 2009 to 35 GW/a in 2013. In the same time market prices of photovoltaic modules have been reduced by factor five and the market prices of photovoltaic systems by a factor of almost three [6]. The levelized costs of electricity (LCOE) were calculated to be in a range of 7.8 to 14.2 ¢cent/kWh, depending on the type of solar power plant, in the end of 2013 in southern Germany [7]. For comparison the LCOE for brown coal was calculated to be between 3.8 to 5.3 ¢cent/kWh and for hard coal between 6.3 to 8 ¢cent/kWh [7]. The authors of this study state that: “...utility scale PV power plants in southern Germany will drop considerably below the average LCOE for all fossil fuel power plants by 2030” [7]. To reach this forecast, the trend of decreasing costs for solar cell production has to be continued. This can be reached by increasing the efficiency of the cells or by lowering the production costs using cheaper processes and materials. The costs of solar cell production are dominated by the metallization costs and especially by the cost contribution of the silver used for front side metallization [8]. In the last years the silver price was subject to fluctuations. Due to influences of the economic crises, it increased from ~400-500 €/kg in 2010 to a maximum level of ~1228 €/kg in 2011. Copper is ~100 times cheaper than silver and offers the potential to reduce the production costs for solar cells and additionally increases the planning reliability for solar cell producers because the price is not that volatile. Fig 1.1 shows the development of the silver and copper price from 2008 to the end of 2014.

To realize the use of copper for the front side metallization of silicon solar cells in mass production a seed-and plate approach is followed at Fraunhofer ISE and investigated in this work. A fine printed silver seed-layer thickened by electrochemically deposited nickel, copper and silver offers the possibility to reduce the silver amount used for the front side metallization of industrially produced silicon solar cells by ~80% compared to the standard screen-printed front side metallization. This technology has the potential to make a substantial

contribution to the process of cost reduction and offers the use of an alternative material with comparably high conductivity as front side contact of silicon collar cells.

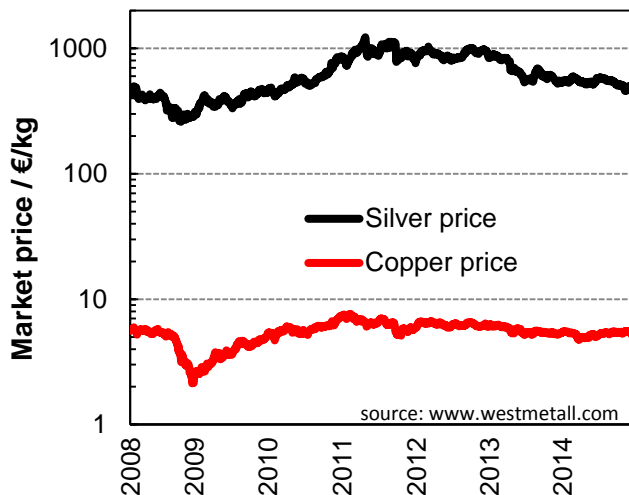


Fig. 1.1: Market price of silver (black curve) and copper (red curve) between 2008 and the end of 2014 in logarithmic scale

1.2 Aim of the thesis

In the context of the novel process approach followed in this thesis (plating nickel, copper and silver on top of a printed seed-layer) there are several open questions and challenges. The aim of this thesis is to gain scientific knowledge about challenges which complicate or hinder the implementation of a copper front side metallization based on the seed- and plate approach into industrial solar cell production. Based on the findings, the industrial production process can be optimized. Fig 1.2 shows the investigated metallization architecture at a microscope cross section image of a solar cell contact on a monocrystalline silicon wafer (a). The metallization is based on a screen-printed silver seed-layer (b) which enables the contact formation to the solar cell emitter by penetration of the silicon nitride layer underneath in the firing process. To protect these opened silicon nitride area from copper penetration a plated nickel diffusion barrier (c) is plated on top of the silver seed-layer. In further plating steps the copper conductive layer (d) and a fine silver capping (e) are deposited.

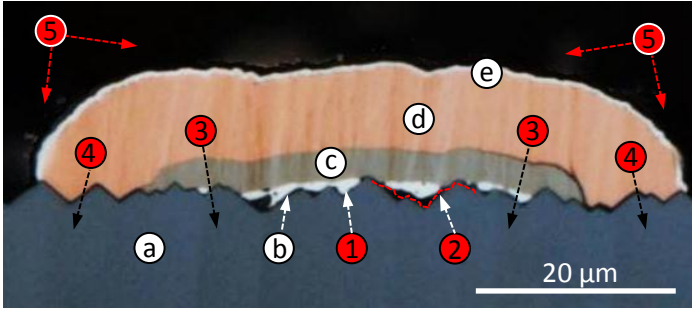


Fig. 1.2: Microscope cross section image of a solar cell contact on a monocrystalline silicon wafer (a) based on a printed silver seed-layer (b), a plated nickel diffusion barrier (c), a plated copper conductive layer (d) and a fine silver capping (e). The topics of scientific research relevant for this thesis are indicated at their respective locations within the contact cross section: seed-layer geometry and silver consumption (1), seed-layer adhesion on the silicon substrate (2), effectiveness of the nickel diffusion barrier (3), barrier properties of the silicon nitride layer against copper migration (4) and contact corrosion on module level (5).

The key issues, seed-layer geometry and silver consumption (1), seed-layer adhesion (2), effectiveness of the nickel diffusion barrier (3), barrier properties of the silicon nitride layer against copper migration (4) and contact corrosion mechanisms on module level (5) addressed in this work are indicated at their respective positions within the contact cross section in Fig. 1.2.

This work is focussed on experimental research to achieve scientific understanding of the mechanisms influencing these factors, which are particularly important for the development of the seed- and plate copper metallization. More details on each topic and its role in industrial production are given in the following.

1. Seed-layer geometry and silver consumption: the printing of fine silver seed-layers with low silver consumption is the basis for this copper metallization realized with the seed- and plate approach. An economical advantage can only be achieved if very little silver paste is consumed in comparison to the state of the art contacts, while the cell efficiency need to be at similar level. The understanding of seed-layer formation using the wide spread screen-printing technology including research regarding the ideal

paste rheology and the best printing process configuration have been subjected to intensive studies. The evaluation of seed-layers printed by alternative printing technologies regarding silver consumption and electrical parameters is another focus in this context.

2. **Seed-layer adhesion on the silicon substrate:** the contact adhesion of the printed seed-layer on the silicon wafer after the Ni-Cu-Ag plating sequence is a key issue for module integration of the produced solar cells. The understanding of corrosion processes which cause adhesion loss is crucial to implement the nickel and copper plating process on printed seed-layers in the industry. Therefore, such corrosion processes have been studied thoroughly.
3. **Effectiveness of the nickel diffusion barrier:** the long term stability of the solar cells due to the possible migration of copper through the nickel diffusion barrier into the semiconductor device is an important issue. As a long solar cell lifetime needs to be ensured for industrial implementation, this topic has been studied.
4. **Barrier properties of the silicon nitride layer against copper migration:** the plated copper layer overlaps the nickel diffusion barrier plated before at the edges of the contact structure. At this spots the copper gets in direct contact with the silicon nitride antireflection coating. The evaluation of the barrier properties of the silicon nitride layer is important to check if this position in the contact architecture causes long term stability problems.
5. **Contact corrosion on module level:** the deeper understanding of corrosion mechanisms occurring at encapsulated solar cell contacts on module level due to the interaction with the encapsulation materials offer the possibility to realize extended module lifetime and is additionally of interest also for fully screen-printed standard solar cell contacts.

1.3 Thesis outline

In **chapter 1**, the motivation and the research aims of the present work are introduced. **Chapter 2** focusses on the theoretical background. The basic structure and operation principle as well as the most important loss mechanisms of crystalline silicon solar cells are presented. Additionally the basics of electrochemical metal deposition and copper diffusion in silicon are described. In **chapter 3** the general requirements, a solar cell front side metallization has to satisfy, are discussed. Furthermore the seed- and plate approach for the copper front side metallization investigated in this work is described and compared to

the standard screen-printed metallization and an alternative copper front side metallization approach. **Chapter 4** gives an overview of the different methods for optical, mechanical and electrical characterization of silicon solar cells as well as the chemical, electrochemical and rheological characterization techniques used in this work. As this work is based on experimental research, the methods and tools used and developed to analyse the mechanical contact adhesion and the solar cell long term stability are introduced in **chapter 5**. In **chapter 6**, the experimental results regarding the realization of fine screen-printed seed-layers with low silver consumption and the analysis of seed-layers printed with alternative techniques are presented. **Chapter 7** is dedicated to the results on the corrosion mechanism behind the contact adhesion loss of the printed seed-layers after the Ni-Cu-Ag plating sequence. Special attention is drawn on the corrosion caused by the nickel electrolyte. A model of the corrosion mechanism is presented which explains the experimental results and provides general scientific understanding of the interaction between electrolyte solutions and screen-printed solar cell front side contacts. In **Chapter 8** experimental results regarding the question of long term stability are shown. It focusses on the barrier properties of the silicon nitride layer and the effectiveness of the nickel diffusion barrier against copper migration into the solar cell. In **chapter 9**, the corrosion mechanisms of printed solar cell contacts due to interaction with the module encapsulation materials during the module lifetime are presented. **Chapter 10** gives a brief cost-comparison of different solar cell front side metallizations, comparing the standard fully screen-printed metallization with a direct plated copper front side metallization approach and the copper metallization based on printed seed-layers investigated in this work. In **Chapter 11**, the results presented in this work are summarised and an outlook to the upcoming research issues triggered by the scientific understanding gained in this work is provided.

2 Theoretical background

In this work, a copper front side metallization for silicon solar cells with a p-type doped base and an n-type doped emitter is investigated. This is the basic structure of most industrially produced solar cells on multi crystalline or mono crystalline silicon material nowadays. In this chapter the fundamentals of the working principle of this cell structure are explained (section 2.1) with a focus on the composition on the cell structure with p-type doped base (section 2.1.1) the electrical characteristics (section 2.1.2), the loss mechanisms (section 2.1.3) and the industrial realization of this type of solar cells (section 2.1.4). As in this work a front side metallization based on a printed seed-layer and electrochemical deposition of nickel, copper and silver is investigated, the basics for electrochemical deposition of metals (section 2.2) and especially the light induced plating technique, used for solar cell metallization are described (section 2.3). In section 2.4, copper diffusion into silicon is introduced.

2.1 Crystalline silicon solar cells

Crystalline silicon solar cells convert the sunlight directly into electrical energy. In order to achieve this, the physics of silicon as a semiconductor material and the ability of a p-n junction to separate positive and negative carriers generated by the incoming sunlight are utilized.

The theoretical background knowledge discussed in this chapter and further information can be found in literature [5, 9-12], sources for pictures and further information of specific issues are cited individually.

2.1.1 Structure and operation principle of crystalline silicon solar cells

Typical industrial silicon solar cells are fabricated as so called “back surface field” (BSF) solar cells out of boron-doped p-type silicon with a phosphorous-doped n-type emitter. Fig. 2.1 shows a schematic drawing of this solar cell structure. The emitter is located at the sun facing side and passivated with a silicon nitride layer. The metal front side contacts are realized as a grid pattern. Between emitter and base, a p-n junction with space charge region is formed by intimate contact between the p-type silicon and the n-type silicon (enlarged section in Fig. 2.1). During the formation of the p-n junction in the p-type region

of this interface, the “holes” (majority carriers) recombine with free electrons coming from the n-type region by diffusion due to a concentration gradient. In the n-type region of the interface the reverse process happens, electrons (majority carriers) recombine with holes from the p-type region.

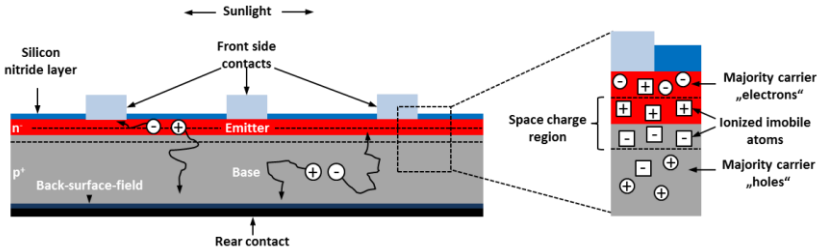


Fig. 2.1: Schematic drawing of the structure of a p-type back-surface-field silicon solar cell with n-type emitter, silicon nitride anti-reflection coating, a metal contact grid on the sun facing front side and a p-type base with full surface metal contact and back surface field on the back side. The enlarged section illustrates the space charge region at the p-n junction.

This results in a positively charged layer in the n-type doped region formed by immobile phosphorous atoms and a negatively charged layer in the p-type doped region formed by immobile boron atoms. The static electric field between these layers triggers a drift current flow in the opposite direction of the diffusion transport until equilibrium is reached and drift and diffusion have the same magnitude. This region is called space charge region (SCR) or depletion region as it is depleted of free carriers. The p-n junction separates the electron-hole pairs continuously generated under irradiation, the electrons to the n-type doped part of the cell and the holes to the p-type doped part of the cell. The excited carriers can be used as photo-generated current flow by an external load applied between the metal contacts at the rear side and the front side.

2.1.2 Current-voltage curve

The general characteristic electrical parameter of a solar cell is the energy conversion efficiency. It describes the ratio of the incident power density of the photons and the electrical power delivered by the cell per area and can be determined by the measurement of a current-voltage curve under illumination (light I - V -curve). The light I - V curve is measured under standard conditions at

25°C, 1000 W/m² and shows the current density and the power density over the voltage as shown in Fig. 2.2 for a solar cell operated under illumination (light I - V curve, black continuous line). The short circuit current density j_{SC} and the open circuit voltage V_{OC} are defined as the intersection points of the light I - V -curve with the current and the voltage axis. The product of current density and voltage defines the power density of the solar cell (red dashed line). The point where the power density reaches its maximum is called maximum power point (mpp) with the corresponding current density j_{mpp} and voltage V_{mpp} . The fill factor FF is defined following equation 2.1 as the area ratio of the largest rectangle fitting under the illuminated I - V -curve (black dashed rectangle) to the rectangle of side length V_{OC} and j_{SC} (blue continuous rectangle).

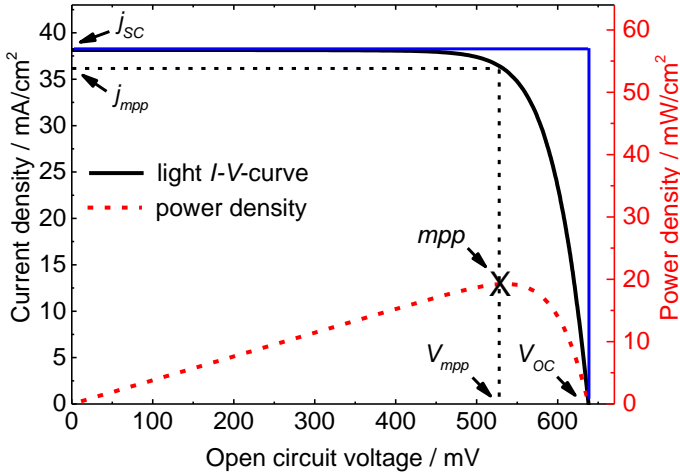


Fig. 2.2: Light I - V -curve (black continuous line) and power density (red dashed line, red axis) of a monocrystalline standard back surface field solar cell with defined positions of the open circuit voltage V_{oc} , the short circuit current density j_{sc} , the maximum power point mpp and the related current density j_{mpp} and voltage V_{mpp} . The area ratio between the largest rectangle that fits under the I - V -curve (black dashed rectangle) and the rectangle of side length V_{oc} and j_{sc} (blue continuous rectangle) defines the fill factor FF .

$$FF = \frac{j_{mpp} \cdot V_{mpp}}{j_{sc} \cdot V_{oc}} \quad 2.1$$

The energy conversion efficiency is described following Equation 2.2 with Φ as the incident power density of the photons.

$$\eta = \frac{j_{mpp} \cdot V_{mpp}}{\Phi} = \frac{j_{SC} \cdot V_{oc} \cdot FF}{\Phi} \quad 2.2$$

Regarding the basic physical principles of charge carrier transport inside a solar cell, the ideal I - V -curve can be described by the one-diode-model based on equation 2.3:

$$j(V) = j_0 \left(e^{\frac{q \cdot V}{k \cdot T}} - 1 \right) - j_{PH} \quad 2.3$$

with q representing the elementary charge, k the Boltzmann constant, j_0 the dark saturation current density, and j_{PH} the photo-generated current density.

Real solar cells are influenced by resistance and recombination losses. To take this into account, the one diode model has to be extended and a two diode model was developed by Chan *et al.* [13] and can be expressed with equation 2.4. The ideality factors n_a and n_b describe the quality of the single diodes, they are assumed to be $n_a = 1$ and $n_b = 2$ in the model case. For real solar cells the values can be different.

$$j(V) = j_{01} \left(e^{\left(\frac{q(V - |j \cdot r_s|)}{n_a \cdot k \cdot T} \right) - 1} \right) + j_{02} \left(e^{\left(\frac{q(V - |j \cdot r_s|)}{n_b \cdot k \cdot T} \right) - 1} \right) + \frac{V - |j \cdot r_s|}{r_p} - j_{PH} \quad 2.4$$

Fig. 2.3 shows the corresponding equivalent circuit of a solar cell. The first diode D_1 represents the recombination current in emitter and base (j_{01}), the second diode D_2 represents the recombination current in the space charge region (j_{02}), the series resistance r_s and the parallel resistance r_p represent electrical losses.

The I - V -curve of a solar cell can also be measured in the dark by applying a varied voltage and recording the corresponding current. The dark I - V curve describes the diode characteristic of the solar cell and is usually plotted semi-logarithmically with the measured current density against the voltage.

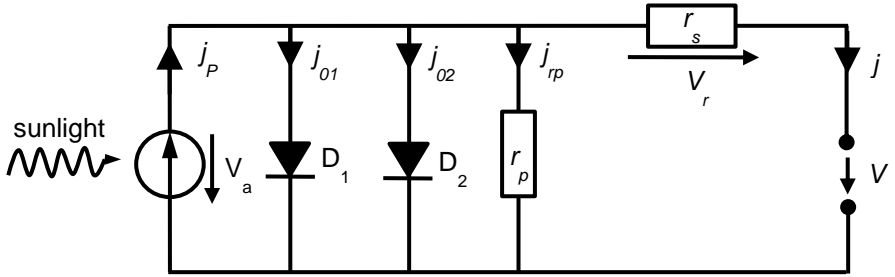


Fig. 2.3: Equivalent circuit of a solar cell, based on the two diode model. The first diode D_1 represents the recombination current in emitter and base (j_{01}), the second diode D_2 represents the recombination current in the space charge region (j_{02}), the series resistance r_s and the parallel resistance r_p represent electrical losses.

The shape of the dark I - V -curve is influenced by the parallel resistance r_p and the junction dark saturation density j_{02} in the lower voltage region. For higher voltages, the emitter dark saturation current density j_{01} and the series resistance r_s are the main influencing factors. Fig. 2.4 shows the dark I - V -curve of a solar cell with the marked indication areas.

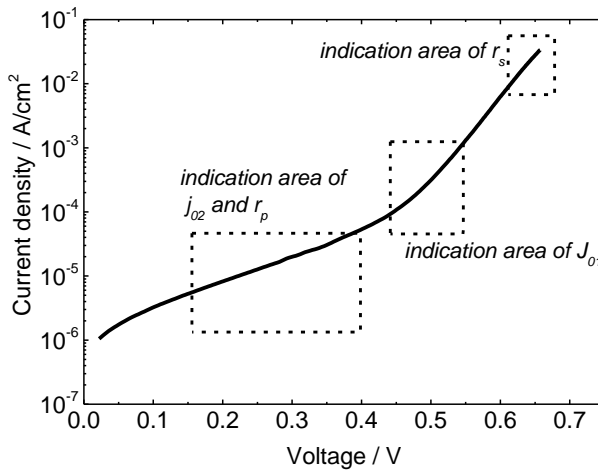


Fig. 2.4: Dark I - V -curve of a solar cell with marked indication areas

2.1.3 Loss mechanisms in silicon solar cells

The energy conversion efficiency of silicon solar cells is limited by electrical, optical and physical loss mechanisms. The sum of these losses reduces the theoretical maximum energy conversion efficiency to ~29% [14],[15]. The highest energy conversion efficiency for a monocrystalline silicon solar cell, reported by Panasonic in 2014, measured under standard testing conditions, is 25.6% [16], which is already quite close to the theoretical limit. For a multi crystalline silicon solar cell 20.76% is published 2014 [17] as record efficiency. Four main *physical loss mechanisms* cause the non-optimal exploitation of the offered solar spectrum and restrict the energy conversion efficiency:

Sub band gap photons

Photons with energy smaller than the band gap energy of silicon E_g^1 are not able to generate electron-hole pairs.

Excess energy photons

Photon energy exceeding the band gap energy is transferred into thermalisation. Each photon can create just one electron-hole pair, excess energy photons contribute only with the quasi-Fermi energy.

Fermi-level separation

The maximum achievable open circuit voltage is not equivalent to the band gap energy, it is far below because the separation of the quasi-Fermi levels defines the maximum achievable voltage [5].

Power limitation

The maximum power of a solar cell can offer is not given by the product of open circuit voltage and short circuit current density because the current depends exponentially on the voltage. This is illustrated by the non-rectangular shape of the I - V -curve (compare Fig. 2.2). Due to non-avoidable recombination currents the fill factor is limited to ~85%.

Fig. 2.5 shows the AM 1.5 g spectrum² [18] (indicated in grey) , while the red marked area illustrates the part of the spectrum which can be used for energy conversion by silicon solar cells. Photons with a higher wavelength than the band

¹ $E_g = 1.12$ eV for crystalline silicon at 300 K

² AM 1.5 g (Air mass 1.5 global) is the reference spectral distribution defined in the IEC 600904-3 [18] for terrestrial application. It corresponds to an irradiance of 1000 W/m² on a sun-facing plane surface with a tilt angle of 37° to the horizontal.

gap equivalent³ have not enough energy to generate electron-hole pairs and the energy of photons with a shorter wavelength is used only to some extent.

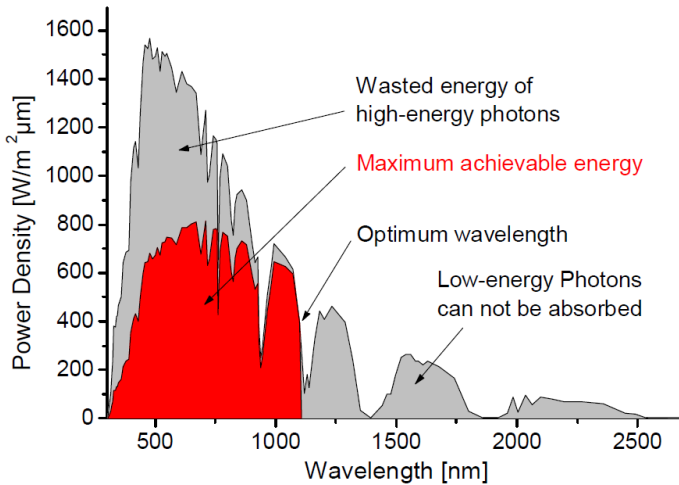


Fig. 2.5: Schematic drawing of the AM 1.5 g spectrum (grey) The red indicated area illustrates the part of the spectrum used for energy conversion by silicon solar cells [12].

The *electrical losses* can be divided in resistive losses and recombination losses.

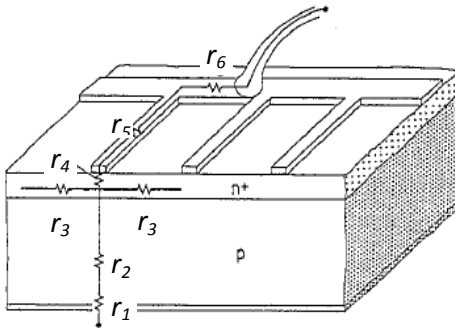
Resistive losses

The resistive losses are caused by the series resistance r_s and the parallel resistance r_p as it is illustrated in the equivalent circuit in

Fig. 2.3. The parallel resistance represents the quality of the electrical barrier between n- and p-type region in a solar cell. Parasitic currents between n- and p-type region due to carrier recombination, do not contribute to the electrical power generation.

The series resistance r_s of a solar cell is the sum of the resistivity contributions of the different parts in a standard solar cell structure as shown in Fig. 2.6 in a schematic drawing.

³ A wavelength of ~1104 nm corresponds to the band gap energy of silicon



- r_1 - contact resistance between the base and the metal contact
- r_2 - resistance of the semiconductor base
- r_3 - resistance of the semiconductor emitter
- r_4 - resistance of the emitter to metal contact
- r_5 - resistance of the contact fingers
- r_6 - resistance of the busbars

Fig. 2.6: Schematic drawing of the series resistance contributions (r_1 - r_6) at the structure of a standard back surface field solar cell [11]

The resistivity in the backside metallisation is not considered in Fig. 2.6, it is typically negligible due to the full area aluminium layer. The resistivity of the front side metallization is determined by the cross section of the metal contact structures and has to be sufficiently low to enable a current transport with as little losses as possible and simultaneously a preferably small shading area to minimize the optical losses. A good overview of the equations required for this optimisation can be found in [19].

Recombination losses

The photo generated minority carriers in a solar cell need to reach the p-n-junction by diffusion to contribute to the generated photo current. Several independently occurring recombination mechanisms in the cell limit the time and therefore the statistical diffusion length electron-hole pairs are able to travel until recombination. For each recombination process i a minority carrier lifetime τ_i and a recombination rate U_i can be defined for electrons and holes following equation 2.5, with the excess carrier concentrations Δ_n for electrons and Δ_p for holes:

$$\tau_i = \frac{\Delta_n}{U_i} \quad \text{for electrons or} \quad \tau_i = \frac{\Delta_p}{U_i} \quad \text{for holes} \quad 2.5$$

Fig. 2.4 illustrates the different recombination mechanisms: radiative-recombination (a), Auger-recombination (b), Shockley-Read-Hall recombination (c) and surface recombination (d).

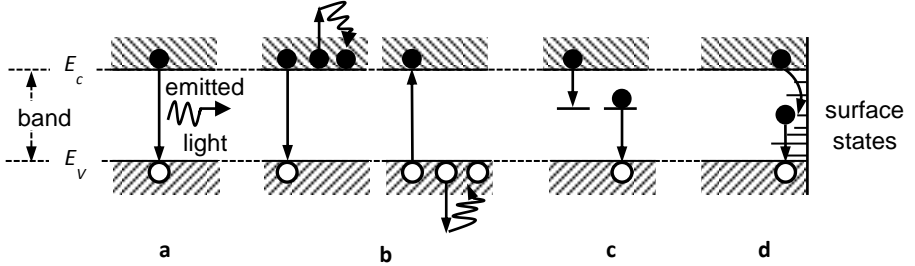


Fig. 2.7: Illustration of the recombination mechanisms in silicon solar cells at a schematic drawing of the band gap with the energy levels of the valence band E_V and the conduction band E_C for radiative recombination (a), Auger recombination (b), Shockley-Read-Hall recombination (c) and surface recombination (d)

Radiative-recombination

Radiative recombination (Fig. 2.7 a) is the reverse process of carrier generation by light absorption. Electrons and holes recombine under emission of light with the band gap energy E_g . In the indirect semiconductor silicon this recombination mechanism is unlikely because the participation of a phonon is required. However, it still occurs to some extent in regions where other recombination paths are weak and the detection of this photoluminescence is used to characterize solar cells (compare section 4.3.2). The recombination rate U_{rad} following equation 2.6 depends on the excess carrier concentration in the valence and conduction band and is negligible for usual doping concentrations.

$$U_{rad} = \frac{1}{\tau_{rad}} = B_{rad}(n_0 + p_0 + \Delta n) \quad 2.6$$

Auger-recombination

Another intrinsic recombination process in silicon is Auger-recombination discovered by Lise Meitner in 1922 and Pierre Victor Auger in 1923 [20]. During recombination the recombining carrier transfers its energy to a second electron or hole at the same energy level, which emits the energy to the lattice structure in form of phonons as it is illustrated in Fig. 2.7 b. The Auger-recombination rate depends on the amount of free electrons in the conduction

band or holes in the valence band and is therefore increased under high injection and at highly doped parts of the cell, like the emitter.

The carrier lifetime for n-type- and p-type-doped regions by Auger-recombination can be described with equation 2.7,

$$\tau_{Auger,n} = \frac{1}{C \cdot n \cdot p + D_e \cdot n^2} \quad \text{or} \quad \tau_{Auger,p} = \frac{1}{C \cdot n \cdot p + D_p \cdot p^2} \quad 2.7$$

where C is the Auger recombination rate constant and D_e , D_p are the diffusion constants of electrons and holes.

Recombination through impurity centres and crystal defects

Impurities and dislocations in the crystal lattice of silicon create energy states in the band gap of the semiconductor. These “trap” states can cause electrons to recombine by falling from the energy level of the conduction band to the energy level offered in the band gap and from there back to the energy level of the valence band (Fig. 2.7 c). This recombination mechanism was first described analytically by Shockley, Read [21] and Hall [22] and represents, in contrast to the recombination mechanisms described below, a non-intrinsic recombination mechanism defined by equation 2.8:

$$\tau_{SRH} = \frac{\sigma_p^{-1}(n_0 + n_1 + \Delta n) + \sigma_n^{-1}(p_0 + p_1 + \Delta n)}{v_{th} \cdot N_T(n_0 + p_0 + \Delta n)} \quad 2.8$$

with n_l and p_l defined as:

$$n_1 = N_C \cdot \exp\left(\frac{E_T - E_V}{k \cdot T}\right) \quad p_1 = N_V \cdot \exp\left(\frac{E_V - E_T}{k \cdot T}\right) \quad 2.9$$

With σ_n and σ_p the capture cross-sections for electrons and holes, E_T the energy level of the state created by an impurity in the band gap, v_{th} ⁴ the thermal velocity of the charge carrier and N_T the trap state density. The carrier lifetime τ_{SRH} depends on the amount of trap levels, the capture cross section and the energy level of the trap state in the band gap. The higher the capture cross-section and

⁴ $v_{th} = \sim 10^7$ cm/s at 300 K

the closer the energy level to the middle of the band gap the lower is the resulting carrier lifetime.

For standard industrial mono crystalline and multi crystalline solar cells this is the main recombination process. It can be influenced by the production process.

Recombination at the surface

The recombination at the surface of a semiconductor occurs due to a continuum of surface states with energy levels over the complete range of the band gap, created by abrupt ending of the crystal lattice and defects. These states can be used by electrons to fall from the conduction band level back to the valence band level (Fig. 2.7 d). To describe this recombination mechanism the recombination activity of all energy levels is integrated assuming a continuous distribution over the surface [23]. The surface recombination velocity S can be described following equation 2.10:

$$S = \frac{U_S}{\Delta n} = \frac{v_{th}(n_s p_s - n_i^2)}{\Delta n} \int_{E_v}^{E_c} \frac{D_{it} \cdot E_T}{\frac{(n_s + n_1)}{\sigma_p(E_T)} + \frac{(p_s + p_1)}{\sigma_n(E_T)}} d(E_T) \quad 2.10$$

with p_s and n_s defined as the electron and hole concentration at the surface, D_{it} the surface density of the states and n_i the electron or hole concentration. The surface density of states can be technologically reduced by covering the surface with an appropriate passivation layer (e.g., SiO_2 or SiN_x), which passivates dangling bonds by oxygen or hydrogen atoms. The reduction of the minority carrier density near the surface can be realized by doping the surface layer or building in fixed charges at the surface in a dielectric layer. A detailed analysis of the methods for reducing the surface recombination can be found in [23].

The *optical losses* are caused by mechanisms which keep away the light from the semiconductor by shading, reflexion, transmission or absorption in the metal contacts. This part of the light cannot be used for the generation of electron-hole pairs. In industrial solar cell production the wet chemical etching of a random pyramid structure on the monocrystalline silicon surface and the deposition of a 70 nm thick silicon nitride layer as anti-reflection-coating (ARC) are implemented to maximize the light trapping in the cell and to reduce reflection losses. The random pyramid structure on the monocrystalline silicon surface is

schematically shown in Fig. 2.8. The incident light striking the pyramids is refracted in angle ranges more flat than the refraction on a plane surface and it is refracted more than one time at the pyramid side surfaces. This reduces the light reflection by about $\sim 19\%_{\text{abs}}$ (at a wavelength of 600 nm) compared to a silicon wafer without random pyramid texture, as it is shown in Fig. 2.9.

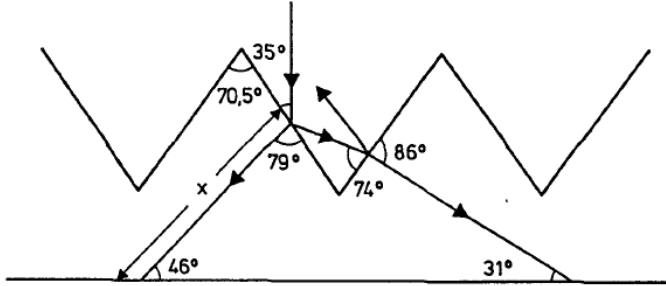


Fig. 2.8: Refraction of incident light at a random pyramid texture [24]

The refractive index and the layer thickness of the silicon nitride anti reflection coating is designed to reduce the total light reflection by destructive interferences at wavelengths of 600 nm. At this wavelength the solar spectrum offers the highest intensity. The ARC additionally serves as passivation of the silicon surface to reduce surface recombination as described above. Fig. 2.9 shows the total reflection of a mono crystalline silicon wafer surface over the wavelength of the incident light for different surface conditions: a surface in raw condition (continuous black line) a surface textured with random pyramids (dashed line) and a surface textured with random pyramids and covered with a silicon nitride layer as ARC (dotted line). The combination of the random pyramid texture and the ARC reduces the light reflection down to $\sim 0.15\%$ at a wavelength of 600 nm.

Fig. 2.10 shows the absorption length in silicon (dashed line, right axis) and the absorption coefficient of silicon (continuous line, left axis) over the wavelength. For photons with long wavelengths the absorption length is several times the wafer thickness, these photons have to be reflected internally at the rear side and the front side of the wafer several times to contribute to current generation.

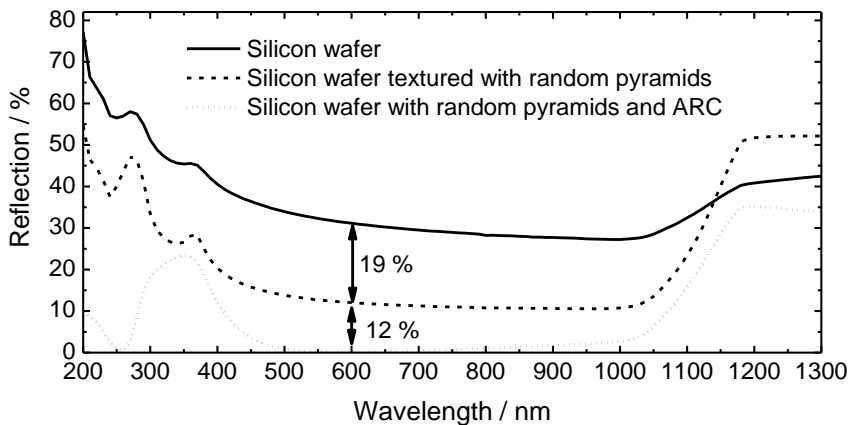


Fig. 2.9: Reflection over wavelength of a monocrystalline silicon wafer surface in raw condition (continuous line) textured with random pyramids (dashed line) and textured with random pyramids and covered with a 70 nm thick SiN_x anti- reflection-coating (dotted line)

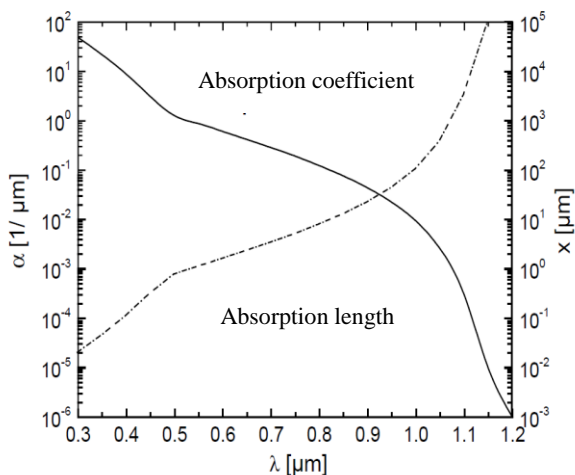


Fig. 2.10: Absorption length in silicon (dashed line, right axis) and the absorption coefficient of silicon (continuous line, left axis) over the wavelength [25]

2.1.4 Industrial realization of silicon solar cells

The p-type BSF solar cell with fully screen-printed silver front side metallization is the standard solar cell architecture in industrial mass production. The production process is relatively simple, the used techniques for the single process steps are well known and high throughput rates can be realized. $156 \times 156 \text{ mm}^2$ monocrystalline or multi crystalline silicon wafers, cut out of a silicon ingot by a multi wire saw are the raw material for the production process. For monocrystalline silicon two types of raw silicon can be distinguished. The so called “Czochralski-grown” monocrystalline silicon (Cz-silicon) [26] and mono crystalline silicon with a significantly higher purity level due to an additional purification by vertical zone melting [27], the so called float-zone silicon (FZ-silicon). For production of industrial monocrystalline solar cells, Cz-silicon material is used. The wafers are p-type doped by boron, which is added to the silicon melt to realize the basis doping.

Fig. 2.11 shows the schematic drawing of the process steps of the industrial production for silicon solar cells. The process chain can be grouped in the wet-chemical front-end processes (grey) and the back end processes (blue) with the deposition of the silicon nitride layer and the implementation of front and rear side contacts. As in this work a copper front side metallization is investigated, the back-end processes are of particular interest.

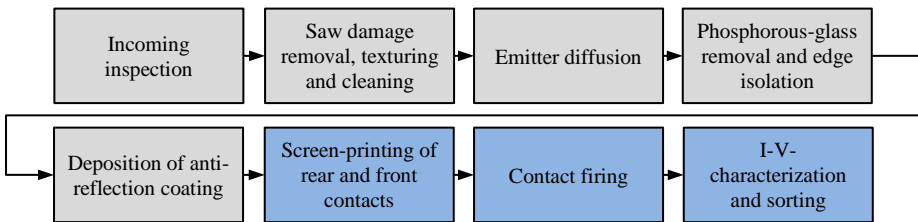


Fig. 2.11: Schematic drawing of the industrial basic production process for silicon solar cells. The production can be grouped in the wet-chemical front end processes (grey) and the back end processes (blue).

1. **Wafer inspection:** the wafers are inspected for μ -cracks using infrared transmission and sorted into the automation system of the production.
2. **Saw damage removal, texturing and cleaning:** in a first etching step the damages by wafer cutting are removed to get a flat and undisturbed wafer surface. Then the wafers are textured. For monocrystalline wafers sodium

hydroxide (70-80°C) with organic additives is used. For multi crystalline wafers a solution out of HF and HNO₃ is used (10-15°C).

3. **Emitter diffusion:** the emitter formation is realized by phosphorous diffusion in a tube furnace. Nitrogen is used as carrier gas, guided through a container of liquid phosphorous oxychloride (POCl₃) and released in the process chamber together with oxygen. The diffusion process is controlled by the temperature profile and the flow of the involved gasses.
4. **Phosphorous glass removal and emitter etch-back:** after emitter diffusion on both sides of the wafer, the surface is covered with a nanometre fine layer of phosphorous glass (PSG). As this glass is an insulator it has to be removed by hydrofluoric acid. Additionally the diffused emitter has to be removed completely on the backside of the wafer. This is realized in combination with the PSG removal using a single side etch process, which simultaneously removes the emitter in the edge zone of the wafer front side for junction isolation.
5. **Deposition of the anti-reflection coating:** a 70 nm thick silicon nitride layer is deposited by plasma enhanced chemical vapour deposition (PECVD) or sputtering. It acts as an anti-reflection coating and simultaneously passivates the emitter at the cell surface.
6. **Screen-printing of the rear- and front side contacts:** for contact definition three screen-printing steps using three different metal pastes are performed. At the rear side, busbar pads are printed with a paste containing aluminium and silver. On these pads the ribbon for the backside contact is soldered later on during module integration. The remaining cell surface at the backside is fully printed with an aluminium paste. The front side contacts are realized in the third printing step. A contact grid is printed with a silver paste directly on the silicon nitride anti-reflection coating (a detailed description of the screen-printing process is given in section 3.2.1). After printing, the paste is dried in an inline oven at ~250°C.
7. **Contact firing:** for sintering and contact formation between the printed metal structures on the rear and the front side to the silicon wafer, a firing step in a fast firing conveyor belt furnace is performed. For detailed description of the firing process and the contact formation, compare section 3.2.2.
8. **I-V-characterization and sorting:** under a flash light the *I-V*-parameters of the solar cells are measured and the cells are sorted in efficiency groups. The measurements are performed as close to the standard measurement

conditions as possible, with an irradiance of 1000 W/m^2 , and a spectral distribution in accordance with the normalized spectrum AM 1.5 g.

2.2 Electrochemical deposition of metals

The production of the copper front side metallization for silicon solar cells investigated in this work includes the electrochemical deposition of nickel, copper and silver on a printed seed-layer. The basic working principle of electrochemical metal deposition and the light induced plating technique used for solar cell plating are briefly introduced in this and the following section. The theoretical background knowledge discussed in section 2.2 and 2.3 and further information can be found in literature [28-30], sources for pictures and further information of specific issues are cited in the section.

The working principle of electrochemical metal deposition at an electrode (cathode) is based on the electrical discharge of metal ions in an electrolyte solution by intimate contact with the electrode surface. The positively charged ions receive an electron from the electrode, are reduced and consequently deposited as metal atoms on the electrode surface. If the needed electrons are delivered by an external power supply the process is called electrochemical metal deposition⁵. The sources of the metal ions are metal salts (e.g. nickel sulphate or copper sulphate) contained in the electrolyte solution. The counter process of the metal reduction is an oxidation process, which occurs at a sacrificial electrode (anode). The metal atoms of the anode are dissolved in the electrolyte by electron release and replenish the metal ion content. The principle of the electrochemical metal deposition is shown in a schematic drawing in Fig. 2.12.

The process of the electrochemical deposition can be divided in several sub-steps

- Transfer of the metal ions from the electrolyte to the cathode
- Removal of the hydrate shell the ions are covered with
- Charge transfer and formation of ad atoms
- Surface diffusion on the cathode and formation of a crystal nucleus
- Thermodynamically favoured growth of crystals to a metal layer

⁵ Another possibility is, that the electrons are delivered by the electrolyte itself, this process is called chemical metal deposition and is not further discussed in this work.

The steps of this simplified description of electrochemical deposition are schematically drawn in Fig. 2.13 a. The metal ions have to reach the cathode surface from the electrolyte where they appear covered with a hydrate shell. Inside the electrolyte the transport of this so called “solvated ions” is dominated by convection and diffusion. In the direct vicinity of the cathode surface the ions have to pass the Nernst diffusion layer (NDL) [31] and the compact Helmholtz layer (CHL) [32, 33].

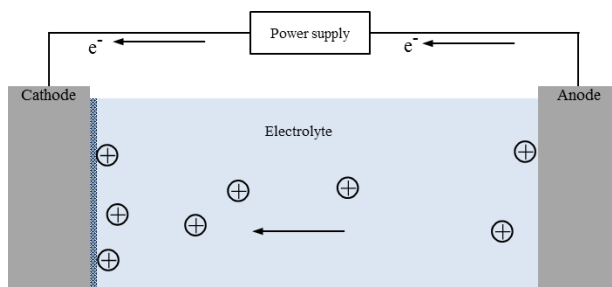


Fig. 2.12: Schematic drawing of the working principle of electrochemical metal deposition. Metal atoms from the anode are oxidized, dissolved in the electrolyte and reduced at the surface of the cathode ([30], redrawn).

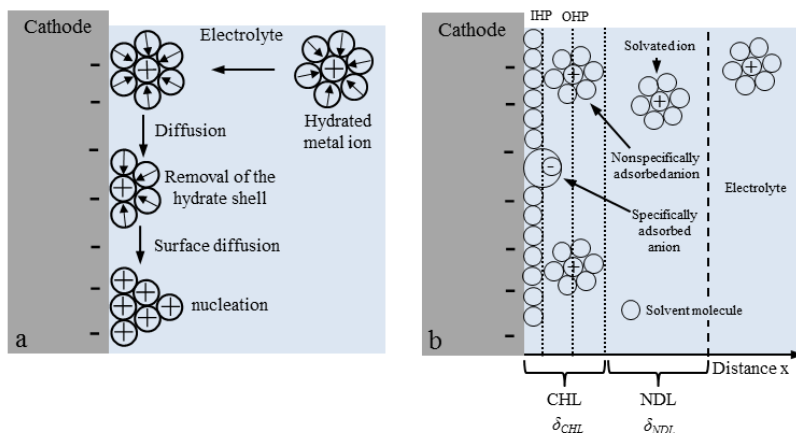


Fig. 2.13: Schematic drawing of the sub steps of electrochemical metal deposition (a) and the electrochemical double layer at the cathode surface. To be reduced the ions have to pass the Nernst diffusion layer (NDL) and the compact Helmholtz layer (CHL) composed of the outer Helmholtz plane (OHP) and the inner Helmholtz plane (IHP).

The model of an electrochemical double layer was developed to explain the behavior and the different states of the ions near the electrode surface. Almost the entire potential difference between electrolyte and electrode is determined by the electrochemical double layer especially by the Helmholtz layer. At the phase interface two oppositely charged layers are facing each other like in a capacitor; the negatively charged cathode surface and a layer of positively charged ions in the solution. The ions near the surface are in “specifically absorbed” condition; they can be both positively charged (before charge exchange) or negatively charged (after charge exchange). The line of their centers is called the inner Helmholtz plane (IHP). The still solvated ions can approach the cathode surface only to a specific distance; they are called “nonspecifically adsorbed”. The centers of these nearest solvated ions form the so called outer Helmholtz plane (OHP) (compare Fig. 2.13 b). The interaction between these ions and the electrode surface is based on long-range electrostatic forces and is independent of the chemical properties of the ions. In the Nernst diffusion layer (NDL), which is located between the OHP and the bulk of the electrolyte solution, the movement of the solvated ions is solely determined by diffusion. This layer cannot be removed by strong convection. This means that the reduction of the metal ions is always coupled to ion diffusion processes near the cathode in the electrolyte. The thickness of the compact Helmholtz layer δ_{CHL} is $\sim 10^{-8}$ cm and the thickness of the Nernst diffusion layer δ_{NDL} is $\sim 10^{-2}$ cm [30]. The thickness of the entire electrochemical double layer depends on the mobility of the ions in the electrolyte solution and the concentration of the electrolyte. It is characterized by the Debye length⁶.

If the described principle of electrochemical metal deposition is used to deposit metal layers on a work piece, the work piece acts as cathode. In the context of this work the front side metallization of a solar cell is used as cathode and consequently thickened by the deposited metal.

The local thickness of the deposited metal layer depends on the primary and secondary current density distribution in the process. The primary current density distribution is determined by the distribution of the electric field lines between anode and cathode. The distribution depends on the shape and the dimensions of anode and cathode and of their distance to each other as well as on the

⁶ The Debye length is the measure of the electrostatic effect of a net of charge carriers in a solution. It represents the radius of the Debye volume, which describes how far the electrostatic effect persists.

arrangement of anode and cathode in the electrolytic bath. At tips and edges the electric field lines are concentrated and the cathodic current density is higher. This leads to enhanced metal deposition. The smaller the electrolyte conductivity the more pronounced is the appearance of this phenomenon. At positions on the cathode with different distances to the anode, the current density is inversely proportionate to the distance. This is expressed with equation 2.11, where i_A and i_B are the two locations on the cathode and d_A and d_B are the corresponding distances to the anode.

$$\frac{i_A}{i_B} = \frac{d_B}{d_A} \quad 2.11$$

For simple electrode configurations the primary current density can be calculated according to equation 2.12. With R_{EB} and R_{EA} representing the electrolyte resistivity of position i_A and i_B to the anode.

$$\frac{i_A}{i_B} = \frac{R_{EB}}{R_{EA}} \quad 2.12$$

A balancing of the resistivities R_{EB} and R_{EA} leads to a homogeneous current density distribution and consequently to homogeneous metal deposition. For small inhomogenities between the different positions on the cathode, the extension of the distance between cathode and anode leads to a more homogeneous metal layer.

The secondary current density distribution is influenced by the conductance of the electrolyte. The conductance is proportional to the distance between electrode and work piece and describes the charge transfer. Fig. 2.14 shows the distribution of the electric field lines between anode and cathode (work piece) as reason for inhomogeneous deposition of the electrochemical deposited metal layer.

A more homogeneous metal layer can be achieved by the addition of leveling agents to the electrolyte solution. These chemical additives decelerate the metal deposition at exposed positions and are used to level the roughness of plated layers on work pieces. Another possibility is the adaptation of the anode configuration to the shape of the work piece or the application of auxiliary

anodes to reach a more homogenous distribution of the electric field lines between anode and cathode and therefore a more homogeneous metal deposition.

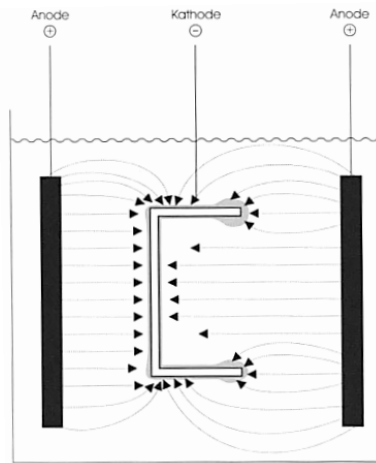


Fig. 2.14: Schematic drawing of the distribution of the electric field lines between anode and cathode (work piece) as reason for a inhomogeneous distribution of electrochemical metal deposition [30]

2.3 Light induced plating of solar cells

The Light induced Plating (LIP) technique uses the ability of the solar cell to generate a voltage under irradiation for selective metal deposition on the front side contacts. The idea to use the photovoltaic effect for electrochemical metal deposition of semiconductors with p-n-junction was patented in 1975 [34]. Related especially to the purpose of metal deposition on solar cells, this technique is mentioned in a patent from 1979 [35]. The description which is close to the LIP-process used in this work can be found in a patent by Grenon in 1981 [36].

The front side contacts of a p-type silicon solar cell are negatively charged under illumination and the backside contacts are positively charged. This is used to realize the selective reduction of the positively charged metal ions delivered by an electrolyte solution on the front side contacts of the cell. Consequently the front side contacts are thickened by the reduced metal. In contrast to electroplating, where the metal is mostly deposited at the area connected to the

applied negative voltage and the homogeneity of the plated layer on the work piece depends on its lateral conductivity, metal is deposited everywhere at the metallization grid during light induced plating because the electron-hole pairs are homogeneously generated over the cell area if a homogeneous irradiation is offered. In this work, metals were deposited on screen-printed and fired seed-layers on the cell front side. Even if the seed-layer is very thin and the lateral conductivity is small, the electrochemical deposition occurs on the entire front side grid. The silicon nitride layer which covers the cell surface between the printed contacts is non-conductive and acts as deposition mask. To prevent the simultaneous dissolution of the backside contacts (especially the silver pads) the oxidative counter process to the metal reduction is shifted to a sacrificial anode by a negative protective voltage which is applied to the solar cell backside. The positive thread of this voltage is applied to a sacrificial anode. Consequently the metal ions from the sacrificial anode are dissolved into the electrolyte and thus replenish it. Fig. 2.15 shows a schematic drawing of the working principle of light induced plating used in this work. The deposition speed during this process can be adjusted by the intensity of the illumination and the applied backside voltage.

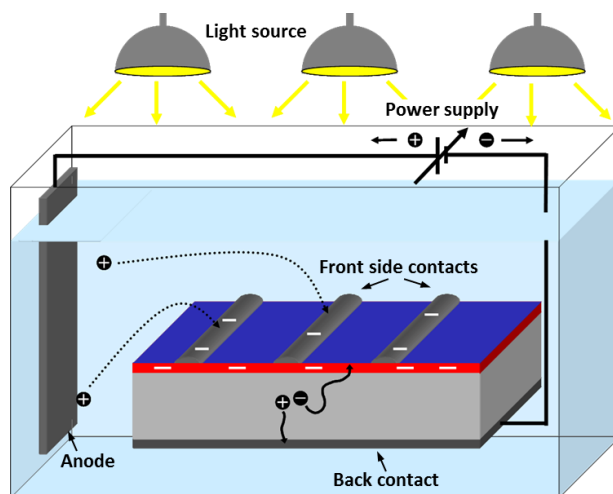


Fig. 2.15: Schematic drawing of the working principle of light induced plating for silicon solar cells

The cell is totally immersed in the electrolyte and illuminated by LEDs. The deposited metal can be chosen by the use of the electrolyte containing the respective metal ions and by the use of the corresponding anode material.

For industrial scale production the working principle is adapted to an inline process where the cell is moved through the electrolyte bath by rolls and is connected at the backside by contact brushes. The cell is immersed into the electrolyte only with the front side whereas the backside stays dry. This avoids the contamination of the porous backside metallization with chemicals from the electrolyte. Regarding copper this is possibly important in terms of long term stability.

2.4 Copper diffusion into silicon

Copper is a deep level defect in silicon and forms several acceptor and donator levels within the forbidden band gap if it is able to migrate into the solar cell. Those levels act as effective recombination centres with a strong negative influence on the resulting cell performance.

In general the diffusion process can be described by Fick's first and second law [37]. The diffusion is determined by the diffusion coefficient D according to Fick's first law according to equation 2.13, which depends on the species-specific factor D_0 , the Boltzmann constant k , the activation energy E_A and the temperature T .

$$D = D_0 \cdot \exp\left(\frac{-E_A}{k \cdot T}\right) \quad 2.13$$

Equation 2.13 describes the temperature dependence of the diffusion coefficient and is an Arrhenius type equation. The weak temperature dependence of D_0 is unattended.

Fick's second law can be used to get an expression for the diffusion length with the following boundary conditions:

- The diffusion source is infinite and offers a constant source concentration.
- Diffusion takes place in a semi-infinite medium.

With these boundary conditions, the solution of the differential equations of Fick's second law can be used to calculate the diffusion length L of a species into

a medium for a specific time according to equation 2.14 with the knowledge of the diffusion coefficient D at the considered temperature T .

$$L = \sqrt{D \cdot t} \quad 2.14$$

Inserting the expression for D given by equation 2.13 into equation 2.14 and solving the resulting term for the diffusion time t , results in equation 2.15:

$$t = \frac{L^2}{D_0 \cdot \exp\left(\frac{-E_A}{k \cdot T}\right)} \quad 2.15$$

Using the natural logarithm equation 2.15 can be written as:

$$\ln(t) = \left(\frac{E_A}{k \cdot T}\right) + \ln\left(\frac{L^2}{D_0}\right) \quad 2.16$$

Equation 2.16 can be rearranged to the form of a general linear equation ($y = a \cdot x + b$) resulting in equation 2.17:

$$\underbrace{\ln(t)}_y = \underbrace{\frac{E_A}{k \cdot 1000}}_a \cdot \underbrace{\frac{1000}{T}}_x + \underbrace{\ln\left(\frac{L^2}{D_0}\right)}_b \quad 2.17$$

For constant diffusion lengths L term b is constant. This means if the time to reach a specific diffusion state is experimentally evaluated at different temperatures the results can be plotted using an Arrhenius plot. The activation energy can then be determined from the slope of the linear regression through the data points. In the case of solar cells the specific diffusion state can be determined by measuring and evaluating full I - V characteristics of the solar cells as it is suggested by Grenon *et al.* [38]. As this implies great effort and requires the permanent availability of a cell-tester equipment if the degradation behaviour of the cells wants to be monitored over several hundreds of hours, another approach was followed in this work. It uses the advantage that the pFF can be used as measure for the degradation state and is published by Bartsch *et al.* [39].

This procedure assumes that a certain degradation of the pFF represents a certain depth of copper diffusion in the solar cell.

The diffusion coefficient of copper in silicon is determined by interstitial copper diffusion, the influence of substitutional diffusion can be neglected. In silicon, copper diffuses as positively charged ion, this was shown by Gallagher [40] and Hall and Racette [41]. Further analysis of copper diffusion in silicon by Weber confirmed this model [42]. This means that the diffusion coefficient of copper in silicon depends on the doping level and the doping type of the silicon (besides temperature). The first data for copper diffusion in intrinsic silicon was published by Struthers [43]. Later, Hall and Racette [41] published for copper diffusion in silicon: $D = 4.7 \cdot 10^{-3} \exp(-0.43 \text{ eV}/kT) \text{ cm}^2 \text{ s}^{-1}$. Istratov *et al.* [44] showed that this value is only true for highly boron doped silicon ($5 \cdot 10^{20} \text{ cm}^{-3}$) in the temperature range where the data points were taken ($\sim 900^\circ\text{C}$). Istratov *et al.* [44] take copper-acceptor pairing into account and determined for copper diffusion in intrinsic silicon in a temperature range between 265 K and 1173 K by the transient ion drift technique to: $D = 3 \cdot 10^{-4} \exp(-0.18 \text{ eV}/kT) \text{ cm}^2 \text{ s}^{-1}$. This agrees with the theoretical predictions by Estreicher [45]. This value is true for intrinsic or n-type silicon, while in moderately boron doped silicon ($N_a \leq 10^{17} \text{ cm}^{-3}$) the effective diffusion can be determined by the convenient numerical equation 2.18 dependent on the acceptor concentration N_a and the temperature T [44]:

$$D_{eff} = \frac{3 \times 10^{-4} \exp\left(-\frac{2090}{T}\right)}{1 + 2.584 \times 10^{-20} \exp\left(\frac{4990}{T}\right) \left(\frac{N_a}{T}\right)} \quad 2.18$$

Following equation 2.16 the effective copper diffusion coefficient in p-doped silicon with a acceptor concentration of $2 \times 10^{15} \text{ cm}^{-3}$ at 300 K ($\sim 27^\circ\text{C}$), is: $1 \times 10^{-7} \text{ cm}^2 \text{ s}^{-1}$. For comparison the diffusion coefficient of copper in nickel is determined to $2.51 \cdot 10^{-12} \text{ cm}^2/\text{s}$ [46] at 900°C . This means to diffuse a distance of $100 \mu\text{m}$ in silicon copper would need 1000 seconds or ~ 17 minutes at 300 K. To diffuse the same distance in nickel copper would need ~ 1.3 years at 900°C . This makes nickel a suitable diffusion barrier for copper.

If copper has penetrated into a silicon crystal, out-diffusion to the surface or precipitation are possible reaction paths. After analysis of the diffusivity of copper in p-type silicon, Istratov *et al.* [47] published a model, that suggests the conclusion that out-diffusion or precipitation in p-type silicon is determined by the Fermi level position. According to the model, precipitation is determined by

the electrostatic interaction between the copper ions and the copper precipitates. Especially n-type regions would promote copper precipitation and could act as gettering sites for Cu in silicon. The recombination activity of copper was analysed in a literature review by Istratov and Weber [48]. They found that copper forms at least four deep level states in the forbidden band gap, two in the upper half of the bandgap and two in the lower half of the bandgap. The experimental determination of the exact position of these states in the bandgap of silicon is a challenge due to the mobility of copper. The published results are diverse. However, according to Hopkins and Rohtagi [49] the critical copper contamination which leads to significant decrease in solar cell efficiency for cells out of mono crystalline silicon (Czochralski grown) is $\sim 10^{17} \text{ cm}^{-3}$. For gold, a concentration of $\sim 10^{13} \text{ cm}^{-3}$ and for titanium only a concentration of $\sim 10^{12} \text{ cm}^{-3}$ can be tolerated. According to [48] these differences correlate with the diffusion behaviour of the metals in silicon. Slow diffusors like Au and Ti stay in interstitial states with electrically very active multiple energy levels, whereas copper as very mobile impurity in silicon tends to agglomerate or precipitate meaning that the recombination activity depends on the availability of nucleation sites. This shows that the recombination activity of copper in silicon depends not only on the concentration but also on the composition of the silicon. In this work only solar cells from Cz grown monocrystalline silicon were investigated. The results are therefore not transferable to solar cells from multi crystalline silicon because multi crystalline silicon offers more inter crystalline precipitation sites (grain boundaries) which lowers the tolerable copper concentration compared to Cz-silicon significantly and would most probably lead to shorter long term stability due to copper migration.

3 State of the art of front side metallization for silicon solar cells and novel approaches

In this chapter the fundamental requirements for solar cell front side metallization are introduced (section 3.1). Contact geometry and silver consumption (section 3.1.1), contact adhesion (section 3.1.2), long term stability (section 3.1.3) and contact resistance as well as electrical conductivity (section 3.2.4) are important parameters with influence on solar cell performance and suitability of the respective metallization process for module integration. In section 3.2 the standard screen-printed front side metallization is described with a focus on the screen-printing process (section 3.2.1) and the contact formation (section 3.2.2). The novel copper front side metallization, investigated in this work, based on the seed- and plate approach is introduced in section 3.3. The process route (section 3.3.1), the state of the art (section 3.3.2) and the challenges, which hinder or complicate the industrial implementation of this metallization, are explained. In section 3.4 aerosol-jet printing (section 3.4.1), ink-jet printing (section 3.4.2) and flexographic printing (section 3.4.3) as alternative processes to screen-printing regarding the seed-layer deposition are presented. In section 3.5 the direct plating approach as alternative copper metallization is shortly introduced.

3.1 Requirements for solar cell front side metallization

A solar cell front side metallization has to satisfy physical, mechanical and economical requirements to enable a low-loss solar cell operation and to be considered for industrial production. Contact geometry and silver consumption, long term stability, contact adhesion, contact resistance and electrical conductivity are introduced in the following sections.

3.1.1 Contact geometry and silver consumption

The needed silver consumption per cell decreased over the last years due to progress in screen-printing. In 2014 a silver consumption for front side metallization of ~100 mg per cell is assumed to be realistic by leading PV manufacturers [50]. Fig 3.1 shows the needed silver consumption per cell in

2013 and 2014 and the estimated decrease of the silver consumption in the future (black triangles).

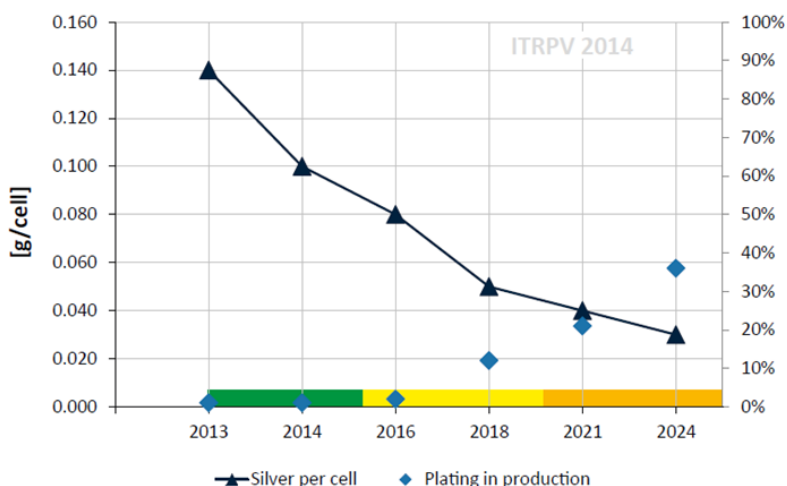


Fig. 3.1: Proportion of needed silver per cell ($156 \times 156 \text{ mm}^2$) and the predicted share of the plating technology in production. The colour code refers to the technical solution to achieve the predicted reduction of the silver consumption: existing industrial solution (green), industrial solution is known but not jet in mass production (yellow) and interim solution is known, but too expensive or not suitable for production (orange) [50].

According to the International Technology Roadmap for Photovoltaics (ITRPV) [18] copper is the intended substitute for silver on the front side of the cells. Copper can be deposited in an industrial scale by plating techniques. The blue diamonds in Fig. 3.1 show the predicted market share of plating technologies in solar cell production, which is expected to rise from 2016 on. The high cost pressure in solar cell production and the progress in the screen-printing technology led to a strong reduction in silver consumption needed for the front side metallization of silicon solar cells over the last years. Fig 3.2 shows published values for paste consumption between 2010 and 2014. A decrease of down to less than 100 mg paste per solar cell front side on lab scale can be observed, which means significant progress for this metallization technique in terms of costs.

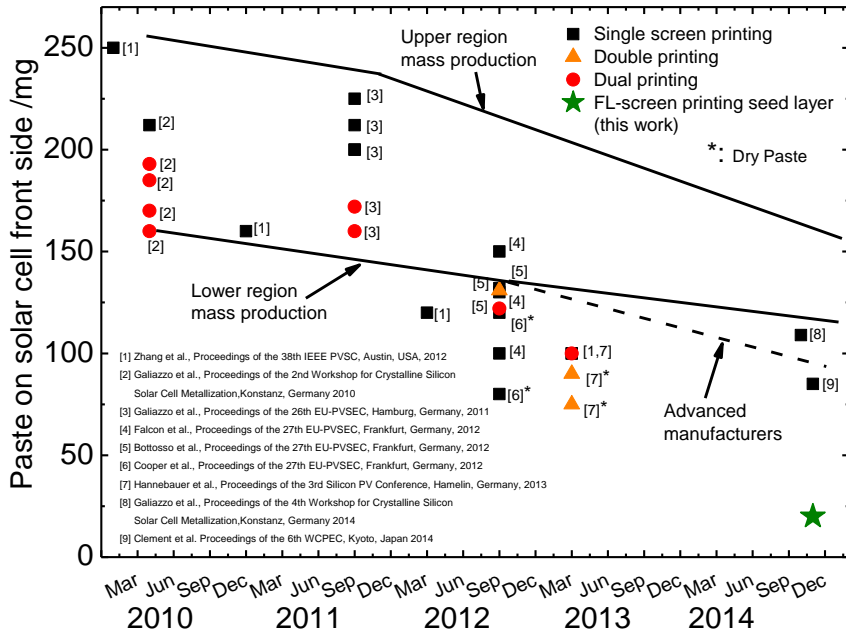


Fig. 3.2: Silver paste consumption for solar cell production published between 2010 and 2014 for single printing (black squares) double printing (red circles) and dual printing (orange triangles) and the paste amount for fine line screen-printing achieved in this work (green star)

Technologically less paste transfer could result in narrower contact fingers, which is always desired because of the reduced shading losses. At the same time a certain contact finger cross-section is needed to enable sufficient lateral conductivity. This resulted in the development of pastes which enable high aspect ratios (ratio contact height/width).

The requirements for lateral conductivity are not crucial for seed- and plate metallization because lateral conductivity is realised by the plated layer and not by the printed seed. This offers the advantage to optimize the printed seed-layer regarding fine contact structures, low paste consumption per cell and a good contact resistance to the emitter.

3.1.2 Contact adhesion

Sufficient adhesion of solar cell front side contacts is important for the automated interconnection of the cells to strings by tabber-stringer machines. The strings are interconnected and laminated to solar modules. As these production steps are done automatically, the contacts have to stand the stress due to automated handling otherwise the rejection rate exceeds the order of magnitude which is economically feasible in industrial production. The standard DIN EN 50461 “Solar Cells” [51] defines the standard peel-force value of 1.0 N/mm; while the details of the peel-force test procedure are defined in DIN EN 28510 [52] and IEC 61189-2 [53]. However, solar cell producers often define their own specifications according to the individual requirements of the interconnection processes and quality standards. A contact adhesion specification of 1.5 N/mm is often communicated. Both the mode of determination (peel force measurement procedure) and the mode of analysis of the result (averaged peel force, determination of the highest peaks etc.) are not consistent throughout the PV community. To achieve acceptance in the market for a new front side metallization architecture sufficient contact adhesion is a key issue.

3.1.3 Long term stability

The long term stability qualification of PV-modules refers to the test standards defined in the IEC 61215 standard [54]. Table 3.1 shows an overview of the temperature related stress tests (column 1) conducted with the modules in different test sequences with the respective test procedure (column 2) during IEC testing.

Table 3.1: Temperature related procedures for PV-modules according to IEC 61251 [54]

Test according to IEC	Procedure	Power output criteria
Damp Heat	1000 h, 85°C, 85% r. h.	< 5% degradation
Thermal cycling	50/200 cycles: -40°C, +85°C	
Humidity freeze	40 cycles: -40°C, +85°C at 85% r.h.	
UV-test	15 kWh/m ²	

The tests are complemented by wet leakage current tests, a hail-test, a mechanical load test and different tests regarding outdoor exposure and hotspot endurance. The pass criterion is a degradation of the output power of $< 5\%$. Additionally a visual inspection is conducted before and after the test procedures. The aim of these test procedures is to simulate the environmental impact a module is subjected to during its lifetime in an accelerated manner. To achieve this, the stress level applied to the modules during the test procedures is higher than the real stress level in standard module operation.

Fig. 3.3 shows the percentage of module failure of tested modules at Fraunhofer ISE and TÜV Rheinland [55] for the temperature related tests listed in table 3.1. Damp Heat test, thermal cycling test and humidity freeze test have the largest impact on PV-module performance. The IEC qualification test determines the minimum long term stability requirement for all PV-modules to be admitted into the market. There is no guarantee that a module which passes the IEC test sequence with less than 5% degradation will stand 20 or 30 years in the field with similarly low loss because the real stress in module operation depends strongly on the specific module location. The tests are designed to test the long term stability of the encapsulation materials and the electrical interconnection of the cells.

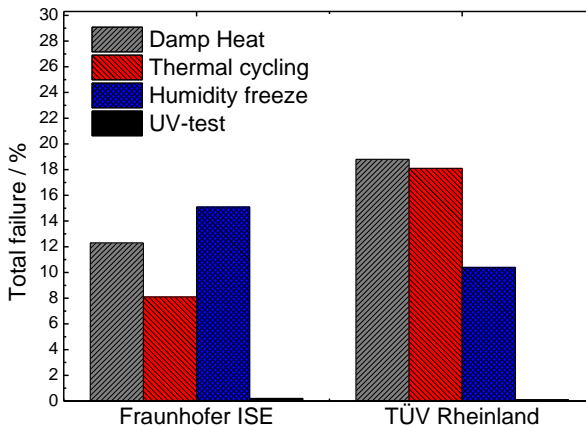


Fig. 3.3: Total failure of tested modules for damp heat test, thermal cycling test, humidity freeze test and UV-test at Fraunhofer ISE and TÜV Rheinland [55]

As the solar cell itself is not the final product on the PV-market there is no test standard for solar cell long term stability.

3.1.4 Electrical conductivity and contact resistance

The solar cell front side metallization has to collect the current generated in the solar cell and transport it, with as little resistivity losses as possible, to the cell connectors. To realize this, the metallization has to feature a small contact resistance to the emitter and a sufficient lateral conductivity of the metal grid. Otherwise the series resistance of the cell rises, which limits the fill factor and consequently the cell efficiency (compare section 2.1.3). Pysch *et al.* revealed that an increase of $1 \Omega\text{cm}^2$ in series resistance reduces the fill factor by $\sim 5\%$ absolute [56]. The contact formation of all standard printed front side metallizations is realized by a glass frit, which etches the non-conductive silicon nitride layer during the firing of the cells (the process of contact formation is described in more detail in section 3.2.2). This contact formation principle is the same for fully screen-printed contacts as well as for contacts produced with the seed- and plate approach using a printed seed-layer, with the difference that the silver paste used for fully printed contacts has to realize both contact formation and lateral conductivity whereas the seed-layer paste can be optimized for contact formation only, while the lateral conductivity is realized by the plated metal.

Hörteis *et al.* investigated the electrical properties of seed- and plate contacts featuring aerosol-jet printed seed-layers subsequently silver plated. They found that: “...the contact formation between the seed-layer and the emitter of a solar cell is more efficient with a thin seed-layer...” due to the formation of a very thin glass layer [57]. Seed-layer paste development and therefore contact resistance engineering is not in the focus of this work, but as the focus of paste development has never been only on contact formation so far, there is possibly great potential for further optimizations especially for screen-printed seed-layers.

The lateral conductivity of fully screen-printed contacts is enabled by the sintering of the silver particles in the firing furnace. The air filled cavities and glass particles distributed inside the contact (compare Fig 3.4) have a negative effect on the lateral conductivity. This makes a bigger contact cross section area necessary to enable sufficient lateral conductivity, which inevitably leads to shading losses. A plated copper layer does not contain entrapped air or glass particles (compares Fig 3.8) and offers sufficient lateral conductivity with a smaller cross section area. A point of reference for the lateral conductivity of the contact fingers can be given by the resistivity measured between the busbars of a solar cell, which is included in the automated cell tester measurement procedure.

The resistivity should be between 30-50 Ω/m to represent a value of sufficient lateral conductivity for solar cell performance that is not limited in efficiency by lateral grid conductivity.

3.2 Screen-printed silver front side metallization

Screen-printing is today the most common and wide spread technique used for solar cell front side metallization, printing a silver paste for full contact creation in one step. It came into the focus of solar cell research in the 1970s [58] and was implemented into solar cell production in the 1980s [59], [60]. The process is cheap, fast (throughput rates of > 1200 wafers per hour and printer) and implemented in solar cell production lines all over the world. The working principle of the screen-printing process and the subsequent contact formation in the firing furnace are described in the following subsections.

Fig. 3.4 shows a microscope cross section image of a fully screen-printed contact finger after firing on a monocrystalline silicon solar cell.

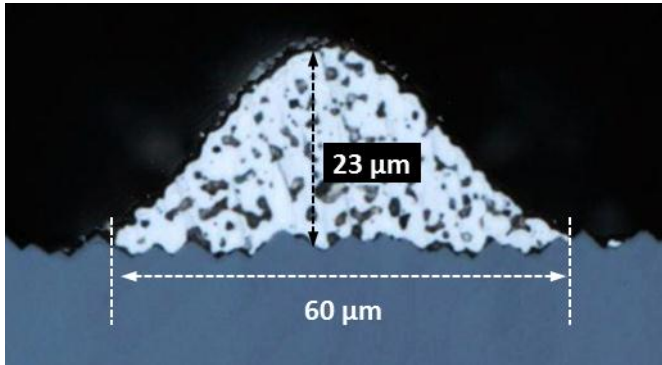


Fig. 3.4: Microscope cross-section image of a fully screen-printed contact finger with a width of 60 μm and a height of 23 μm

3.2.1 Screen-printing of the front side metallization

In screen-printing a screen is patterned in the desired printing design by crafting openings into the organic emulsion that covers the mesh. For solar application a paste composed of silver particles, glass frit, organic compounds and solvents is forced through the mesh at the open positions onto the solar cell surface by a squeegee. A printing screen consists of a mesh of wires, usually out of stainless

steel, which is clamped into a frame. The desired printing layout is photo-lithographically structured into an emulsion layer. Fig. 3.5 shows a schematic cross section of a screen (a) and a detailed illustration of the wires (b). A top view SEM image of the fine line screen used for seed-layer screen-printing in this work is shown in Fig. 6.1.

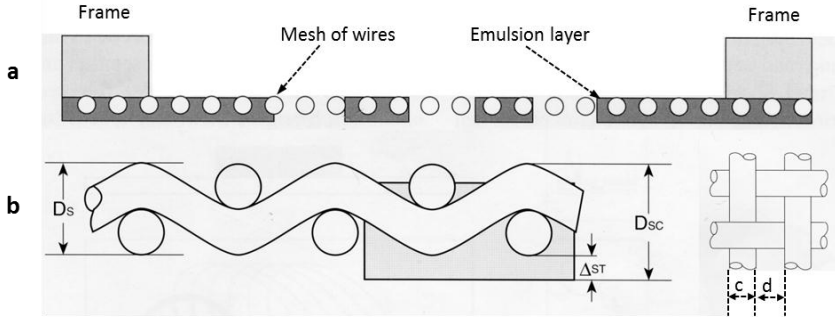


Fig. 3.5: Schematic drawing of a screen cross section (a) and detailed illustration of the screen wires with D_s the thickness of the screen mesh, Δ_{st} the thickness of the emulsion layer, D_{sc} the total screen thickness, c the wire diameter and d the wire distance [61]

During the printing process a silver paste is forced through the openings in a screen, by the motion of a squeegee onto the solar cell surface. The printing process can be divided in three phases:

1. The fill phase: the screen (especially the open areas in the emulsion) is flooded with paste by the horizontal movement of the squeegee. The flooding is realized either directly by the paste bead in front of the squeegee or by a floodbar, which is firmly installed at the squeegee and runs in front of it.
2. The contact phase: the squeegee runs over the flooded screen by applying a vertical force. This presses the screen onto the substrate and forces the paste through the screen openings. The paste sticks on the surface of the printing substrate.
3. The release phase: the squeegee pressure ends and the screen is lifted from the printing substrate releasing the paste, which sticks on the substrate [62].

Fig. 3.6 illustrates the described phases of a screen-printing step at a schematic drawing.

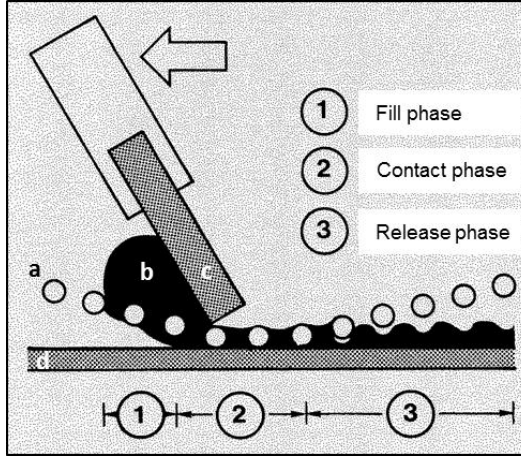


Fig. 3.6: Schematic drawing of the screen-printing process in three phases: 1) fill phase: the screen (a) is flooded with paste (b), 2) contact phase: the squeegee (c) presses the screen onto the substrate (d) and forces the paste through the screen openings, 3) release phase: the screen is lifted from the substrate and the paste is released from the screen and sticks to the silicon surface [62].

The printing result is influenced by the interaction of the used screen, the behaviour of the paste (influenced by viscosity, solid content, particle size, yield stress etc. compare chapter 6), the used substrate and the printing parameters. The printing speed, the printing pressure and the snap-off (distance between screen and substrate before the contact phase) can be set by the operator to adjust the printing result.

The number of wires per inch defines, combined with the wire diameter, the distance between the wires, which represents the minimal possible resolution defined by the screen parameters. The screen opening fraction a_0 as ratio of the screen opening area to the total screen area is defined as shown in equation 3.1.

$$a_0 = \frac{d^2}{(c+d)^2} \quad 3.1$$

For fine line printing a mesh with fine wires and therefore a high wire separation distance is desirable. In this work a screen with 400 mesh (wires per inch) and a wire diameter $c = 18 \mu\text{m}$ was used (compare chapter 6). This

corresponds to a wire distance $d = 45.5 \text{ } \mu\text{m}$. The minimum achievable line width w_{min} can be calculated by an empirical equation defined in [62, 63]:

$$w_{min} = c \frac{(2c+d)\sqrt{2}}{d} \quad 3.2$$

For a screen with the described dimensions $w_{min} = 45 \text{ } \mu\text{m}$. This value represents a point of reference and not an absolute value. It can be smaller in practise if the angle between the fine openings in the emulsion and the wire mesh is 22.5° [62], which was the case for the used screen. The finest contact finger width achieved experimentally during this work was $30 \text{ } \mu\text{m}$ by specific adjustment of the paste rheology (compare chapter 6). This shows that the reached result is close to what is possible with the given screen configuration. Nakayama *et al.* used a special screen featuring 900 mesh, a wire diameter of $12 \text{ } \mu\text{m}$ and an emulsion opening of $25 \text{ } \mu\text{m}$ but the printing resulted also in a contact finger width of $30 \text{ } \mu\text{m}$ [64]. However, as this result was obtained for full contact deposition, an optimization for seed-layer printing might still show some width reduction potential. For smaller printed contact fingers a screen with finer wires and finger emulsion openings is needed.

3.2.2 Contact formation in the firing furnace

During the firing step in the inline fast firing belt furnace, several processes occur that influence the solar cell and especially the metallization:

1. The printed aluminium backside metallization sinters to a solid metallization layer and forms the so called back surface field (BSF). The back surface field represents a highly doped p^+ -region, which is formed by an eutectic between aluminium and the silicon. It is formed during the cooling phase by recrystallization at the eutectic temperature of 577°C [65]. The BSF reduces the surface recombination at the rear side [66].
2. The front side surface passivation is enhanced by hydrogen, which leaves the silicon nitride layer (SiN_xH_y) and passivates dangling bonds and unsaturated states at the silicon surface [67].
3. The front side metallization is fired and a contact is formed between the front side metallization and the emitter. Additionally the silver particles in the printed and dried paste sinter to a solid metallization structure.

Fig 3.7 schematically shows a typical temperature profile of the fast firing process for the contact formation on crystalline silicon solar cells in a conveyor belt furnace. It can be divided in four temperature zones: In the first zone the solvents are evaporated from the paste at temperatures between 200 and 400°C. In the second zone the organics and binders are burned at temperatures between 400°C and 600°C. In the third zone the contacts are formed. The temperature is rapidly elevated to a peak temperature of 800-900°C. This temperature is held for 1-3 seconds, during this period the front side silver contact to the phosphorus doped n^+ emitter are formed and the (full area or local) aluminium p^+ back surface field (BSF) is alloyed. In the fourth zone the wafer is rapidly cooled down to room temperature. The total processing time for zones 1 to 4 is about 60 s. The exact temperatures of the four zones are respectively adapted to the fired cells and the used metallization pastes to obtain an optimal contact formation.

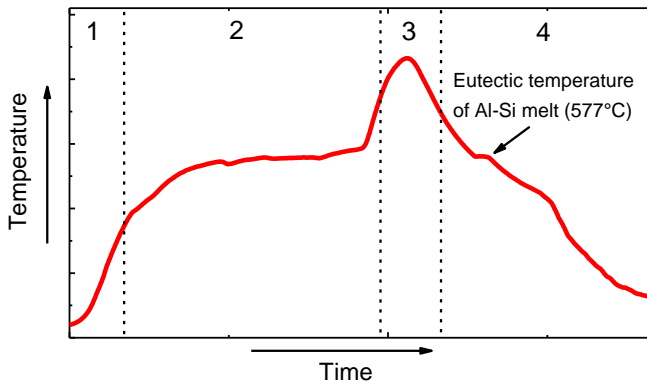


Fig. 3.7: Temperature profile of a typical fast firing process for the contact formation on crystalline silicon solar cells in a conveyor belt furnace. The process can be divided in four temperature zones: in zone 1 at 200-400°C the solvents are evaporated, in zone 2 at ~400-600°C organics and binders are burned, in zone 3 the contacts are formed at peak temperatures between 800°C and 900°C and in zone 4 the wafer is cooled down to room temperature.

The contact between the front side metallization and the emitter is formed by the etching of the silicon nitride layer under the printed paste by the glass frit, which is contained in the silver paste. Schubert investigated in 2006 the underlying reactions in detail and published the following model of the contact formation in the firing step shown in Fig. 3.7 [68].

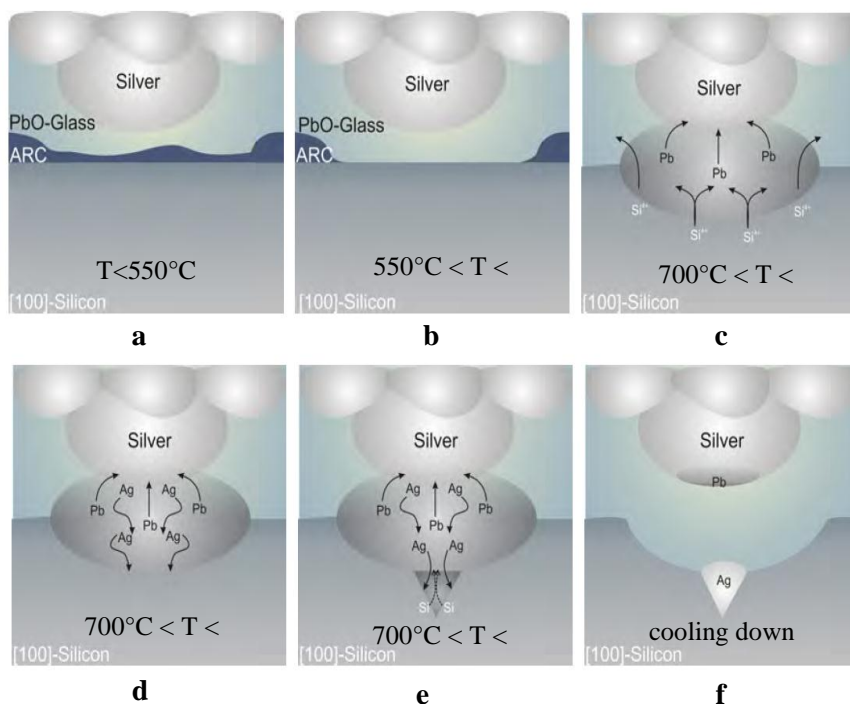


Fig. 3.8: Schematic drawing of the contact formation process according to the model published by Schubert [68]

At temperatures between room temperature and 550°C the viscosity of the glass frit decreases and initial melting of the silver particles might occur (a). Between 550°C and 700°C the molten glass wets the silver particles and removes the silicon nitride layer by etching (b). Between 700°C and 800°C the contact formation occurs. The lead oxide in the glass reacts with the silicon, additionally lead is formed and silver crystals start growing (c). Lead promotes the melting of silver and a liquid lead-silver phase is formed (d). This phase melts the [100] silicon planes an inverted pyramid grow into the silicon (e). During the cooling phase silver grows into the silicon and forms crystallites, whereas the lead migrates to the bottom side of the silver fingers (e).

A study by Hong 2009 [69] investigated the role of the glass frit for the silver crystallite formation, and revealed that the solubility of the silver and the viscosity of the glass frit are important factors to control the size and the

distribution of the silver crystallites at the glass silicon interface. The silver crystallites are regarded as important current path between emitter and metallization and thereby influence the contact resistance. A detailed study of possible current paths especially for plated contacts can be found in [19].

3.3 Ni-Cu front side metallization on printed seed-layers

In this work a metallization based on a fine line screen-printed silver seed-layer, a nickel diffusion barrier, a copper conductive layer and a thin silver capping is investigated. With this metallization architecture the silver consumption can be lowered down to < 15 mg per cell which corresponds to a reduction of about 84% compared to advanced thick film silver front side metallization in 2014. Fig. 3.9 shows a microscope cross section image of a contact finger with Ni-Cu-Ag metallization based on a screen-printed silver seed-layer.

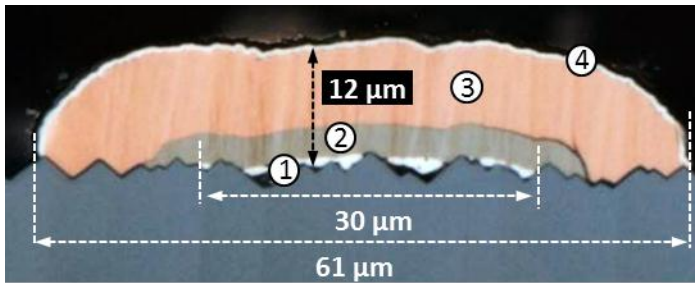


Fig. 3.9: Microscope cross-section image of a Ni-Cu-Ag metallization based on a screen-printed silver seed-layer (1), a plated nickel diffusion barrier (2), a plated copper conductive layer (3) and a fine silver capping (4) with a width of $61\ \mu\text{m}$ and a height of $12\ \mu\text{m}$

Besides the reduction in silver consumption the seed-and plate metallization approach offers the advantage that the needed technologies are available and approved in industrial scale. Fundamental questions regarding the technological requirements for solar cell front side contacts like contact geometry; contact adhesion and long term stability are addressed in this work and discussed in the following sections.

Additionally, the Ni-Cu metallization offers the advantage of partial substitution of silver by nickel and copper. The nickel layer acts as diffusion barrier to enable a sufficient long term stability of the cells and copper acts as

conductive layer offering a similar conductivity than silver. The process route, the technological state of the art and the challenges for this metallization architecture are introduced in the following subsections.

3.3.1 Process route

The Ni-Cu metallization offers the advantage of partial substitution of silver by nickel and copper with little process adaptations of the common front side metallization process route (compare section 2.1.4). The light induced plating of nickel, copper and silver has to be implemented and the existing screen-printing process has to be adapted regarding the printing of fine seed-layers (e.g. fine line screens and fine line Ag-pastes have to be used).

The light induced plating process was already established in industry for silver plating on silver seed-layer for solar cell front side metallization, industrial scale inline capable machines are available in the market. Fig. 3.10 shows the back-end process route, the additional process compared to the screen-printed standard front side metallization is the light induced plating, indicated in grey.

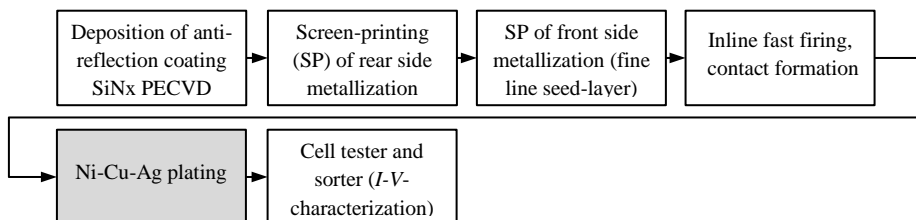


Fig. 3.10: Process route (back-end) for solar cell front side metallization by plating of Ni-Cu-Ag on top of a screen-printed silver seed-layer

Standard fully screen-printed silver metallization has to realize both the contact formation to the emitter and a sufficient lateral conductivity. The decoupling of these requirements by the seed-and plate approach offers the advantage to optimize the seed-layer paste for optimal contact formation while the lateral conductivity is realized by the plated metal layers.

3.3.2 State of the art

The first results of nickel and copper plated contacts on printed seed-layer were published by the supplier of inline plating machines RENA in 2009 [70]. They show a 0.5% efficiency advantage for cell plated with Ni-Cu-Sn on screen-printed seed-layers compared to standard fully screen-printed references. Further

results for nickel and copper metallization on printed seed-layers with high efficiency potential and sufficient long term stability of the cells were published by Bartsch *et al.* in 2010 [71]. On $2 \times 2 \text{ cm}^2$ cells out of high efficiency material (FZ-silicon, $110 \text{ } \Omega$ shallow emitter), with passivated front and rear side and an aerosol printed seed-layer, efficiencies of 20.3% were shown. The authors came to the conclusion that the industrial production of such cells is possible. Binder *et al.* published promising results on $20 \times 20 \text{ mm}^2$ cells with aerosol printed seed-layer and plated Ni and Cu [72]. Mette *et al.* showed results of a Q-Cells pilot line experiment for standard solar cells on industrial scale, with screen-printed seed-layer and silver plating [73]. Thus the proof of concept for the seed- and plate approach with plated silver on screen-printed contacts and for plated nickel and copper on aerosol printed seed-layers is already done. However, no results of solar cells metallized with Ni-Cu-Ag contacts based on screen-printed seed-layers for silicon solar cells were published so far. Apart from principal demonstrations on lab-scale solar cells, no investigations regarding the practicability of the approach from general process considerations until the realization of solar cell modules have been done. In this work, solar cells with standard industrial size of $156 \times 156 \text{ mm}^2$ were produced using screen-printed, aerosol printed and ink-jet printed silver seed-layers (compare section 6). The focus of this work is to address the challenges that come along with the industrial production of full scale solar cells and modules, described in the following subsection.

3.3.3 Challenges

In this work the focus of research is on industrial scale processes for solar cells with copper front side metallization based on a printed silver seed-layer. In addition to the mere proof of concept at lab type cells, several challenges for cells with the described front side metallization have to be addressed:

1. Practical experiences with the production of full scale $156 \times 156 \text{ mm}^2$ solar cell with Ni-Cu-Ag plated front side metallization based on a screen-printed seed-layer are very rare, as described above. Obstacles often occur upon implementation and have to be identified and described to specify the issues of further research.
2. Contact adhesion of the printed seed-layer after the plating processes is known to be a problem, which is not entirely understood to date. The

reactions and corrosion mechanisms in the interaction between the electrolyte solution and the printed contacts have to be investigated and understood to enable process improvements and incorporation on the cells into modules by soldering. Additionally, corrosion mechanisms of printed contacts are of interest from the perspective of module long term stability.

3. As copper can migrate into the solar cell and cause considerable cell degradation the long term stability of solar cells with copper front side metallization has to be investigated. The existing standard IEC tests for long term stability are not designed to show cell degradation for instance due to copper migration into the silicon. If copper metallization-methods gain a growing market share a rapid test should be designed for cell qualification.
4. Seed-layer printing using the screen-printing technology has not been optimized yet. The printing process with best qualification for industrial production is screen-printing because it is already widely used for front side metallization in the solar industry. The challenge is to print fine seed-layers with this technique which are comparable in geometry and silver consumption to seed-layers printed by ink jet or aerosol jet printing.

3.4 Alternative seed-layer printing technologies

In this work a nickel-copper metallization based on the seed- and plate approach is investigated. A printed silver seed-layer enables the contact formation to the emitter of the solar cell in the firing process and works a seed-layer for the electrochemical metal deposition of nickel, copper and silver. Even though the investigations in this work focus on seed-layers realized with the screen-printing process, as it is closest to the present industrial standard (compare section 3), the three alternative seed-layer printing technologies, aerosol-jet printing, inkjet-printing and flexographic-printing were used and compared with the benchmark data of the screen-printing process. These processes have been developed in the past to represent alternatives to screen-printing for seed-layer formation with narrow line width and low paste consumption potential. They are introduced and discussed briefly in the following subsections. Besides the introduced metallization techniques alternative printing technologies exist, which have been also used for solar cell metallization or are still investigated like stencil printing, dispensing, roller printing and pad printing. These technologies have not been

considered for seed-layer formation in the present work, as better perspectives were seen for the alternatives addressed in the following.

3.4.1 Aerosol jet printing

Aerosol jet printing is a contactless printing method, in which a metal ink becomes nebulized and is guided to the wafer substrate. To nebulize the ink different techniques like ultrasonic transducers or pneumatically driven nozzles can be applied. The formed aerosol is transported through a deposition head and focused on the substrate supported by sheath gas. Fig. 3.11 shows a schematic drawing of the aerosol jet print head. The sheath gas to aerosol flow ratio influences the fluid flow and thereby the mass throughput and line width and has to be adjusted to the print head design and the desired printing structure [74]. The focused aerosol beam flows through the pint nozzle and impacts onto the substrate surface.

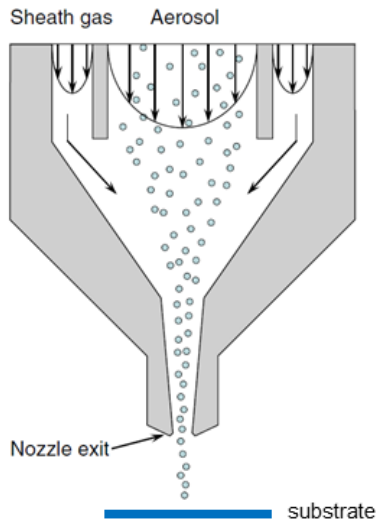


Fig. 3.11: Schematic drawing of the aerosol jet print head [74]

In this work a half automated aerosol jet system developed at Fraunhofer ISE featuring a printing head with ten nozzles with a nozzle diameter of 150 μm was used. The substrate was placed 2-3 mm below the printing nozzle on a heatable chuck. To avoid spreading of the printed seed-layer the chuck was heated to 150 $^{\circ}\text{C}$ during the printing step. The used silver ink was developed at

Fraunhofer ISE based on the results of Hörteis *et al.* [75], Binder *et al.* [72] and Kalio *et al.* [76].

With the aerosol jet system fine and narrow seed-layers with a silver consumption < 10 mg per Wafer [77] can be achieved which become subsequently thickened by plating to reach sufficient lateral conductivity. Seed-layer inks are optimized for contact formation between metallization and emitter. Major research and development regarding aerosol printing for silicon solar cells was done by Mette [19], [78]. Based on this work the contact formation of aerosol seed-layers also to emitters with high sheet resistance was analysed by Hörteis [79, 80], [81].

3.4.2 Ink jet printing

Ink-jet-printing is a contactless, computer controlled, direct write printing technique with high line resolution. The printing pattern is defined in a file and the print head, equipped with several nozzles transfers the grid structure on the silicon wafer by drop wise printing of a silver ink. First experimental results regarding solar cell metallization were published by Teng in 1988 [82]. Two general methods for drop generation allow the classification of ink-jet printers in two families: drop-on-demand and continuous-jet systems. The working principles are shown in a schematic drawing in Fig. 3.12.

The continuous-jet system (Fig. 3.12 a) generates a continuous ink-jet which is forced through the nozzle by high pressure. Electrical signals divide the continuous jet into droplets. The non-needed droplets are deflected by an electrical field and collected in a gutter. Droplet output frequencies in the MHz-range enable a high printing speed [83].

The drop-on-demand systems (Fig. 3.12 b) generate and precisely control every single droplet, which are generated by piezo-electric pulses in the nozzle [84]. Droplet output frequencies in the kHz range restrict the printing speed but several advantages like less ink consumption and the fact that the ink does not have to be charged like in continuous-jet systems make the drop-on demand system to the most used ink-jet technology [85].

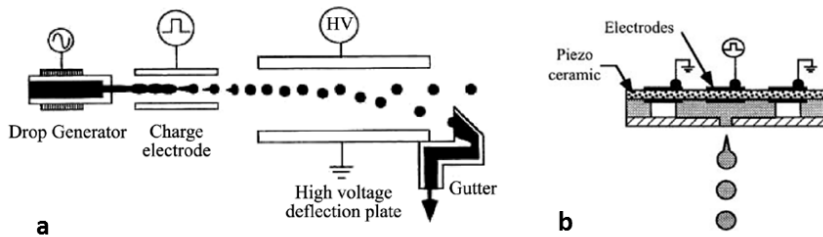


Fig. 3.12: Schematic drawing of a continuous-jet binary deflection inkjet system (a) and a drop on demand (shear mode) ink-jet system (b) [83]

To be printable through the fine nozzles, the viscosity of the used silver ink is considerably lower than the one of screen-printing pastes. The inks consists a higher fraction of solvents and exclusively use silver particles in the nanometre scale. These factors make inks more costly than standard printing pastes. To realize full metallization of solar cells several printing steps have to be conducted to reach contacts with sufficient lateral conductivity. For seed-layer purpose the small ink laydown achieved by one or only few printing repetitions is desired because the lateral conductivity of the contact grid is realized by the plated metal. Promising solar cell results have been published using the inkjet technique for seed-layer purpose with silver plating in 2010 [86].

In this work the half automated ink-jet printing system MiniJet developed by XJet Solar, working with the drop on demand system (saving costly ink) was used. The drop volume for contact finger printing was set to ~ 4 pl. The printing system works with 11 printing heads, each equipped with 512 nozzles. To reduce the process time, two wafers can be printed in parallel on two heatable vacuum chucks. To minimize the spreading of the fine printed lines, due to the low viscosity of the ink, theses operation chucks were heated to 230°C .

3.4.3 Flexographic printing

Flexographic printing is a roll-to-roll based printing method using flexible relief printing plates. A so called anilox roller (a steel cylinder with finely textured ceramic or chromium surface) transfers a specific amount of silver containing ink from the ink reservoir to elevated areas of the printing plate, which is mounted on the printing cylinder. Traditionally, photopolymer-based printing plates are used for flexographic printing. This type of plate is fabricated by UV exposure and subsequent development of the non-exposed areas of the printing

form. Laser engraved elastomer printing plates represent a new alternative with an improved durability against solvents, a considerably higher resistance against abrasion as well as a higher resolution of the fine line elements [87]. The plate is fabricated by laser-removal of the non-printing areas, sparing the printing layout that consequently remains at an elevated level. The ink is transferred from the anilox roll onto the elevated elements of the printing plate and the printing cylinder deposits it by low pressure contact of the printing plate to the solar cell substrate [88]. Fig. 3.13 shows a schematic drawing of the functional principle (a) and a picture of the used printing cylinder with printing plate (1) and printed solar cell (2).

The method offers the potential of a high throughput (~3000-5000 wafers/h [88]) and is well suited for the application of seed-layer front side grids. The low ink transfer in one printing step enables a wet-ink consumption for the seed-layer of < 10 mg/cell [88] and creates fine and narrow lines. Research about flexographic printing for silicon solar cells has been started by Fraunhofer ISE [88], [89], TU Darmstadt [90] and the laboratory of pulp and paper science [91], but no inline capable tool optimized for solar cell printing exists so far. In this work the half automated flexographic printing device Angstromer S15 from Nissha was used. Standard $156 \times 156 \text{ mm}^2$ solar cells were positioned manually on a height adjustable vacuum substrate holder chuck and were printed using a elastomer printing plate featuring a H-pattern front side grid with 90 contact fingers.

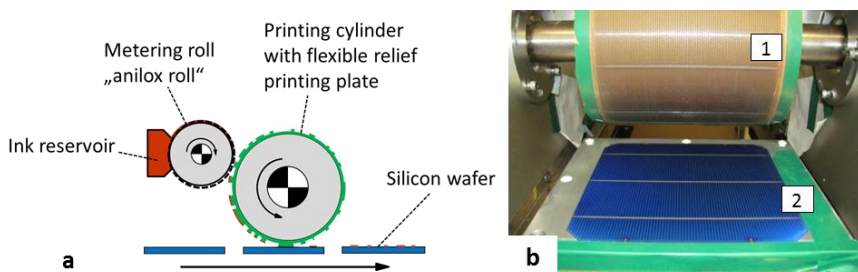


Fig. 3.13: Schematic drawing of the functional principle of flexographic printing (a): the ink (red) is transferred by an anilox roller from the ink reservoir to the printing plate (blue). The printing plate is mounted on the printing cylinder, which transfers the ink to the substrate by low pressure contact. Picture of the used printing cylinder (b) with flexible relief printing plate (1) and printed solar cell (2) [88]

3.5 Ni-Cu front side metallization by direct plating

An alternative process to realize Ni-Cu metallization on the front side of silicon solar cells is the direct plating approach. The Ni-Cu direct plating enables a solar cell front side metallization without silver by direct plating of the nickel diffusion barrier on the silicon surface. Fig. 3.14 shows the microscope cross section image of a direct plated contact with a nickel diffusion barrier (1), a copper conductive layer (2) and a tin capping layer (3), a copper conductive layer (2) and a tin capping layer (3).

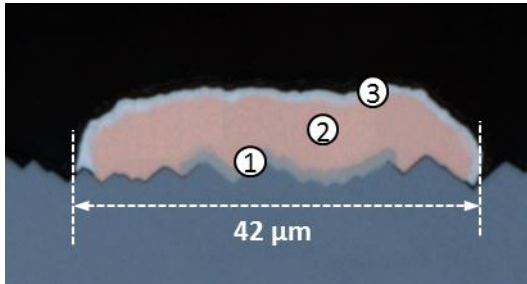


Fig. 3.14: Microscope cross section image of a direct plated contact finger with a nickel diffusion barrier (1), a copper conductive layer (2) and a tin capping layer (3) with a contact finger width of 42 μm

In 1990 BP Solar produced the so called “Saturn Cells” featuring laser grooved buried contacts [92] and in 2009 SunTech started an attempt to bring the “Pluto” modules containing solar cells with direct plated nickel and copper front side metallization into the market [93]. The SunTech approach shows a reduced process complexity compared to the production of BP, but most probably due to adhesion problems, SunTech was not able to commercialize this product. In the last years several technical problems with the direct plating of Ni-Cu, such as poor contact adhesion, were addressed by the research of institutes [94], [95] and companies [96]. Challenges like back ground plating, the long term stability of the cells or shunting due to nickel spiking through the emitter [97] hinder the introduction on an industrial scale to date. The question which is the optimal process route for direct plating of Ni-Cu contacts is not definitely answered. Several paths are under research [98]. A review about direct plated Ni-Cu contacts can be found in [99].

Fig. 3.15 introduces the simplest process route for back-end of a solar cell production by direct plating of Ni-Cu-Sn, which is under research at Fraunhofer ISE and offers the potential of industrial scale implementation. The process steps marked with an X are additional processes compared to the standard screen-printed front side metallization and the processes marked with an V are additional processes compared to the seed-and-plate approach investigated in this work. The only process which can be skipped compared to the other approaches is the front side screen-printing step.

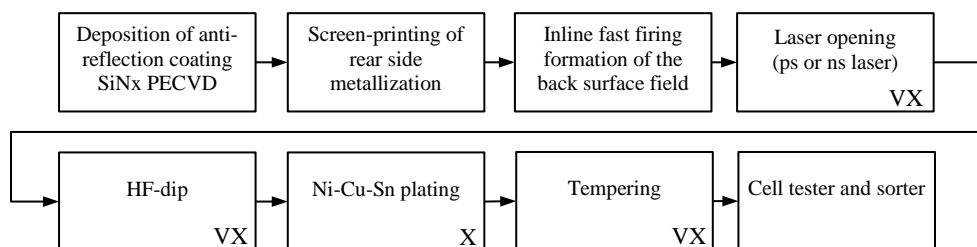


Fig. 3.15: Process route (back-end) for solar cell front side metallization by laser opening of the anti-reflection-coating and direct plating of Ni-Cu-Sn

The positioning of the plated grid is realized by laser opening of the desired pattern in the silicon nitride layer prior to the plating process. The silicon nitride anti-reflection coating is electrically not conductive and acts as mask for the non-opened areas. The plating occurs only directly on the silicon surface and is realized by light induced plating. To achieve a good contact between the plated nickel and the silicon a HF-dip as pre-treatment is needed after laser opening. Also an additional tempering step after plating is required, which lowers the contact resistance and is also beneficial for contact adhesion. The advantage of this metallization is the complete substitution of silver by nickel and copper and tin at the front side of silicon solar cells. On the other hand additional processes like laser opening and HF-dip increase the process complexity and therefore the process costs for front side metallization production (compare section 10) compared to the standard screen-printed silver front side metallization (compare section 3.2) and the seed-and-plate approach investigated in this work (compare section 3.3).

4 Characterization methods for solar cells and solar cell contacts

In this chapter the most important characterization methods and tools, used to obtain the experimental results this work is based on, are introduced and briefly discussed. For optical characterization of the solar cell contacts, confocal laser scanning microscopy was performed (section 4.1.1). Further scanning electron microscopy (section 4.1.3), scanning transmission electron microscopy (chapter 4.1.3) and atomic force microscopy (section 4.2.4) were used to analyse the microstructure of the contacts. The preparation of investigated cross sections was done by ion polishing (chapter 4.1.2). To evaluate the contact adhesion after the plating process and to characterize the effect of different solutions and process conditions, the quantitative peel-force-test (section 4.2.1), combined with the analysis of the different contact failure mechanisms (section 4.2.2) of solar cell contacts, was an important procedure. For electrical characterization for solar cells and lifetime samples Suns Voc measurements (section 4.3.1), photoluminescence measurements (section 4.3.2), electroluminescence measurements (section 4.3.3) and quasi steady state photo conductance measurements (section 4.3.4) were used. To analyse the species dissolved out of the contacts during exposure in different chemical solutions, inductively coupled plasma enhanced optical emission spectroscopy (section 4.4.1) as well as cyclic voltammetry (section 4.4.2) and powder X-ray diffraction measurements (section 4.4.3) came into operation. For the investigations of possible correlations between screen-printed seed-layer geometries and the rheological parameters of silver pastes, a controlled shear stress test (section 4.5.1) with additional evaluation of the yield stress (section 4.5.2) were conducted.

4.1 Optical characterization of solar cell contacts

4.1.1 Confocal laser scanning microscopy

Confocal laser scanning microscopes enable the detection of optical images from the measured surface with depth selectivity. The working principle is based on the possibility to alter the vertical distance between light sensor and sample while detecting the light reflection from the sample surface. Every height plane of the sample profile is scanned detecting the intensity of the reflected light. Out of the measured data the software calculates a three dimensional image by

combining the data of every plane of focus measured over the detected height profile of the sample. By combining a white light signal and a laser (405 nm) signal, the microscope is able to record a microscopic image and a 3D profile to achieve colour illustration of the sample surface. The software is additionally able to stitch several images to increase the measurement area and allows the calculation of average profiles along a chosen length of the measured structure. In this work the LEXT OLS-4000 from Olympus was used to characterize solar cell front side metallization structures. A 1000-times magnification (100-times from the objective with a highest magnification and 10-times from the ocular) can be realised. Fig. 4.1 shows the exemplary image in the colour 3D-illustration (a) the laser signal (b) and the calculated height profile in false colour rendering (c) of a solar cell front side metallization contact finger.

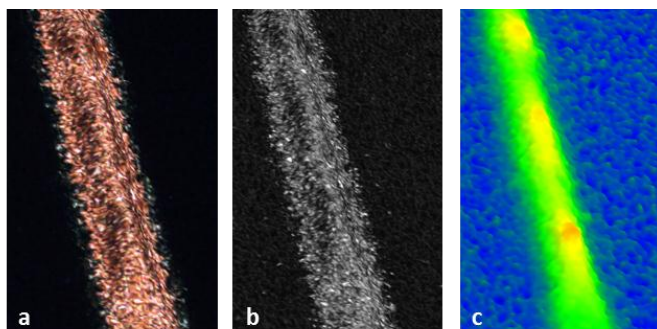


Fig. 4.1: Confocal laser microscope image of a copper plated contact finger in color illustration (a), the measured laser signal (b) and the calculated height map in false color rendering (c)

4.1.2 Cross-section preparation

To investigate cross-sections of the Ni-Cu-Ag solar cell front side contacts with microscopic methods (i.e. SEM, TEM, AFM or confocal laser microscopy) the cross-sections were prepared using an ion beam polisher. Especially for the SEM microstructure analysis of the boundary layer between the printed seed-layer and the silicon wafer an accurate preparation of the cross-section was indispensable to achieve a flat cross-section surface at which every detail is visible and where the interfaces were unaffected by possible damages or delamination due to high local forces from mechanical polishing. The rough cross-section preparation of the solar cell samples was done by dicing or laser cutting, both methods produce

residues due to the mechanical or thermal impact which make the undisturbed evaluation of the cross section impossible. In order to remove these residues and to polish the cross-section surface the ion milling system IM4000 by Hitachi was used. An ion gun accelerates argon ions, creating a beam which is directed to the cross section of the sample, placed behind a titanium mask providing a sharp edge. The ions gradually remove the part of the sample which is not protected by the mask. Fig. 4.2 a shows a schematic drawing of the sample installation in the milling system and Fig. 4.2 b illustrates the sputtering of the sample part which overlaps the titanium mask by the ion beam at a schematic drawing.

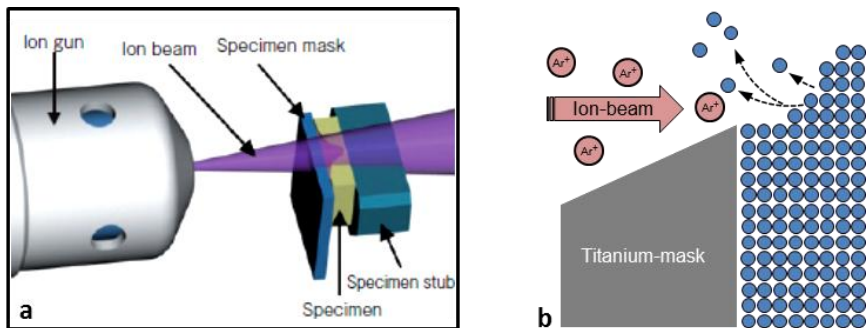


Fig. 4.2: Schematic drawing of the sample orientation to the ion gun in the cross-section milling system (a) [100] and a schematic drawing of the sputtering of the sample part which overlaps the titanium mask by the ion beam (b)

Fig. 4.3 shows the cross-section of a Ni-Cu-Ag metallization plated on top of a screen-printed seed-layer after cutting with the dicing saw (a) and after cutting and subsequent polishing of the cross-section surface using an ion beam (b).

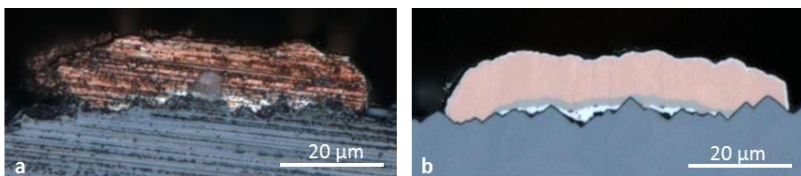


Fig. 4.3: Microscope image of a contact cross-section after dicing (a) and after dicing and subsequent polishing of the cross-section surface using an ion beam (b)

In the raw condition after dicing the different metal layers are not visible due to the rough surface and the smearing of the copper over a wide part of the cross-section area. After polishing the cross section appears flat and the different metal layers can be studied.

4.1.3 Scanning electron microscopy and energy dispersive X-ray spectroscopy

An important tool for microstructure analysis of solar cell contacts in the sub micro meter range is the Scanning Electron Microscope (SEM) invented by Max Knoll and Ernst Ruska [101]. To create an image, electrons are used instead of light as in an optical microscope. Since the wavelength of electrons is lower than that of visible light, this technique enables far higher resolutions. An electron beam is rasterized under vacuum over the sample, controlled by lenses and focused by magnetic fields. The interdependency of the electrons with the sample is used to create an image of the surface. The electrons are accelerated from a cathode under high voltage to the sample where they are reflected and detected as backscattered electrons (BSE) or where they release other electrons from the sample detected as secondary electrons (SE). The detector converts the collected electrons into a voltage signal and a grey scale intensity picture is created [102]. Fig. 4.4 shows the arrangement of the detectors at the used SEM SU70 by Hitachi.

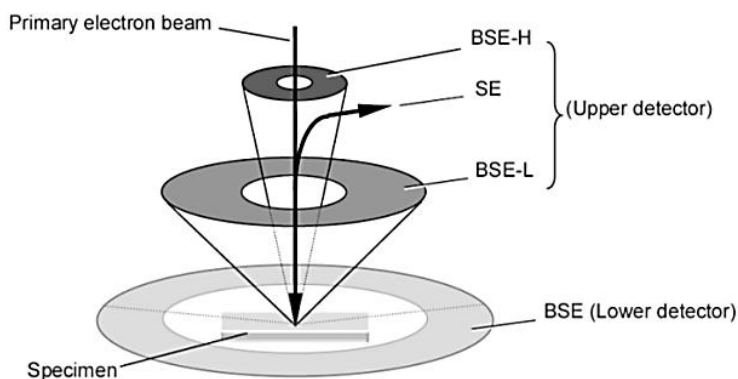


Fig. 4.4: Schematic drawing of the detector installation at the Hitachi SU 70. Back scattered electrons (BSE) and secondary electrons (SE) generated at low angles (L) and at high angles (H) can be detected by different detectors positioned at the optimal position [103].

The energy dispersive X-ray spectroscopy (EDXS or EDX) enables the determination of the elemental composition of the measured sample. By a special EDX-detector the energy/wavelength of X-rays generated at the sample during electron bombardment can be detected and correlated to the specific data of elements. The X-rays are excited from a large interaction volume even at low acceleration voltages; this restricts the resolution and complicates the measurement analysis especially for characterization of microstructures. For SEM applications the lateral spatial resolution of the EDX signal is $\sim 1\text{ }\mu\text{m}$ [104]. In combination with transmission electron microscopy (method description in the following section) considerably higher resolutions of $\sim 10\text{ nm}$ [104] can be obtained.

4.1.4 Scanning transmission electron microscopy

Scanning Transmission Electron Microscopy (STEM) enables far higher resolutions than SEM. In contrast to SEM the electron beam is focussed at a sample lamella with a thickness in the nanometre scale. The resulting image is generated by electrons transmitted through the sample [105]. Fig. 4.5 shows an example of a lamella mounted on a micro manipulator, prepared out of a random pyramid textured wafer at Fraunhofer ISE.

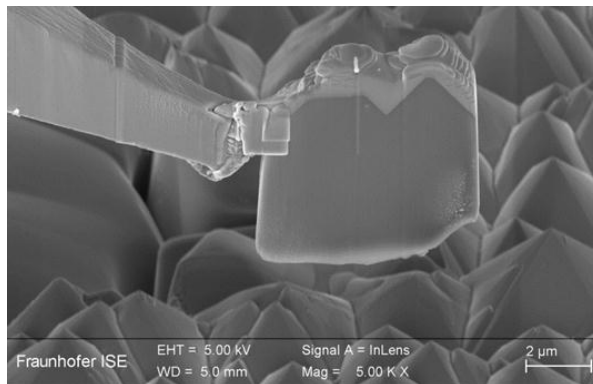


Fig. 4.5: Lamella mounted on a micro manipulator prepared out of a random pyramid textured wafer using a focused ion beam at Fraunhofer ISE

In cooperation with the Max Planck Institute (MPI) in Halle, a TEM analysis of the glass-silver interface inside solar cell contacts was performed during this work. For this analysis a specimen was prepared which is translucent to an

electron beam, i.e., a 100 to 200 nm-thick slice. This lamella was taken in cross-section orientation out of a solar cell contact by means of a focused ion beam (FIB) with Ga⁺ ions using a FEI Nova Nanolab 600 FIB at the MPI. In order to analyse the distribution of the elements included in the glass-layer of the solar cell contact, scanning transmission electron microscopy imaging and EDXS were carried out using a FEI TITAN3 G2 60-300 electron microscope equipped with an image spherical aberration (Cs) corrector and a super-X EDX detector system. This detector offers the advantage of very low dwell times per pixel, which minimizes the damage of the material under the electron beam. The EDXS-maps in Fig. 7.16 were acquired with a physical resolution of 0.44 nm / pixel and a total measurement time of 7 ms / pixel.

4.2 Mechanical characterization of solar cell contacts

4.2.1 Peel-force-test

In this work the contact adhesion of solar cell front side contacts out of a Ni-Cu-Ag metallization based on a printed Ag-seed-layer is investigated. Only soldered contacts, either continuously manually soldered or spot wise automatically soldered contacts were used to check the contact peel-force. For the detailed description of the used soldering processes compare section 5.3.

Before executing the peel-force test the soldered contacts rested for at least 24 hours, to allow the soldered joint to settle. Afterwards the soldered cell connector was peeled off at an angle of 90° while recording the measured peel-force. Complementary to the measured peel-force, the evaluation of the rip-out mechanism is necessary to allow a precise interpretation of the results.

To evaluate the adhesion of soldered front side contacts the peel-force tester Frolyt PCE FM 50, shown in Fig. 4.6, was used. The tester is designed according to DIN EN 28510-1 [52] and enables the quantitative measurement of the contact peel-force of standard solar cell contacts ($1.5 \times 156 \text{ mm}^2$) at different angles. A ribbon which is longer than the contact was soldered in a way that it reaches over the cell edge. This extension of about ~3 cm was fixed, with a clamp mechanism using a locking bolt, to the force gauge while the cell is mounted in a hold down unit. The casing with the cell moves down at a constant speed of 0.92 mm/s driven by a motor, while the clamped ribbon is fixed. By means of a thread rod, the angle at which the ribbon is pulled is kept constant to the set value. The force used to pull off the ribbon is measured and recorded.

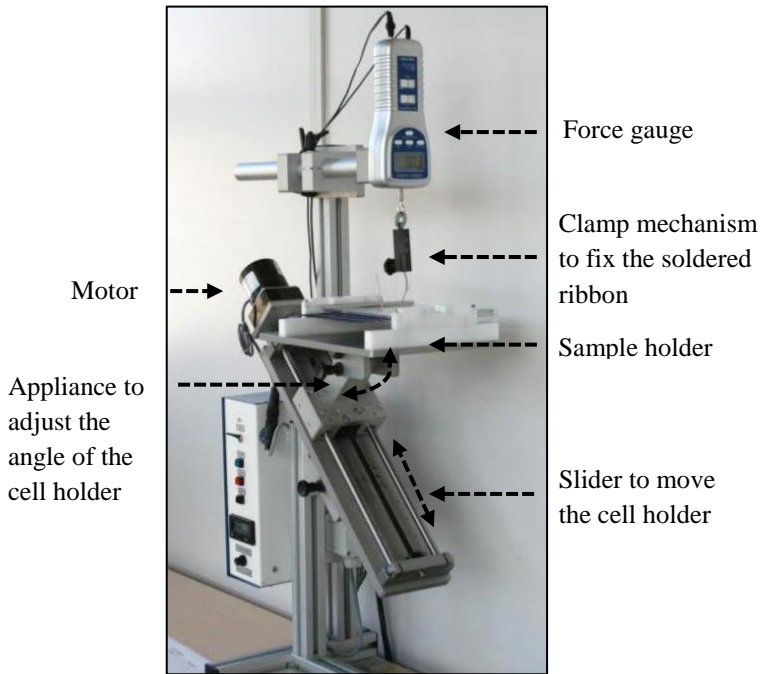


Fig. 4.6. Peel-force tester Frolyt PCE FM 50 used to measure the quantitative contact peel-force of solar cell contacts at Fraunhofer ISE

4.2.2 Contact failure mechanisms

The evaluation of the resulting contact failure mechanisms after the peel-force-test is important to analyse which interface inside the contact architecture failed. Fig. 4.7a shows the observed failure positions (1-4, marked with dashed lines) at a schematic drawing of a soldered Ni-Cu-Ag contact cross section, based on a printed seed-layer. Fig. 4.7 b-e show images of three solar cell busbars after soldering and peel-test resulting in different failure mechanisms. For each example, the contact area on the cell (I) and the bottom side of the peeled busbar (II) are shown.

Position 1: failure inside the silicon wafer under the metallization, also known as chipping, appears as shining conchoidal fracture at very low pull strengths of < 0.2 N/mm and was observed to appear if soldering pressure and/or soldering temperature are too high. Position 2: failure between the printed seed-

layer and silicon wafer is observed at peel-forces between 0 and ~ 0.6 N/mm if the seed-layer is corroded due to the plating process or due to exposure to acidic chemicals with pH-value $< \sim 2$. In this case the whole metal stack sticks to the ribbon (c II) and the bare silicon is visible at the contact area (c I). Position 3: failure between the plated Ni- and the plated Cu-layer. The Cu sticks to the ribbon (d II) and the seed-layer with the plated Ni sticks to the wafer (d I). Position 4: failure of the soldering joint. The Cu sticks to the ribbon (d II) and the seed-layer with the plated Ni sticks to the wafer (d I).

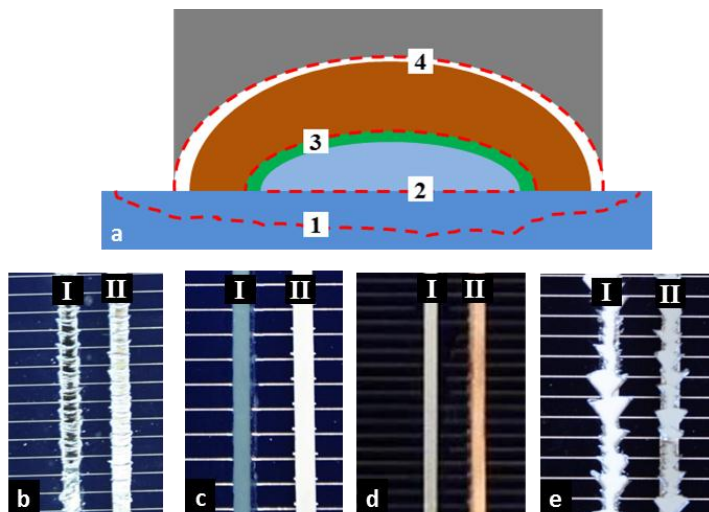


Fig. 4.7: The observed contact failure positions (marked with red dashed lines) at the schematic drawing of a Ni-Cu-Ag front side metallization based on a printed seed-layer (a). Position 1: failure inside the silicon wafer (chipping), illustrated with a picture of the peeled contact area (b I) and the bottom side of a peeled ribbon (b II). Position 2: failure between the printed seed-layer and the silicon wafer illustrated in picture (c). Position 3: failure between plated nickel and plated copper illustrated in (d). Position 4: failure of the soldering joint. Picture e illustrates the breakage of the silicon wafer during the peel-force test.

This failure mechanism was observed in a range between 0 and ~ 0.7 N/mm. Position 4: failure between the metallization and the soldered ribbon due to a weak soldering joint (not shown as a photograph). The interface between printed seed-layer and plated Ni and the interface between the plated Cu and the plated Ag capping-layer were never observed to be the failing interface in this work. If the contact does not fail at one of the discussed positions, the peel-force-test results in breakage of the entire silicon wafer. This was observed to appear at

peel-forces between $\sim 1\text{N/mm}$ and $\sim 2.5\text{ N/mm}$ using $160\text{ }\mu\text{m}$ thick monocrystalline silicon wafers with and without aluminium backside metallization. In this case the breakage force of the wafer is measured instead of the contact adhesion meaning that the contact adhesion of the metal stack is sufficient. If the characterization of the peel-force between metallization and wafer is desired, the wafer has to be stabilized by sticking to a rigid substrate to avoid wafer breakage.

4.2.3 Dependence of the peeling angle

The measured peel-force of solar cell contacts depends on the peeling angle at which the peel-force test is conducted. Kinloch *et al.* defined in their theory for peel-tests of flexible laminates the fracture energy G_A which is an angle independent mechanical parameter for adhesion strength [106]. This parameter reflects the energy needed to break the internal bonding forces and the energy dissipated locally ahead of the peel front. It incorporates the dimensions of the ribbon and its stress-strain-curve. Eitner and Rendler applied the adhesive fracture method by Kinloch to solar cell contacts and ribbons and obtained the dependency of the peeling angle to the peel-force shown in Fig. 4.8.

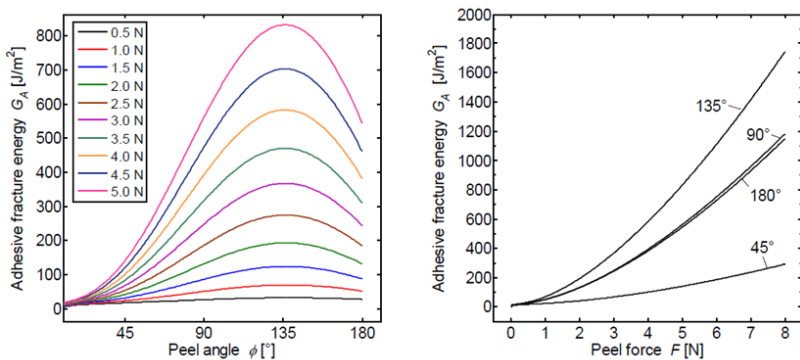


Fig. 4.8: Calculation of the adhesive fracture energies over different peeling angles (a) and the relation of the peel-forces to the adhesive fracture energies for different peel-angles for solar cell ribbons (1.6 mm wide and 0.16 mm thick) by Eitner and Rendler [107]

It becomes clear that peel-force results can only be interpreted and compared if the related peel-angle is taken into account. For a given joint strength an angle of 135° gives the lowest peel-forces while an angle of 45° gives peel-forces

higher by a factor of 6. In this work every peel-test was conducted by a constant angle of 90° .

4.2.4 Atomic force microscopy

The Atomic Force Microscopy (AFM) is a method to investigate the surface roughness of a sample published by Binnig *et al.* [108]. The sample surface is scanned with a sharp tip featuring tip radiuses of < 2 nm. Fig. 4.9 a shows the tip used in this work. The tip is part of a flexible cantilever mounted on a cylindrical, piezoelectric tube. Voltages applied to the x- and y electrodes enable a precise raster scan over the sample. The schematic drawing in Fig. 4.9 b illustrates the raster scan of the cantilever over a random pyramid textured surface. By scanning the surface the tip is deflected in z- direction. With the voltage detected at the z electrode of the piezoelectric tube the topography of the surface can be determined. The AFM measurements in this work were done in the tapping mode with a tap frequency of 327 kHz and a tip velocity of $3.37 \mu\text{m/s}$. Further information about this characterization method can be found in [109].

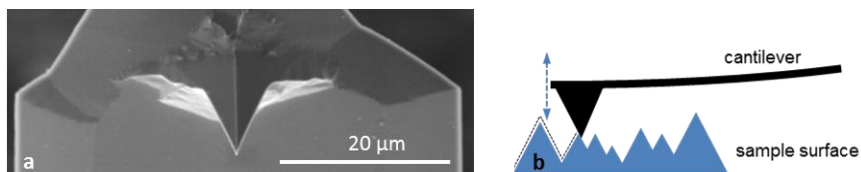


Fig. 4.9: SEM picture of the AFM tip with a tip radius < 2 nm (a) used in this work and a schematic drawing of the cantilever scanning over a sample surface (b)

4.3 Electrical characterization of solar cells and lifetime samples

4.3.1 Suns Voc measurement

The Suns Voc measurement is a method to determine the pFF of solar cells with formed p-n junction based on the measurement of the open circuit voltage, developed by Sinton *et al.* [110]. The cell is manually contacted at the front side while lying on a conductive chuck working as back side contact. The open circuit voltage characteristic is measured during the monotone decay of a flash light in a fraction of a second. The intensity of the flash light is monitored in parallel by a calibrated reference cell integrated into the experimental setup. The assumption of a linear dependency of the short circuit current density from the light intensity enables the calculation of a “pseudo” current-voltage curve from the measured open circuit voltage of the cell and the simultaneous measurement of the light intensity by the reference cell. From this curve the pFF of the cell can be derived. Fig. 4.10 shows the comparison of a light I - V -curve (black triangles) and the pseudo I - V -curve (red circles) measured with the Suns Voc method from the same solar cell. The difference between FF and pFF can be attributed to series resistance losses.

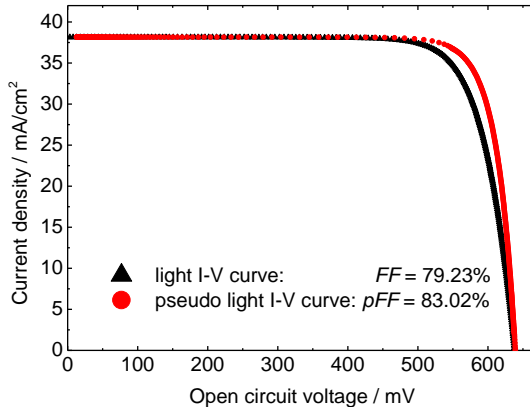


Fig. 4.10: Comparison of the light I - V -curve (black rectangles) and the pseudo I - V -curve (red circles) of a monocrystalline back surface field solar cell measured under standard conditions; the difference between FF and pFF can be attributed to the series resistance losses of the cell.

The Suns Voc method is quick in examination, non-destructive and free of influences by the series resistance, like contact resistance contributions, because there is no direct current measurement included. The pFF gives information about the solar cell material properties and is influenced by recombination and shunting effects. In this work the method was used to characterize the degradation of the pFF due to copper migration from the front side metallization into the solar cell. To minimize the influence by ambient light, the used measurement device from Sinton instruments was additionally equipped with housing.

4.3.2 Photoluminescence imaging

Photoluminescence imaging (PLI) is a spatially resolved, fast and contactless characterization method for silicon solar cells. It is based on the detection of light emission from the cell caused by illumination with a laser [111]. The dominant recombination mechanism in industrial solar cells is Shockley-Read-Hall recombination (thermalisation), but a fraction of the laser-generated carriers recombine via the radiative pathway, emitting photons. These photons are detected with a CCD camera obtaining a pseudo colour image, bright at spots where the carrier lifetime and therefore the light emission in the cell is high and darker where the carrier lifetime is small. The experimental PLI setup for this work consists of a cooled mega pixel (1024×1024) silicon CCD camera, a spatially homogenous excitation light source at 1 sun (equivalent to AM 1.5 intensity) by a 790 nm infrared diode laser, a bipolar power source, a temperature controlled measurement chuck and a stack of optical long-pass filters between the camera and the sample. The filters avoid the detection of reflected laser light. The experiments were conducted in a housing to exclude ambient light. In this work PLI was used to characterize the degradation of the carrier lifetime due to copper migration into the cell. Fig. 4.11 shows a schematic drawing of the experimental setup with an exemplary greyscale PL-image of a standard BSF solar cell front side.

Photoluminescence imaging was used in this work to visualize the spatial distribution of carrier lifetime decrease of solar cells and lifetime samples due to copper diffusion before and after exposure of the cells to thermal stress on hotplates.

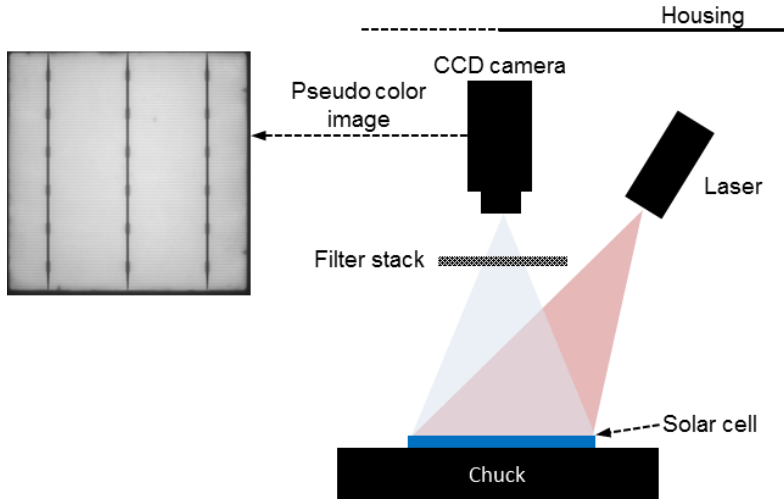


Fig. 4.11: Schematic drawing of the setup used for photoluminescence imaging executed in a housing to exclude ambient light, featuring a 790 nm laser, a silicon CCD camera, a filter stack between camera and solar cell sample and a temperature controlled measurement chuck

4.3.3 Electroluminescence imaging

Electroluminescence imaging (ELI) uses the same working principle as photoluminescence imaging with the difference that the measured solar cell or module is connected to a power supply. The detected luminescence is generated by the current in the cell induced by an applied voltage in forward direction [112].

In general, every defect which reduces the photo generation is visible in the EL-image, like micro-cracks, contact finger interruptions or regions with increased recombination due to copper migration. The experimental ELI setup for this work consisted of a silicon CCD camera (2048×515 pixels), a power supply, and a housing to exclude ambient light. A current of 4 A was applied for an exposure time of 1.5 s to detect the EL-images of single-cell modules before and after climate chamber exposure to characterize the degradation due to copper migration into the cell. Fig. 4.12 shows the schematic drawing of the experimental setup with an exemplary EL-image of a single-cell module with encapsulated standard BSF solar cell front side.

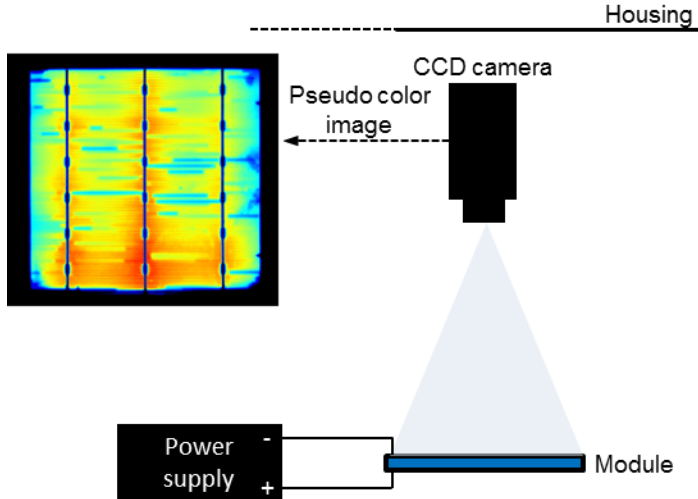


Fig. 4.12: Schematic drawing of the setup used for electroluminescence imaging executed in a housing to exclude ambient light, featuring a silicon CCD camera, and a power supply

4.3.4 Quasi steady-state photo conductance measurement

The quasi steady state photo conductance measurement is a method to characterize the minority-carrier lifetime using a contactless photo conductance instrument in quasi steady state mode published by Sinton *et al.* 1996 [113]. The concept is based on the photo-generation of carriers in the sample and the measurement of the photo conductance σ_L by the inductive coupling of the sample to the coil of a calibrated high frequency LC-resonator. The sample and a calibrated reference cell are illuminated in parallel by a flash light that varies slowly compared to the effective lifetime in the sample (quasi-steady-state). This enables the measurement of the photo conductance (LC-resonator) and the incident light intensity (reference cell). The photo generated excess carrier density, $\Delta n = \Delta p$, results in an increase of the wafer conductance. In the steady-state the generation and recombination of electron-hole pairs is in balance and the photo generation can be expressed as current density j_{PH} . Under the assumption that the carrier density Δn is uniform across the wafer it can be substituted by the wafer photo conductance σ_L ending up in equation 4.1 for the effective carrier lifetime τ_{eff} with the mobility of electrons μ_n and holes μ_p [16].

$$\tau_{eff} = \frac{\sigma_L}{j_{PH}(\mu_n + \mu_p)} \quad 4.1$$

The current density for photo generation j_{PH} depends on the measured illumination and the production parameters of the sample (e.g. surface reflection, light trapping features, wafer thickness). If these parameters are known the current density can be estimated. With this method the resulting minority carrier lifetime cannot be detected in a space resolved manner, only the average carrier lifetime of the measurement area is measured.

In this work a measurement tool from Sinton instruments with a temperature controlled chuck (25°C) was used and the carrier lifetime was evaluated at a minority carrier density of $1 \cdot 10^{-15} \text{ cm}^{-3}$.

4.4 Chemical and electrochemical material characterization

To analyse the amounts of silver and lead dissolved out of the contact after exposure in different chemical solutions, to verify the reduction of the dissolved lead and to clarify the material change in the solid contact after electrolyte exposure the following characterization methods were executed in this work.

4.4.1 Inductively coupled plasma optical emission spectroscopy

Inductively coupled plasma optical emission spectroscopy (ICP-OES) is a technique to analyse the qualitative and quantitative elemental composition of solid, fluid and gaseous samples. The atoms and ions in the sample are excited to optical emission by contact with an argon plasma (~6000-10.000 K). The emitted light is disjointed in its discrete wavelengths by an Echelle monochromator and detected by a charge coupled detector (CCD). The specific wavelengths enable the identification of the elements in the sample and the intensities are used for quantification. The plasma destroys the sample completely which means that the measured result is not influenced by the chemical bonding of the elements in the analysed sample [114], [115]. In this work only fluid samples were investigated. The samples were nebulized into the plasma by nozzle injection. The method was practiced to analyse the amount of lead and silver dissolved out of exposed solar cell contacts in different chemical solutions. The Agilent 720-ES tool with axially viewed plasma torch, as shown in Fig. 4.13, was used and calibrated with ICP-OES standard solutions before starting the measurements. To calibrate the

measurements and to analyse the influence of the matrix solutions to the analytical signal the method of standard addition [116] was performed for silver and lead adding three known silver and lead concentrations to the original sample.

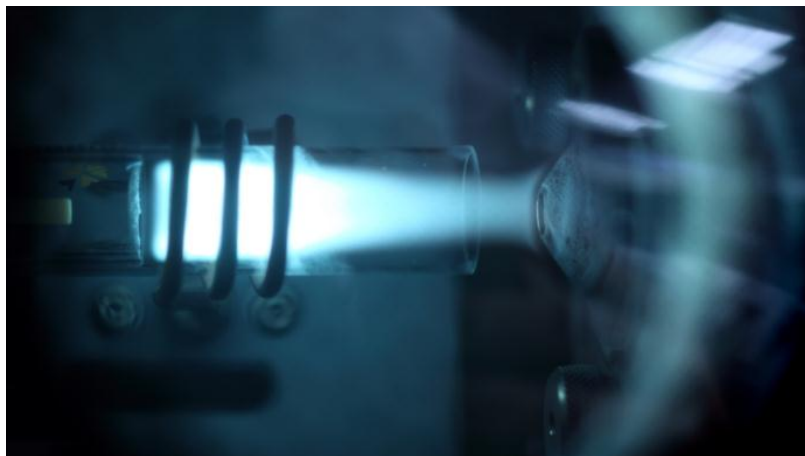


Fig. 4.13: Picture of the inductively generated plasma torch in horizontal position in the ICP-OES tool at Fraunhofer ISE

4.4.2 Cyclic voltammetry

Cyclic voltammetry is a wide spread method to characterize the electrochemical behaviour of unknown systems by obtaining information about the electrode reactions. Cyclic voltammetry is done in a three electrode configuration. At the working electrode a linearly increasing and decreasing voltage is applied against a counter electrode. The potential at the working electrode is determined by a reference electrode and plotted against the recorded current response. If there is an electrochemically active species contained in the analysed solution, the transfer mechanisms at the electrodes at the related reduction and oxidation potentials become visible as current peaks [117], [118].

In this work the method was used to analyse the oxidation and reduction reactions of species dissolved out of the solar cell contacts after exposure to acetic acid solutions. The three electrode configuration shown in Fig. 4.14 a with a platinum net in the dimension of $A = 4 \text{ cm}^2$ as counter electrode (CE), a silver silver-chloride double junction reference electrode (RE) and a glass embedded

silver wire with a diameter of 1 mm as working electrode (WE) was used. Cyclovoltammograms were recorded using a multichannel potentiostat (VSP multi potentiostat by BioLogic) applying a potential sweep of $dE = [-550; +300]$ mV, scanned with a sweep rate of $dE/dt = 20$ mV/s as shown in Fig. 4.14 b. In order to ensure constant signals, each sample was cycled at least three times. The potentiostat may calculate the applied voltage to voltage values rated against the normal hydrogen electrode (NHE).

The counter electrode was cleaned by flame oxidation for 5 minutes before usage. The working electrode was polished manually before application. All electrochemical measurements were performed in a faraday cage to prevent electromagnetic interferences using a cleaned 50 ml glass beaker. Fig. 4.15 shows an overview of the experimental setup (a) and a detail image of the electrode configuration in the glass beaker with reference electrode (RE), working electrode (WE) and counter electrode (CE).

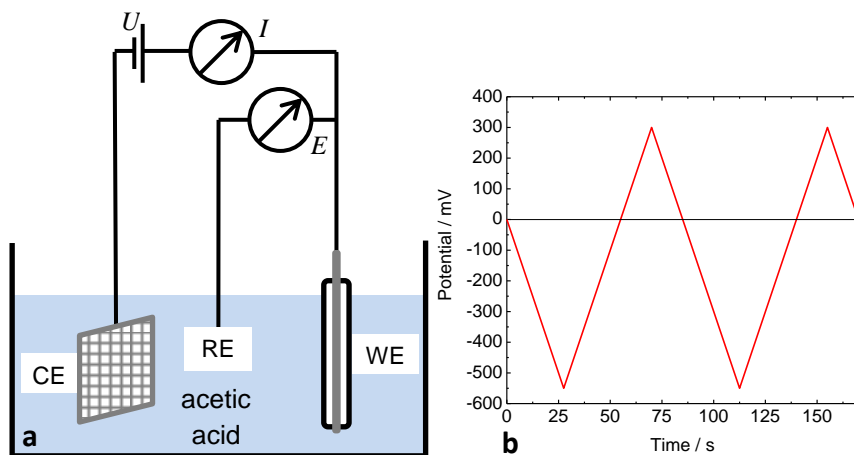


Fig. 4.14: Schematic drawing of the three electrode setup used for the cyclic voltammetry experiments (a) with working electrode (WE), reference electrode (RE), counter electrode (CE), applied voltage U , current measurement I and the electrode potential E measured to the reference electrode. A voltage sweep -550 mV to + 300 mV scanned with a sweep rate of $dE/dt = 20$ mV/s was applied (b).

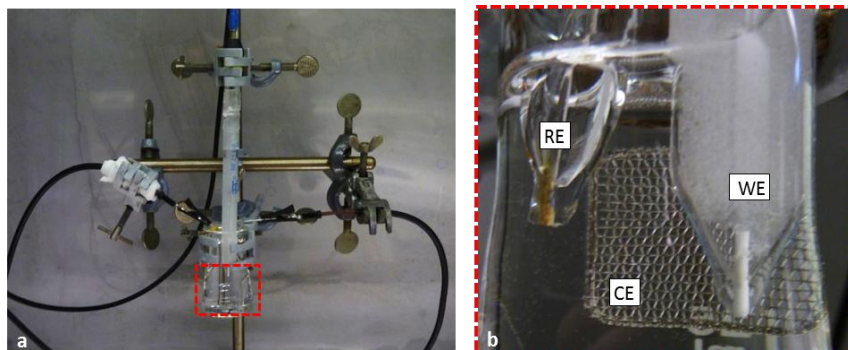


Fig. 4.15: Overview image of the three electrode setup installed in a faraday cage (a) and detail image of the electrode configuration inside the 50 ml glass beaker (b) with reference electrode (RE), working electrode (WE) and counter electrode (CE)

4.4.3 Powder X-ray-diffraction measurement

Powder X-ray diffraction (XRD) measurement is a material characterization technique which provides accurate information about the structure of the measured sample. The measurement principle of the x-ray diffraction is based on Bragg's law, expressed in equation 4.2. The variable d is the distance between the atomic layers in a crystalline sample, the angle λ describes the wavelength of the incident X-ray beam, n_A is an integer and θ is the angle of diffraction, between the incident ray and the scattering planes.

$$n_A * \lambda = 2 * d * \sin\theta \quad 4.2$$

When incident parallel X-ray beams strike the crystalline sample, the planes of atoms will reflect the X-rays differently depending on the position of the atomic layer at which the beam is reflected. Fig. 4.16 shows the geometrical illustration of Bragg's law. Two monochromatic X-ray beams of a specific wavelength strike a crystal structure at an incoming angle of theta. Ray 1 is reflected from the top atomic plane, while ray 2 is reflected from the second atomic plane. Since ray 2 has to cross deeper into the sample material, it travels a distance 2Δ farther than ray 1 [119].

At specific wavelengths and incident angles, crystals produce intense peaks of reflected radiation, known as Bragg peaks. The diffraction pattern consists of a plot of reflected intensities versus the detector angle 2θ . This can be used to identify components in a sample, by comparing the resulting diffractogram

with the X-ray diffraction pattern of known substances, using a computer based search and match procedure.

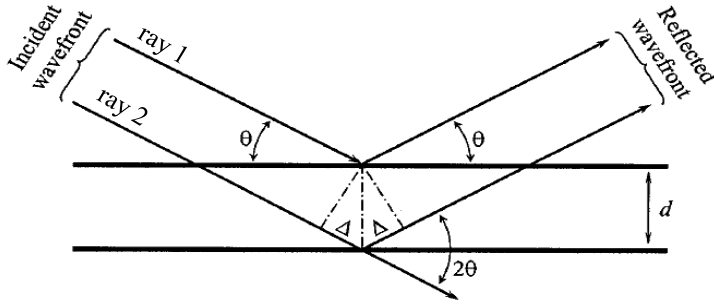


Fig. 4.16: Geometrical illustration of Bragg's law: θ - Bragg's angle, d - distance between the atomic layers in the sample, 2Δ - path difference of the reflected wave fronts [119]

For the powder X-ray-diffraction measurements in this work the D8 advance measurement tool by Bruker was used with a copper anode tube at 40 kV/40 mA with a Ni filter and constant sample illumination spot size (broadness 12 mm) offering a $K\alpha$ wavelength of 1.54 Å. An angle range from 5° to 85° was scanned with a resolution of 0.01° and a measurement time of two seconds. A rotating sample holder was used and the measurement was done in ambient atmosphere.

4.5 Rheological characterization of silver pastes

In general, screen-printing silver pastes are Non-Newtonian fluids, pseudo plastic with a shear thinning flow behaviour. Herschel and Buckley introduced in 1926 a model to describe the plastic behaviour of pastes in steady-state condition [120] following equations 4.1 and 4.2:

$$\tau(\dot{\gamma}) = \tau_y + c_c \cdot \dot{\gamma}^{n_p} \quad 4.3$$

$$\eta_v = c_c \dot{\gamma}^{n_p-1} + \frac{\tau_y}{\dot{\gamma}} \quad 4.4$$

The relation between the shear stress τ and the shear strain rate $\dot{\gamma}$ is described by means of the parameters c_c for consistency, τ_y for yield stress and the power law index n_p . The viscosity η_v depends on the shear strain rate.

4.5.1 Controlled shear stress test

To investigate the relation between the resulting geometry of screen-printed seed-layers and the yield stress τ_y of the used silver pastes, a controlled shear stress test (CSS-test) was performed with the silver pastes using a rotational rheometer with cone-plate measurement geometry. A shear stress ramp from 10 Pa to a maximum of 2000 Pa was applied to the paste samples by adjusting the torque M of the cone. Following equation 4.3, the shear stress $\tau_{\theta\theta}$ at a constant cone angle θ and a given angle of twist \varnothing is a function of the actuating variable M . The angle of twist \varnothing is measured to determine the deformation γ following equation 4.4, using the given cone angle α [121].

$$\tau_{\theta\theta} = \frac{3M}{2\pi R^3} \quad 4.5$$

$$\gamma = \frac{\varnothing}{\alpha} \quad 4.6$$

The measurements were done at a constant temperature of 25 °C, with a constant measurement time of 5 seconds per measuring point and 40 point per decade. A cone-plate geometry with a cone angle α of 1°, a gap width a of 50 μm , and a cone radius R of 25 mm was used at an Anton Paar MCR 502 rotational rheometer equipped with an air suspended cone. Fig. 4.17 shows a drawing of the used cone plate geometry.

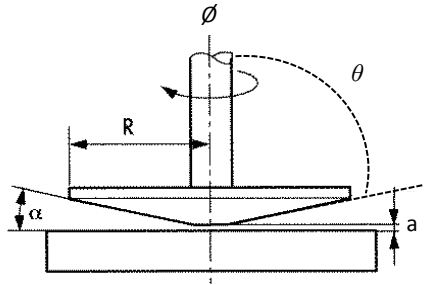


Fig. 4.17: Drawing of the used cone-plate measurement geometry with the gap width a between cone and plate, the cone angles α and θ , the cone radius R and the angle of twist \varnothing [122]

For exact and reproducible measurements the gap between cone and plate has to be filled accurately with the sample paste. After descending the cone for automated gap setting, protruding paste was removed with a spatula. Fig. 4.18 shows a picture (a) of the cone (1) and plate (2) measurement geometry after automatic gap setting with protruding paste (3) and after removing the protruding paste with a spatula (b).

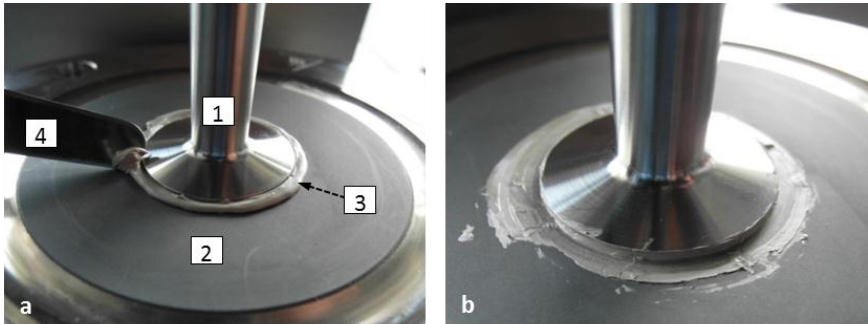


Fig. 4.18: Pictures of the cone and plate measurement geometry with protruding paste (a) and after removing the protruding past with accurately filled measurement gap (b) with cone (1), plate (2), protruding paste (3) and spatula (4)

4.5.2 Evaluation of the yield stress

To analyse if the yield stress τ_y of the used screen-printing pastes correlates with the two key ambitions for screen-printed seed-layers, fine contact finger geometry and small wet-paste consumption, the yield stress was evaluated using the method of two best fit lines by Metzger [122]. The deformation of the pastes was measured for a given shear stress ramp applied to the paste sample using a rotational rheometer with cone-plate geometry (compare section 4.5.1). The measurement results were plotted in double logarithmic scale: the applied shear stress τ at the x-axis and the measured deformation γ on the y-axis. The resulting curve shows a constant gradient for low τ and γ values. This represents the linear elastic deformation behaviour of the paste. In this region Hook's law, which describes the elastic behaviour of solids, is valid because τ and γ rise proportionally. This zone of the curve is fitted with a first best fit line. The second best fit line is applied in the liquid regime at high τ and γ values. The corresponding value for the yield stress is then found at the τ -value of the intersection of the two fits. [122].

Fig. 4.19 shows the exemplary determination of the yield stress with a measured curve of paste 9 (for complete results compare section 6.1.3).

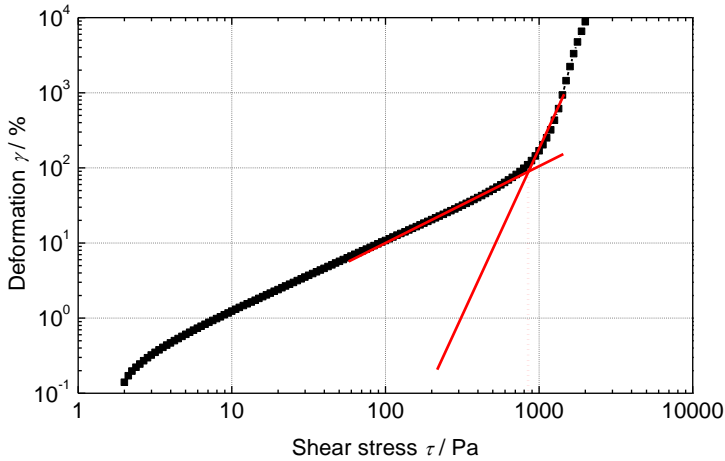


Fig. 4.19: Exemplary determination of the yield stress using the method with two best fit lines (red continuous lines) in the double logarithmic τ - γ diagram according to Metzger [122]

To ensure a systematic and reproducible determination of the yield stress, the evaluations for the pastes in the experiment were conducted using tool based on Microsoft Excel developed at Fraunhofer ISE. The tool starts the fit of the first line at the lowest gradient of the measured curve and the fit of the second line at the highest gradient of the measured curve. Every measured value is fitted until the y-distance between the fitted line and the next value is bigger than 10% of the measured value.

5 Experimental setups and procedures

In this chapter the tools and electrolytes used for electrochemical metal deposition in this work are introduced (section 5.1). The functional principles of a used lab scale tank set up (section 5.1.1) and inline plating tools developed in project cooperation with an equipment manufacturer during this thesis (section 5.1.2) are explained. The composition of the Watts-type nickel electrolyte used for the investigations of the interaction between nickel electrolyte and screen-printed contacts is introduced in section 5.1.3 besides the commercial electrolytes for Cu and Ag plating. In section 5.2 the production parameters of the used solar cell contacts (section 5.2.1) and the contact exposure test for rapid contact corrosion investigations without applied voltage (section 5.2.2) and with applied voltage (section 5.2.3) developed in this work are presented. Section 5.2.4 explains the soldering procedure, executed to prepare the contacts for the contact adhesion measurement. These experimental methods and setups were used to investigate general contact corrosion (for results compare chapter 7 and chapter 10) supplemented by SEM, TEM, XRD and AFM analysis. In section 5.3 a method for rapid cell degradation characterization due to copper diffusion, which was used and evaluated in this work to analyse the long term stability of solar cells, is shown.

5.1 Electrochemical Ni-Cu-Ag deposition – electrolytes and tools

In this section, the tools used for electrochemical metal deposition, the recipe of the Watts-type nickel electrolyte and the used commercial Cu and Ag electrolytes are introduced.

5.1.1 Lab scale tank setup

In a parent thesis [123] a tank set-up for electrochemical metal deposition was developed at Fraunhofer ISE. The central unit of the tool is a polypropylene (PP) process chamber (270 mm wide 180 mm long and 300 mm high) with a polymethyl methacrylate (PMMA) window (diameter of 248 mm) at the front side to realize illumination of the cell in the light induced plating process. Fig. 5.1 shows the schematic drawing of the tank setup with flow circuit (a) and an

image of the tank setup in application in the lab (b). A pump driven flow circuit with filter, flowmeter and choke valve, connected by chemically stable tubes outside the tank, enables the reproducible electrolyte convection in the process chamber.

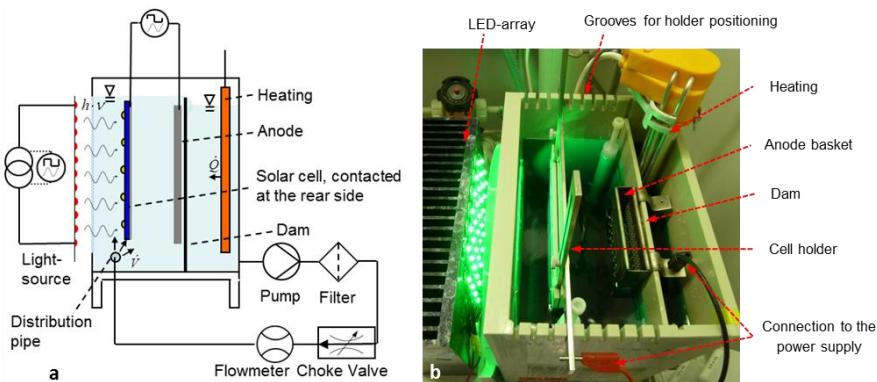


Fig. 5.1: Schematic drawing of the lab scale tank setup with process chart of the flow circuit (a) [123] and image of the tank setup in application (b)

The inlet of the electrolyte is located at the bottom of the tank and is realized by a distribution pipe with several injectors. A dam in the back of the process chamber regulates the electrolyte level and forces the electrolyte flow to pass the cell. The flow rate was set to 500 l/h for every experiment.

The electrolyte outlet to the pump driven circuit is located behind the dam at the bottom of the tank. An electrical heating with temperature control and minimum liquid level cut out (inductive) enables the temperature setting. Grate grooves in the tank side walls allow the reproducible positioning of a cell holder (compare Fig. 5.2). A titanium anode basket filled with anode material is positioned behind the cell and an LED-array at the front side of the tank illuminates the cell through the tank window during the light induced plating process. The power supply for the LED's and the voltage applied to the solar cell is realized by a lab voltage source offering two channels. Five tools with the described working principle are installed at Fraunhofer ISE for Ni, Cu, Ag plating using different electrolytes. The low electrolyte volume of ~12 l compared to the inline tools offers flexibility for the investigation of different electrolytes and electrolyte variations. Fig. 5.2 shows the cell holder (a)

developed at Fraunhofer ISE used for metal deposition on solar cells in the tank setup shown in Fig. 5.1.

The holder is composed of a titanium rack (1) adjustable in height (2) for positioning of the cell in the tank, and a polypropylene rack with a titanium wire proceeding in a notch (3) to connect the backside of the cell with the titanium rack during the plating process. The polypropylene rack is equipped with a front panel (4) and bolts (5) to clamp the cell to the holder with a rubber lip to avoid cell breakage (6) and three struts (7) to support the cell in the electrolyte convection.

Fig. 5.2 b shows the holder with connected solar cell as for operation. During plating the cell is immersed completely in the electrolyte. At the area where the cell front side is covered with the front panel of the cell holder no metal is deposited during the plating process. Therefore the tank setup was not used to produce cells for long term stability experiments because this part and the backside wetted with copper electrolyte represent potential weak points regarding copper diffusion into the cell.

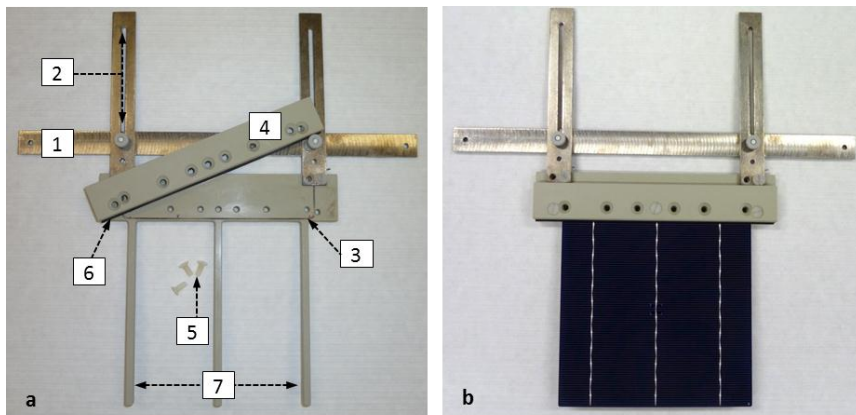


Fig. 5.2: Cell holder for the tank setup (a) composed of a titanium rack (1) adjustable in height (2) for positioning of the cell in the tank, and an polypropylene rack with a titanium wire proceeding in a notch to connect the backside of the cell with the titanium rack (3), a front panel (4) and bolts (5) to clamp the cell to the holder with a rubber lip to avoid cell breakage (6) and three struts (7) to support the cell in the electrolyte convection; cell holder with connected solar cell (b)

5.1.2 Inline tool for electrochemical metal deposition

During this work two one track inline plating tools, identical in construction, for automated nickel and copper deposition on solar cells were installed at Fraunhofer ISE in project cooperation with the wet chemistry and plating tool manufacturer RENA. The “InCellPlate” lab tool enables an inline single side light induced plating process featuring the same functional principle as industrial scale tools, which are additionally equipped with several tracks in parallel to enhance the wafer throughput (>3000 wafers/h possible [124]. Fig. 5.3 shows the plating tool composed of a plating process chamber (1) and a rinsing and drying unit (2).

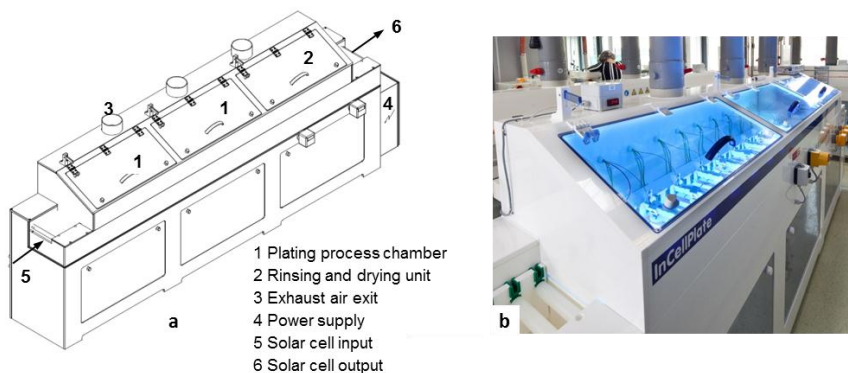


Fig. 5.3: Schematic drawing (a) [125] and photo (b) of the one track plating tool developed by RENA in project cooperation with Fraunhofer ISE

The cells are transported on a continuous track of conveyor rolls in a way that only the front side is immersed in the electrolyte, maintained by surface tension. The residence time for a cell in the electrolyte bath can be adjusted by the rotational speed of the transport rolls in a range between 38 seconds and 5 minutes. The rear side of the cells stays dry and is connected to a negative voltage by stationary contact brushes. Illumination is enabled from the bottom by LED lines positioned in the electrolyte bath under the conveyor rolls. The anodes are placed at a meshed metal sheet on the ground of the electrolyte tank. The metal sheet is connected to the positive terminal of the power supply. Fig. 5.4 shows an overview of the process track in the copper plating tool (a) and a detail picture (b) of a solar cell (1) connected by a contact brush (2) passing through

the plating chamber filled with nickel electrolyte, transported by conveyor rolls (3) with switched-off LED lines (4). The distance of the brushes is optimized on the standard solar cell size ($156 \times 156 \text{ mm}^2$) which enables an uninterrupted voltage supply during the passage of the wafers through the plating tool. The inline tool is equipped with an electrolyte tank (150 l) where the electrolyte is stored when the pump cycle, which realise electrolyte circulation in the process chamber, is switched off. In the pump cycle, a heating regulated by a temperature sensor in the process chamber and a filter are installed.

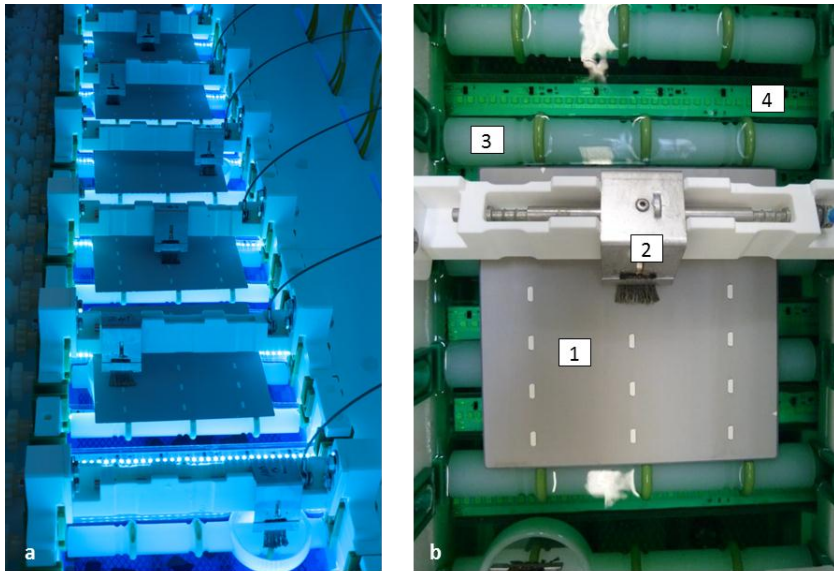


Fig. 5.4: Images of the inline plating tools: overview of the process track with LED illumination and copper electrolyte (a). Detail image (b) of a solar cell solar cell (1) connected by a contact brush (2) passing through the plating chamber filled with nickel electrolyte, transported by conveyor rolls (3) and LED lines switched off (4)

5.1.3 Used electrolytes for metal deposition

For the investigation of the interaction between the nickel electrolyte and the screen-printed silver front side metallization, a Watts-type electrolyte was used. The electrolyte recipe was developed based on the general Watts-type electrolyte recipe published in [126], adding dihexyl sulphosuccinate and 1-octane sulphonic acid sodium salt as surfactants. The composition is presented in Table 5.1. For investigations of the reactions during contact-electrolyte interaction it is

important to know what exactly is contained in the electrolyte, which is typically this is not the case for commercial electrolytes.

Table 5.1: Recipe of the used Watts-type nickel electrolyte

Compound	Molecular formula	Concentration
Nickel sulphate	NiSO_4	310 g/l
Nickel chloride	NiCl_2	50 g/l
Boric acid	H_3BO_3	40 g/l
Diethyl sulphosuccinate	$\text{C}_{16}\text{H}_{29}\text{NaO}_7\text{S}$	170 mg/l
1-Octane sulphonic acid sodium salt	$\text{C}_8\text{H}_{17}\text{O}_3\text{SNa}$	350 mg/l

For copper and silver plating commercially available electrolytes were used shown in Table 5.2.

Table 5.2: Used commercially available electrolytes for copper and silver deposition

Metal	Manufacturer	Product name	Metal content g/l	Operating Temp. /°C	pH-range
Cu	OMG Electronic chemicals	Solar plate Cu PV 37M	15	20-30	2.3-3
Ag	Rohm and Haas	Enlight 620	20	30-40	10-10.5

5.2 Exposure procedure for adhesion evaluation of solar cell contacts

To evaluate the influence of different chemicals and electrolyte solutions on the contact corrosion, a rapid exposure test was elaborated during this work. The results described in chapter 7 and chapter 9 were obtained executing the experiment procedure described in this paragraph with variations in the used solutions and exposure durations.

5.2.1 Solar cell contact precursors for exposure experiments

For the contact exposure experiments, solar cell contacts were screen-printed on p-type, Cz-silicon material with random pyramid texture, a $90\ \Omega$ emitter and a silicon nitride antireflection coating. The same standard front side silver paste was used for all precursors and printed by an inline screen-printing machine. The contacts were fired at a set peak temperature of 900°C in an inline furnace. The samples used in the exposure experiments without applied voltage had no back side metallization, to exclude any influences of the rear aluminium contact to the chemical trace analysis executed with dipping solutions. The samples used for exposure experiments with applied voltage featured a standard aluminium back side metallization with silver pads to enable the application of a negative voltage. For the effective use of the available wafer material a screen layout was designed to print five standard busbar contacts ($1.5\ \text{mm} \times 156\ \text{mm}$) per wafer ($156 \times 156\ \text{mm}^2$). The wafers were cut after firing to get single wafer stripes ($30\ \text{mm} \times 156\ \text{mm}$) with one busbar respectively, as shown in Fig. 5.5.

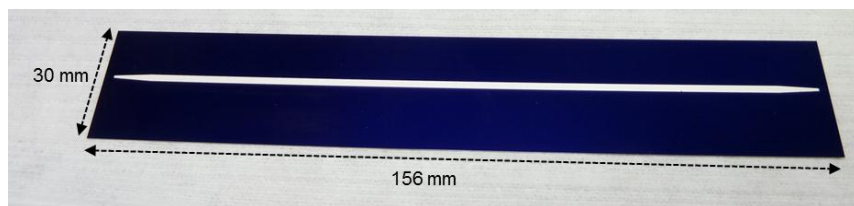
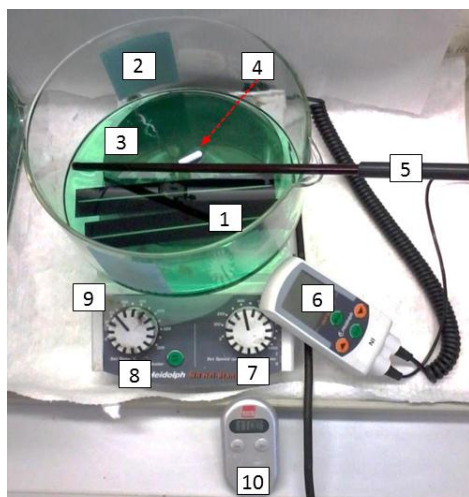


Fig. 5.5: Picture of a single solar cell busbar contact used for exposure experiments with subsequent solder and peel-test to characterize contact adhesion

5.2.2 Contact exposure without applied voltage

For every exposure experiment, two solar cell contacts at a time, produced according to section 5.2.1, were face up introduced in a glass vessel with 200 ml of freshly set up solution. A temperature sensor, coupled with the hot plate underneath the vessel, was used to keep the temperature constant at 50°C , which is the usual temperature used during nickel plating. In order to heat up homogeneously and to promote the interaction between the contacts and the solution, a magnetic stirrer was introduced in the solution with a set speed of 250 rpm. During the experiments the glass vessel was covered with aluminium foil to reduce evaporation of the solution and to exclude the biggest part of the ambient light. A picture of the setup used for the exposure experiments is presented in Fig 5.6.

As standard exposure duration, 45 minutes was chosen for most of the experiments. This duration was found to be suitable to show corrosion effects with an impact on contact adhesion due to exposure in the electrolyte solutions. After exposure the contacts were rinsed with deionized water, dried with an air pistol and stored for one day at room temperature before preparing them for the peel-test. To ensure sufficient statistics, 4 busbar contacts were used for every experimental point.



- 1 Exposed contacts
- 2 Glass vessel
- 3 Dipping solution
- 4 Magnetic stirring bar
- 5 Temperature sensor
- 6 Temperature controller
- 7 Stirring speed adjustment
- 8 Temperature adjustment
- 9 Hot plate
- 10 Timer

Fig 5.6: Experimental set up used for contact exposure experiments without applied voltage

5.2.3 Contact exposure with applied voltage

To show the influence of an applied voltage on the corrosion mechanism of the contacts, an experimental installation similar to the light induced plating setup described in section 5.1.1 was used. One litre exposure solution was used in a glass bath at 50°C, controlled with a temperature sensor and a hotplate. Fig. 5.7 shows the used setup with description of the equipment and switched of LEDs (a) and in operation mode with LED illumination (b).

The solution was constantly stirred using a stirring bar with a set stirring speed of 250 rpm. During the experiment the contacts were illuminated by LEDs (wavelength 525 nm) and a voltage of -0.7 V was applied between the backside of the cells and an anode, which was positioned behind the cell at the same position for every experiment.

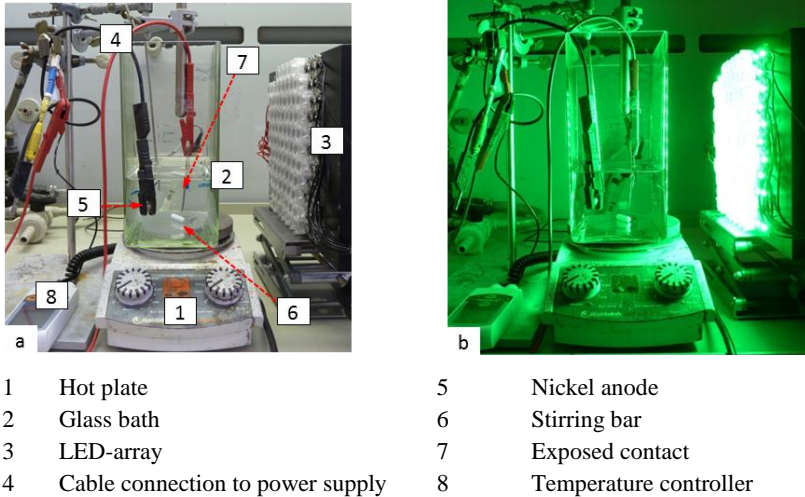


Fig. 5.7: Experimental setup used for the contact exposure experiments with applied voltage with LED's switched off and description of the details (a) and with LED illumination (b)

The exposure duration for experiments with applied voltage was considerably shorter than for experiments without applied voltage and ranged between 30 seconds and 300 seconds because contact corrosion was observed to be accelerated by the applied voltage. After exposure the contacts were rinsed with deionized water, dried with an air pistol and stored for one day at room temperature before preparing them for the peel-test.

5.3 Soldering procedures for solar cell contacts

In order to measure the contact adhesion, after the exposure tests in different solutions, a ribbon was soldered onto the solar cell contacts analogous to module integration. Before soldering the contacts were rinsed with deionized water, dried with an air pistol and stored for one day in ambient air and at room temperature before soldering.

Two soldering procedures were used in this work, manual soldering and automated soldering on a soldering station. In both cases standard Cu ribbons with Sn-Pb-Ag coating, a width of 1.5 mm and a thickness of the Cu core of 130 μm were used. Fig. 5.8 b shows a microscope cross-section image of the

used ribbon. A standard flux (Kester soldering flux 952S) was used in order to dissolve the oxide layer on top of the metallization and promote a stable soldered connection. Most of the contacts were soldered manually: The samples were pre heated to 100°C on a hotplate to reduce the thermal stress induced during soldering; the temperature of the soldering rod was set to 250°C. Fig. 5.8 a shows a picture of the manual soldering setup. The flux wetted ribbon (1) was fixed on the hotplate (2) with a temperature-stable tape (3) to enable flat positioning on the wafer (4). A 15 mm wide flat soldering tip (5) was used to solder the ribbon on the solar cell busbar underneath. This simple and fast manual soldering process enabled the production and characterization of many solar cell contacts in short periods. However, it causes deviations in the average contact adhesion results (~ 0.3 N/mm) for similarly produced contact samples due to the not exactly controllable soldering pressure and soldering time. To evaluate clear trends in the experiments four contacts were evaluated per experimental point.

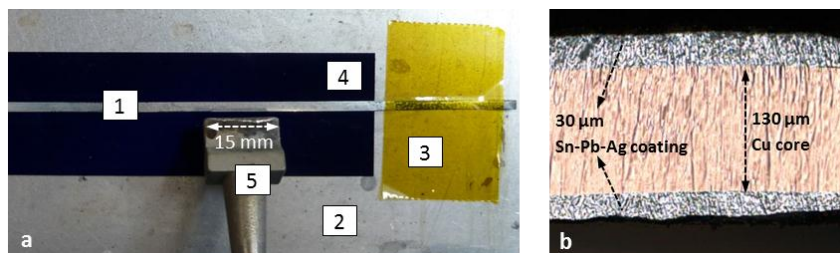


Fig. 5.8: Picture of the manual soldering setup (a): a flux wetted ribbon (1), fixed on the hotplate (2) with a temperature-stable tape (3). The contact on the wafer (4) is positioned under the ribbon and soldered with a flat 15 mm wide soldering tip (5). Microscope cross-section image of the used ribbon (b) with a 130 μm thick copper core and ~ 30 μm thick Sn- Pb-Ag solder coating

In cases of metal surfaces different to silver (i.e. plated copper or nickel) or sensitive differences in the adhesion results an automated soldering station developed at Fraunhofer ISE was employed. At this station the pre heating, the soldering pressure and the soldering time can be set precisely and reproducibly for every soldering joint. Fig. 5.9 shows the soldering station (a) with hotplate soldering rod and control system and a diagram of the precise adjustable soldering temperature black squares, left axis) and pressing force (red circles, right axis) over soldering time (b). The temperature at the soldering tip is

measured contactless using a pyrometer and the detection of the pressing force is realized using a strain gauge in the soldering head.

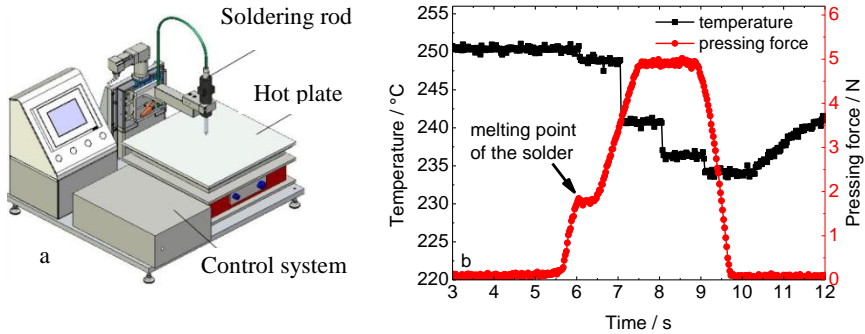


Fig. 5.9: Semi-automatic soldering-station with a hotplate for pre heating and a controllable soldering rod (a) and a diagram of the precise adjustable soldering temperature (red circles) and the soldering force (black squares) over the soldering time (b)

After soldering, quantitative peel-force tests, as described in section 4.2, were conducted with the solar cell samples.

5.4 Fast degradation of plated solar cells at elevated temperature

To evaluate the degradation behaviour of solar cells due to copper diffusion, long term stability experiments at elevated temperatures were performed. The used procedure and the solar cell precursor production are described in the following subsections.

The method for accelerated aging of solar cells published by Bartsch *et al.* [39] aims for the characterization of the cell degradation due to copper diffusion to evaluate the long term stability of the cells. As the copper diffusion speed increases with increasing temperatures the cells were thermally treated at elevated temperatures on hotplates to accelerate the degradation. The highest operating temperatures of modules in the field depend on the location, where the module is operated. In the hottest parts of the world, rack mounted modules age as if they were constantly operated at 42°C-53°C [127]. For good comparability

to field conditions such a temperature range would be convenient. But at these temperatures the degradation of the cells would last too long and exceeds feasible experiment possibilities. At temperatures above 275°C alternative degradation mechanisms besides the copper diffusion will influence the measurements, like nickel diffusion as deep as the junction ending up in emitter shunts, or softening of the glass-layer, which changes the contact structure and may influence the copper diffusion behaviour. A temperature range between 175°C and 275°C was used in this work for thermal stress and is considered to represent a good compromise between the aims of accelerating the cell degradation and measuring of effects exclusively induced by copper migration. The cells were at least treated at three different temperatures to evaluate the linearity in the trend of diffusion activation energy. In short breaks between two periods of thermal stress the *pFF* of the solar cells was measured using Suns Voc measurement (compare section 4.3.1) in regular intervals. The average measurement interval ranged between 20 and 25 h.

Temperature/time data pairs leading to a *pFF* loss of 5%_{rel.}⁷ were plotted in an Arrhenius plot as $\ln(t)$ versus the inverse temperature. By a linear fit of the measured data, the time needed for the same degradation at module operating temperatures can be extrapolated. Additionally the effective activation energy for a given system can be determined from the slope of the curve in the Arrhenius plot. If the temperature time pair at a relative degradation of the *pFF* down to 95%_{rel.} is not exactly measured a linear interpolation of the measurement points with the smallest distance to 95%_{rel.} in the degradation curve gives a satisfactory estimation. For temperature treatment, hotplates from the manufacturer Harry Gestigkeit GmbH equipped with a PID controller for temperature setting were used. Fig. 5.10 shows the used set up.

⁷ A degradation of the module performance of less than 5% in 25-30 years is the central element of the most warranties offered by module manufacturers. In general the Arrhenius plot evaluation can be conducted for every desired degradation range.

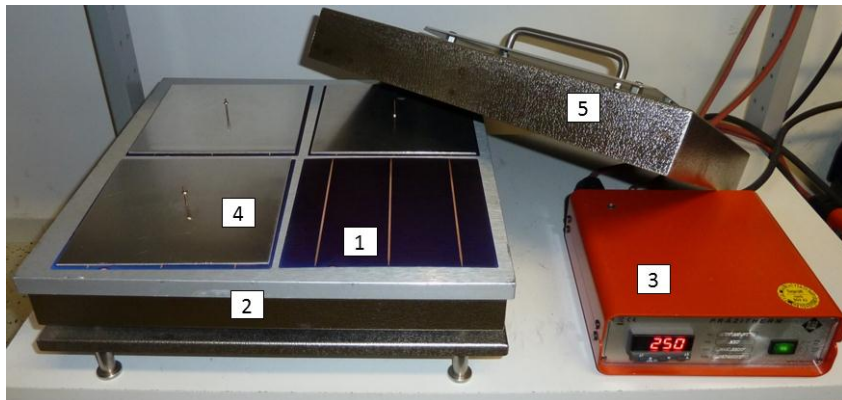


Fig. 5.10: Equipment for degradation experiments at elevated temperatures. Solar cell (1) on a hotplate with aluminium surface (2). The temperature can be set by a proportional–integral–derivative (PID) controller (3). In operation the cells are covered with an aluminium plate (4) and the hotplate itself is covered with a lid (5).

5.5 Solar cell precursors for experimental research

For the long term stability experiments, full size ($156 \times 156 \text{ mm}^2$), p-type solar cells were produced by screen-printing fine-line front side contacts on textured (random pyramids) Cz-silicon wafers with PECVD silicon nitride anti-reflection coating, a $90 \text{ } \Omega$ phosphorous emitter with a junction depth of about 200–300 nm and a standard aluminium backside with silver pads. A standard H-pattern grid with 90 fingers and 3 busbars (1.5 mm) was screen-printed on the samples using a commercial fine line Ag-paste and an industrial, automated inline screen-printing machine. The screen openings for the contact fingers were $25 \text{ } \mu\text{m}$ wide. The samples were fired at a set peak temperature of 920°C in an inline furnace. Nickel as diffusion barrier, copper as conductive layer and silver as capping layer were plated on the fired contacts using a single side, light induced plating process in inline machines (compare section 5.1.2). During this process the backside of the cells does not get in touch with the electrolyte. The plated nickel mass and therefore the thickness of the diffusion barrier were varied for the long term stability experiments.

6 Printed silver seed-layers for copper front side metallization

The copper front side metallization for silicon solar cells investigated in this work is based on a printed silver seed-layer. Screen-printing is the wide-spread process in the PV-industry to realize the front side metallization of silicon solar cells (compare section 3.2). In this chapter the influences of paste rheology on the resulting seed-layer geometry and the silver consumption of screen-printed seed-layers are evaluated (section 6.1). The chapter focusses on the influence of the paste viscosity (section 6.1.1), the particle size (section 6.1.2) and the yield stress (section 6.1.3) on the printing result regarding contact finger geometry and wet-paste consumption. Besides screen-printing, alternative printing techniques especially suited to print fine lines on solar cell front sides, were evaluated (section 6.2). Silver seed-layers printed with inkjet-printing (section 6.2.1), aerosol-jet printing (section 6.2.2) and flexographic-printing (section 6.2.3) are compared with seed-layers realized by the screen-printing process (section 6.2.4) and cells with a fully screen-printed standard front side metallization (section 6.2.5), regarding seed-layer geometry, silver consumption and I-V parameters of the produced cells. Section 6.3 gives a brief summary of the presented results.

6.1 Influence of paste rheology on screen-printed seed-layers

A deeper understanding of the correlation between paste rheology and achieved printing results for screen-printed fine line silver seed-layers has been worked out in project cooperation with the paste manufacturer Heraeus. Heraeus provided the paste, all other investigations were done autonomously as a part of this thesis. The key ambition was to realize screen-printed seed-layers with narrow, well contacting fingers and simultaneously small Ag-paste consumption per printed wafer and to correlate the results with rheological parameters of the used paste. The general understanding of the rheological determining factors will enable a more systematic development of seed-layer pastes. The rheology of the used silver paste has a major influence on the shape of the printed contact structure after the screen-printing process. To elucidate the correlation between contact finger geometry, wet-paste consumption and rheology, different experimental pastes, produced by Heraeus were printed on $156 \times 156 \text{ mm}^2$ mono

crystalline wafers with random pyramids and silicon nitride anti reflection coating (a detailed description of the used solar cell precursors can be found in section 5.5). The used substrate, the screen configuration and the printing parameters like printing pressure, printing speed, snap off and used squeegee influence the printing results besides the rheology of the pastes. The wafer substrate, the used screen and squeegee were kept constant for the experiments. The printing parameters were optimized for every paste to reach the best printing result. The used fine line screen featured openings for the contact fingers of 25 μm , an emulsion height of 5-9 μm and a 400 mesh with a wire diameter of 18 μm . The screen mesh was calendered and coated with a functional material promoting the paste release from the screen. The small contact finger opening of 25 μm was hard to realize for the screen manufacturer and is close to what is currently possible for commercial screens. Fig. 6.1 shows an SEM top view image of the used screen with a contact finger opening in the emulsion.

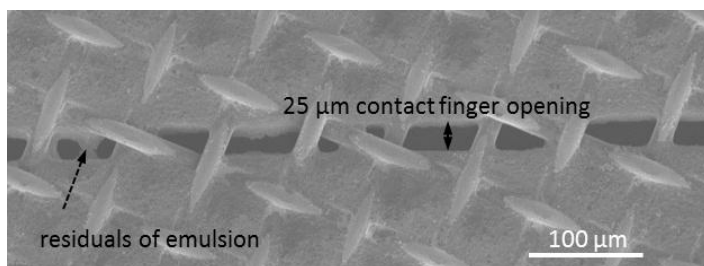


Fig. 6.1: SEM top view image of a used fine-line screen with a wire diameter of 18 μm and a contact finger opening in the emulsion of 25 μm . Residuals of not perfectly washed-out emulsion were observed, which can cause contact finger interruptions after printing.

At some spots not perfectly washed out emulsion residuals were found, which increases the probability of contact finger interruptions after the printing process.

The achieved contact finger geometries after printing and firing were evaluated using the confocal laser microscope described in section 4.1.1. Ten contact finger positions over the cell were evaluated and at every position 10 measurements of the contact finger width were done. The results presented in this section represent the average value of these measurements. The needed wet-paste consumption per wafer was weighted during the printing process by an automated balance included in the screen-printing line weighting the wafer before and directly after the printing step. This parameter was compared with the

measured viscosity and yield stress of the pastes (description of the measurement procedure compare section 4.5). A summary of the characterized key parameters of all investigated pastes can be found in Table 6.1 at the end of this section. The starting point for the investigation was the printing of a commercial silver fine-line paste from a different supplier (paste 1) and a not adapted standard silver front side paste from Heraeus (paste 2) using the described fine line screen. Fig. 6.2 shows top view microscope images and average contact finger geometry of the achieved contact fingers after printing and firing of the fine-line paste (a and b) and the standard Ag-paste (c and d). For the fine-line paste, a wet-paste consumption of ~ 20 mg/cell and for the standard paste a wet-paste consumption of 108 mg/cell was measured. This difference is reflected in the contact finger geometry. Whereas the fine line paste results in ~ 1 μm thin and 47 μm wide contact fingers (random pyramids were observed not to be totally covered by the silver layer), the standard paste ends up in 12 μm high and 70 μm wide contact fingers.

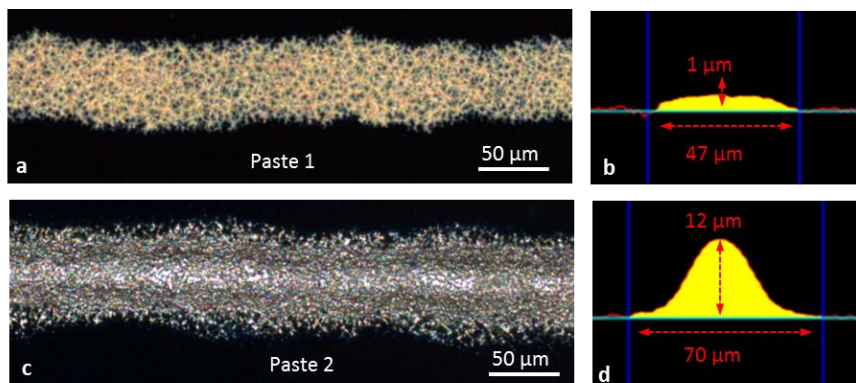


Fig. 6.2: Microscope top view image of a commercial Ag-fine-line paste (a, paste 1) with an illustration of the average contact finger geometry: 47 μm wide and 1 μm high (b) and microscope top view image of a standard Ag-front side paste (c, paste 2) with an average contact finger geometry: 70 μm wide and 12 μm high (d), printed through the fine line screen

Based on this result three generations of rheologically adapted experimental pastes were produced by Heraeus to investigate the influence of the paste viscosity, the silver particle size and the influence of the yield stress.

6.1.1 Influence of the paste viscosity

In the first generation, two pastes with specifically adapted viscosity were produced. Paste 3 features a viscosity of ~ 16 Pas (at $\dot{\gamma} = 100 \text{ s}^{-1}$) and paste 4 was set to ~ 8 Pas (at $\dot{\gamma} = 100 \text{ s}^{-1}$) which is half of the viscosity of paste three. Fig. 6.3 shows top view microscope images and the average contact finger geometry after printing and firing of paste 3 (a-b) and paste 4 (c-d). The contact finger geometry shows clearly that lower paste viscosities result in wider contact fingers due to pronounced diffidence of the paste on the substrate (paste 4).

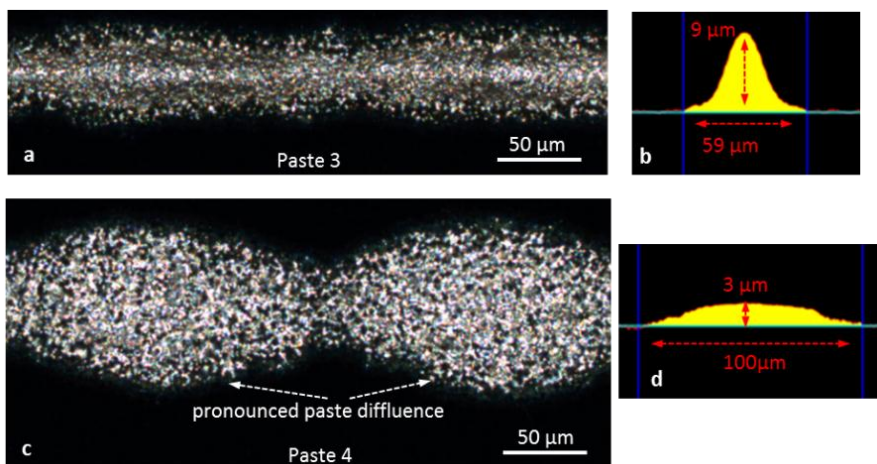


Fig. 6.3: Microscope top view image and the average contact finger geometry of printed and fired Ag-pastes: paste 3 with a viscosity of ~ 16 Pas (a-b) and paste 4 with a viscosity of ~ 8 Pas (c-d), printed through the fine line screen. Paste 4 shows pronounced diffidence of the paste ending up in considerably wider contact fingers.

Fig. 6.4 shows the contact finger width (left axis, black diamonds) and the wet-paste consumption (right axis, red circles) over the paste viscosity for all pastes investigated in the experiment (the results of the already discussed pastes 1-4 are indicated in the graph).

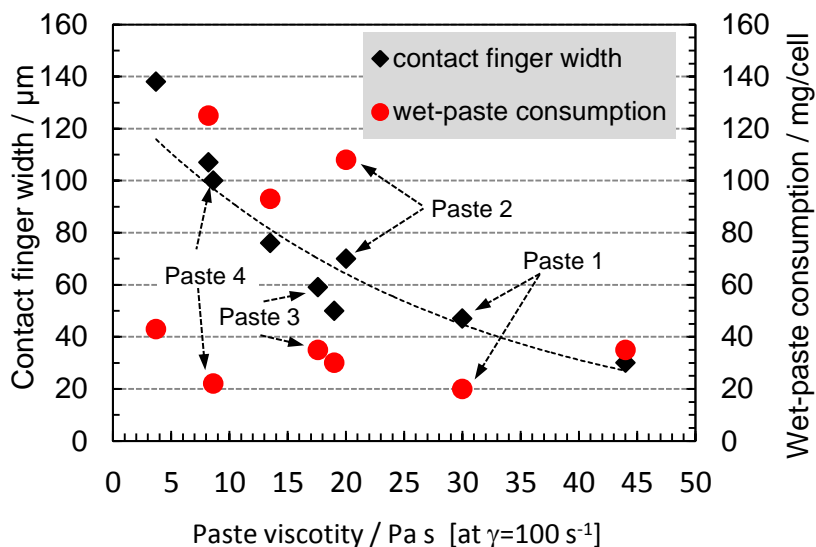


Fig. 6.4: Contact finger width (left axis, black diamonds) and wet-paste consumption (right axis, red circles) over paste viscosity for all pastes evaluated in the screen-printing experiments. The data points of the already discussed pastes 1-4 are indicated in the graph.

The figure reveals that the printed contact finger width (black diamonds) correlates nearly linearly with the paste viscosity: the higher the paste viscosity, the finer the achieved contact finger width. However, the wet-paste consumption (red circles) does not correlate with the paste viscosity. This means paste viscosity as rheological set point alone is not sufficient to develop an optimal paste regarding both key parameters for screen-printed seed-layers: small contact finger width and low wet-paste consumption.

6.1.2 Influence of the particle size

In generation two, the particle size of the silver particles contained in the pastes and the solid content were varied. Paste 5 contains silver particles with a diameter of $3 \mu\text{m}$ and paste 6 contains particles with a diameter of $1 \mu\text{m}$. For both pastes the solid content was kept constant at $\sim 91.5\%$. Paste 7 was produced with small particles ($1 \mu\text{m}$ diameter) and additionally with a lower solid content of $\sim 71\%$. Fig. 6.5 shows top view microscope images and average contact finger cross section areas of the contact fingers after printing and firing of paste 5 (a-b)

and paste 6 (c-d). The particle size changes the rheology of the pastes and has therefore an influence on the resulting seed-layer geometry. Reducing the silver particle diameter from 3 μm to 1 μm leads to a viscosity increase of ~ 5 Pas (at $\dot{\gamma} = 100 \text{ s}^{-1}$) from 8.6 Pas (at $\dot{\gamma} = 100 \text{ s}^{-1}$) for paste 5 to 13.5 Pas (at $\dot{\gamma} = 100 \text{ s}^{-1}$) for paste 6, and therefore to a smaller contact finger width. Additionally, paste 6 allows less wet paste consumption, which is desired. Lowering the particle size leads to less diffuence of the paste. Lowering the solid content at constant particle size leads to lower viscosity, wider contact fingers and to less wet-paste consumption. This means that smaller particle sizes increases the viscosity of the paste and helps to get finer seed-layers with smaller wet-paste laydown.

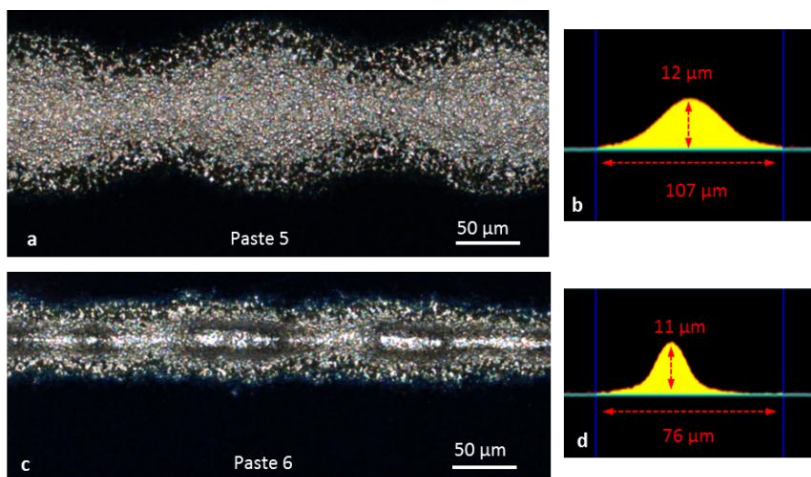


Fig. 6.5: Microscope top view image and average contact finger geometry of printed and fired Ag-pastes: paste 5 with a silver particle diameter of 3 μm (a-b) and paste 6 with a particle diameter of 1 μm (c-d), printed through the fine line screen. Paste 6 containing the smaller particles shows less diffuence and less wet-paste consumption.

The use of silver particles in the nanometre scale offer the potential of a further decrease of the solid content by simultaneously achieving a high viscosity as it is the case for the commercial fine line paste 1. Fig. 6.6 shows an SEM cross section image of paste 1 in dried condition (not fired) with indicated measurement of the particle size. It becomes clear that round silver particles with a diameter of ~ 70 -230 nm are contained in paste 1. This shows that small particles in the paste facilitate a paste formulation which leads to small paste laydown and simultaneously fine contact fingers after screen-printing and firing.

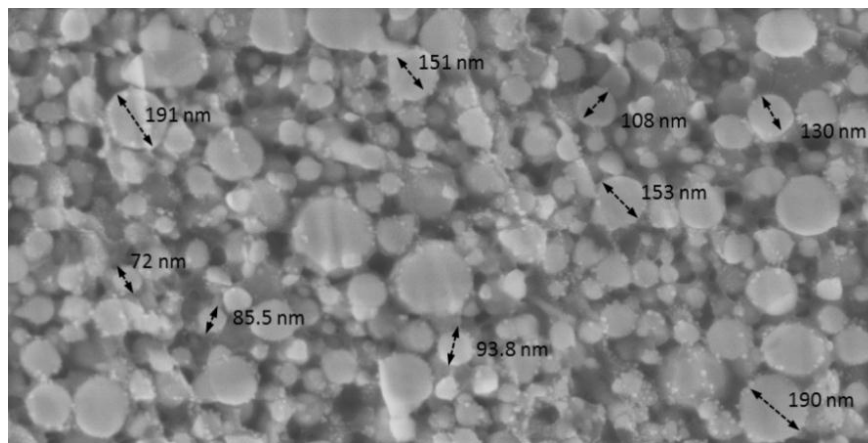


Fig. 6.6: SEM cross section image of paste 1 (dried, not fired) and indicated measurement of the Ag particle size

In the following section the correlation between the yield stress of the experimental pastes and the key parameters for seed-layer formation is investigated.

6.1.3 Influence of the yield stress

The yield stress τ is the value of shear stress where the region of linear elastic paste deformation ends. It marks the point where reversible elastic deformation passes to irreversible deformation. It was already shown by Pospischil *et al.* [128], [129] that the yield stress of dispensed silver pastes correlates with the contact finger geometry. For the experimental screen-printing pastes the yield stress was characterized according to Metzger [122] as described in detail in section 4.5. Fig. 6.7 shows the contact finger width (left axis, black diamonds) and the wet-paste consumption (right axis, red circles) over the evaluated yield stress for every experimental paste.

A clear correlation of decreasing contact finger width and paste consumption with increasing yield stress can be observed especially for yield stress values > 250 Pa. High yield stress values are beneficial because diffuence of the paste on the substrate after the printing process is strongly reduced and only the paste parts which touch the substrate during the printing process can be released from the screen, this leads to reduced wet-paste consumption.

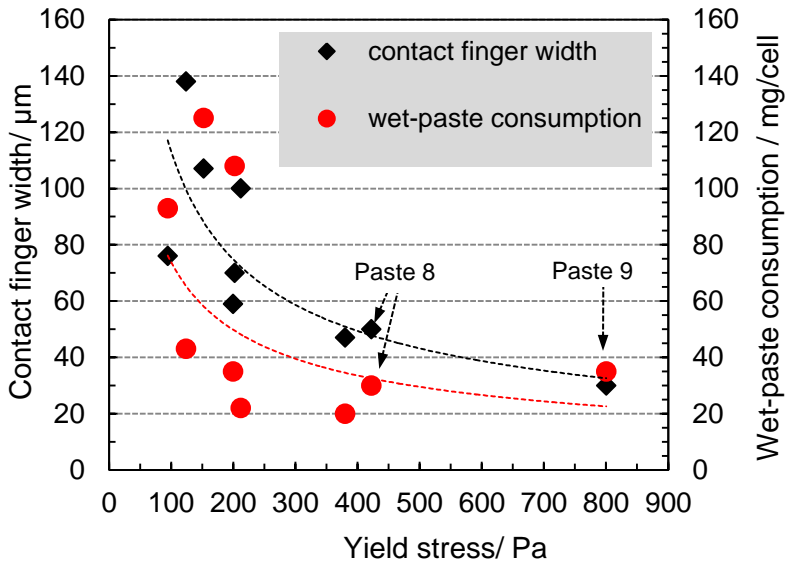


Fig. 6.7: Reached contact finger width (left axis, black diamonds) and wet-paste consumption (right axis, red circles) over the yield stress for all pastes used in the screen-printing experiments

With the knowledge of this behaviour in generation 3 paste 8 and 9 were produced setting the yield stress to ~ 400 Pa for paste 8 and to ~ 800 Pa for paste 9. With paste 9, the combination of $30\ \mu\text{m}$ fine printed contact fingers (Fig. 6.8 a) and a low wet-paste consumption of $35\ \text{mg/cell}$, which corresponds to a silver consumption of $\sim 25\ \text{mg/cell}$, were reached printing a grid with three full $1.5\ \text{mm}$ busbars.

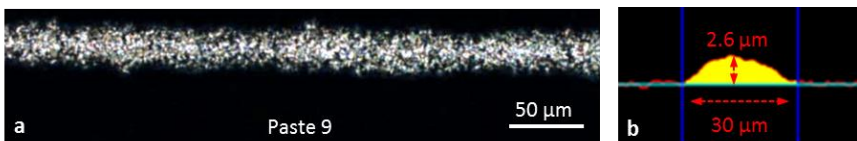


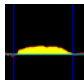
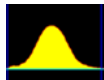
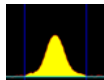

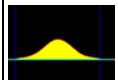
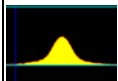
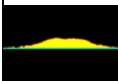
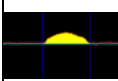
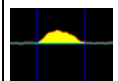
Fig. 6.8: Microscope top view image and average contact finger geometry of the printed and fired Ag-paste 9 with a yield stress of ~ 800 Pa (a-b), printed through the fine line screen

Paste 8 resulted in a contact finger width of $\sim 50\ \mu\text{m}$ and a slightly lower wet paste consumption of $\sim 30\ \text{mg/cell}$. This means creating a paste for screen-printed

seed-layers with the aim of low paste consumption and small printed structures for solar cells featuring a random pyramid texture the rheology of the paste should be set to yield stress limits of > 400 Pa.

Table 6.1 shows an overview of the silver pastes used in this section, and the achieved key parameters contact geometry and wet-paste consumption and the evaluated rheological parameters viscosity and yield stress. The contact finger profile in column 2 represents an average profile evaluated by the laser confocal microscope (compare section 4.1.1). The given viscosity was measured at a shear rate of 100 s^{-1} , at 25°C using a rotational rheometer equipped with a cone-plate geometry and the yield stress was evaluated as described in section 4.5.

Table 6.1: Key parameters of the silver pastes used in this section

No.	Contact finger profile	Solid content / %	Paste viscosity / Pa s	Yield stress / Pa	Wet-paste consumption / mg/cell	Contact finger width / μm	Contact finger height / μm
1		38.5	30	380	20	47	1
2		90.5	12-20	202	108	70	12
3		89.8	17.6	200	35	59	9
4		67.8	8.6	212	22	100	3
5		91.5	8.2	152	125	107	12
6		91.4	1.5	95	93	76	11
7		71.3	3.7	123	43	138	3
8		70.8	18.9	422	30	50	2.4
9		70.8	44	800	35	30	2.6

6.2 Evaluation of printed seed-layers

Besides the wide spread standard screen-printing technology, seed-layers for plated copper metallization can be printed using alternative printing technologies especially suited for seed-layer deposition. Aerosol jet printing (described in section 3.4.1), ink-jet printing (described in section 3.4.2) and flexographic printing (described in section 3.4.3) were used to produce cells with plated Ni-Cu-Ag front side metallization and compare them with cells featuring a screen-printed seed-layer and reference cells with standard fully screen-printed front side metallization. The seed-layer geometry achieved with the different technologies, the silver consumption and the *I-V*-parameters were evaluated. Standard $156 \times 156 \text{ mm}^2$ solar cell precursors as described in section 5.5 were used and printed with the identical grid of 90 contact fingers with each seed-layer printing technology. As the busbar printing is not possible in a comparable way with all seed-layer printing technologies (different busbar shape and ink amount) the busbars were screen-printed in a second printing step for all samples using the same segmented busbar geometry and the same paste to enable good comparability of the groups (for the busbars a wet paste consumption of 10 mg/cell were achieved which corresponds to a silver consumption of 4 mg/cell, compare table 6.2). This assures that the differences in the *I-V*-parameters are exclusively caused by the contact fingers. A dependency on the process-specific busbar design can be suspended. The cells were fired at set-peak temperatures of 880°C, 900°C and 920°C in an inline firing furnace. Higher firing temperatures than 920°C affect the used PECVD silicon nitride layer. Blistering of the silicon nitride was observed, which leads to “ghost plating” outside the contacts structures. The Ni-Cu-Ag plating was done in inline machines described in section 5.1.2. A nickel mass of ~15 mg/cell, a copper mass of ~90 mg/cell and a silver capping of 7 mg/cell was plated identically for all groups.

6.2.1 Solar cells with plated copper metallization on ink-jet printed seed-layer

For the ink-jet printing, the printing tool described in section 3.4.2 was used. Contact fingers with an average finger width of 35-40 μm and an average contact finger height of 2.6 μm were achieved after printing and firing. Fig. 6.9 shows a microscope top view image of an inkjet-printed contact finger (a) and the

average contact finger geometry evaluated by the laser microscope (b). The wet ink consumption for the printing of 90 contact fingers was ~ 12 mg which represents a silver consumption of ~ 6 mg (the solid content of the silver ink was characterized to 47%). The contact fingers printed with ink-jet-printing show a very uniform shape at every position of the cell. The bleeding of the silver ink is small and the contact fingers cover the pyramids of the structured monocrystalline surface completely.

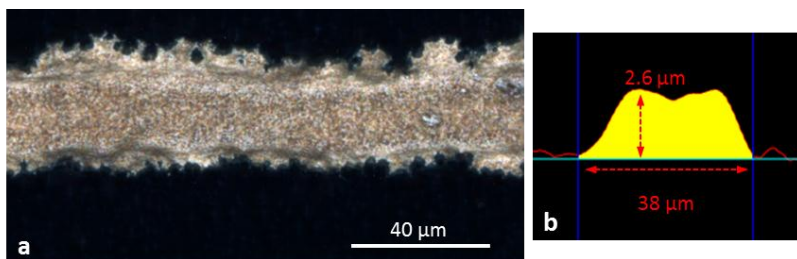


Fig. 6.9: Top-view microscope image of an ink-jet printed contact finger (a) and the illustration of an average contact finger geometry (b) with a width of $\sim 38\ \mu\text{m}$ and a height of $\sim 2.6\ \mu\text{m}$

Fig. 6.10 shows the microscope image of an ink-jet printed seed-layer contact finger cross section (1), with plated nickel diffusion barrier (2), plated copper layer (3) and the fine silver capping (4). A total contact finger width of $60\ \mu\text{m}$ and a contact finger height of $12\ \mu\text{m}$ were achieved after plating. This corresponds to an aspect ratio of 0.2.

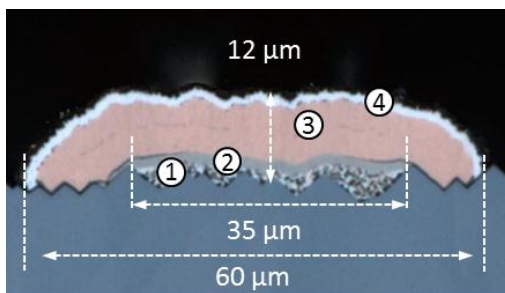


Fig. 6.10: Microscope image of a plated contact finger cross-section with ink-jet printed seed-layer (1), nickel diffusion barrier (2), copper conductive layer (3) and silver capping (4)

The I - V -parameters of the cells with ink-jet printed seed-layer are shown in Fig. 6.11. The cells fired with a set peak temperature of 920°C show the best efficiency results (a) with a maximum efficiency of 19.2%, an average efficiency of 19.1% and a very narrow efficiency distribution. For the lower set-peak temperatures of 880°C and 900°C the efficiency is limited by the fill factor (b). The fill factor limitation is caused by increased series resistance losses, which traces back to a higher contact resistance. The back side metallization and the total plated mass for the front side metallization are identical for all cells and do not contribute to differences in the series resistance, as was confirmed by measurements of the grid resistivity from busbar to busbar (compare Fig. 6.22).

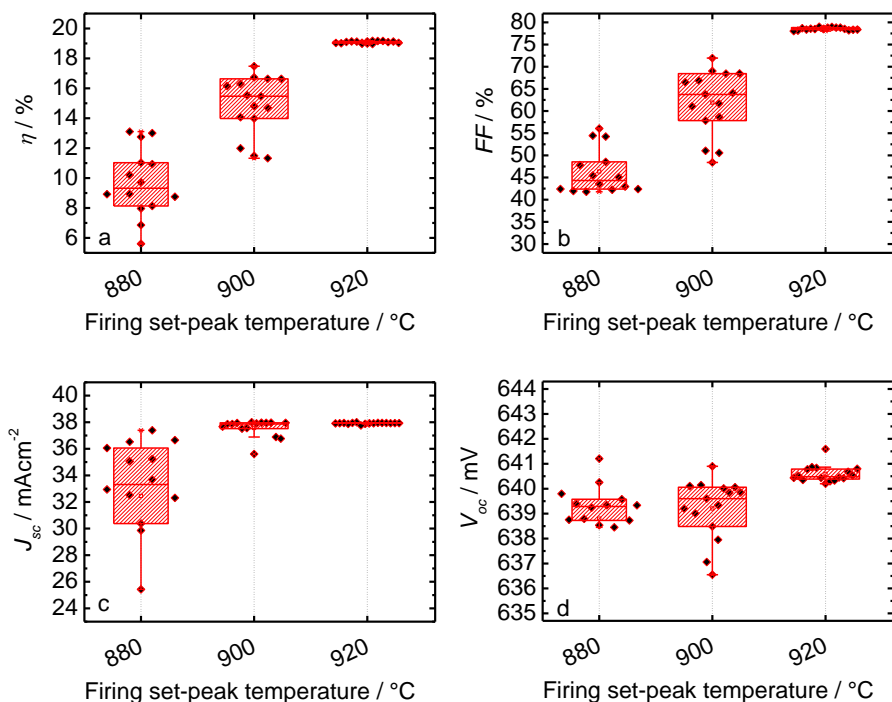


Fig. 6.11: I - V -parameters efficiency (a), fill factor (b), short circuit current (c) and open circuit voltage (d) of the cells with ink-jet printed seed-layer fired at 880°C, 900°C and 920°C, subsequently plated with a Ni-Cu-Ag metallization

6.2.2 Solar cells with plated copper metallization on aerosol-jet printed seed-layer

For the aerosol-printing the printing tool described in section 3.4.1 was used. Contact fingers with a width of 30-40 μm and an average contact finger height of 1.4 μm were achieved. Fig. 6.12 shows a microscope top view image of an aerosol printed contact finger (a) and an illustration of the average contact finger geometry evaluated by the laser microscope (b) before plating. The wet ink consumption for the printing of 90 contact fingers was ~ 5 mg/cell, which represents a silver consumption of 3.6 mg (the solid content of the silver ink was characterized to 71.5%). The contact fingers printed with aerosol-jet printing show a uniform shape at every position of the cell. The bleeding of the silver ink is small. The contact fingers do not completely cover the random pyramids of the monocrystalline surface.

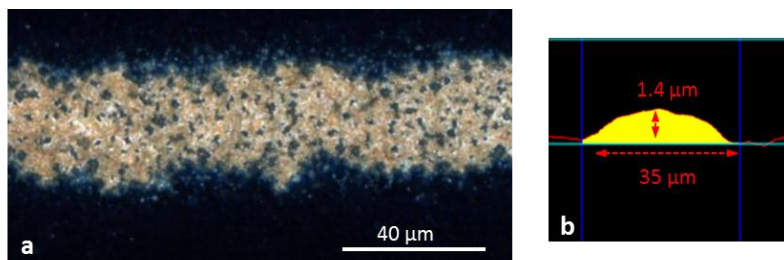


Fig. 6.12: Top-view microscope image of an aerosol printed contact finger (a) and the illustration of an average contact finger geometry (b) with an average finger width of ~ 35 μm and a contact finger height of ~ 1.4 μm

Fig. 6.13 shows the microscope image of a contact finger cross section with aerosol-jet printed seed-layer (1), plated nickel diffusion barrier (2), plated copper conductive layer (3) and the fine silver capping (4). A total contact finger width of 55-65 μm and a contact finger height of 12 μm were achieved after plating. This corresponds to an aspect ratio of 0.18-0.22.

The I - V -parameters of the cells are shown in Fig. 6.14. The cells fired with a set peak temperature of 920°C show the best results with a maximum efficiency of 17.3% and an average efficiency of 16.6%.

For the lower set-peak temperatures of 880°C and 900°C the efficiency limitation by the fill factor (b) is higher. The fill factor limitation is caused by increased series resistance losses, which can be traced back to a higher contact

resistance because the back side metallization and the total plated mass for the front side metallization is identical for all cells and do not contribute to differences in the series resistance (compare Fig. 6.22).

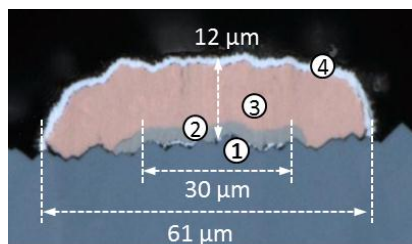


Fig. 6.13: Microscope image of a plated contact finger cross-section with aerosol-jet printed seed-layer (1), nickel diffusion barrier (2), copper conductive layer (3) and silver capping (4)

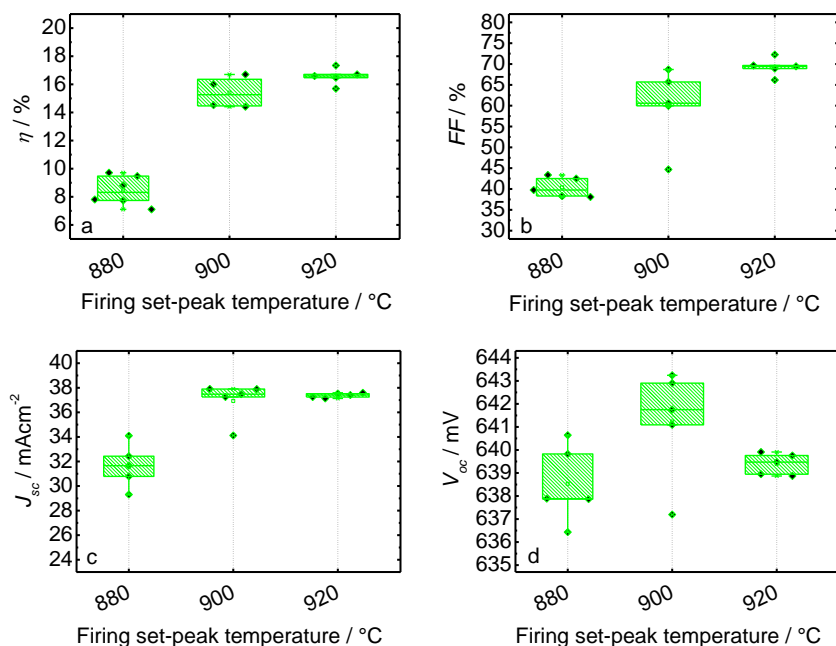


Fig. 6.14: The I - V -parameters efficiency (a), fill factor (b), short circuit current (c) and open circuit voltage (d) of the cells with aerosol printed seed-layer fired at set-peak temperatures of 880°C, 900°C and 920°C, subsequently plated with a Ni-Cu-Ag metallization

Compared to the cells with ink-jet printed seed-layer the contact formation to the emitter is limited. The decrease in the open circuit voltage for a firing temperature of 920°C indicates that the glass frit in the used silver ink induces slight emitter damage.

6.2.3 Solar cells with plated copper metallization on flexographic-printed seed-layer

Flexographic printing is in an early research state for silicon solar cell metallization. The results shown here are the first using flexographic printing as seed-layer for Ni-Cu metallized cells in industrial scale. The printing tool described in section 3.4.3 was used for seed-layer printing. Contact fingers with a finger width of 40-80 μm and a maximum contact finger height of 0.9 μm were achieved. Fig. 6.15 shows a microscope top view image of a flexographic printed contact finger (a) and an average contact finger geometry evaluated by the laser microscope (b) before plating. The wet ink consumption for the printing of 90 contact fingers was ~ 7 mg which represents a silver consumption of 4 mg (the solid content of the silver ink was characterized to 57.1%). The contact fingers printed with flexographic-printing show a non-uniform shape over the cell. At some positions the seed-layer is up to 80 μm wide and at other positions it is ~ 40 μm wide. Most probably, due to inhomogeneous printing pressure over the wafer the contact fingers show line fringing with a pronounced ink deposition on the finger edges whereas in the middle of the line, less ink deposition can be observed. The random pyramids are not completely covered.

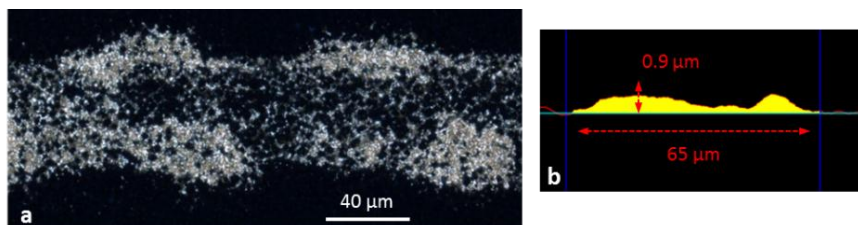


Fig. 6.15: Top-view microscope image of a flexographic printed contact finger (a) and the illustration of an average contact finger geometry (b) with a seed-layer width of ~ 65 μm and a maximum finger height of ~ 0.9 μm

The inhomogeneous ink distribution leads to inhomogeneous plating of the contact fingers. Fig. 6.16 shows the microscope image of a contact finger cross

section with flexographic printed seed-layer (1), plated nickel diffusion barrier (2), plated copper layer (3) and fine silver capping (4). Some contact fingers show a homogenous distribution of the plated metal (a) and at some spots the metal distribution appears inhomogeneous (b). This influences the electrical parameters, especially the fill factor, due to insufficient lateral conductivity of the contact fingers.

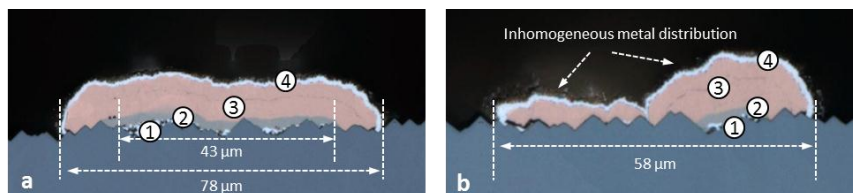


Fig. 6.16: Microscope cross section images of a Ni-Cu-Ag plated contact finger with flexographic printed seed-layer. A homogeneous cross section (a) and cross section with inhomogeneous metal distribution (b) due to inhomogeneous deposition of the seed-layer with seed-layer (1), plated nickel diffusion barrier (2), plated copper conductive layer (3) and silver capping (4)

The I - V -parameters of the cells are shown in Fig. 6.17. The cells fired with a set peak temperature of 880°C show the best results with a maximum efficiency of 18.3% and an average efficiency of 12.8%. The efficiency shows a big spreading for all firing temperatures and is strongly limited by the fill factor (b). The fill factor limitation is caused by increased series resistance losses, which can be traced back to insufficiently low contact resistance and an inhomogeneous distribution of the plated metal. The back side metallization and the total plated mass for the front side metallization is identical for all cells and do not contribute to differences in the series resistance. The inhomogeneity and the very thin printed seed-layer cause areas with good contact to the emitter and areas with insufficient contact to the emitter. This leads to well plated and nearly non plated contact finger regions, which explains the wide spreading of the results and the suffering fill factor for every firing temperature. The short circuit current (c) and the open circuit voltage (d) are limited by the series resistance. The open circuit voltage further decreases with higher firing temperatures; this is a hint for etching damages caused by the used silver ink.

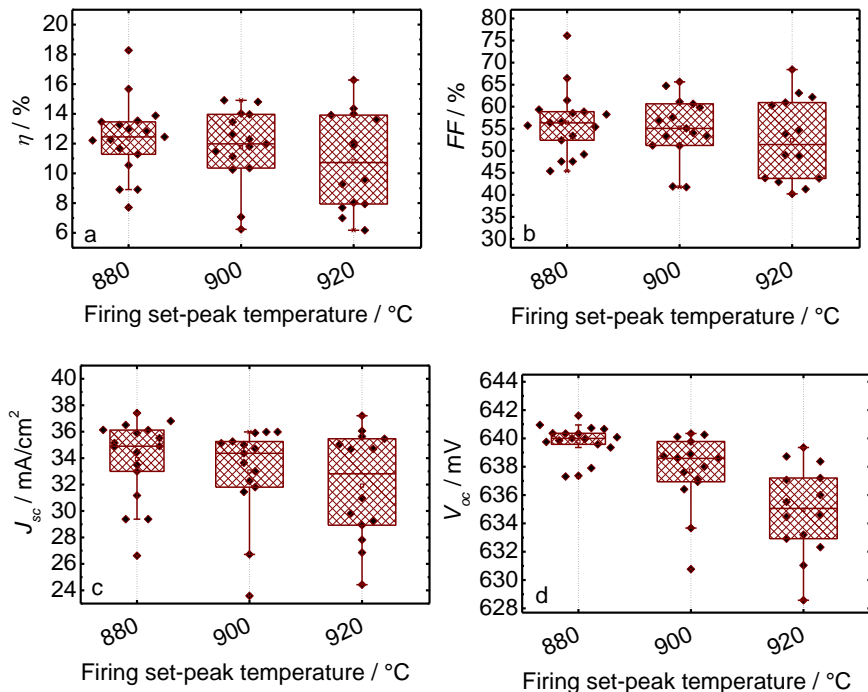


Fig. 6.17: The I-V-parameters efficiency (a), fill factor (b), short circuit current (c) and open circuit voltage (d) of the cells with flexographic printed seed-layer and plated Ni-Cu-Ag metallization for the set-peak firing temperatures of 880°C, 900°C and 920°C

6.2.4 Solar cells with plated copper metallization on screen-printed seed-layer

For the production of the screen-printed seed-layer a 400 mesh fine line screen with a wire diameter of 18 μm , a contact finger opening of 25 μm and an emulsion height of 5-9 μm was used. With a commercial fine line silver paste contact fingers with an average width of 30-45 μm and an average height of ~ 0.8 μm were achieved. Fig. 6.18 shows a microscope top view image of a screen-printed seed-layer (a) and an average contact finger geometry evaluated by the laser microscope (b).

The wet paste consumption for the printing of 90 contact fingers was ~ 8 mg/wafer, which represents a silver consumption of ~ 3 mg (the solid content of the silver paste was characterized to $\sim 38\%$).

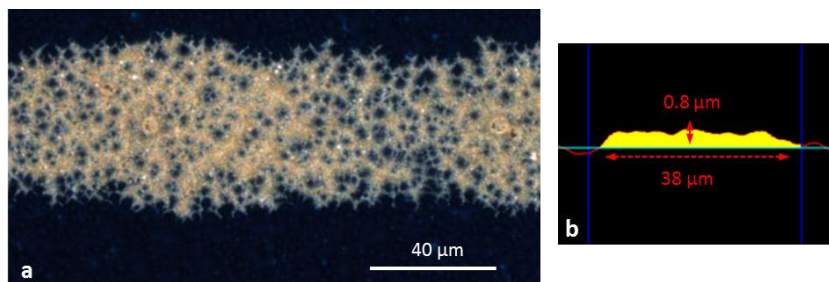


Fig. 6.18: Top-view microscope image of a screen-printed contact finger (a) and the illustration of an average contact finger cross-section (b) with a seed-layer width of $\sim 40\text{--}50\text{ }\mu\text{m}$ and a height of $0.8\text{ }\mu\text{m}$

Fig. 6.19 shows the microscope image of a contact finger cross section with screen-printed seed-layer (1), plated nickel diffusion barrier (2), plated copper conductive layer (3) and the fine silver capping (4). A total contact finger width of $65\text{ }\mu\text{m}$ and a contact finger height of $13\text{ }\mu\text{m}$ were achieved after plating. This corresponds to an aspect ratio of 0.2.

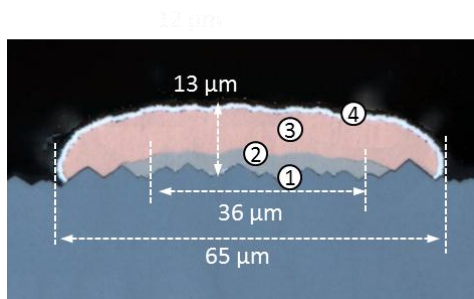


Fig. 6.19: Microscope image of a plated contact finger cross-section with screen-printed seed-layer (1), nickel diffusion barrier (2), copper conductive layer (3) and silver capping (4)

The I - V -parameters of the cells are shown in Fig. 6.20. The cells fired with a set peak temperature of 920°C show the best results with a maximum efficiency of 18.3% and an average efficiency of 17.3%. The efficiency shows spreading for all firing temperatures and is limited by the fill factor (b). The fill factor limitation is caused by increased series resistance losses, which can be traced back to an insufficient contact resistance because the back side metallization and

the total plated mass for the front side metallization is identical for all cells and does not contribute to differences in the series resistance.

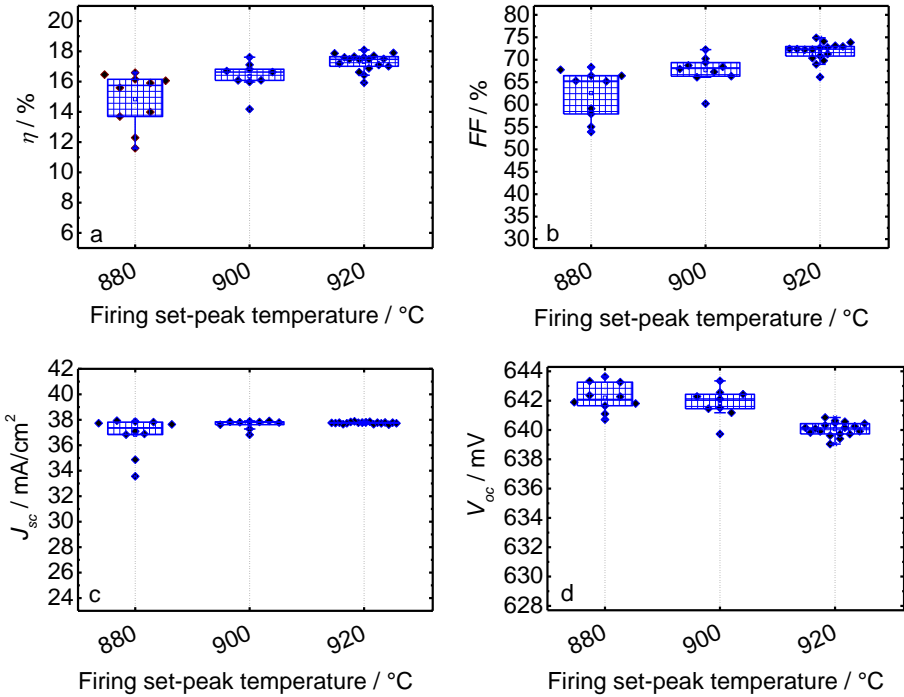


Fig. 6.20: The I - V -parameters efficiency (a), fill factor (b), short circuit current (c) and open circuit voltage (d) of the cells with screen-printed seed-layer and plated Ni-Cu-Ag metallization for the set-peak firing temperatures of 880°C, 900°C and 920°C.

6.2.5 Comparison and classification with fully screen-printed solar cells

In this section the key parameters silver consumption and electrical performance for cells with Ni-Cu-Ag plated metallization based on different seed-layers, introduced in the subsections above are compared with the parameters of cells with standard fully silver screen-printed front side metallization. Table 6.2 shows the total silver consumption needed for the front side metallization of each group. The silver consumption needed for the backside metallization (silver pads) is not considered in Table 6.2, it is ~20 mg and equal for all cells. The silver consumption for the front side metallization is composed of the solid part

of the measured wet paste/ink consumption, 4 mg silver needed for the busbar printing and 7 mg silver consumed for the plated capping layer. A total silver consumption for the front side metallization of <18 mg could be realized for the seed-layer cells, which is ~80 mg or ~82% less than for the standard solar cells with fully screen-printed metallization

Table 6.2: Silver consumption for the front side metallization of all experimental groups

Front side metallization	Wet-paste/ink consumption / mg/cell	Solid content of paste/ink / %	Busbar + Ag capping / mg/cell	Total Ag consumption / mg/cell
Flexographic printed seed + Ni-Cu-Ag	7	57.1	4+7	15
Aerosol jet printed seed + Ni-Cu-Ag	5	71.6	4+7	14.6
Screen-printed seed + Ni-Cu-Ag	8	38.5	4+7	14
Ink jet-printed seed +Ni-Cu-Ag	12	47	4+7	17
Fully screen-printed Ag metallization	108	96	-	104

To compare the electrical parameters the best cell set (firing temperature) for each seed-layer group is compared with the electrical results of fully screen-printed solar cells produced by a solar cell manufacturer on similar precursor material. Fig. 6.21 shows the efficiency (a), the fill factor (b), the short circuit current density (c) and the open circuit voltage (d) for all groups. The results show that the reduced efficiency of the cells with flexographic printed, aerosol printed and screen-printed seed-layers, compared to the standard screen-printed reference cells, is clearly caused by a fill factor limitation. The short circuit current density is in the same range with exceptions for the cells with flexographic printed seed-layer. This shows that the reached contact geometry for the cells with screen-printed, aerosol jet printed and ink jet printed seed-layer does not cause significantly higher shading losses than the screen-printed

reference, due to similar contact geometry. The open circuit voltage is ~ 2 mV higher for the plated cells than for the screen-printed reference due to reduced emitter damage by paste etching during the firing process.

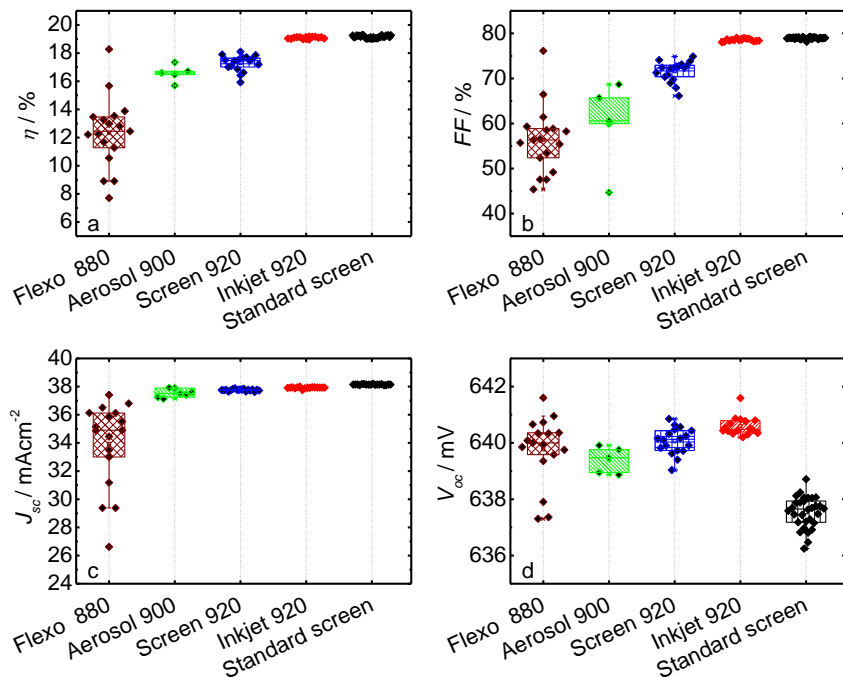


Fig. 6.21: The I-V-parameters efficiency (a), fill factor (b), short circuit current (c) and open circuit voltage (d) of the plated cells based on the different seed-layers (best group respectively) and a fully screen-printed reference cells produced out of the same cell material

To further analyse the fill factor limitation the parameters pFF minus FF , which is a measure for the losses due to the series resistance and the grid resistance between the busbars, which gives information about the lateral conductivity of the contact fingers were evaluated for all groups. Fig. 6.22 shows the results. The FF limitations are clearly caused by series resistance because the parameter pFF minus FF shows the covers the reverse characteristic than the FF (Fig 6.22 a). For the groups with high FF the losses due to the series resistance

are small and vice a versa. The difference in the series resistance contribution can be traced back to the front side metallization because the backside metallization and the wafer material (emitter, base, silicon nitride anti reflection coating) were the same for all cells. This leads to the conclusion that the series resistance is limited by the contact resistance and in the case of the cells with flexographic printed seed-layer additionally by insufficient lateral conductivity of the grid fingers due to inhomogeneous metal distribution. This is clearly indicated by a high grid resistance (Fig. 6.22 b).

The example of the cells with ink-jet printed seed-layer reveals an optimisation potential of the aerosol jet silver ink and the screen-printing fine line silver paste regarding contact formation to the emitter. The cells with flexographic printed seed-layer show the highest losses due to contact resistance as well as a high grid resistivity. This is due to the inhomogeneous metal distribution and contact finger parts with less plated nickel and copper as already discussed and shown in Fig. 6.15. The cells with screen-printed seed-layer also show a slightly higher grid resistivity than the screen-printed reference. As the same Ni, Cu and Ag mass was plated than for the other cell groups and no finger interruptions could be detected, the higher grid resistivity is most probably caused by thin parts at the contact fingers where the low paste deposition cause higher contact resistance and consequently the plated metal layer is smaller at such positions.

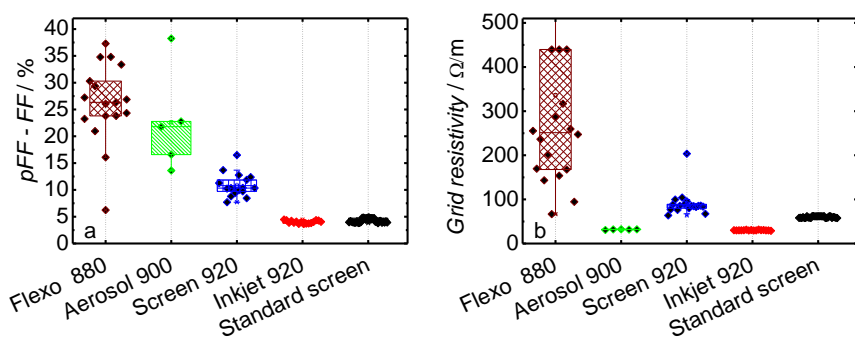


Fig. 6.22: Pseudo fill factor minus fill factor (a) and grid resistivity (b) of the best group for each seed-layer compared with a standard fully screen-printed reference

6.3 Chapter summary

In this chapter, the correlation between the rheological parameters viscosity and yield stress as well as silver particle size of experimental and commercial silver pastes to the resulting seed-layer geometry and the needed wet-paste consumption after printing and firing were investigated (section 6.1).

- The viscosity of the used paste was found to correlate with the resulting contact finger width: the higher the viscosity the smaller the resulting contact fingers. The wet-paste consumption does not correlate with the paste viscosity (section 6.1.1).
- A smaller particle size influences the viscosity of the pastes. Reducing the particle size from 3 μm to 1 μm using a constant solid content increases the paste viscosity and therefore reduces the printed contact finger width and also the wet-paste consumption. This means the reduction of the particle size offers the potential to improve fine-line seed-layer pastes in the desired direction (section 6.1.2).
- The results in section 6.1.3 reveal that the yield stress of the pastes correlates with both key parameters, the wet-paste consumption and the contact finger width. A desired fine contact finger geometry and a simultaneously low wet-paste consumption for screen-printed seed-layers can be reached by adapting the paste rheology resulting in a yield stress of $> 400 \text{ Pa}$.

In section 6.2 standard $156 \times 156 \text{ mm}^2$ industrial scale solar cells with plated Ni-Cu-Ag front side metallisation based on seed-layers printed with ink-jet printing (section 6.2.1), aerosol-jet printing (section 6.2.2), flexographic printing (section 6.2.3) and screen-printing (section 6.2.4) were produced and compared with cells featuring a standard fully screen-printed front side metallization produced on the same cell material, regarding the total silver consumption for the entire front side metallization, the contact geometry and the electrical parameters.

- For the cells based on the ink-jet printed seed-layer the same efficiency level as for the screen-printed reference cells of 19.2% were achieved. For the cells with aerosol-jet and screen-printed seed-layer, potential for

contact resistance improvement was shown. The cells with flexographic printed seed-layer show a strongly increased lateral contact finger resistivity due an inhomogeneous distribution of the seed-layer material and consequently an inhomogeneous distribution of the plated metal.

- With all four seed-layer printing technologies a total silver consumption < 18 mg/cell for the front side metallization (seed-layer + silver capping) were achieved which is ~80% less than for the standard silver metallization.

7 Corrosion mechanism of the screen-printed silver seed-layer

In this chapter, the mechanisms behind the observed phenomenon of reduced adhesion of printed and fired silver seed-layers after nickel, copper and silver plating (chapter 7.1) are investigated in detail. The corrosion of the contacts due to the interaction with single electrolyte compounds (chapter 7.2) and especially the Watts-type nickel electrolyte (chapter 7.4) is evaluated. A microstructure analysis using SEM, TEM, and AFM shows the glass-layer to be corroded by plating solutions (chapter 7.3). In chapter 7.5 the influence of the light induced plating process to the observed corrosion is analysed. Finally a model of the mechanism responsible for contact corrosion during electrochemical metal deposition is developed based on the experimental results (chapter 7.6). Possible strategies to reach sufficient contact adhesion following nickel, copper and silver plating are discussed in chapter 7.7. Chapter 7.8 gives a summary of the presented findings.

7.1 Contact adhesion after Ni-Cu-Ag plating

During the Ni-Cu-Ag plating sequence the contact adhesion between silicon wafer and the front side metallization is observed to decrease compared to the initial adhesion of a screen-printed seed-layer. This compromises the automated module integration of the plated cells and is probably critical with respect to the long term stability of the cell interconnection in the module. Fig. 7.1 shows the measured contact peel-force of a screen-printed and fired silver contact without any plating (blue curve and triangles), with copper plating only (red curve and circles), and with nickel plating only (black curve and squares). The figure illustrates that the nickel plating step with a duration of two minutes and a pH of the Ni-electrolyte of ~ 4 affects adhesion clearly, whereas the copper plating step with a duration of five minutes and a pH of ~ 2.8 does not lead to an adhesion drop compared to the non-plated reference. This means that the contact adhesion is not only influenced by the pH of the plating solution as described in [130] where contact corrosion was observed only for highly acidic and highly alkaline chemicals.

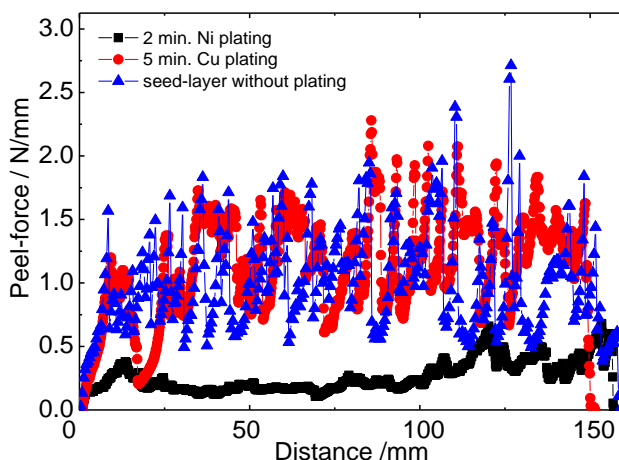


Fig. 7.1: Contact peel-force of a screen-printed Ag seed-layer without any plating (blue curve and triangles), with only Cu plating (red curve and circles) and with only Ni plating (black curve and squares)

To study the adhesion after varied plating durations contacts were plated with the entire metal stack of Ni, Cu and Ag. For the plating, the experimental lab setup (compare section 5.1.1) and for the nickel plating the self-mixed Watts-type electrolyte including boric acid and nickel sulphate (compare Table 5.1) was used. For the copper plating, a commercially available electrolyte with a pH of 2.8 including sulphuric acid and copper sulphate was used (compare Table 5.2). Silver capping was similar for every sample using a commercially available silver electrolyte (compare Table 5.2) with a plating duration of one minute. The contacts were soldered with six soldering spots on each busbar under reproducible conditions on the experimental soldering station as described in section 5.3.

Fig. 7.2 shows the quantitative peel-force results of the plated busbars for varied nickel plating times between two and eight minutes.

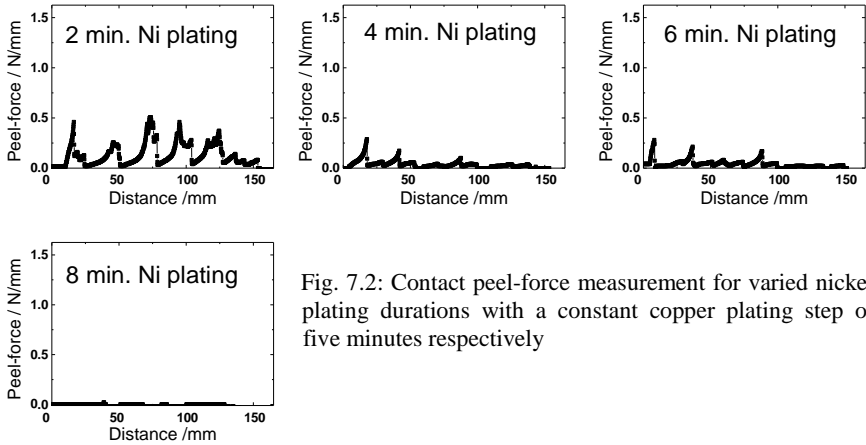


Fig. 7.2: Contact peel-force measurement for varied nickel plating durations with a constant copper plating step of five minutes respectively

The copper plating duration was constant at 5 minutes for this experiment. A clear adhesion drop with increased nickel plating durations can be observed. Fig. 7.3 shows the peel-force results for varied copper plating times between five and twenty minutes.

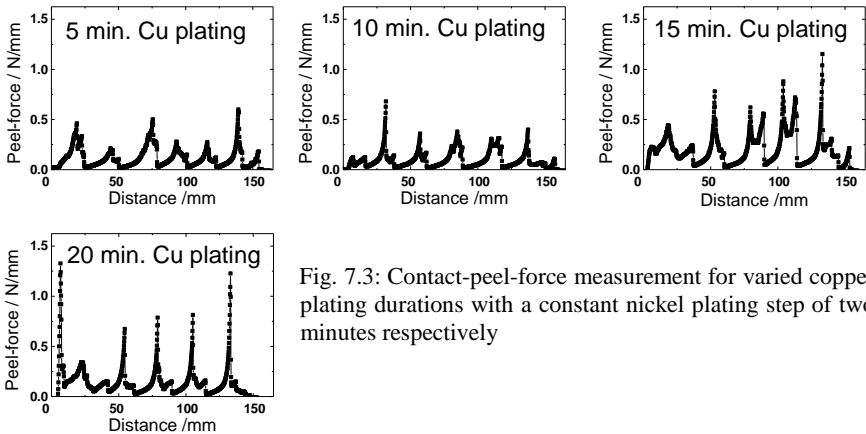


Fig. 7.3: Contact-peel-force measurement for varied copper plating durations with a constant nickel plating step of two minutes respectively

In this case the nickel plating time was constant at two minutes. The maximum peel-force values rises from 0.57 N/mm for five minutes Cu plating to 1.32 N/mm for twenty minutes Cu plating, but the average peel-force does not change much.

This result confirms that the adhesion drop after Ni-Cu-Ag plating is clearly caused by the nickel plating step. Copper plating does not cause adhesion problems, although it takes longer and is conducted with an electrolyte offering a lower pH than the nickel electrolyte. To elucidate the origin of this effect and to clarify if there is a pH dependency, the interaction between screen-printed contacts and different chemicals used in the plating solutions is analysed in the following section in more detail.

7.2 Interaction between plating chemicals and screen-printed Ag-contacts

Regarding the contact adhesion loss of screen-printed contacts after plating it seems likely that the chemicals used in the electrolytes are responsible for contact corrosion. In exposure experiments, screen-printed silver contacts, produced with three different front side pastes made at Fraunhofer ISE, were exposed to different chemicals. The Contacts were soldered, the peel-force was characterized and the silver amount dissolved from the contacts during exposure was analysed by ICP-OES (compare section 4.4.1). The solar cell samples were produced according to the description in chapter 5.2.1 and for comparability fired in an inline belt furnace at the same set peak temperature of 900°C. It is worth to mention that additional firing optimizations would improve the adhesion results slightly, depending on the paste, but this was not the scope of this experiment. The general trends in the results between sufficient (~1 N/mm compare section 3.1.2) and zero adhesion are not expected to change dramatically. Table 7.1 shows the used silver pastes and their composition.

Table 7.1: Front side Ag-paste formulations set up for the chemical exposure experiments

Paste	Glass system	General composition of the paste
1	3wt% lead glass	73wt% silver 24wt% binder and solvents
2	3wt% bismuth glass	
3	0.5wt% lead glass + 2.5wt% zinc oxide	
4	basis paste without glass	

The glass system was varied using a paste with lead glass (paste 1) and a paste with bismuth glass (paste 2). Lead glass is the standard glass used in the PV-industry to form the contact between metallization and emitter in the firing process. Bismuth glass was shown to work as an alternative with similar contact formation properties [131]. For paste 3, zinc oxide was added to the lead glass and paste 4 was printed without any glass as a reference, to show the influence of the glass on contact adhesion and on the dissolved silver content in general. The remaining basis components, silver, binder and solvents were constant for every paste.

The contacts were dipped for 10 minutes at room temperature in 15 ml of the chemicals listed in Table 7.2. These solutions were set to the pH-values of usual commercial nickel, copper, silver and tin electrolytes.

Table 7.2: Chemicals used for the exposure experiments

Dipping solution	Molecular formula	pH	A substance of
methane sulphuric acid	$\text{CH}_4\text{O}_3\text{S}$	1	rinse after Ag plating, tin electrolyte
sulphuric acid	H_2SO_4	1	copper electrolyte
sulphuric acid	H_2SO_4	2.8	copper electrolyte
boric acid	H_3BO_3	3.8	nickel electrolyte
potassium hydroxide	KOH	12	silver electrolyte

The used concentrations correlate to the pH and were chosen to represent the value of the related electrolytes. After the exposure, the contacts were manually soldered as described in section 5.3, and an ICP-OES analysis was done with the dipping solutions. Fig. 7.4 shows the silver content of the different dipping solutions (bar chart, left axis) and additionally the average (red dashed curve) and maximum (blue continuous curve) contact peel-force values of the contacts (right axis), after exposure to the different chemicals. The peel-force values are normalized to the width of the soldered ribbon. In case of methane sulphuric acid and sulphuric acid at pH 1 the adhesion values are zero after 10 minutes exposure for all pastes. This correlates with the amount of detected silver that is the highest in these solutions. In the KOH solution with a pH of 12 and in the boric acid solution with a pH of 3.8 nearly no silver was found after dipping and an average contact adhesion of ~ 1.2 N/mm was measured.

The silver paste without glass (paste 4) did just form a very weak mechanical contact. The metallization stuck to the wafer after firing but the measured peel-force was zero even for the non-dipped sample. The amount of silver found in the solutions after dipping was significantly lower than for the other pastes, especially for exposure in methane sulphuric acid and sulphuric acid at pH 1. This reveals that the major part of the silver measured in the dipping solutions is dissolved from the glass-layer in the contacts. Comparing paste 1 (3 wt% lead glass), paste 3 (0.5 wt% lead glass) and paste 4 (0 wt% lead glass) it becomes clear that the measured silver concentration in the dipping solution is lower with a lower glass content in the paste.

If glass is present during the firing process, silver is dissolved in the glass [69] and a transition layer of silver atoms and adjoining chemically bonded oxygen atoms, which are also part of the glass structure, is formed between glass and silver. This intermediate layer is responsible for providing good adhesion between silver and glass [132]. It is indicated by Pourbaix diagrams (compare Appendix A.1) of silver oxide in acidic media that this transition layer can be dissolved by acidic solutions [133].

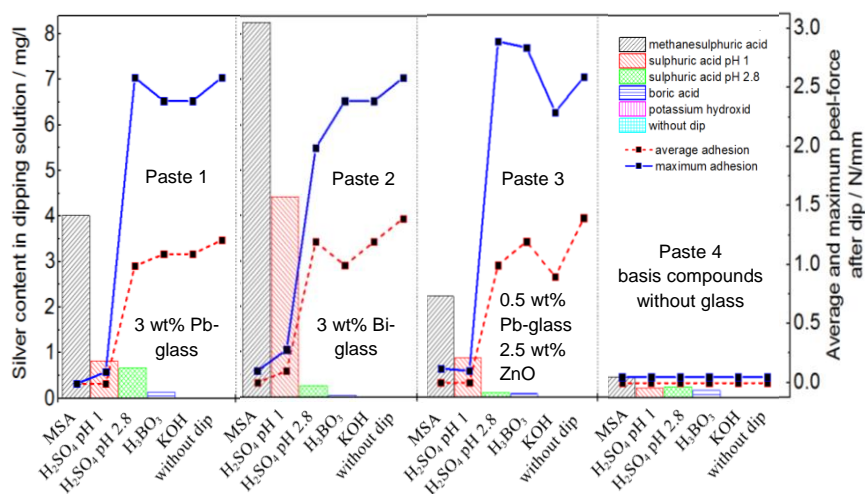


Fig. 7.4: Correlation between the amount of dissolved silver (left axis, bar chart) and the measured adhesion (right axis, average adhesion value red, dashed curve and maximum adhesion value blue curve). The x-axis shows the different used chemicals.

The substitution of lead glass in the paste with bismuth glass did not show an advantage. The amount of dissolved silver for the contacts with bismuth glass is the highest regarding methane sulphuric acid and sulphuric acid with pH 1. This indicates that different glasses exhibit different corrosion rates and that a simple change of glass system using a nobler network former does not lead to reduced corrosion in highly acidic media.

To evaluate the adhesion failure mode, top-view and cross-section SEM-images and EDX-measurements of the contact area after peeling off the contacts were performed. The top-view SEM-image in Fig. 7.5 shows the wafer surface underneath the contact after peeling off the soldered ribbon (paste 1).

The surface is covered with the remaining part of the glass-layer and silver crystals underneath (position 2) except for some few spots, where foursquare shaped areas indicate that entire pyramids were ripped out (position 1). This is proven by EDX measurements which show silicon at position 1 and an increased silver content and traces of lead at position 2. The surface looks similar for all glass containing contacts with an adhesion force of zero. With increasing adhesion, more base areas of ripped pyramids can be observed in the SEM images. For the samples with an average adhesion value >1 N/mm the wafer breaks during the peel-force test and the investigation of the interface is impossible.

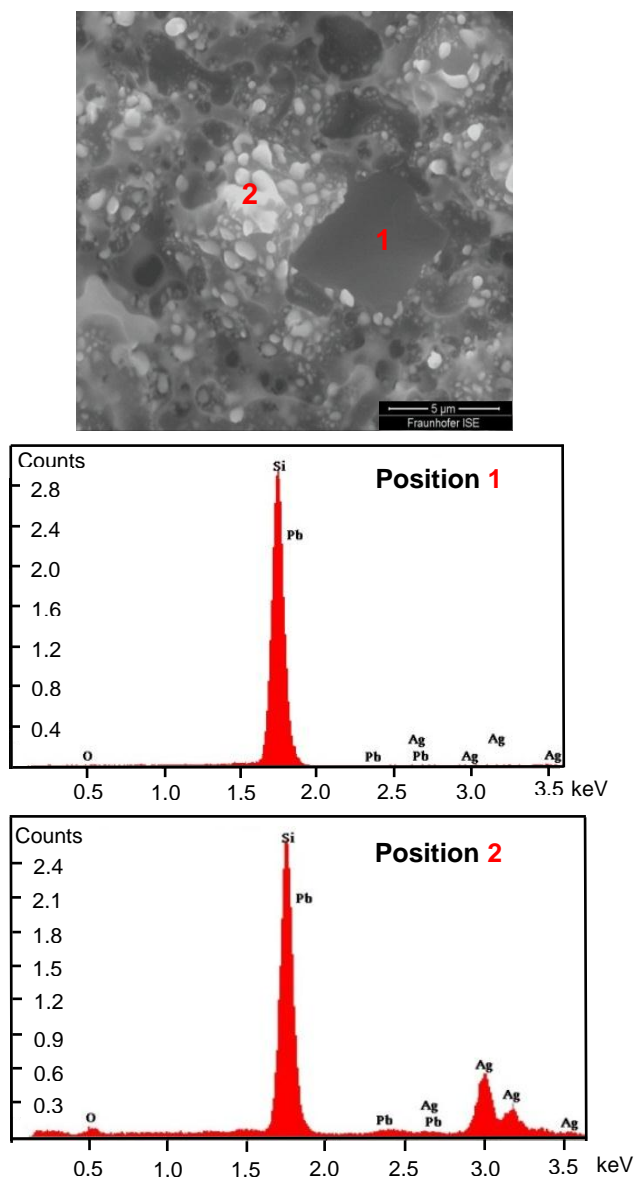


Fig. 7.5: SEM top-view image and EDX measurement of the contact area after peeling off the busbar. Base area of a ripped pyramid (position 1) and silver crystallites underneath the glass layer (position 2)

The cross-section SEM-images of the wafer surface after peeling off the soldered ribbon (Fig. 7.6) show, that the silver crystallites are located under the glass layer (a). The interface between silicon and glass is not affected.

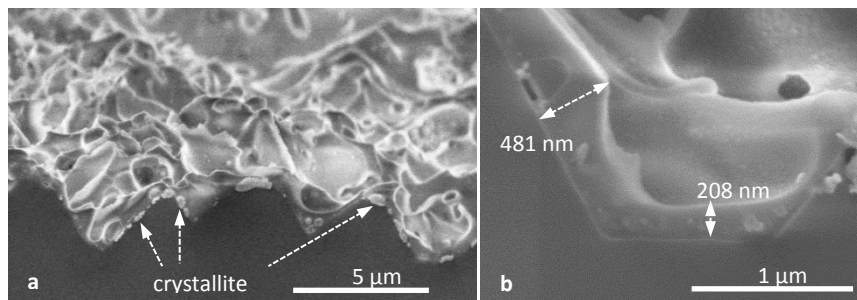


Fig. 7.6: SEM cross-section images of the contact area after peeling off the metal contact. Overview image with crystallites under the glass-layer (a) and a detail image of the glass-layer with thickness measurement (b)

The bulk silver, which was on top of the glass-layer, is entirely removed and sticks to the ribbon. The remaining glass-layer is ~200-500 nm thick (Fig. 7.6 b). It can be concluded that the failing interface is located between the glass layer and the bulk silver. The edges of the remaining glass-layer show rounded shapes (Fig. 7.6 b), which is a hint for a chemical dissolution of the glass.

To reproduce and verify the results shown in Fig. 7.4 that indicates a correlation between dissolved silver, the pH-value of the solution and the adhesion of the contacts in a more systematic fashion, an exposure experiment with contacts produced according to 5.2.1 using a commercial silver paste containing standard lead glass, were conducted. The chemical trace analysis was expanded by additionally measuring the dissolved lead content in the dipping solutions. The contacts were exposed to nickel chloride (one of the compounds of the nickel electrolyte, compare Table 5.1) varying the pH-value by adding hydrochloric acid (HCl). The exposure experiment was executed according to 5.2.2 at 50°C with a duration of 25 minutes. Fig. 7.7 shows the measured silver (left axis, blue bars) and lead content (left axis, red bars) in the dipping solutions with different pH-values. The black triangles represent the average contact peel-force (right axis) along one solar cell contact respectively (156 mm).

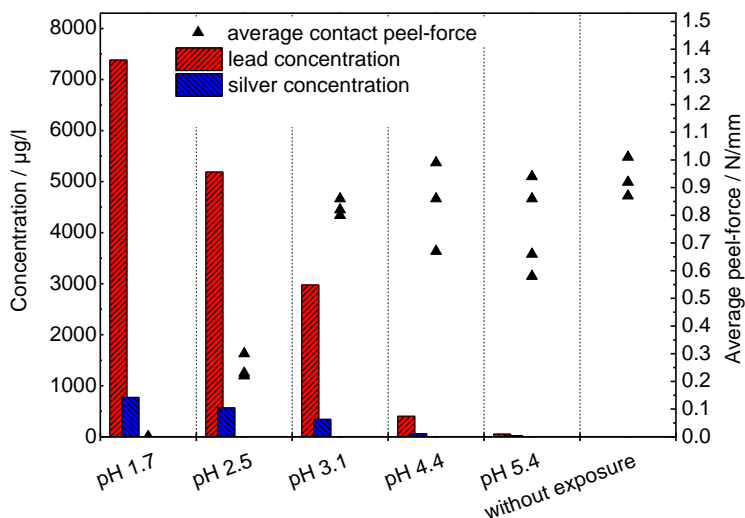


Fig. 7.7: Measured amount of dissolved silver (left axis, blue bars), the dissolved lead (left axis, red bars) and the measured adhesion (right axis, average adhesion along one contact, black triangles) of contacts exposed to nickel chloride solutions with different pH-values set by adding HCl

The correlation between the contact peel force, the pH-value and the dissolved amount of silver can be confirmed. Also the amount of dissolved lead correlates with the resulting adhesion. The amount of lead is ~10 times higher than the dissolved amount of silver; this is due to the fact that the contacts feature a lead glass. A lower pH-value leads to a higher silver and lead amount measured in the dipping solution and also to a lower adhesion.

The results suggest the use of lowly acidic electrolytes. This is definitely advisable for copper electrolytes and leads to greatly improved adhesion comparing the results for sulphuric acid at pH 1 and pH 2.8 (Fig. 7.4). However, as shown in Fig. 7.1 and Fig 7.2, the Watts-type nickel electrolyte (pH ~4) affects adhesion more severely than the copper electrolyte (pH ~2.8). This reveals that apart from pH another mechanism influences contact corrosion.

In the following section the microstructural appearance of the contact corrosion caused by the nickel electrolyte is evaluated before the chemical reaction going on during contact corrosion will be clarified in section 7.4.

7.3 Microstructure analysis of the Watts-type nickel electrolyte impact on screen-printed contacts

Besides a negative influence of acidic chemicals with a pH of 1 the results above show that the nickel plating process causes poor contact adhesion. To analyse this behaviour accurately, SEM, TEM and AFM analyses of the contact microstructure, were done. As precursors for the exposure experiments, solar cell contacts according to section 5.2.1 were used. The self-mixed Watts-type nickel electrolyte according to section 5.1.3 (recipe shown in Table 5.1), which consists mainly of nickel sulphate as a nickel source, nickel chloride to promote anode solubility, boric acid as a buffer, and surfactant agents, were used. The exposure durations were varied. Temperature and execution of the exposure experiments were done according to the descriptions in sections 5.2.2.

7.3.1 SEM analysis of the contact microstructure

To understand the effect of the interaction between printed solar cell contacts and the Watts-type Ni-electrolyte in the contact microstructure, a SEM analysis was done. Contacts were analysed before and after exposure to the electrolyte. To evaluate the cross section, the contacts were cut using a laser to avoid mechanical damage due to possibly low adherence. The cross-sections were prepared using an ion-polisher to remove the region of thermal influence by the laser and to get a flat cross-section surface with minimal impact to the area of interest (compare chapter 4.1.2).

In a first step the failing interface was localized in the contact to determine the microstructural reason for the poor contact adhesion following Ni-electrolyte exposure. SEM pictures were taken from the contact cross-sections before and after electrolyte exposure. Fig. 7.8 shows the cross section of a printed, fired and non-dipped, Ag front side contact. Under the ~15 μm thick, porous Ag-bulk, a glass-layer is present on top of the silicon.

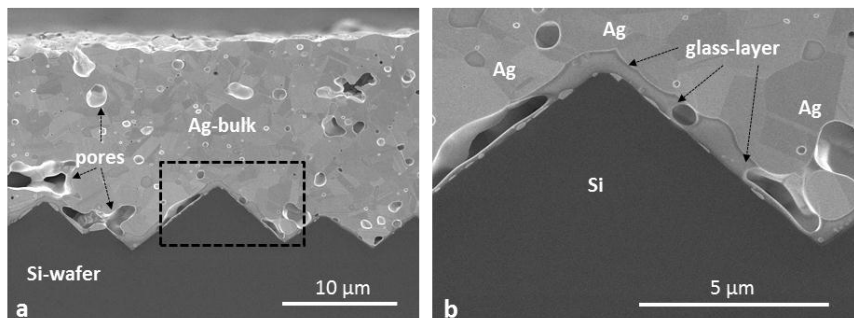


Fig. 7.8: SEM cross-section images of a non-dipped, unaffected solar cell contact (a). The bulk material mainly consists of silver and shows a lot of pores and cavities. Detail image (dashed box in figure a) of the characteristic glass-layer which is located between the silicon and the bulk-silver (b)

Fig. 7.9 shows a contact cross section after an exposure of the contact to the electrolyte for 90 minutes. A clearly visible gap can be observed between the bulk silver and the glass layer in the contact (marked with arrows). This gap is found everywhere along the contact width and marks the failing interface. The screen-printed silver contact is very porous after the firing process, which allows the electrolyte to reach the identified failing interface at many spots along the contact.

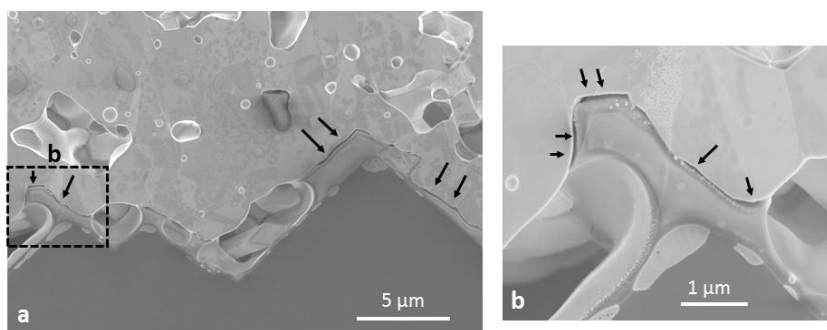


Fig. 7.9: Glass-silver interface after exposure to the Watts-type nickel electrolyte for 90 minutes (a), gap formation between glass and silver marked with arrows and detail picture (dashed box in figure a) of the gap formation (b)

Additionally screen-printed contacts usually show an inhomogeneous thickness. Fig. 7.10 shows the cross-section of an Ag-contact with details of thin

and thick metallized areas after an exposure to the Watts-type nickel electrolyte for 120 minutes. In areas of the printed structure, where the silver layer is thin ($\sim 5 \mu\text{m}$) the probability for the electrolyte to reach the glass-silver interface is high because only little material is present above the interface to shield it from the electrolyte by forming a continuous layer without any channels. Accordingly, in these areas the gap formation is pronounced with a width up to 300-400 nm (Fig. 7.10 a).

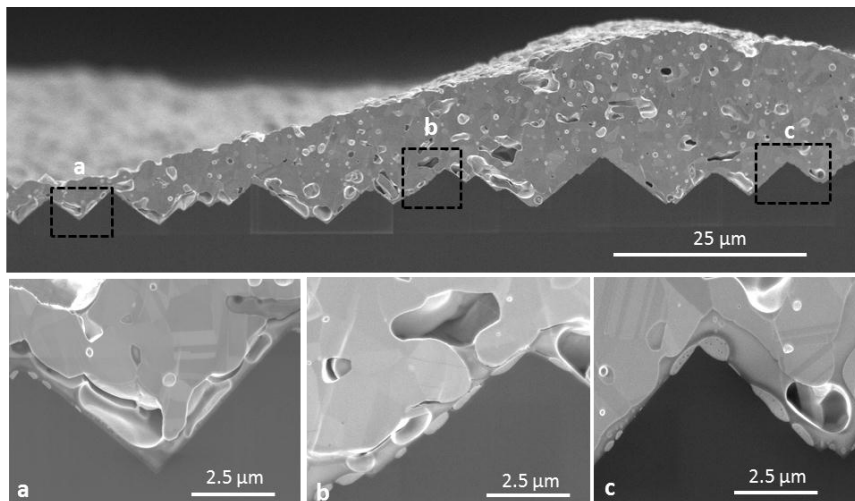


Fig. 7.10: SEM cross-section images of a screen-printed Ag-contact after electrolyte exposure for 120 minutes. The contact parts with thin metallization ($\sim 5 \mu\text{m}$) show a considerable gap formation of about 300-400 nm (a), the parts with medium thick metallization ($\sim 10 \mu\text{m}$) show medium gap formation of 50-100 nm (b) and under the thick metallization parts ($> 15 \mu\text{m}$) also unaffected interface areas were found (c).

Underneath areas where the silver metallization is $> 15 \mu\text{m}$ thick and big cavities are rare, it is more difficult for the electrolyte to penetrate the silver-layer and even after 120 minutes of exposure some spots of the interface remain unaffected (Fig. 7.10 c).

At spots where larger cavities within the Ag-contact connect the electrolyte bath with the glass layer, pronounced gap formation, was observed, regardless of the Ag-layer thickness (Fig. 7.11 a).

Fig. 7.11 b shows a cross-section image of two adjacent glass particles encapsulated in the silver bulk. One can be reached by the electrolyte through an

existing channel, resulting in a gap formation which can be observed in Fig. 7.11 b II, noticeably wider toward the channel opening. The other one is unaffected because the electrolyte did not have access to it (Fig. 7.11 b I). This shows that the access of the electrolyte to the glass-silver interface offered by the pores and cavities determines the degree of detachment between silver and glass and therefore the resulting contact adhesion.

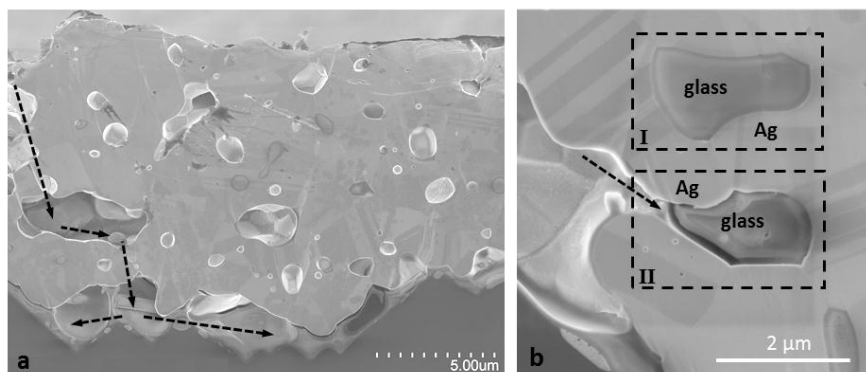


Fig. 7.11: SEM cross-section image of a screen-printed Ag-contact after 120 minutes electrolyte exposure. Parts with continuous cavity channels from the metallization top to the glass-silver interface show pronounced gap formation regardless of the metallization thickness (a). Interface parts without channels look unaffected (b I), whereas those connected to a channel are affected by the electrolyte (b II) and show a clear gap formation.

Electrolyte access to the pores can be prevented either by changing the morphology of the printed paste (i.e. to a less porous paste) or by closing the pores with a plated layer that does not affect adhesion. The former approach has already been studied in the context of paste densification [134], [135]. Yajima and Yamaguchi reported that the glass content, the powder characteristics of silver and glass and the glass properties have an impact on the densification behaviour of the metallization [136]. They further reported that the firing temperature at which the uniform Ag-glass composite structure develops decreases with increasing glass content and increasing film thickness [137]. Adding surfactant agents to the paste also leads to denser metallization films [138], [139]. Reducing the porosity of the fired silver contact can also be achieved by adapting the firing conditions. All of these approaches aim at creating highly conductive contacts made by screen-printing and firing. For the

approach investigated in this work, lateral conductivity is achieved by plated metal, which limits the requirements of the paste to the two functions of etching the dielectric layer to enable electric contact formation while simultaneously providing an adhesive layer between the plated metal and the silicon wafer. As high conductivity is no longer needed for the printed seed-layer, paste development focused on the two above mentioned criteria could allow completely new formulations that would enable improved contact formation and sufficient adhesion. However, paste development was not in the focus of this work and was only done in a particular range (see chapter 6).

To verify whether closing the pores can prevent contact adhesion loss due to nickel electrolyte exposure, screen-printed contacts were plated with silver for 5 minutes before dipping them into the nickel electrolyte for 45 minutes. The plating resulted in a $\sim 5\mu\text{m}$ dense layer of silver, which has been demonstrated not to be critical with respect to contact adhesion. Samples without prior Ag-plating or any electrolyte exposure were processed as references. Fig. 7.12 shows the adhesion results obtained by soldering and 90° peel testing.

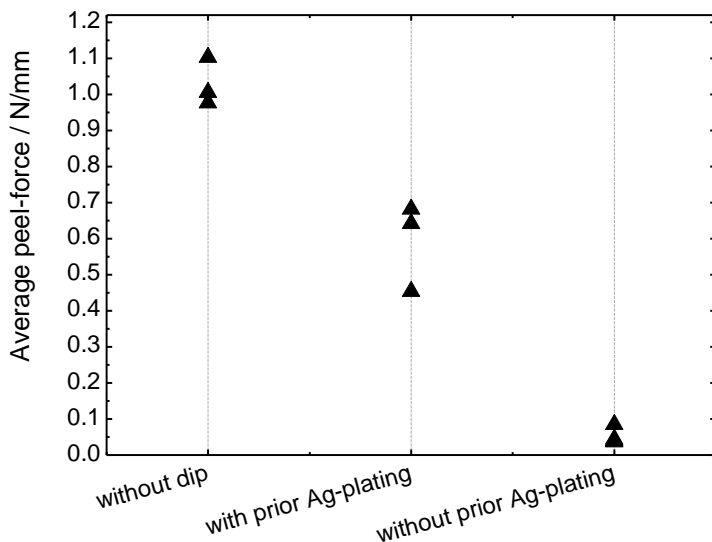


Fig. 7.12: Peel-force results for contact exposure to the Watts-type nickel electrolyte with and without prior Ag-plating

With prior Ag- plating the average adhesion values after electrolyte exposure are around 0.6 N/mm, whereas for the contacts without prior silver plating the adhesion is virtually 0 N/mm. Compared to the contacts without any electrolyte treatment the prior silver plating avoided half of the adhesion drop. This shows that closing pores and cavities in the screen-printed metallization prevents the electrolyte from reaching the glass-silver interface at many spots, thus resulting in improved contact adhesion.

The results up to this point show the electrolyte attack coming from the top of the metallization like in a plating setup. To analyse which part of the glass-silver interface can be dissolved by the electrolyte in general, a cross-section prepared in advance was exposed to the electrolyte. In this configuration, the electrolyte has access to all parts of the glass layer from the front face. The cross-section was exposed to the electrolyte for a total duration of 30 minutes with an interruption every 10 minutes to take SEM pictures of the same area. Fig. 7.13 shows the glass-silver interface prior to exposure (a), after 10 minutes of exposure (b), after 20 minutes of exposure (c) and after 30 minutes of exposure (d).

A growing gap between the silver and the glass is observed. The dissolution of the glass is found only in the direct vicinity to the silver, whereas the glass-layer at the interface of the silicon wafer remains unaffected. Fig. 7.14 shows the cross-section SEM images of a glass particle encapsulated in the silver bulk before (a) and after 30 minutes of exposure in the electrolyte (b). In Fig. 7.14 c and d the glass parts, before and after exposure, are compared in a schematic adaptation. The glass parts are marked in yellow, the silver parts are marked in grey and the modified part of the cross section after exposure, which shows the newly formed gap, is marked in blue. It becomes clear that the gap forms at the expense of the former glass-layer. This reveals that the dissolution of the glass is site-specific, i.e. a lot faster at the glass-silver interface. This raises the question as to whether a specific material composition in the glass at the glass-silver interface promotes the dissolution there. To clarify this, a TEM analysis was done at the glass-silver interface, shown in the following section.

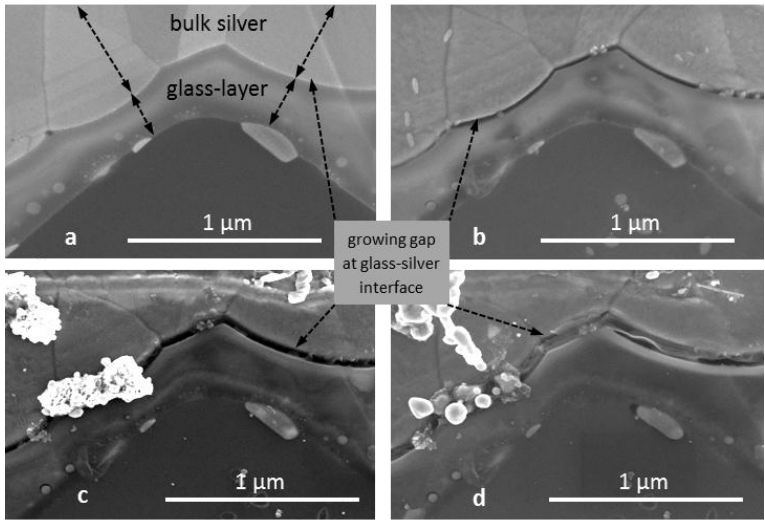


Fig. 7.13: SEM cross-section images of a cross-section prepared in advance and exposed to the Watts-type nickel electrolyte. Before exposure (a), after 10 minutes of exposure (b), after 20 minutes of exposure (c), and after 30 minutes of exposure (d)

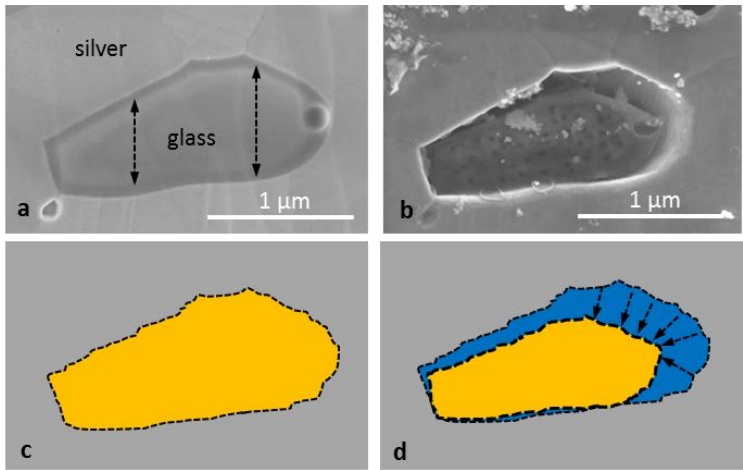


Fig. 7.14 SEM cross-section images of a glass particle encapsulated in the bulk silver before exposure (a) and after exposure to the Watts-type nickel electrolyte for 30 minutes (b). Schematic drawings taken from the SEM pictures before exposure (c) and after exposure (d) with the glass parts marked in yellow, the silver parts marked in grey and the newly formed gap marked in blue

7.3.2 TEM analysis of the glass-silver interface

To analyse the material composition at the identified failing glass-silver interface inside the screen-printed silver contact a TEM analysis was conducted including EDX mapping as described in section 4.1.4 in cooperation with the Max-Planck-institute in Halle.

The annular dark-field STEM image in Fig. 7.15 left shows an overview of the interfacial region between the silicon (bottom left), the glass (from bottom right to upper left), and the Ag-bulk (at the top). In accordance with the accepted contact formation theory [68], [81] the silver diffuses from the bulk-silver through the glass-layer to the silicon during the firing process, where it forms crystallites upon cooling. These particles grow up to 1 μm along the interface between the silicon and the glass and show inclusions of elemental Si, which can be seen as dark patches in Fig. 7.15 left.

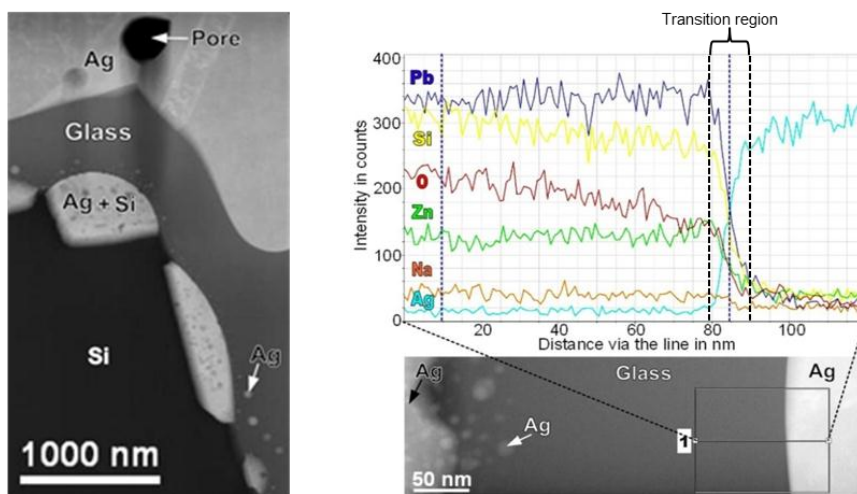


Fig. 7.15: Annular dark-field STEM-image of the interfacial region between the silicon and the bulk silver, which are separated by lead silicate glass (left). EDXS-intensity profiles of the detected elements at the glass-silver interface. STEM image of the glass layer between a silver precipitate at the silicon surface and the bulk silver, with the marked region of interest in the mapping of Fig. 7.16, along the length of which the profiles were calculated by integrating (right)

Also in accordance with former findings [68], [69], the Ag precipitates in the glass. Round Ag-particles were found near the Si-interface in particular. As

revealed by the SEM-investigations, peeling off the contact from the silicon occurs at the fracture between the glass and the silver. For the region between the bulk-silver and the glass-layer in Fig. 7.16, which is marked with a green rectangle, EDXS mappings were generated. The maps show two-dimensional distributions of the integrated intensity signals of the Pb-L lines (blue), the Ag-K lines (turquoise), the Zn-K lines (green), the O-K lines (red), the Si-K lines (yellow) and the Na-K lines (orange), respectively. In general, the distribution of the detected elements inside the glass seems to be nearly homogeneous.

The intensity profiles in Fig. 7.15 right were calculated from the maps in Fig. 7.16 by integrating over a 98 nm wide area (marked in the bottom right STEM-image of Fig. 7.15 right). A continuous drop of in the silicon and oxygen concentrations over a 75 nm wide glass area next to the interface with the bulk silver can be observed, which also represents a relative enrichment of the other glass components. The approximate interface between the silver and the glass is marked in the diagram in Fig. 7.15 right by the dashed line. At the interface the elemental signals show a nearly 10 nm wide transition region from the glass to the silver. It is unclear whether this transition region results from overlapping glass and silver along the depth of the lamella or rather represents an enrichment of silver dissolved in the glass close to the bulk-silver.

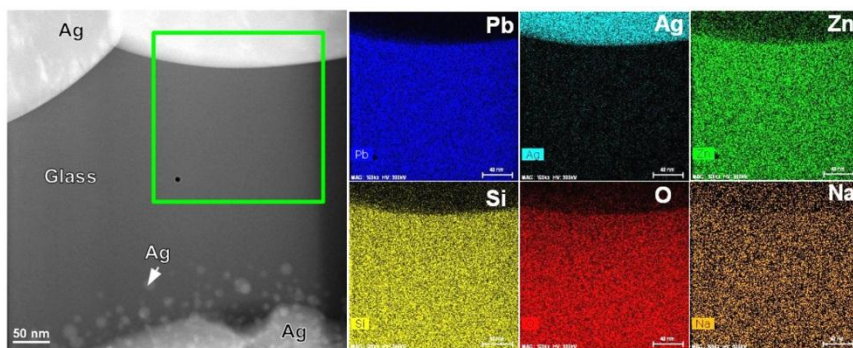


Fig. 7.16: EDXS-mapping of the interfacial region between the glass and the bulk-silver within a solar cell contact with the STEM-ADF image on the left, the maps of the integrated intensities of the signals of the Pb-L lines (blue), the Ag-K lines (turquoise), the Zn-K lines (green), the O-K lines (red), the Si-K lines (yellow) and the Na-K lines (orange)

However, a diffusion of silver atoms throughout the glass towards the silicon cell is clearly indicated by the Ag-crystallites at the interface between the silicon

and the glass. As further proof for silver dissolution in the glass, EDXS-spectra were calculated by integrating over an area located in the glass (Fig. 7.17 a) and another located in the bulk-silver (Fig. 7.17 b). The EDXS-spectrum on pane a) was calculated from a window in the glass in a distance of about 120 nm from the interface between glass and bulk-silver. The Ag-L and Ag-K lines are indeed visible in the spectrum, which proves a certain Ag-content in the glass. The signals of C, Ga, Fe, Cu and Zr are not related to the sample, they are rather to be associated with both sample preparation and stray background from the measuring system.

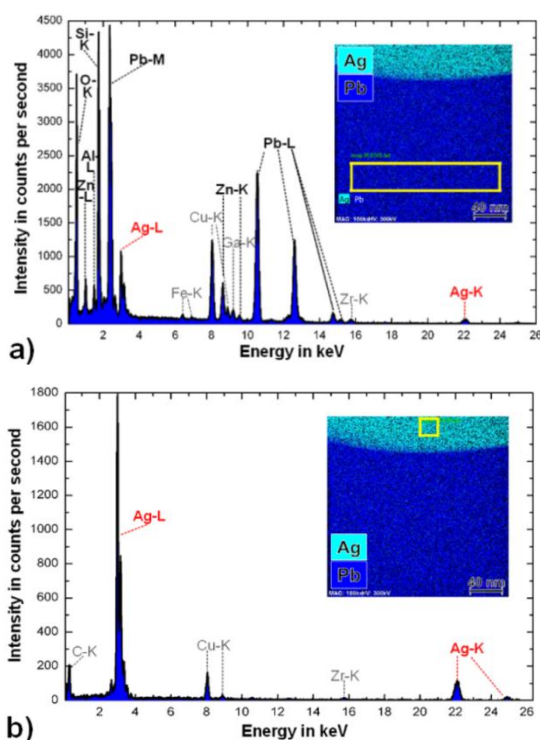


Fig. 7.17: EDXS-spectra calculated by integrating over rectangular regions being defined in the map of Fig.7.16. The regions are located in the glass (a), and in the bulk silver (b), in a distance of about 120 nm, and 30 nm from the interface between glass and silver, respectively

During the TEM analysis, several spots at the glass-silver interface were analysed, not only the one shown here. The results resemble each other in appearance; no direct evidence of a specific phase with distinct dimensions of a different material composition at the glass-silver interface, which could have been an explanation for the site-specific glass dissolution observed in section 7.3,

was found in the TEM analysis. The observed weak trends of changing EDX signal (within the measurement noise) toward the glass-silver interface, and the uncertainty regarding the exact position of that interface do not allow an explicit conclusion.

According to the literature a transition layer of silver atoms and adjoining chemically bonded oxygen atoms, which are part of the glass structure, is formed between the glass and the silver during the firing process. This intermediate oxidation layer is responsible for providing good adhesion between the silver and the glass [132], [140]. It is probably very thin so only hints of that layer could be found, but its existence could not be proven without a doubt with the TEM analysis.

7.3.3 AFM analysis of the gap formation at the glass silver interface

To verify the visual impression of a gap formation between silver and glass detected in the SEM investigations, an AFM analysis was performed at the cross-section of a solar cell busbar before and after nickel electrolyte exposure (for method description compare section 4.2.4). Fig. 7.18 shows the SEM cross-section images of the area measured with AFM before (a) and after 20 minutes of exposure to the Watts-type nickel electrolyte (b). The characteristic gap formation is visible at the boundary layer between glass and silver (Fig. 7.18 b). In the SEM image before electrolyte exposure, grain boundaries of different sintered silver particles can be identified by slight differences in the SEM contrast (marked with white arrows).

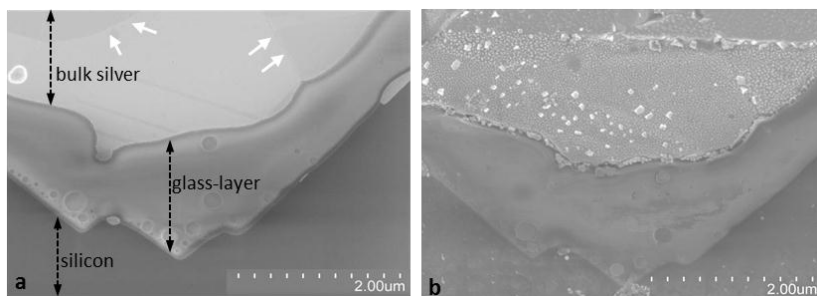


Fig. 7.18: SEM cross-section images of the silver glass contact interface analysed with AFM before electrolyte exposure (a) and after 20 minutes of electrolyte exposure (b). At the interface near the glass-layer, grain boundaries of sintered silver grains can be observed (marked with white arrows).

Fig. 7.19 shows the AFM measurements of the contact interface area presented in Fig. 7.18 before electrolyte exposure. An overview image (a) and a detail image of the transition between silver and glass (b); with a height profile of one corresponding line scan (white line in the images) are shown. The height profile along the line scans is presented in the diagrams below the AFM measurements, the phase boundaries between silver and glass (1) and glass and silicon (2) are marked in the line scan diagrams with dashed lines. Characteristic features that were found in the SEM images are marked. The contact interface is flat before electrolyte exposure in the overview image as well as in the detail image.

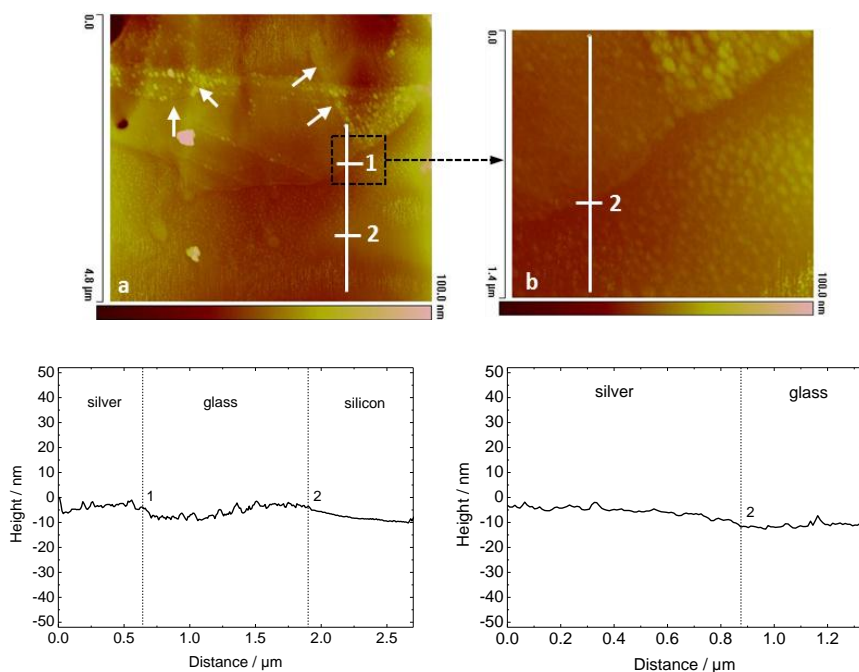


Fig. 7.19: AFM measurement before electrolyte exposure. Overview (a) and detail image (b) with a height profile of one line scan (white line in the height images) presented in the diagrams below. The transition between silver and glass (1) and between glass and silicon (2) is marked with a dashed line in the diagrams. The white arrows mark boundaries between different silver grains already observed in the SEM image.

Fig. 7.20 shows exactly the same contact interface area after electrolyte exposure. Along the glass silver interface a ~ 30 nm deep trench can be observed. The real depth might be bigger because if the trench gets to narrow the AFM

needle is not able to penetrate the sample completely and measure the depth accurately. The silver interface near the glass layer show an increased roughness and additional wider grooves which are in good accordance with silver grain boundaries (white arrows) pointed already out in Fig. 7.18. This indicates that the silver grain boundaries are wetted with glass which dissolves during electrolyte exposure. The silver parts further away from the glass-layer show the same height as the silicon. The AFM analysis confirms the formation of a gap along the glass-silver interface in the contact and indicates that near the glass layer the bulk silver is nerved with glass, which is preferably dissolved especially for the case that the electrolyte has the possibility to reach the contact from the face side of a cross-section prepared in advance to the exposure experiment.

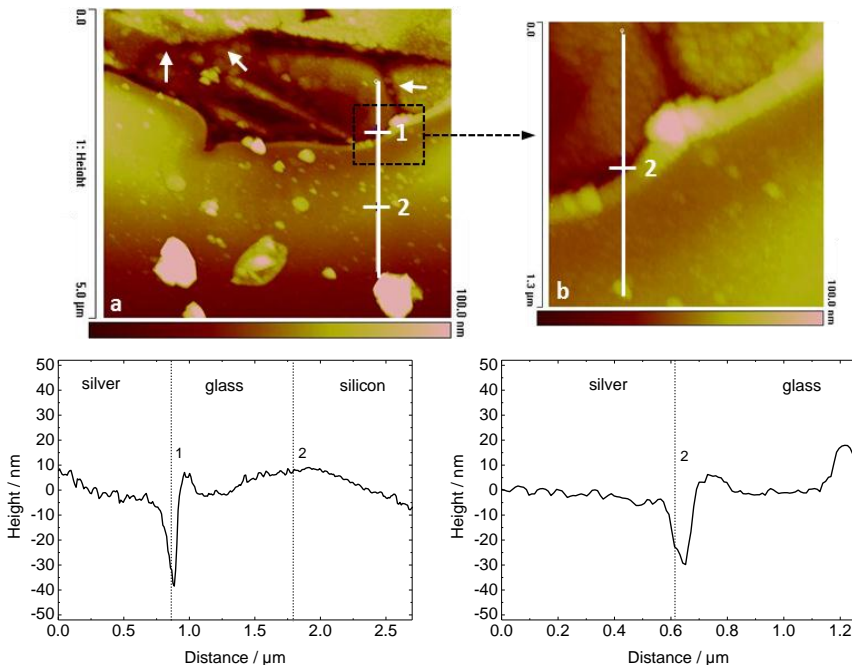


Fig. 7.20: AFM measurement after 20 minutes of electrolyte exposure. Overview (a) and detail image (b) with a height profile of one line scan (white line in the height images) presented in the diagrams below. The transition between silver and glass (1) and between glass and silicon (2) is marked with a dashed line in the diagrams. The white arrows mark boundaries between different silver grains already observed in the SEM image.

7.4 Chemical interaction between Watts-type nickel electrolyte and printed Ag-contacts

The results shown in chapter 7.1 revealed that the interaction between Watts-type nickel electrolytes and screen-printed Ag front side contacts causes low contact adhesion. The results in chapter 7.2 showed that dipping in boric acid (which offers the H^+ ions in the Watts-type nickel electrolyte) and in chemical solutions with a pH of 4 does not lead to poor contact adhesion. This means that an additional mechanism besides the pH dependency and/or a different compound or a compound combination besides boric acid alone has to be responsible for poor contact adhesion after Ni plating. In the following, exposure experiments with the single compounds and compound combinations of the Watts-type nickel electrolyte and an additional XRD-analysis of the material change in solid contact compounds before and after electrolyte exposure will provide an insight into the chemical reactions the observed corrosion is based on.

7.4.1 Contact adhesion after Watts-type nickel electrolyte exposure

To identify the compound or the compound combination in the Watts-type nickel electrolyte which is responsible for the adhesion drop after Ni-plating, printed and fired solar cell contacts (produced according to section 5.2.1) were exposed to the single compounds of the electrolyte using the concentrations given in Table 5.1 and the procedure described in section 5.2.2. After 45 minutes of exposure the contacts were soldered and quantitative peel-force measurements were done. Fig. 7.21 shows the average peel-force results. Each mark in the graph represents the average adhesion value along one solar cell contact (156 mm). Section a shows the peel-force results of non-dipped reference contacts, section b shows the results after exposure to a concentration of 100%, 50% and 25% of the Watts-type nickel electrolyte, section c shows the peel-force results after exposure in the single electrolyte compounds and section d shows the results after dipping in combinations of two of the three main components (nickel sulphate, nickel chloride and boric acid) of the electrolyte.

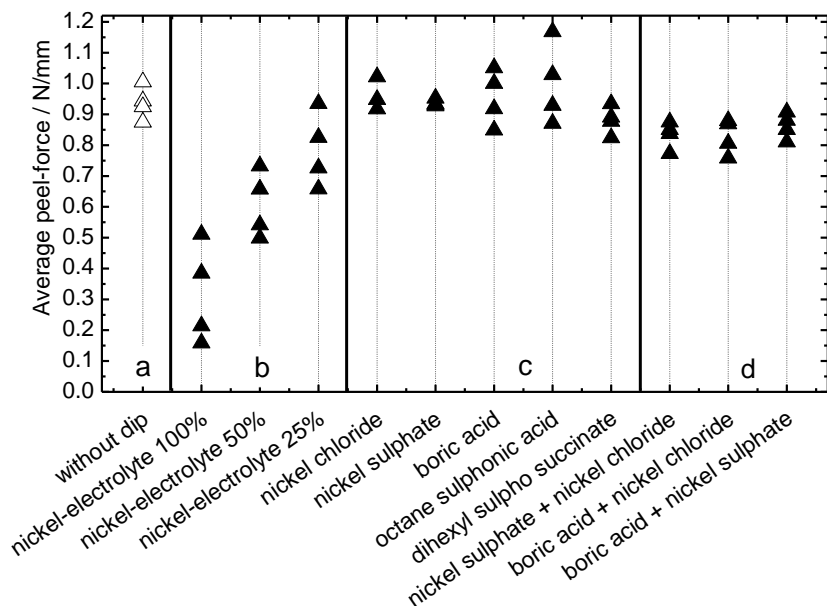


Fig. 7.21: Peel-force results of the non-dipped reference contacts (section a), for contacts exposed (50°C, 45 minutes) to different concentrations of the Watts-type nickel electrolyte (section b), for contacts dipped in the single compounds of the electrolyte (section c) and for contacts exposed to a combination of two of the main compounds of the electrolyte (section d)

The contacts dipped in the Watts-type nickel electrolyte with 100% concentration show a significantly lower peel-force (0.15-0.5 N/mm) than the non-dipped reference (0.9-1 N/mm). Diluting the electrolyte leads to rising peel-force results. This indicates a chemical dissolution process behind the peel-force drop, which is faster for a higher electrolyte concentration. The peel-forces of the contacts exposed to the single electrolyte compounds (section c) at their respective concentration do not show a significant difference compared to the measured adhesion without dip. This shows that for exposure durations of 45 minutes no single compound in the electrolyte alone is responsible for the adhesion loss. Also an exposure to the different combinations of two of the electrolyte main compounds did not show a significant effect (Fig. 7.21, section d).

To analyse how the three main compounds in combination affect adhesion, the contacts were dipped into a basis solution of boric acid and nickel sulphate, adding the third main compound nickel chloride in different amounts. It should be noted that the concentration of nickel chloride is small compared to the other two compounds (compare Table 5.1). The upper diagram in Fig. 7.22 shows the peel-force results. Adding just 25% of the original nickel chloride concentration leads to a significant drop of adhesion of around 0.66 N/mm.

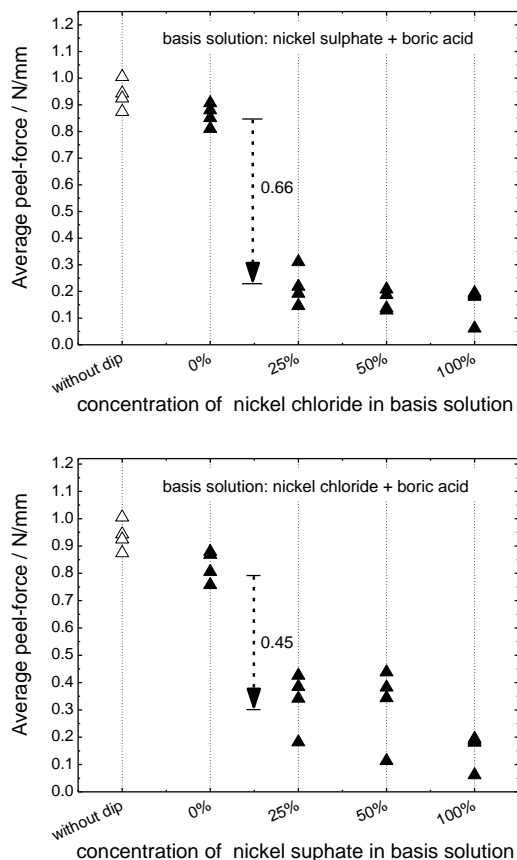


Fig. 7.22: Peel-force results for contact exposure to the different combinations of two main compounds of the Watts-type nickel electrolyte adding the third compound successively. Basis solution out of nickel sulphate and boric acid adding nickel chloride (upper) and basis solution out of nickel chloride and boric acid adding nickel sulphate (lower)

In a similar experiment, adding 25% nickel sulphate to a basic solution of boric acid and nickel chloride results in a drop of adhesion of about 0.45 N/mm (Fig. 7.22 lower diagram). This clarifies that the three main compounds of the Watts-type Ni electrolyte (boric acid, nickel sulphate and nickel chloride) in combination lower the contact adhesion, executing a contact exposure of 45 minutes at 50°C. To verify if the presence of nickel plays a role in the corrosion process a solution without nickel was set up using sodium chloride instead of nickel chloride, sodium sulphate instead of nickel sulphate and boric acid; chloride and sulphate concentrations were kept identical than the one of the Watts-type nickel electrolyte according to Table 5.1. Fig. 7.23 shows the peel-force results of the nickel free solution (2) compared to the solution with the three electrolyte main compounds (1). Both solutions show the same clear adhesion drop. This means that the chemical dissolution reaction is due to the combination of sulphates, chlorides and boric acid independent of the presence of nickel.

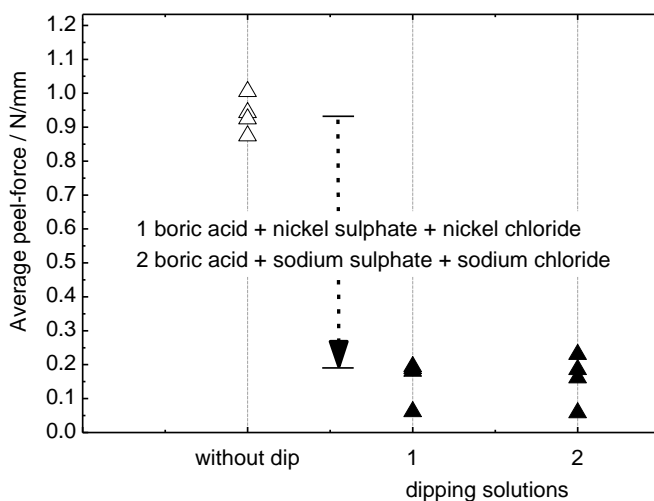


Fig. 7.23: Peel-force results for exposure to solution 1: boric acid, nickel sulphate and nickel chloride (main compounds of the nickel electrolyte) and solution 2: boric acid, sodium sulphate and sodium chloride (solution without nickel)

7.4.2 Material changes in the solid contact compounds

After the firing process, screen-printed solar cell contacts consist of silver (~95-98%) and lead glass (~2-5%). Different phases are formed in the contact during firing, as has been described and analysed in various publications [68], [81]. Depending on the used Ag-paste, different metal oxides can be part of the glass, for example zinc oxide is often added by paste manufacturers and was observed to be part of the glass-layer (see section 7.3.2, Fig. 7.16). To simulate the solar cell contact and analyse the solid material changes during electrolyte exposure, the single contact compounds and contact compound combinations shown in Table 7.3 were taken in form of powders, fired and exposed to the Watts-type nickel electrolyte shown in Table 5.1.

To obtain mixed phases, powder mixtures were heated up to 1000°C with a temperature ramp of 5 K/min using a muffle furnace. Afterwards, they were rapidly cooled and milled using a ball mill with milling spheres of 1 cm diameter, obtaining particles with a size of around 20 µm. Each powder was exposed to 30 ml of Watts-type nickel electrolyte for 20 minutes at 50 °C in a plastic tube.

Table 7.3: Compounds and compound combinations exposed to the Watts-type nickel electrolyte

No.	Compounds	Mass / %	Firing temperature / °C	Heating ramp K/min	Cooling treatment
1	Lead	100	-		-
2	Lead oxide (II)	100	-		-
3	Silver	100	-		-
4	Silver oxide	100	-		-
5	Lead Silver	95 5	500	5	40 K/min
6	Lead glass Silver	70 30	1000	5	Water
7	Lead glass Silver Silicon	50 25 25	1000	5	Air
8	Lead glass Silver Silicon Silicon nitride	40 20 20 20	1000	5	Air

The tubes were constantly agitated during the exposure to promote the contact between the compound powders and the electrolyte. Powder XRD-measurements were done according to section 4.4.3 before and after electrolyte exposure. The resulting diffractograms were compared to analyse the material change. Fig. 7.24 shows, as an example, the XRD-results of silver oxide (compound no. 4) before (black curve, triangles) and after electrolyte exposure (red curve, stars). Comparing the peaks in the diffractogram with the specific bars of silver oxide (black dashed arrows) and silver chloride (red continuous arrows) marked at the x-axis of Fig. 7.24, a clear shift from silver oxide to silver chloride could be observed due to interaction with the electrolyte.

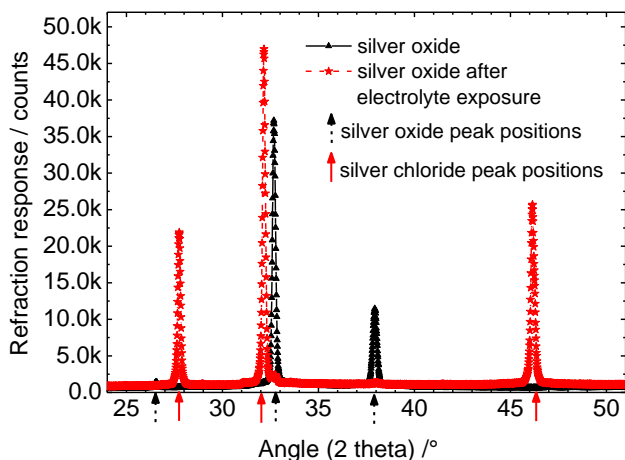


Fig. 7.24: Diffractogram of silver oxide before (black triangles) and after nickel electrolyte exposure (red stars). The peak positions for silver oxide (black dashed arrows) and silver chloride (red continuous arrows) are marked at the x-axis.

This kind of comparison before and after electrolyte exposure was done with every compound shown in Table 7.3. The species found in the XRD-analysis before and after electrolyte exposure are summarized in Table 7.4. New species, only found after electrolyte exposure, are set in bold letters in the fourth column, species which were only found before but not after electrolyte exposure, are set in bold letters in the third column.

Lead powder (compound no. 1) is easily oxidized in air, which is the reason why oxides are found before exposure. After exposure, lead sulphate is detected.

The same behaviour was found for lead oxide (compound no. 2) as primary material. This is a product from the reaction presented in equation 7.1, where sulphate and hydronium ions from the electrolyte react with elemental lead forming lead sulphate. Lead (II) oxide reacts similarly following equation 7.2.

Both reactions are predicted by the Pourbaix diagram of lead and lead oxide in acidic media which can be found in literature [141], [142] and in Appendix A.2. If no sulphates are present in the solution reaction 7.3 is possible due to the presence of H^+ ions.

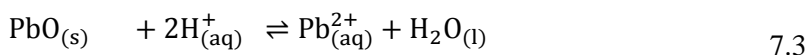
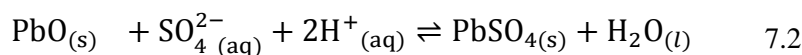
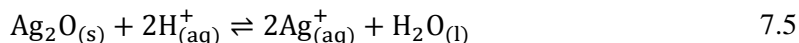
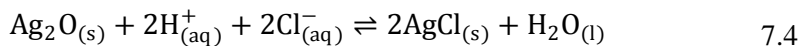


Table 7.4: Species identified in the powder XRD-analysis before and after exposure of different compounds and compound combinations to the Watts-type nickel electrolyte

No.	Compounds	XRD results before exposure	XRD results after exposure
1	Lead	Pb + PbO + Pb₃O₄	PbSO₄ + Pb + PbO
2	Lead oxide (II)	PbO	PbSO₄ + PbO
3	Silver	Ag	Ag
4	Silver oxide	Ag ₂ O	AgCl + Ag ₂ O
5	Lead Silver	PbO + Ag ^{99.5} Pb ^{0.5} + Pb ₃ O ₄	PbSO₄ + PbO + Ag ^{99.5} Pb ^{0.5} + Pb ₃ O ₄
6	Lead glass Silver	PbO + Ag₂PbO₂	PbSO₄ + AgCl
7	Lead glass Silver Silicon	Si + Ag + Pb + PbO + SiO ₂	PbSO₄ + Si + Ag + Pb + SiO ₂
8	Lead glass Silver Silicon Silicon nitride	Si + Ag + Pb + PbO + SiO ₂	PbSO₄ + Si + Ag + Pb + SiO ₂

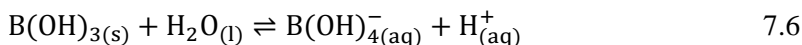
Pure silver (compound no. 3) does not interact with the electrolyte. This confirms that the silver detected in dipping solutions (compare Fig. 7.4 and Fig. 7.7) originates from the glass layer. Silver is too noble to react with the offered species. But silver oxide (compound no. 4) forms silver chloride, according to

equation 7.4. These reaction are predicted by the Pourbaix diagrams of silver in aqueous solution and in solutions containing chlorides found in literature [133] and in appendix A.1. If no chlorides are present in the solution equation 7.5 is possible due to the presence of H^+ ions.



For these principle investigations, the species can be considered individually. In the actual system, element mixtures are present, which complicates matters. There will be mixed potentials between different phases, complicating the assignment of a potential to a specific phase, as needed to locate the position in the Pourbaix diagram. The presence of complexing or salt building ions changes the underlying thermodynamics. A superposition of the solubility equilibrium and the electrochemical equilibrium is the result.

For the compounds 5 to 8 similar behaviour was observed for lead oxide, while none of the silicon compounds changed. It can be concluded that equations 7.1-7.5 are possible when the solar cell contact gets in touch with the Watts-type Ni electrolyte. Two general dissolution paths exist: one dissolving lead or lead oxide (forming lead sulphate in the presence of sulphate ions) and another one dissolving silver oxide (forming silver chloride in the presence of chloride ions). These equilibrium reactions will be shifted if locally high amounts of lead sulphate or silver chloride are present. In Watts-type nickel electrolytes the needed H^+ ions for the reactions will be constantly provided by further dissociation of the boric acid following equation 7.6.



Other highly acidic media feature high H^+ concentration at all times, leading to fast contact corrosion at low pH (compare section 7.2).

The results in the subsection 7.4 reveal that for a corrosion of the contact at exposure durations of 45 minutes, which leads to low contact adhesion the dissolution paths of silver and lead have to be active in parallel. However in the plating process contact adhesion fails a lot faster this indicates and accelerating

influence of the plating process compared to simple contact exposure. This influence is investigated in the following section.

7.5 Influence of the plating process on contact adhesion

In the sections above the corrosion mechanism of screen-printed silver seed-layers and its microstructural appearance due to exposure in electrolyte solutions and acidic chemicals is investigated in detail. The pure exposure experiments do not consider the fact that solar cell contacts in a light-induced plating setup are usually subjected to a voltage (compare section 2.3). In the current section the influences of an applied voltage, as it is present in the light induced plating setup, to the observed contact corrosion is analysed.

7.5.1 Impact of an applied voltage to the contact microstructure

The SEM cross-section images in Fig. 7.25 a-e show the interface between the glass-layer and the bulk-silver of five different samples following Ni-plating for durations ranging from 1 min. (a) to 5 min. (e).

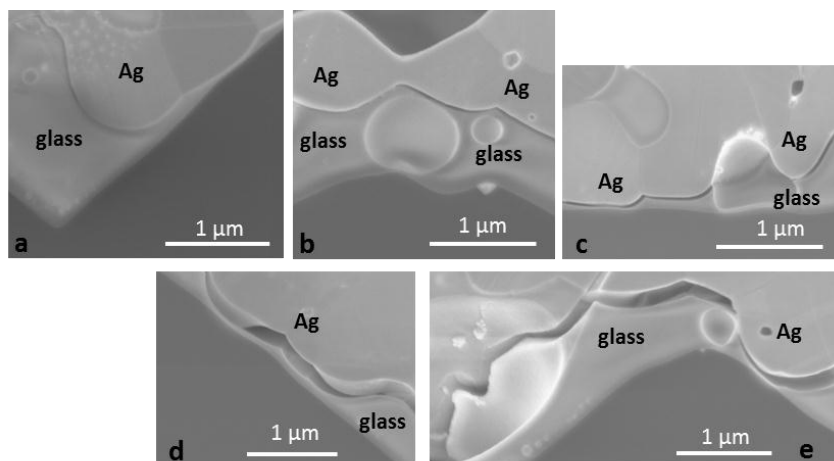


Fig. 7.25: SEM cross-section images of the interface between the bulk-silver and the glass-layer after Ni-plating for different durations. One minute plating (a), two minutes plating (b) three minutes plating (c) four minutes plating (d) and five minutes plating (e)

A gap can be observed at the interface between silver and glass which becomes larger for longer plating durations. After one minute the gap is hardly

visible (a), after two minutes it is < 50 nm wide (b), after three minutes it is ~100 nm wide (c), and after four and five minutes it is ~200 nm wide (d and e). The detected gap did not show a constant width along the contact.

Each of the images in Fig. 7.25 represents the largest gap found for the respective plating duration.

This indicates a chemical dissolution caused by the electrolyte at the glass-silver interface as already observed after electrolyte exposure without applied voltage. The only significant difference for the samples is the experiment time; it takes just a few minutes for plating, but several ten minutes for dipping to reach similar gap formation. This means that an applied voltage accelerates the gap formation observed at the contact microstructure.

7.5.2 Impact of an applied voltage on contact adhesion

To clarify how the applied voltage influences the dissolution process independent of nickel deposition, contacts were dipped with an applied voltage of -0.7 V vs. a nickel anode while illuminating the cells, according to the procedure described in 5.2.3, in a solution of sodium sulphate, sodium chloride and boric acid (corresponding to solution 2, section 7.4). This solution destroys contact adhesion during an exposure of 45 minutes at 50°C without applied voltage (see Fig. 7.23). As there is no cation with suitable reduction potential contained in this solution, a deposition is not possible. Fig. 7.26 shows the peel-force results. After an exposure without applied voltage of two minutes, just a very small adhesion drop is observed, whereas with an applied voltage the adhesion decreases to zero at the same duration. This shows that the applied voltage accelerates the dissolution process tremendously.

A simple explanation for this behaviour is that with an applied voltage lead and silver from the dissolution products (Pb^{2+} and Ag^+) can be reduced on the negatively charged silver bulk to form elemental lead and silver. This takes the dissolved lead and silver out of the system and shifts the dissolution reaction towards further dissolution of lead/lead oxide and silver oxide out of the glass-layer (compare eqns. 7.3 and 7.5). The reduction of the dissolution products is a lot more effective than the precipitation in the exposure without applied voltage (compare eqns. 7.1, 7.2 and 7.4).

If this reduction path exists, the reduction of the dissolved lead and silver is in direct competition to the reduction of any cation in the electrolyte solution and should depend on the respective reduction potential. To clarify this correlation

plating and dipping experiments with sulphate solutions containing metal ions with different reduction potentials were performed.

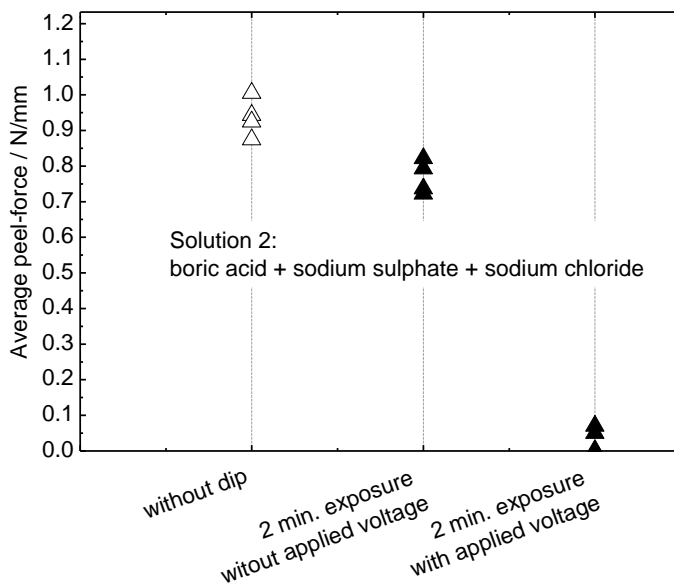


Fig. 7.26: Peel-force results for contacts exposed to solution 2 (boric acid, sodium sulphate and sodium chloride) with and without applied voltage

7.5.3 Influence of the reduction potential on contact adhesion

To understand the role of electrons and cations in the contact corrosion, dipping and plating experiments with sulphate solutions containing cations with different nobility were conducted. Sodium sulphate ($E^0: \text{Na}^+ + e^- \rightleftharpoons \text{Na} \rightarrow -2.71 \text{ V}$), nickel sulphate ($E^0: \text{Ni}^{2+} + 2 e^- \rightleftharpoons \text{Ni} \rightarrow -0.23 \text{ V}$), copper sulphate ($E^0: \text{Cu}^{2+} + 2 e^- \rightleftharpoons \text{Cu} \rightarrow +0.35 \text{ V}$) and iron (III) sulphate ($E^0: \text{Fe}^{3+} + e^- \rightleftharpoons \text{Fe}^{2+} \rightarrow +0.77 \text{ V}$) were chosen for the experiment. The concentrations of all sulphate solutions were set to the same sulphate concentration as in the Watts-type nickel electrolyte (compare Table 5.1). This leads to solutions with different pH-values: for sodium sulphate the pH is ~ 7.2 for nickel sulphate ~ 3.3 for copper sulphate ~ 3.2 and for iron sulphate ~ 1.9 .

Fig. 7.27 shows the peel-force results for contacts exposed to the sulphate solutions for 45 minutes at 50°C (experiment procedure compare section 5.2.3)

without applied voltage. For sodium, nickel and copper sulphate no significant adhesion drop can be detected compared to the non-dipped reference (unfilled triangles) but after exposure to iron sulphate the contact adhesion drops to zero. This is, as previously stated in section 7.2, due to the difference in pH-value. The acidic iron sulphate corrodes the glass-layer inside the contacts due to the higher H^+ -ion concentration (according to eqns. 7.2, 7.3 and 7.5) and causes poor contact adhesion.

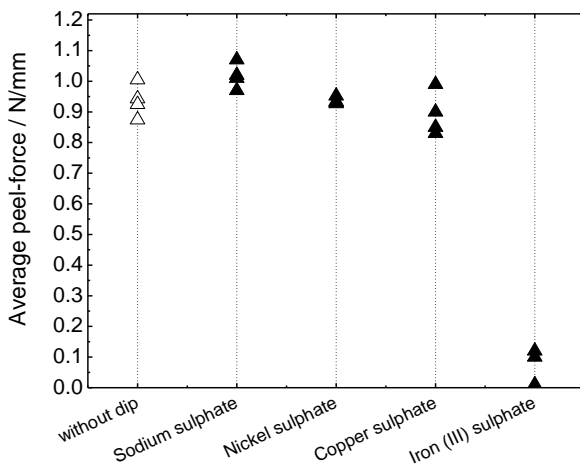


Fig. 7.27: Peel-force results of the dipping experiments in sulphate solutions with varied standard reduction potentials

To examine the influence of the different reduction potentials, exposure experiments with applied voltage using the same solutions were done with a duration of 2 minutes. As there are only sulphate ions present in the solutions, only the reactions according to equations 7.1-7.3 and 7.5, as well as the reduction of cations, are possible. After the contact exposure for nickel sulphate, copper sulphate and iron (III) sulphate the contacts were covered with the reduced metals, this complicates the soldering because different metal surfaces require different soldering conditions to reach sufficient stable soldering joints. To realize this, the automated soldering station (compare section 5.3) was used and the contacts were soldered with three soldering spots on each contact. Fig. 7.28 shows the peel-force curves for contact exposure with applied voltage in sodium sulphate (a), nickel sulphate (b), copper sulphate (c) and iron (III) sulphate (d).

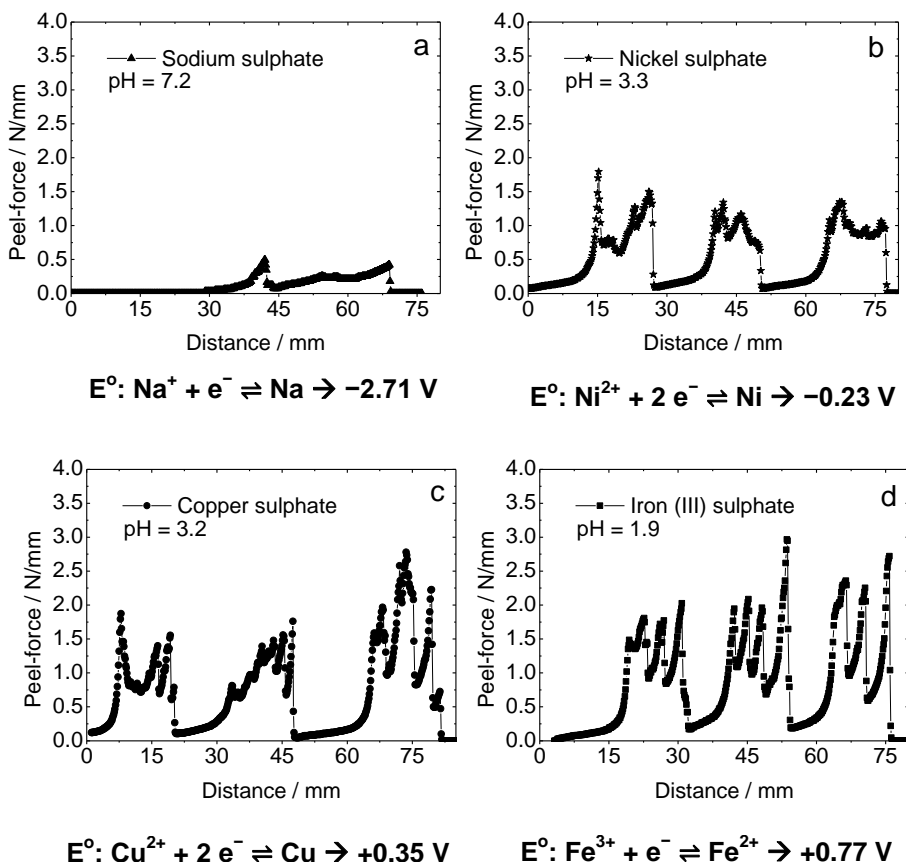


Fig. 7.28: Peel-force results after contact exposure with applied voltage in different sulphate solutions. Sodium sulphate (a), nickel sulphate (b), copper sulphate (c) and iron (III) sulphate (d)

Fig 7.29 shows the average adhesion values evaluated from six soldering spots for each experiment sample and three soldering spots for the non-dipped reference. A correlation between the measured contact adhesion and the nobility of the cations in the sulphate solutions is apparent.

The nobility of the cation affects the contact adhesion and therefore the contact corrosion significantly. In solutions with noble cations (Fe^{3+} , Cu^{2+}), the adhesion is affected far less than in solutions with less noble cations (Ni^{2+} , Na^+). This is despite the fact that $\text{Fe}_2(\text{SO}_4)_3$ shows the lowest pH of the tested solutions

and a significant adhesion drop in the dipping experiment (see Fig. 7.27) for longer durations. According to the Pourbaix diagram all pH conditions below 7 should promote lead oxide dissolution. Also equations 7.3 and 7.5 show that lowering the pH shifts the equilibrium towards dissolution.

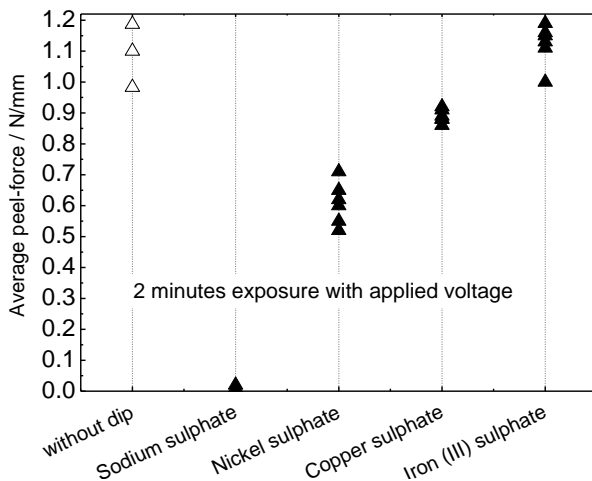


Fig. 7.29: Peel-force results of the exposure experiments with applied voltage in sulphate solutions with varied standard reduction potentials

The shown correlation between contact adhesion i.e. contact corrosion and the reduction potential of the metal cation in the respective electrolyte solution leads to the conclusion that in the case of an applied voltage the dissolution of lead/lead oxide and silver oxide is accelerated by the means of reduction of the dissolution products. In case of a noble cations (Fe^{3+} , Cu^{2+}), the reduction of the cation from the solution is preferred and the dissolution of the glass-layer is not accelerated by reducing the dissolved species. In case of less noble cations (Ni^{2+} , Na^{+}) the reduction of the species dissolved from the glass is preferred and the dissolution is accelerated. This leads to low adhesion in two minutes with applied voltage in solutions containing cations less noble than lead/lead oxide, the main compound of the glass. This nobility dependency of the contact corrosion is another explanation for the observed behaviour that only nickel plating affects contact adhesion in the plating sequence (see Fig. 7.1). The nobility of Cu and Ag compared to lead is high enough to prevent the reduction of the dissolved lead whereas the nobility of nickel which is similar to the

nobility of lead allows the reduction of the dissolved lead. This accelerates the corrosion of the contact in a way that adhesion drops significantly in the time scale of the plating sequence.

7.6 Model of the solar cell contact corrosion by electrolyte solutions

In this chapter a model of the mechanism behind the interaction between solar cell contacts and electrolyte solutions is elaborated based on the experimental results presented in chapter 7.

If the fired silver contacts get in touch with acidic electrolyte solutions, the electrolyte may access the glass-silver interface via pores in the contact structure (compare Fig. 7.11). At these sites, two reaction steps were shown to occur:

1. Silver oxide, lead oxide and other metal oxides present in the glass-layer of the contact are dissolved by H^+ ions according to equations 7.3 and 7.5. These dissolutions depend on the thermodynamics of the specific oxides, which are accessible via Pourbaix diagrams. The more acidic the media, the stronger is the driving force which shifts the equilibrium reactions towards dissolution. In weakly acidic media ($pH > 2$), the reaction runs into equilibrium and the dissolution process slows down. In strongly acidic media ($pH < 2$) the contact corrosion is already in an advanced state when equilibrium is reached, resulting in poor contact adhesion.
2. The dissolved species take different paths of reaction, which influences the equilibrium and determines the reaction speed of further glass dissolution:
 - a. **Transportation, away from the interface by diffusion**, which is a slow process as mass exchange is poor in the porous contact system.
 - b. **Reaction with anions present in the system** if thermodynamically favoured. One possibility is the formation of salts with low solubility and precipitation. This reaction is fast and its effectiveness depends on the concentration and availability of anions. The experimental basis for this conclusion is as follows: silver and lead were found to form heavily soluble salts (that would precipitate in solution) in the presence of chlorides and sulphates, forming silver chloride and lead

sulphate (compare section 7.4.2). The precipitation takes the reaction products out of the solution and shifts the equilibrium towards further dissolution. If either chlorides or sulphates are absent, the precipitation is avoided for one of the ions and the adhesion is less affected (no drop observable during the 45-minute dipping, compare section 7.4.1).

The tested copper electrolyte does not include chlorides. This is a first explanation for the higher impact of the nickel electrolytes on contact adhesion. This is true for low acid copper electrolytes, while highly acidic solutions with a pH-value < 2 lead to significant reduction of the adhesion on the considered timescale, irrespective of the presence of chlorides. This is predicted by the Pourbaix diagrams which suggest that the driving force for glass dissolution gets stronger for lower pH values (compare appendix A.1 and A.2).

- c. **The dissolved cations can be reduced** if electrons with suitable potential are present in the system. The kinetics of this process depends on competing reduction reactions offered by other cations in the system and their concentration compared to the dissolved species.

If a voltage is applied to the contacts the adhesion loss is observed to be accelerated considerably. This can be explained by the presence of electrons in the system which causes a reduction of the dissolved species. The reduction takes the dissolved cations out of the system and thus shifts the equilibrium strongly towards further dissolution. This is analogous to precipitation in the dipping case, but faster and more effective if other cations in the system do not slow it down, resulting in considerably higher impact on contact adhesion. In the case of an applied voltage the on-going dissolution of silver oxide, lead oxide or other metal oxides from the glass is determined by the reduction of the dissolved species. The effectiveness of this reaction path is determined by the electrochemical standard potential of all cationic species in the system. The presence of species with a higher reduction potential than the dissolved metal ions (e.g. copper or silver) leads to the predominant reduction of these species, leaving the dissolution equilibrium almost unaffected. If such species are not present, the dissolved cations are reduced predominantly and the equilibrium is strongly shifted. The standard reduction potential of

nickel ($E^\circ = -0.23 \text{ V}$) is slightly more cathodic than the reduction potential of lead ($E^\circ = -0.19 \text{ V}$). This means that the reduction of the dissolved lead is preferred or at least equally effective in the presence of nickel cations and leads to an acceleration of the dissolution reaction and to poor contact adhesion following nickel plating. This is the explanation for why only the nickel electrolytes cause poor contact adhesion (Fig. 7.1). The effect will be far more pronounced for this system compared to copper due to the absence of chlorides and the nobler reduction potential of copper ($E^\circ = 0.35 \text{ V}$).

- d. **The dissolved cations can be complexed** in the solution by suitable complexing agents. This can potentially suppress other reaction possibilities and could lead to less dissolution of metal oxides.

Fig. 7.30 shows the described mechanisms using a schematic drawing of a typical contact cross section interface for the dissolution path of lead oxide and silver oxide comparing nickel (a-c) and copper (d-f) electrolyte solutions. The electrolytes penetrate the porous Ag-contact (Fig. 7.30 a and d) and dissolve the lead oxide and silver oxide from the glass-layer (Fig. 7.30 b and e). In the presence of sulphate and chloride anions in the nickel electrolyte (Fig. 7.30 b) lead sulphate and silver chloride is formed. In the copper electrolyte only sulphate anions are present forming lead sulphate (Fig. 7.30 e). If electrons at a suitable potential are present, the dissolved species can be reduced (Fig. 7.30 c and f). In the nickel electrolyte the reduction of silver and lead is preferred compared to the reduction of nickel because of the higher reduction potential.

This shifts the equilibrium by the release of sulphates and chlorides for further dissolution and leads to a fast spreading gap formation along the glass silver interface (Fig. 7.30 c, red flash). In the case of sulphate based copper electrolytes the formation of lead sulphate will occur (Fig. 7.30 e) but the reduction of the dissolved lead is unlikely. Copper reduction will be preferred due to the considerably higher reduction potential (Fig. 7.30 f). The equilibrium is not shifted towards further dissolution of lead oxide; the corrosion slows down and does not lead to contact adhesion failure.

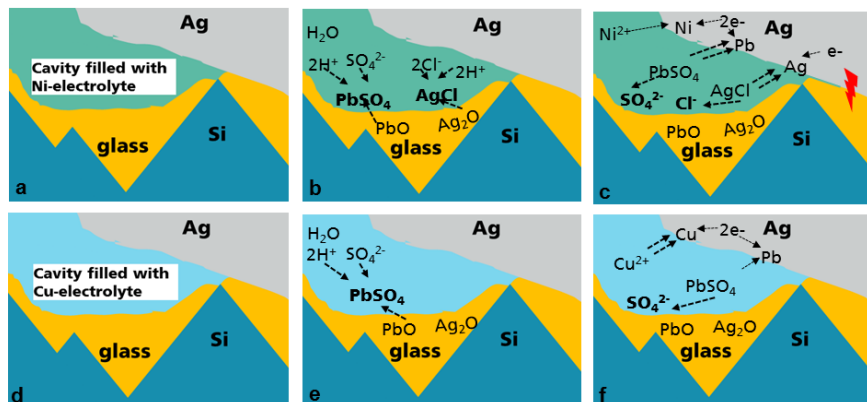


Fig. 7.30: Schematic drawing of a contact cross-section showing a cavity filled with Ni-electrolyte (a-c) and Cu-electrolyte (d-f). In the case of Ni-plating, sulphates, chlorides and H^+ -ions dissolve lead oxide and silver oxide from the glass-layer forming lead sulphate and silver chloride (b). If a voltage is applied lead and silver will be reduced preferably to nickel because of the higher reduction potential (c). This releases sulphates and chlorides for further dissolution and leads to a fast spreading gap formation along the glass silver interface (c red flash). In the case of sulphate based copper electrolytes the formation of lead sulphate will occur (e) but the reduction of lead is unlikely. Copper reduction will be preferred due to the higher reduction potential (f). The equilibrium is not shifted towards further dissolution of lead oxide and the corrosion does not lead to contact adhesion failure.

The described effect is particularly strong at spots where the distance between glass and silver is very small. At such spots the mass transport between the place of dissolution (glass) and the place of reduction (bulk silver) is very fast. This leads to a fast expansion of the gap formation specifically at this site, propagating inside the contacts along the glass silver interface as it was observed in section 7.3.1 and section 7.5.1. The described dissolution process is also possible for other metal oxides that may be part of the glass layer. The used glass in solar cell contacts is usually lead glass containing silver after the contact formation process in the firing furnace. The silver is evenly distributed over the glass layer (see Fig. 7.16). Quantitative studies of the elemental composition of the glass layer by Hönig [143] confirm the homogeneous distribution of silver and quantified an Ag content of ~3.6-5% and a Pb content of ~12% depending on the used paste.

7.7 Strategies to reach sufficient contact adhesion

The general understanding promoted by the model of the interaction between electrolyte solutions and solar cell contacts, elaborated in this work, enables the suggestion of approaches which offer the potential to improve contact adhesion after plating to the desired level.

- A basic requirement for good contact adhesion is the use of electrolytes with a $\text{pH} > 2$. Solutions with a $\text{pH} < 2$ corrode the glass layer independent of the exact electrolyte composition due to the high H^+ ion concentration.
- Dilution of the electrolytes does not prevent corrosion but it slows down the dissolution reactions and allows longer process times.
- Enabling the needed nickel deposition in process times as short as possible (preferably below one minute) leads to better contact adhesion results. The plating ratio in light induced plating can be improved by using a powerful light source and efficient bath convection.
- The development of dense seed-layers, which form less pores and cavities during the firing process can help to prevent the electrolyte from reaching the glass-silver interface and will therefore improve adhesion after plating.
- Specific complexing agents, which shift the reduction potential of lead specifically, could be a possibility to make the nickel deposition more probable compared to the reduction of the dissolved lead. This would help to slow down contact corrosion during the nickel plating process.
- The use or development of corrosion stable glasses to replace the lead glass, which was shown to be corroded during plating, is another possibility to improve adhesion. The glass has to fulfil two conditions: it has to enable a good contact formation during the firing process between emitter and metallization and should be corrosion stable against acidic media. The only glass that has been used successfully regarding contact formation besides lead glass is bismuth glass [131]. Glass formulations of high stability against acidic media are described in [144] using titanium oxide to stabilise the glass against corrosion. But it has been found that titanium oxide hinders silver dissolution in the glass which is a prerequisite for contact formation [69]. The

identification of an optimal formulation serving both purposes might be possible but is beyond the scope of this work.

- The soldering process has an influence on the resulting contact peel force. It can be adjusted regarding soldering temperature, soldering time and pre-heating to achieve the best contact adhesion result with the used metallization architecture.

Some of the described strategies were implemented to produce Ni-Cu-Ag plated solar cells and to build a demonstrator four-cell module. The screen-printed seed-layer (compare section 6.2.4) was plated with a reduced nickel plating time of 1 minute obtaining a nickel layer thickness of $\sim 1 \mu\text{m}$. The electrolyte was diluted to the half concentration compared to the standard recipe shown in table 5.1. After copper and silver plating the cells were soldered using the half automated soldering station (compare section 5.3). For soldering standard parameters were used, equal for every soldering spot. With an additional optimization of the soldering parameters even higher peel-forces are possible.

Fig. 7.31 shows the peel-force results of six soldering spots along one busbar (a) and the four-cell module built with the cells (b).

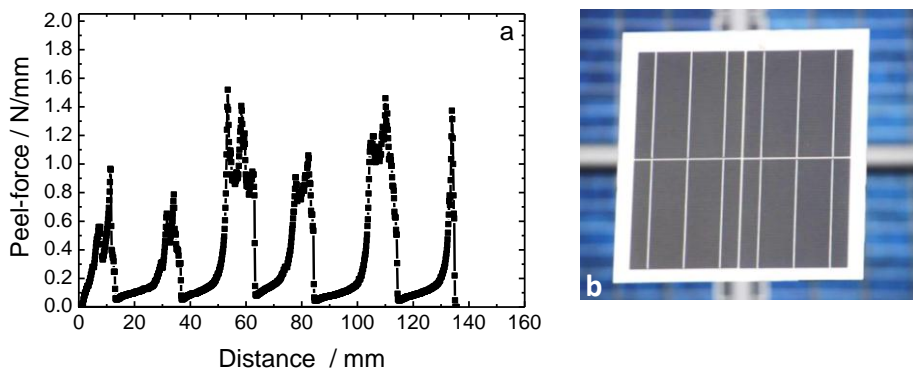


Fig. 7.31: Peel-force results of a Ni-Cu-Ag plated solar cell with screen-printed seed-layer where the nickel plating parameters were adjusted to reach improved contact adhesion (a) and a four cell module built of the cells for presentation at the 28th EU PVSEC 2013 (b).

A maximum contact peel-force of 1.5 N/mm was achieved. With one exception all soldering spots reach a contact adhesion of 1 N/mm, which is the

required standard (compare section 3.1.2). The module was presented at the 28th European Photovoltaic Solar Energy Conference (EU PVSEC) 2013 in Paris. This shows that although the corrosion mechanism of the glass layer during nickel plating cannot be avoided completely, detailed understanding of the corrosion mechanism and few process adaptations allow the production of cells with sufficient front side contact adhesion to realize module integration.

7.8 Chapter summary

In Chapter 7 the interaction between screen-printed solar cell contacts and electrolyte solutions is investigated in detail by SEM, TEM, AFM and XRD analysis supported by exposure experiments with and without applied voltage to characterise the contact peel-force as a measure for the degree of contact corrosion.

- Only nickel plating affects adhesion significantly in the Ni-Cu-Ag plating sequence (section 7.1) for mainly two reasons: the chlorides in the Watts-type electrolyte offer a precipitation possibility for the dissolved silver (section 7.4.2) and the reduction potential of nickel is slightly more cathodic compared to the reduction potential of lead, which makes the reduction of the lead, dissolved out of the lead glass in the contact, preferable, ending up in a more effective dissolution of the lead glass (section 7.5.2).
- pH-dependency: chemical solutions with a pH-value < 2 corrode the contact effectively due to dissolution of lead/lead oxide and silver oxide (section 7.2).
- In the case of exposure without applied voltage, sulphates, chlorides and boric acid (H^+ -ions) in combination independent of the presence of nickel affect adhesion in 45 minutes at 50°C (section 7.4.1).
- Lead, lead oxide and silver oxide in the contact react with sulphates and chlorides in the electrolyte forming lead sulphate and silver chloride (section 7.4.2).
- The failing interface is located between the glass-layer and the bulk silver inside the contact. A site specific dissolution of the glass-layer occurs in the direct vicinity of the bulk-silver, ending up in a spreading gap

formation along the glass-silver boundary layer in the contact (section 7.3.1).

- No layer of material with distinctly different composition was found in the glass in the direct vicinity of the silver which could have explained the site specific dissolution (section 7.3.2).
- An applied voltage accelerates the corrosion i.e. the dissolution of the glass-layer considerably in nickel and sodium containing solutions (section 7.5.1 and 7.5.2).
- The reduction potential of the cation in the solution correlates with contact corrosion. In the presence of noble cations compared to lead the contact adhesion remains unaffected (Ag^+ or Cu^{2+}), in the presence cations with similar or less noble reduction potential (Ni^{2+} or Na^+) than lead, contact adhesion was observed to be destroyed in experiments with applied voltage (section 7.5.3).

The experimental findings summarized above enabled the development of a detailed model of the electrochemical corrosion mechanism during plating. It explains the observed experimental results of poor contact adhesion after nickel and copper plating on printed seed-layers and promotes the general understanding of contact adhesion loss after plating (compare chapter 7.6). On the basis of the generated scientific understanding of the corrosion mechanism, strategies to reach sufficient contact adhesion were developed. Contact adhesion of 1.5 N/mm was achieved and a module was successfully built with standard industrial scale cells (section 7.7).

8 Long term stability of plated copper front side metallization based on screen-printed seed-layers

The long term stability is, besides sufficient contact adhesion, a key issue for solar cells with copper front side metallization. Module manufacturers usually offer a 20-30 years warranty for solar modules. In this time the energy yield should not degrade below 95% of their initial value (compare section 3.1.3). Copper is known to migrate into silicon, even at room temperature, it forms local recombination centres in the emitter, the junction and the bulk, which reduces the carrier lifetime of the cell severely and leads to a considerable efficiency degradation. The silver seed-layer supposedly does not work as a sufficient diffusion barrier. To prevent copper from diffusing into the silicon, a plated nickel diffusion barrier is included into the metallization architecture. In this chapter the copper diffusion in p-type silicon solar cells is investigated (chapter 8.1). The effectiveness of the silicon nitride anti reflection coating (chapter 8.2) and the plated nickel diffusion barrier (chapter 8.3) regarding their ability to avoid copper migration into the solar cell is evaluated in detail. Additionally the influence of the used seed-layer and the firing temperature on the degradation behaviour of the cells is analysed (chapter 8.4). Problematic spots in the micro structure of the printed seed-layer for nickel plating were pointed out in a SEM investigation (chapter 8.5). Additionally, the homogeneity of the plated nickel on the front side metallization is evaluated (section 8.6). Adaptations in the plating setup were analysed to improve the nickel distribution (section 8.7). Section 8.8 gives a summary of the results and findings presented in this chapter.

8.1 Copper diffusion behaviour in silicon solar cells

To investigate the copper diffusion in solar cells the method published by Bartsch *et al.* in 2010 [39] basing on the measurement of the pFF degradation during thermal treatment is used in this work (compare section 5.4 for detailed method description; the experimental results obtained with this method are presented in section 8.3 and 8.4). These experiments can last more than 1000 h and are usually done manually. For each measurement the cell is taken from the hotplate, cools down to room temperature, is measured and heats up again. Depending on the execution, the measurement differs in frequency.

During the degradation measurements conducted in this work, deviations between repetitions of the same point and systematic cell recoveries were observed. Apart from purely statistical variations due to inhomogeneities in the printed and plated layers or the nitride layer, influences from the measurement routine were suspected. For more systematic and controlled studies in the future, experiments which promote general understanding of copper migration in p-type solar cells were performed.

To investigate how differences in the measurement cycle influence the resulting degradation in general, cells with plated copper directly on the screen-printed silver seed-layer (without nickel diffusion barrier) were produced and treated on a hotplate at 275°C for 6.5 hours while measuring the I - V -parameters of cell 1 every 30 minutes and of cell 2 three times in 6.5 h. Fig. 8.1 shows the measured FF (a) and V_{oc} (b) of cell 1 (black squares) and cell 2 (red circles) relative to the initial measurement before thermal stress ($t = 0$) over time.

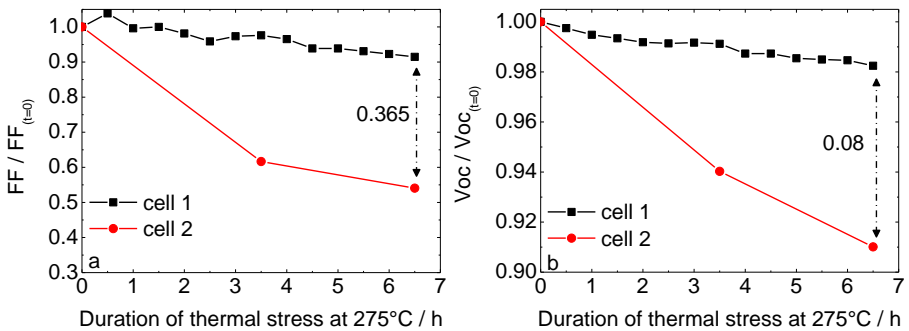


Fig. 8.1: FF (a) and V_{oc} (b) measurements of two copper plated cells without nickel diffusion barrier treated on a hotplate (275°C) for the same total time of 6.5 h, measuring the I - V -parameters of cell 1 every ~ 30 minutes (black squares) and for cell 2 only three times (red circles)

Both cells were thermally treated for the same total time. It can be observed that cell 1 with a higher measurement frequency degrades 8.5%_{rel.} during 6.5 h to a relative FF of 91.5%, whereas cell 2 with only three measurements degrades 45%_{rel.} to a relative FF of 55% in 6.5 h. The degradation of the V_{oc} shows the same behaviour, a significant difference of 8% between the final degradation of cell 1 and 2 was measured. The degradation of the cells was additionally characterized by PL-imaging.

The PL-images recorded before thermal treatment, after 220 minutes and after 390 minutes at the end of the thermal treatment shown in Fig. 8.2, confirm these results. The measured difference in the degradation behaviour is clearly visible. The PL-images of cell b appear considerably darker, which indicates a shorter carrier lifetime. This reveals that differences in the measurement frequency influence the resulting degradation of the cell considerably. It can be assumed that more measurements means more cooling cycles from 275°C to room temperature, which results in less degradation and indicates slower copper migration.

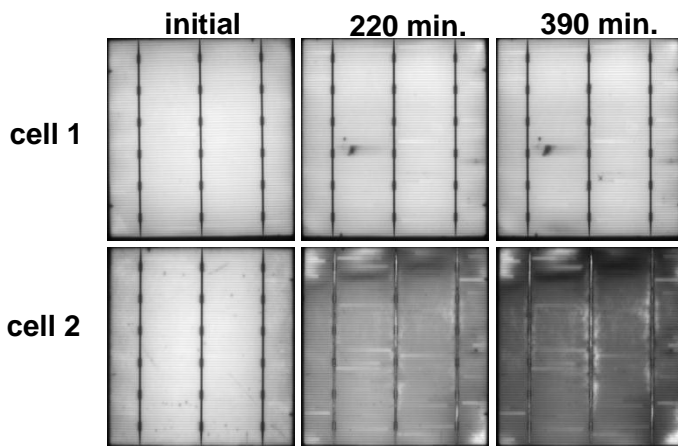


Fig. 8.2: PL-images of copper plated cells without nickel diffusion barrier treated on a hotplate at 275°C for the same total time of 6.5 h before thermal treatment after 220 minutes and at the end of the thermal treatment after 390 minutes. The *I-V*-parameters of cell 1 were measured every ~30 minutes and of cell 2 only three times at all.

To exclude that possible variabilities in production of the two analysed cells were responsible for the measured degradation differences, the experiment was reproduced with four different measurement frequencies (0.5 h, 2 h, 3.5 h and 6 h) and three cells per experimental point. Instead of the more time-consuming *I-V*- and PL-measurement, the *pFF* of the cells was characterized using Suns-Voc measurement (method description see section 4.3.1). Fig. 8.3 shows the *pFF* results relative to the initial *pFF* before temperature treatment which was ~82%_{abs.} for all cells. An influence of the measurement frequency on the degradation behaviour is clearly visible in the graph. For a measurement frequency of 0.5 h (black squares) the cells degrade to a relative *pFF* of ~78%.

For a measurement frequency of 2 h (blue triangles) the cells degrade to a relative pFF of ~64%. For a frequency of 3.5 h (red circles) the cells degrade to a relative pFF of ~47% and for a measurement frequency of 6 h (green stars) the cells degrade to a relative pFF of ~46%. Between the degradation result for 3.5 h and 6 h measurement frequency no significant difference in final degradation can be observed.

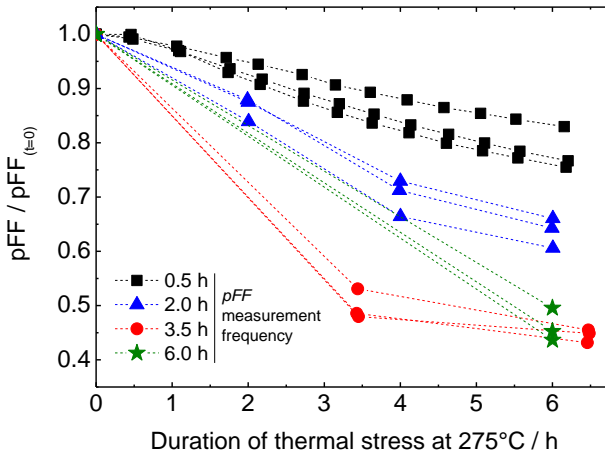


Fig. 8.3: Measurement results of the normalized pFF for copper plated cells without nickel diffusion barrier treated on a hotplate at 275°C for ~six hours measuring pFF every ~0.5 hours (black squares), every 2 h (blue triangles), every 3.5 h (red circles) and only before and after thermal treatment (green stars). The dashed lines between the measurement points are plotted as guide to the eye.

Fig. 8.4 shows the absolute average pFF difference between the measurement before and after thermal stress at 275°C for 6.5 h for cells measured with different measurement frequencies. For rising measurement frequencies the pFF difference decreases and goes into saturation for small measurement frequencies > 3.5 h. This means that an increase in the heating and cooling cycles slows down copper migration depending on the cycle frequency.

For the fast degradation experiments on hotplates a measurement frequency of > 3.5 h leads to degradation results unaffected by frequency effects. This is especially important for the comparison of degradation results reached with different measurement frequencies.

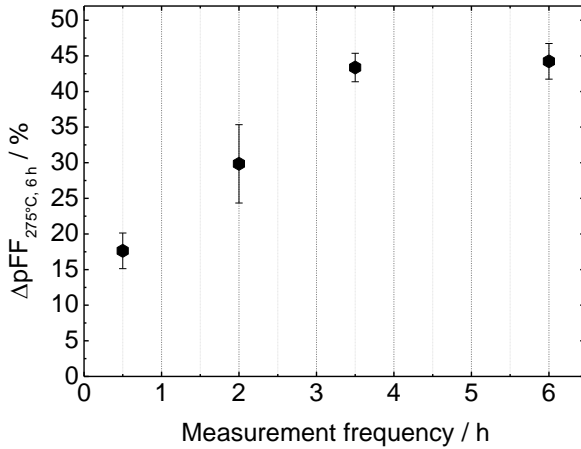


Fig. 8.4: Average pFF difference between the measurement before and after 6 h of thermal stress at 275°C for cells measured with different measurement frequencies

The breaks in the thermal treatment, due to measurements at room temperature, seem to slow down the copper migration into the cell. As no diffusion barrier to hinder copper diffusion was applied and the used silver seed-layer is very thin ($\sim 1 \mu m$) the copper can easily penetrate into the silicon. If the wafer is locally supersaturated with copper near the surface after in-diffusion, two general mechanisms are reported in literature, which can work against further diffusion: out-diffusion back to the surface or precipitation.

Platelet-like Cu precipitates with amphoteric properties and very high recombination activities were reported for high initial copper concentrations and cooling rates larger than 100 K/s in the bulk of n-type silicon [145]. The precipitates can change their state from positive to negative when the Fermi level crosses the neutrality level [145], [146]. Istratov et al. concluded that the electrostatic repulsion between positively charged nuclei of copper precipitates and positively charged copper ions suppresses the precipitation in p-type silicon [146].

Out-diffusion of copper to the wafer surface is published by Shabani *et al.* [147] and Mc Carthy *et al.* [148]. The out diffusion starts at room temperature and the copper can easily be removed from the surface by HF/H_2O_2 [147], which indicates that copper does not tend to form chemical bonds with the silicon. An

out-diffusion effect back to the surface during the cooling cycles will keep the copper at the surface in the emitter area where it can precipitate and attract the successively diffusing copper for some time. This is a possible explanation for the observed degradation difference between cells measured with different frequencies. For cell 1, copper does not diffuse deeply into the wafer during the short period of thermal stress which facilitates out-diffusion to the close surface during cooling for pFF measurement. For cell 2, deeper copper diffusion is expected during the longer period on the hotplate, and penetration to the junction and the bulk becomes more likely. This effect might decrease or even remove the destructive effect of copper on solar cell efficiency in the module application case, because in the field, modules are subjected to a cycle of heating during daytime and cooling during the night depending on the location of the module. If these cycles promote an out-diffusion effect of the copper as it is indicated by the results above modules in the field will degrade slower as usually supposed. On the other hand modules undergo only one cycle of up to 80-90°C in 24 h. The presented results indicate that one cycle per day will not slow down the copper migration significantly at high temperatures. The lower module operating temperature might keep copper penetration close to the wafer surface similar to short durations at high temperatures.

However, more detailed studies in different temperature and time regimes have to be carried out to understand the behaviour of copper migration in silicon solar cells completely. Also, the influence of diffusion barriers and of the degradation speed on spreading of the results needs to be investigated. The studies so far show that the results measured with different measurement frequencies are hardly comparable. The degradation results in this work were measured with the same frequency (in most cases > 12 h) and can be used to show the influences of different plated nickel masses or other parameters (compare section 8.3 and 8.4). For the characterization of degradation data in the future a standard test should be developed, which enables the measurement of solar cells with copper metallization regarding their long term stability under comparable conditions.

8.2 Silicon nitride as diffusion barrier

For plated copper front side metallization techniques, the copper conductive layer usually overlaps the nickel diffusion barrier, plated just before copper, at the side edges of the contact structures.

Fig. 8.5 shows this spot (marked with red dashed arrows) at a microscope cross-section image of a copper metallization contact finger, where the copper is located directly on the usually 70 nm thick silicon nitride. This possible weak point in the metallization is also present in direct plated Ni-Cu contacts (compare section 3.5, especially Fig. 3.14) and in approaches where a copper paste is printed on the silicon nitride layer as busbar metallization [149].

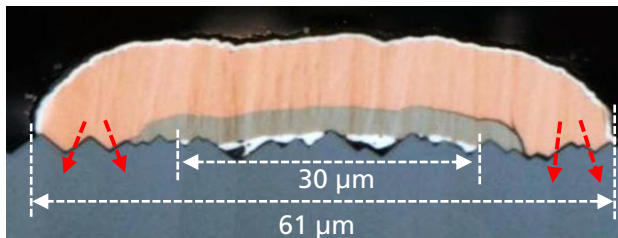


Fig. 8.5: Cross-section microscope image of a Ni-Cu-Ag metallization contact finger, based on a printed Ag seed-layer with marked area where the plated Cu overlaps the Ni diffusion barrier and stays in direct contact with the silicon nitride (red arrows)

To analyse if the silicon nitride avoids copper diffusion in general and to elucidate if this part in the contact structure can become a potential spot of copper diffusion after HF-dip or the mechanical load of the screen-printing process, a long term stability experiment with lifetime samples was performed. Four inch wafers out of 10 Ω cm FZ-silicon with random pyramid texture, a 90 Ω phosphorous emitter and different silicon nitride anti reflection coatings on both sides were produced to get symmetrical lifetime samples. Silicon nitrides deposited by inline PECVD, inline sputtering and in an experimental batch furnace (AK 800 by Roth & Rau) were used. References passivated with 10 nm aluminium oxide (activated with a forming gas anneal; 500°C for 10 minutes) were produced. Following silicon nitride deposition the wafers were fired at a set-peak temperature of 900°C in an industrial inline furnace. The pre-treatment before copper evaporation was varied using a dry screen-printing step (100 N/cm squeegee pressure) or a HF-dip (1%, 30 s). The screen-printing pre-treatment

was done at a half automated screen-printing machine using the same equipment (chuck, screen and squeegee) and conducting the same handling as for standard solar cells to include typical potential damage to the silicon nitride into the simulation. This simulates the normal stress for anti-reflection coatings regarding the seed-and plate process where the silicon nitride can be affected mechanically by the screen-printing of the silver seed-layer. The direct plating alternative, where a HF-dip is conducted to prepare the wafers for nickel plating was simulated with an HF-dip. Also references without pre-treatment were produced. 200-300 nm copper were evaporated on one side in the middle of the wafers. During copper evaporation the edge zone of the wafers was covered with an aluminium mask to avoid copper deposition at the edges where the silicon nitride layer is not perfectly closed. To accelerate potential copper diffusion the wafers were exposed to thermal stress on hotplates at 300°C for 500 h. Based on previous results with the Arrhenius-type diffusion of copper through nickel diffusion barrier layers, this thermal budget should over-represent a typical diffusion case during a solar module life cycle. After temperature treatment the copper was etched chemically using Piranha etch (H_2SO_4 (conc.) and H_2O_2 (30%)) at the rate of 3:1, 10 minutes).

To characterize copper migration through the silicon nitride or aluminium oxide into the samples photoluminescence imaging (PLI) and carrier lifetime measurements (QSSPC) were done before copper evaporation and after temperature treatment and copper etch back. Fig. 8.6 illustrates the described experimental sequence at a schematic drawing and Fig. 8.7 shows the used four inch wafers before (a) and after copper evaporation (b).

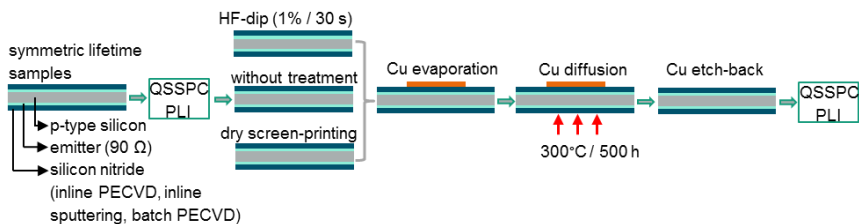


Fig. 8.6: Schematic drawing of the experimental sequence of the lifetime experiment to characterize the copper diffusion through different silicon nitride layers

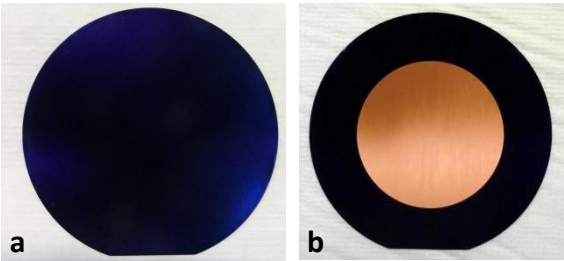


Fig. 8.7: Four inch wafers before (a) and after copper evaporation (b) using a ring like aluminium mask to protect the edge zones of the wafer, where the silicon nitride is not perfectly closed.

Fig. 8.8 shows the PL-images of the lifetime samples without HF or dry screen-printing pre-treatment before copper evaporation (upper line) and after copper etch-back (line below).

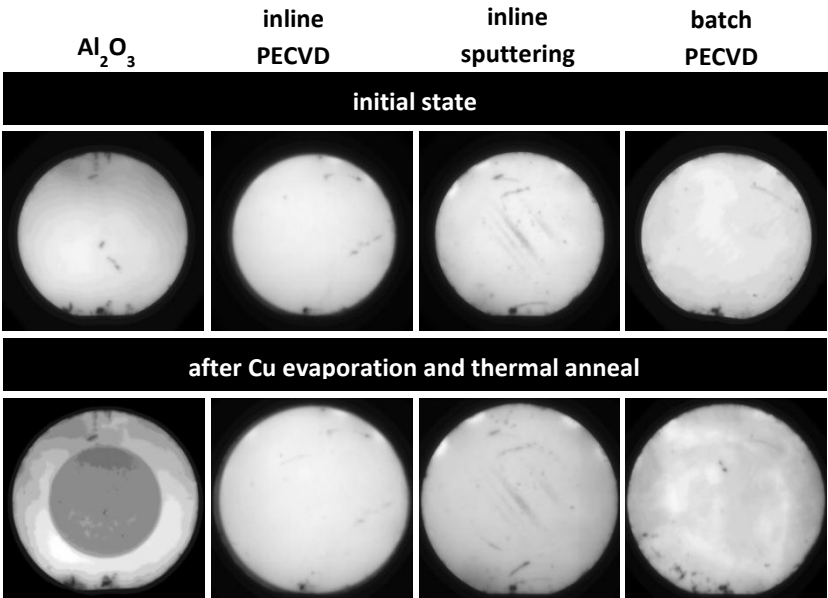


Fig. 8.8: PL-images of the lifetime samples without pre-treatment for the different silicon nitride layers and the aluminium oxide reference before (upper line) and after copper treatment (line below). Only for the aluminium oxide reference a decrease in the carrier lifetime can be observed exactly at the position of copper deposition.

The images reveal that only the samples with aluminium oxide show a PL intensity difference due to the influence of copper migration (darker spot in the middle of the wafer representing a decrease in the carrier lifetime). All samples with silicon nitride do not show significant deviations in the PL-images after copper treatment. It can be concluded that the copper did not diffuse into the junction in 500 h at 300°C. Fig. 8.9 shows the carrier lifetime measurements for all samples at an injection level Δn of $1 \cdot 10^{-15} \text{ cm}^{-3}$.

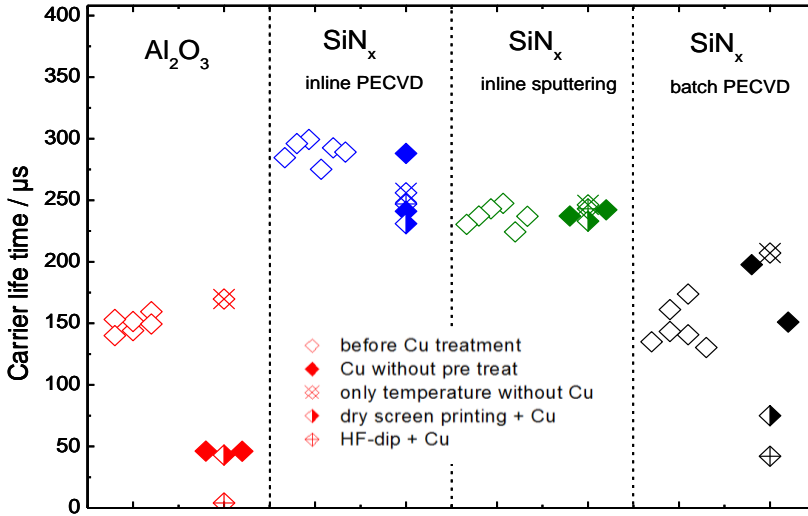


Fig. 8.9: Carrier lifetime measurements before and after copper treatment for samples with different passivation layers. Aluminium oxide (first column, red data), silicon nitride deposited by inline PECVD (second column, blue data), silicon nitride deposited by sputtering (third column, green data) and silicon nitride deposited by batch PECVD (fourth column, black data). The different designs of the symbols represent different groups in the experiment: measurement before copper and temperature treatment (unfilled symbols), without pre-treatment (filled symbols), reference without copper, just temperature treatment (diagonally crossed symbols), screen-printing pre-treatment (half-filled symbols) and HF-dip pre-treatment (normally crossed symbols).

The aluminum oxide reference (first column, red data), the silicon nitride deposited by inline PECVD (second column, blue data) the silicon nitride deposited by sputtering (third column, green data) and the silicon nitride deposited by batch PECVD (fourth column, black data). The unfilled symbols represent the measurement before copper treatment. The diagonally crossed symbols represent a reference measurement with thermal anneal but without

copper on the wafers to validate if the thermal treatment alone affects the carrier lifetime. Only the wafers with inline PECVD show a slight drop of about 30 μs , for the other nitrides the lifetime stays stable or rises slightly due to the temperature treatment. The filled symbols represent the measured carrier lifetime after copper anneal without pre-treatment. As already observed at the PL-images, only the aluminum oxide reference shows a significant drop in the carrier lifetime of about 100 μs . The lifetime for all nitride layers is in the range of the reference measurements.

The half-filled symbols represent the carrier lifetime after copper treatment with screen-printing pre-treatment and the normally crossed symbols show the wafers with HF-dip pre-treatment. In both cases the aluminum oxide reference and the silicon nitride deposited in the batch furnace show a carrier lifetime drop due to copper migration. The PL-images of these groups confirm these results.

The batch nitride is inhomogeneous in thickness compared to the nitrides deposited by inline techniques and the batch procedure is critical regarding contaminations. This obviously leads to deteriorations after the tested pre-treatments, which allow the copper to migrate through the silicon nitride. This means that the choice of the deposition tool/process plays a major role for the diffusion barrier properties of the resulting silicon nitride. The silicon nitride deposited in the batch furnace is designed to achieve good passivation properties directly after deposition. Therefore the hydrogen content is higher than for the inline PECVD silicon nitrides. During firing the hydrogen outgases from the silicon nitride layer and the resulting passivation properties suffer ending up in the lowest initial carrier lifetimes for the silicon nitride deposited in the batch furnace.

In microelectronics the diffusion barrier properties of SiO_2 and SiN_x against Cu diffusion have been investigated in detail. It has been found that a 50 nm thick SiN_x layer offers excellent diffusion barrier properties [150], which is in accordance with the results found in this work. However, SiO_2 enables copper diffusion [150], [151]. Copper diffusion in SiO_2 is traced back to the ionization of copper [151]. The barrier properties of SiO_2 against Cu diffusion during simultaneous thermal and electrical stress were reported to depend on the oxygen concentration in the annealing atmosphere. Even small traces of oxygen cause a significant Cu diffusion in SiO_2 compared to no signs of diffusion using oxygen free atmospheres [152]. Vogt et al. [150] concluded that the transport mechanism of Cu in SiN_x layers is an ion drift mechanism and that the existence of traps in the dielectric layer promotes the Cu ionisation and therefore the possibility of

diffusion. In SiO_2 , deep level acceptors in the forbidden band gap, as offered by oxygen, lower the Fermi-level which results in efficient ionisation of the neutral copper atoms in the oxide [153]. However, SiN_x is known to offer excellent barrier properties against moisture and oxygen diffusion [154]. This is suggested to be the explanation for the better Cu diffusion barrier properties of SiN_x compared to SiO_2 . This means that for good barrier properties against copper diffusion the SiN_x layer has to be realized without impurities or dangling bonds offering traps which enable the ionisation of copper and therefore the ion transport. This was obviously reached in this work using the inline PECVD and the inline sputtering process but not by the batch furnace process, which enabled copper diffusion after HF-dip and the screen-printing pre-treatment.

The results reveal that silicon nitrides deposited by inline PECVD and inline sputtering are able to stop copper diffusion even after HF-Dip or a screen-printing step. This reveals that the spot at the edges of the metallization where the copper gets in direct contact with the silicon nitride layer is not necessarily a weak point in the metallization if the right silicon nitride layer is chosen and deposited clean and homogenous under inline conditions. However, underneath the printed and fired paste, the SiN_x layer is etched and cannot hinder copper diffusion. Here, the plated nickel diffusion barrier has to avoid copper diffusion, which is investigated in the next section.

8.3 Effectiveness of the nickel diffusion barrier

In the last section it was demonstrated that the silicon nitride layer can be optimized to represent no weak point for copper diffusion, the plated nickel barrier layer is now in the focus of interest regarding its influence on cell stability. To evaluate the effectiveness of the nickel diffusion barrier, cells plated with different nickel diffusion barrier masses and identical copper and silver plating were produced. The degradation due to copper migration was evaluated on cell and module level. A comparison of the achieved degradation results allows a first hint whether the used rapid degradation method at elevated temperatures on cell level is able to predict degradation of the related module in the climate chamber and clarifies the nickel mass needed to reach sufficient long-term stability for solar cells.

8.3.1 Degradation of cells at elevated temperatures

For cell degradation at elevated temperatures, solar cell samples were produced according to section 5.5. The plated nickel mass was varied from 10 mg per cell to 40 mg per cell, corresponding to nickel layer thickness of 0.1 μm to 0.8 μm measured at the busbar in the middle of the cells. This spot is known to be the one with the lowest nickel plating (compare section 8.6), the nickel layer will be thicker at the contact fingers and at the edges of the cell. The amount of the plated copper used per cell was 85 mg, corresponding to a thickness of $\sim 8.5 \mu\text{m}$. Also wafers without any diffusion barrier (nickel plating skipped) and without copper were produced as references.

The cells were heat-treated on hotplates at 200°C, 225°C, 250°C and 275°C. The pFF was characterized using a Suns-Voc measurement setup (Sinton Instruments) with containment to exclude an influence from ambient light, to detect the cell degradation due to copper migration into the cells. Before each measurement the cells were allowed to cool down to room temperature for two minutes in ambient air. This method was published by Bartsch *et al.* in 2010 [39] and was employed to characterize cell degradation due to copper diffusion in various publications in the field of silicon PV metallization to date [149], [155], [156].

The measurement intervals were varied depending on the speed of degradation. In a few cases, the measurement interval was chosen shorter than would be recommended, considering the findings in section 8.1. However, short intervals were only chosen for high anneal temperatures, where quick degradation was expected. Here, a delay in degradation due to measurement interval will lead to less steep slope in the Arrhenius plot used for degradation estimation and thus to an overestimation of module degradation. Furthermore, all cells were treated similarly, which allows comparison of the results in any case. The measurement intervals were as recommended in >98% of all cases. Fig. 8.10 shows the normalized pFF over time for thermal stress at 200°C (upper diagram) and 275°C (lower diagram). The reference cells without copper, just plated with nickel and silver (grey pentagons), show a significant degradation at 275°C due to nickel diffusion or silicide formation as deep as the junction. The degradation of the references in general corresponds well with literature values reported regarding nickel silicide formation in silicon [157]. At 250°C the degradation of the cell without copper is slow and does not reach 95% of the initial pFF .

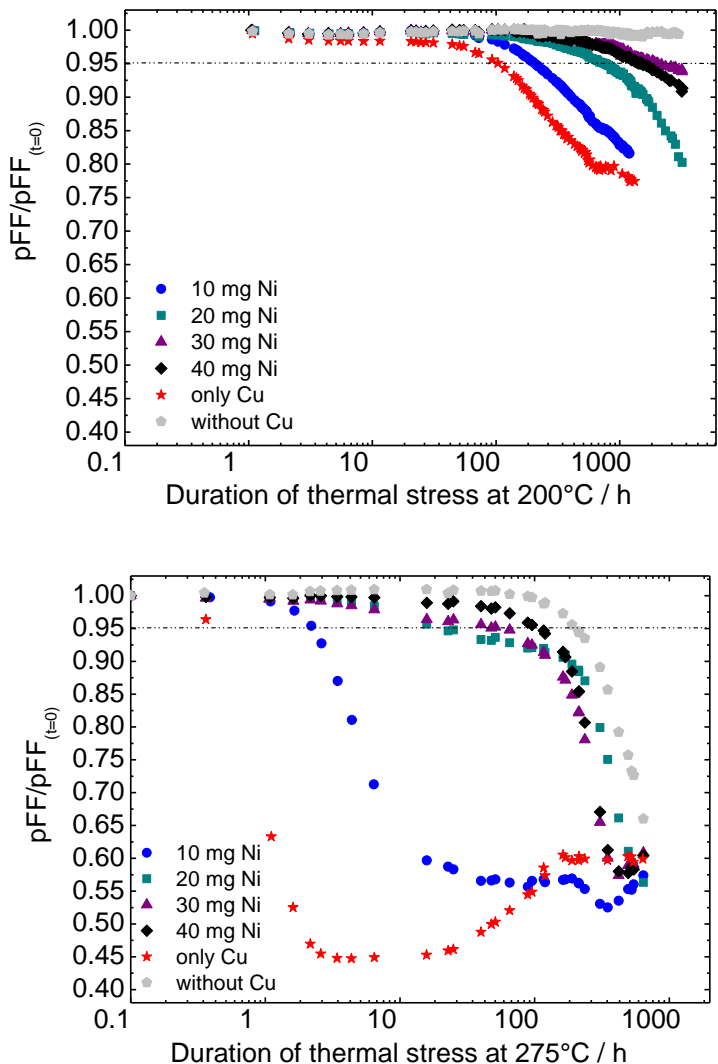


Fig. 8.10: Degradation of the relative pFF over time at a thermal stress of 200°C (above) and 275°C (below) for cells with different nickel diffusion barrier masses: only copper, without nickel diffusion barrier (red stars), 10 mg nickel (blue circles), 20 mg nickel (green squares), 30 mg nickel (purple triangles), 40 mg nickel (black diamonds), without copper and with 20 mg nickel (gray pentagons)

At 200°C and 225°C, the references do not degrade at all during the experimental duration of ~3000 h. However, more plated nickel leads to slower cell degradation. The degradation of the *pFF* is significantly slower for cells plated with at least 20 mg nickel (green squares) or more compared to cells plated without diffusion barrier (red stars) or just 10 mg nickel (blue circles). This trend can be observed at both temperatures.

Fig. 8.11 shows the resulting Arrhenius plot using temperature/time pairs leading to a *pFF* degradation of 5%_{rel.} for cells with different diffusion barrier masses and reference cells without diffusion barrier, treated at 200°C, 225°C, 250°C and 275°C.

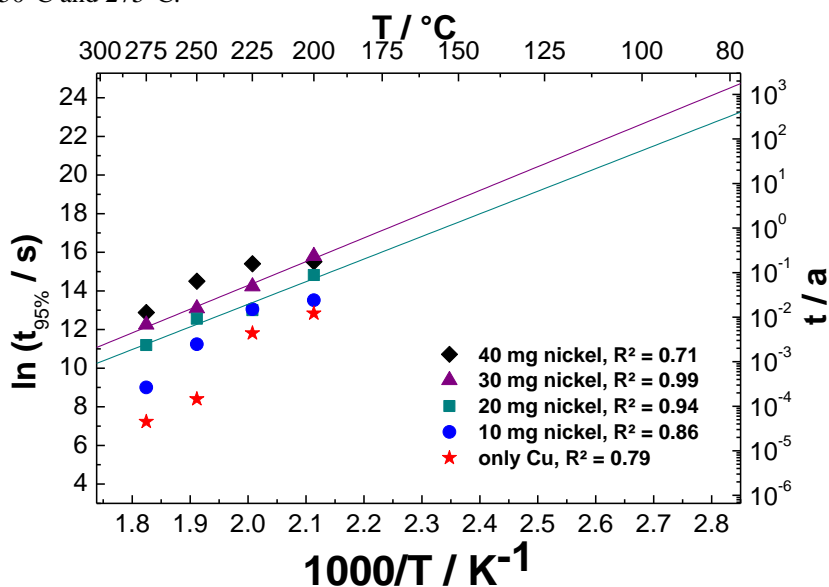


Fig. 8.11: Arrhenius plot of the degradation data; for temperature/time pairs leading to a *pFF* loss of 5%_{rel.} with linear fit for the data of 20 mg plated Ni (green squares) and 30 mg plated Ni (violet triangles). Reference cells without diffusion barrier (red stars) and contacts with 40 mg plated Ni (black diamonds)

Each point in the diagram represents one cell in the experiment. For the cells with 20 mg and 30 mg nickel diffusion barrier the regression indicator R^2 of the linear fit shows values of 94% and 99%. The linear fits predict no cell lifetime limitation due to copper diffusion at 80°C (>100 years). For the other data the regression indicators indicate no reliable fit. More cells per experimental point

are needed to get more information regarding the variance in this type of experiment. 20 mg of nickel seems to be sufficient to reach acceptable long term stability. In the present experiment, this corresponds to a thickness of the plated nickel layer of $\sim 0.2 \mu\text{m}$ at the spot with the lowest nickel deposition. For a fully homogeneous nickel layer, $\sim 10.8 \text{ mg}$ nickel corresponds to a $0.2 \mu\text{m}$ thick nickel layer. As described in section 2.4, the activation energy for copper diffusion through the used solar cell metallization architecture with printed seed-layer and plated nickel diffusion barrier in the temperature range of $200\text{--}275^\circ\text{C}$ can be calculated from the slope of the linear regression in the Arrhenius plot. For the data belonging to 20 mg plated nickel, an activation energy of 1.01 eV and for the data corresponding to 30 mg plated nickel, an activation energy of 1.06 eV were calculated. These are “effective” activation energies, valid for an inhomogeneous system of copper, nickel, solar cell paste (including silver particles, glass frit and pores), silicon nitride and silicon. Depending on specific material combination, the local activation energies for copper to change its position with the neighbouring atom, or to move to the next interstitial position, may differ significantly. The activation energy of copper diffusion in pure nickel is far higher (2.64 eV [46] for a temperature of 900°C). On the other hand the activation energy for copper diffusion in intrinsic p-type silicon is reported by Istratov to 0.18 eV in a temperature range between 265 K and 1173 K [44]. This shows that the activation energies of copper diffusion through the tested metal stack out of a printed silver seed-layer ($\sim 1 \mu\text{m}$) and the plated nickel diffusion barrier (at least $0.2 \mu\text{m}$), evaluated from the slope of the linear regressions in Fig. 8.11, are ~ 5 times the values for copper diffusion in intrinsic silicon and less than half the activation energies of copper in pure nickel. This underlines the diffusion barrier properties of the nickel included in the metal stack and the effectiveness of the inclusion of nickel into the contact design. However, the values are lower than that for pure nickel, which stresses the fact that the heterogeneous system, present in the investigated contact architecture, probably exhibit weaknesses (e.g. non nickel plated areas, cracks or pinholes in the nickel layer, thin parts of the nickel layer or preferred diffusion channels along grain boundaries). Diffusion barrier and weaknesses lead to an averaging of the activation energy in between the extreme cases valid for the pure material systems.

8.3.2 Degradation of modules in the climate chamber

Out of the cells produced as described in section 8.3.1 single cell modules were built. The cells were soldered manually using a standard 1.5 mm ribbon (Sn-Pb-Ag) and a standard flux. Single cell modules ($20 \times 20 \text{ cm}^2$) were laminated with standard glass and encapsulation materials (EVA, white back sheet). The modules were treated in a climate chamber at 85°C and 85% r.h. (IEC damp heat test [8]) for 2000 h. IV-measurements (ISE Callab PV modules) were done before and after 1500 h climate chamber exposure to characterize the degradation due to copper diffusion. Electroluminescence measurements were performed before, after 500 h, 1000 h, 1500 h, and after 2000 h of climate chamber exposure. The power of the modules ranged between 4 and 4.3 W (at *mpp*).

Fig. 8.12 shows the relative efficiency change (a) and the relative fill factor change (b) of the modules after 1500 h of damp heat test.

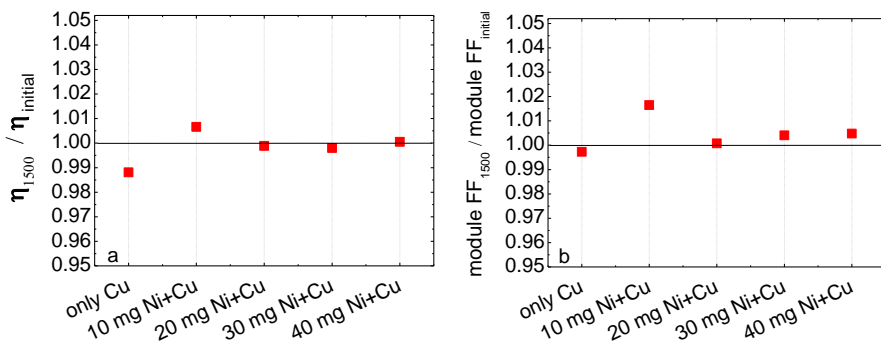


Fig. 8.12: Relative efficiency (a) and relative fill factor (b) of single cell modules after 1500 h of damp heat test (85°C , 85% r.h.) related to the measurement before climate chamber exposition

All modules, even the one without diffusion barrier (copper directly on $1 \mu\text{m}$ thin printed seed-layer), pass the IEC criteria ($<5\%$ degradation compare section 3.1.3). Only the module without diffusion barrier shows a degradation of the fill factor of $0.25\%_{\text{rel.}}$ compared to the initial measurement. As the fill factor is the relevant parameter for accelerated aging on hotplates, it will be used for comparison of the module degradation. For the discussed module, the

degradation of the efficiency of about 1.2%_{rel.} can be traced back mainly to the degradation of the fill factor while V_{oc} was not observed to degrade. However, j_{sc} did degrade of only about ~0.3 mA due to climate chamber exposure. The other modules show a slight improvement of the fill factor after 1500 h damp heat test.

Fig. 8.13 shows electroluminescence images and the related histograms of the single cell modules before and after 1500 h and 2000 h in the climate chamber. The histograms show the distribution of the counts, the black curve refers to the measurement before the climate chamber, the red curve to the measurement after 1500 h and the blue curve to the measurement after 2000 h. A shift of the peaks on the x-axis after climate chamber exposition show differences in the module performance. A shift to higher counts stands for improvement of the module performance. A shift to lower counts stands for module degradation. Aside from some general problems with the cells such as some interrupted fingers due to a non-optimized printing process, the images do not show significant issues due to copper diffusion. The cells with 20, 30 and 40 mg plated nickel diffusion barrier (c-e) do not show degradation after 2000 h damp heat test compared to the initial measurement. The reference cell without nickel diffusion barrier (a) and the cell with 10 mg nickel (b) show slight degradation after 2000 h. Either all modules are stable against copper diffusion under the conditions represented by the IEC procedure and could be used in the field, or the damp heat test does not reveal problems in the metallization architecture causing copper migration into the junction in 2000 h. To check cells regarding long term stability problems caused by a possible copper diffusion into the junction, faster and cheaper tests on cell level at higher temperatures are recommended. Otherwise, longer durations on module level are needed to show effects clearly. Thereby, longer durations will affect the cell and the module in different ways apart from copper diffusion, and these affections will superpose trends induced by copper diffusion and influence the result.

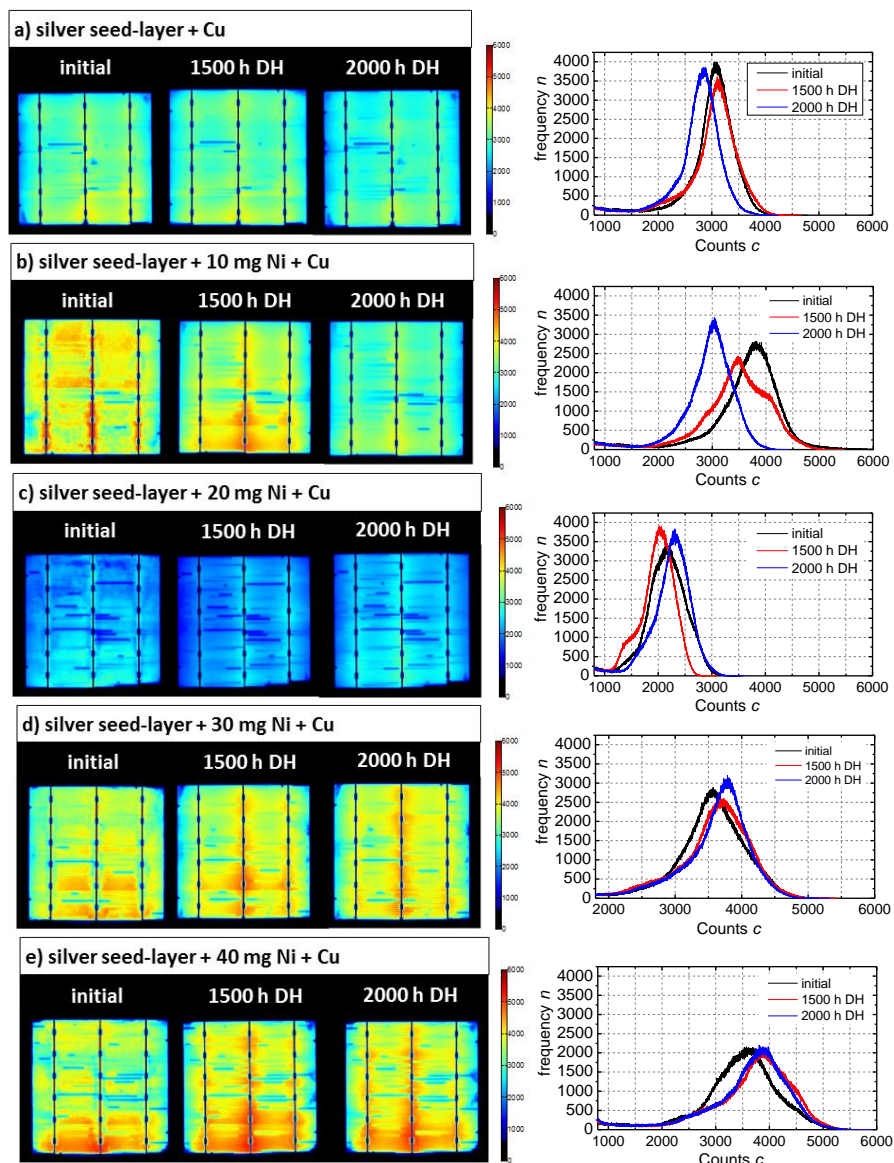


Fig. 8.13: Electroluminescence images of the single-cell modules with encapsulated cells featuring different nickel diffusion barrier masses before and after 1500 h and 2000 h of damp heat test with histogram respectively

8.3.3 Comparison of cell and module degradation

Only for the cell and module configuration produced without nickel diffusion barrier the degradation on cell and on module level can be compared, as this is the only group that showed degradation on module level (compare Fig. 8.12). To clarify if the degradation results achieved at cell level may predict the degradation measured on module level after 1500 h damp heat test, the cell's degradation time needed to reach a pFF loss of 0.25%_{rel.} is plotted in an Arrhenius plot (Fig. 8.14 black diamonds) with a linear fit through the measured data. The measured module degradation reached in the climate chamber at a constant temperature load of 85°C corresponding to the FF loss of 0.25%_{rel.} (Fig. 8.14 red circle) shows good accordance with the linear fit calculated from the cell results.

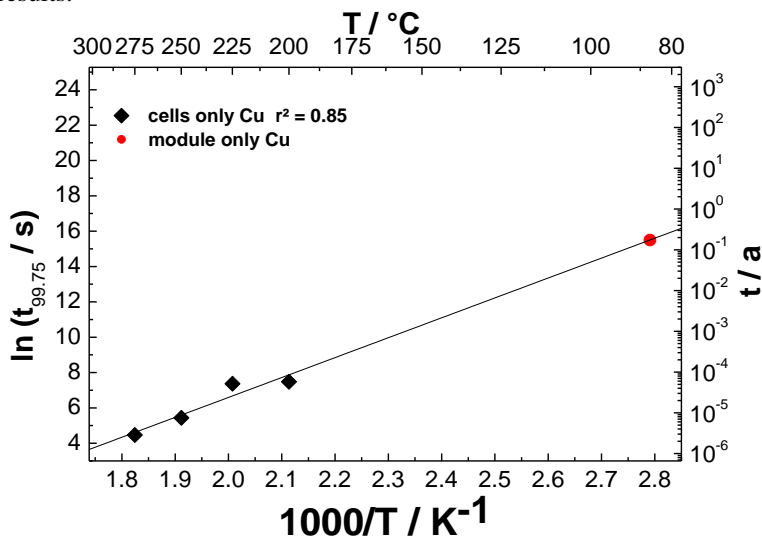


Fig. 8.14: Arrhenius plot of cell degradation data (black diamonds) with corresponding fit (only for cell data) and module degradation data (red circle) from temperature/time pairs leading to a loss in pFF for cells and FF for modules of 0.25%_{rel.}

It has to be pointed out that this comparison assumes that the degradation of the FF at module level traces back to degradation of the pFF of the encapsulated cell and not to degradation of the contacts, or other effects during module climate chamber testing. Such effects may occur, influencing the FF both positively and negatively. Additionally the experiment is restricted by statistics

because only one cell is used per experimental point. However, the results suggest the conclusion that the fast degradation at elevated temperatures on hotplates is at least suitable to give a first estimation for module degradation in the climate chamber. A standard test to evaluate copper metallization systems regarding degradation due to copper diffusion should be on cell level, because it is easier and faster than tests on module level, which are complex, slow and expensive.

In the next chapter, parameters which influence the cell degradation besides the effectiveness of the nickel diffusion barrier are presented.

8.4 Influencing parameters for cell degradation

The results presented in this chapter reveal that besides the effectiveness of the nickel diffusion barrier, the used seed-layer and the firing temperature influence the cell degradation.

8.4.1 Influence of the used seed-layer

For another set of degradation experiments, cells with different printed Ag-seed-layers out of paste 1, paste 3 and paste 4, already shown in chapter 6, were used. Fig. 8.15 shows the average contact finger geometry after firing of the three used seed-layers. The contact finger height varies from 1 μm (paste 1) to 9 μm (paste 3). The contact finger width varies from 47 μm (paste 1) to 100 μm (paste 4). The different seed-layer geometries were achieved by using two different pastes. Paste 1 is a commercial fine line silver paste developed to print fine seed-layers. Paste 3 and paste 4 are silver front side pastes based on the same recipe (different from paste 1) varied only in the resulting viscosity. Paste 3 feature double the viscosity than paste 4 (17.6 Pa s compared to 8.5 Pa s)⁸. These parameters lead to different seed-layer geometries after screen-printing and firing. Table 8.1 shows the different resulting metallized contact finger areas due to the different contact finger geometries shown in Fig. 8.15 and the metallized busbar area for each paste. The busbar area for paste 3 and 4 is smaller because a segmented busbar design was used. Paste 1 was printed with a standard 1.5 mm busbar design.

⁸ Measured at a shear rate of 100 s⁻¹

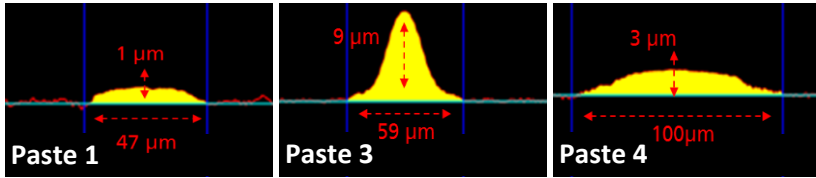


Fig. 8.15: Contact finger profiles of the different used seed-layers after screen-printing and firing. A 47 μm fine and 1 μm thin seed-layer (paste 1), a 9 μm high and 59 μm wide seed-layer (paste 3), and a 3 μm thin and 100 μm wide seed-layer (paste 4)

Table 8.1: Metallized area at the front side of the cells for the used Ag pastes.

Paste	Contact finger area / mm^2	Busbar area / mm^2	Total metallized area / mm^2	Total metallized area / %	Ni-layer at contact fingers ⁹ / μm	Ni-layer at busbar ⁹ / μm
1	660	664	1324	5.4	~1.2-1.5	~0.2
3	830	249	1079	4.4	~2	~0.5-0.6
4	1404	249	1653	6.8	~1.4	~0.1-0.3

The cells were plated with nickel and copper and treated on hotplates as described in section 8.3. Fig. 8.16 shows the resulting Arrhenius plot for temperature/time pairs leading to a pFF loss of 5%_{rel.} at the different used temperatures with a linear fit through the measured data.

The cells made on the basis of different seed-layers show different degradation behaviours. The seed-layer that results in the largest metallized area (paste 4) shows the fastest degradation (red circles). This is probably due to the fact that in the case of paste 4 the same nickel mass was distributed over a bigger metallized area compared to paste 3 (blue triangles). The resulting average nickel layer thickness is smaller (compare Table 8.1) and the probability to get weak points in the nickel diffusion barrier or non-plated areas is higher. Paste 1 (green diamonds) shows the best long term stability although the metallized area is bigger than the one of paste 3. Only the metallized finger area corresponds to the

⁹ Measured in the middle of the cell which represents the spot with the lowest Ni deposition at the contact fingers and at the busbars (compare section 8.6).

degradation result, which may indicate a particularly strong degradation mechanism due to an insufficiently thick barrier at the fingers. Another possible explanation lies in the effect due to differences in the paste formulation.

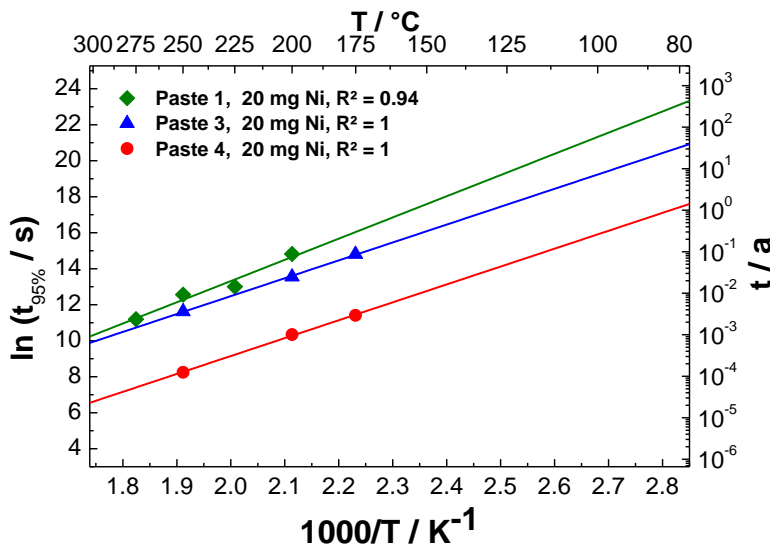


Fig. 8.16: Arrhenius plot for temperature/time pairs leading to a pFF loss of 5%_{rel.} for cells plated with nickel (20 mg) and copper on top of Ag-seed-layers with different geometries: paste 1 (green diamonds), paste 3 (blue triangles), paste 4 (red circles)

Additionally the comparison of paste 1 and 3 shows that printing a high silver seed-layer does not necessarily lead to better long term stability results. Although paste 3 offers a longer average diffusion distance for copper (to reach the cell) than paste 1, due to the higher seed-layer geometry, the long term stability results of paste 1 are better. This means that fine, thin silver seed-layers are not only beneficial to save silver and to reduce shading but also to achieve good long term stability results.

8.4.2 Influence of the firing temperature

Cells based on a seed-layer of paste 3 and paste 4 were fired at 860°C, 890°C and 920°C and plated as described before with nickel masses of 5 mg, 10 mg and 20 mg per cell. Fig. 8.17 shows the Arrhenius plots for temperature/time pairs leading to a pFF loss of 5%_{rel.}. For cells plated with 5 mg nickel (green circles), 10 mg nickel (red triangles) and 20 mg nickel (blue squares) for paste 3 (upper

diagram) and paste 4 (diagram below) and all used firing temperatures. Firstly, it is noticeable that all results show a general Arrhenius type trend, which indicates the validity of the method also with a larger set of data. However, the data points for the different groups show clear deviations and the regression indicator R^2 indices are below 94%, which restricts the prediction quality of the linear fit. Fig. 8.18 and Fig. 8.19 show the Arrhenius plots for the same data ordered by firing temperature for every nickel mass for paste 3 (Fig. 8.18 a-c) and for paste 4 (Fig. 8.19 a-c). Every diagram in Fig. 8.18 and Fig. 8.19 corresponds to one plated nickel mass: a) 5 mg Ni, b) 10 mg Ni, and c) 20 mg Ni. The unfilled symbols represent the degradation results of the cells fired at a set peak temperature of 920°C, the diagonally crossed symbols show the degradation results of the cells fired at a set peak temperature of 890°C and the filled symbols represent the degradation results of the cells fired at a set-peak temperature of 860°C with linear fit respectively. For paste 3 the regression indicators of all the nine linear fits are $\geq 93\%$ with two exceptions. For paste 4 the regression indicators of the linear fits are $>96\%$ with one exception. This improvement of the regression indicators for most of the groups, shows despite of the restricted statistics (only one cell per data point), an indication that the deviation observed in Fig. 8.17 traces back mainly to the different firing temperatures used in the experiment.

For paste 3 the graphs for 5 mg plated Ni (Fig. 8.18 a) and 20 mg plated Ni (Fig. 8.18 c) show the fastest degradation for cells fired at 920°C and the slowest degradation for the cells fired at 860°C. For paste 4 this trend can be observed for all plated nickel masses (Fig. 8.19 a-c). This is probably due to a larger opened silicon nitride area under the metal contacts for higher firing temperatures. If copper penetrates the nickel diffusion barrier, the possibility to diffuse into the cell is higher for a larger opening fraction in the silicon nitride under the contacts. The trend is particularly strong for cells with fast degradation (paste 4 all nickel masses and paste 3 with 5 mg Ni).

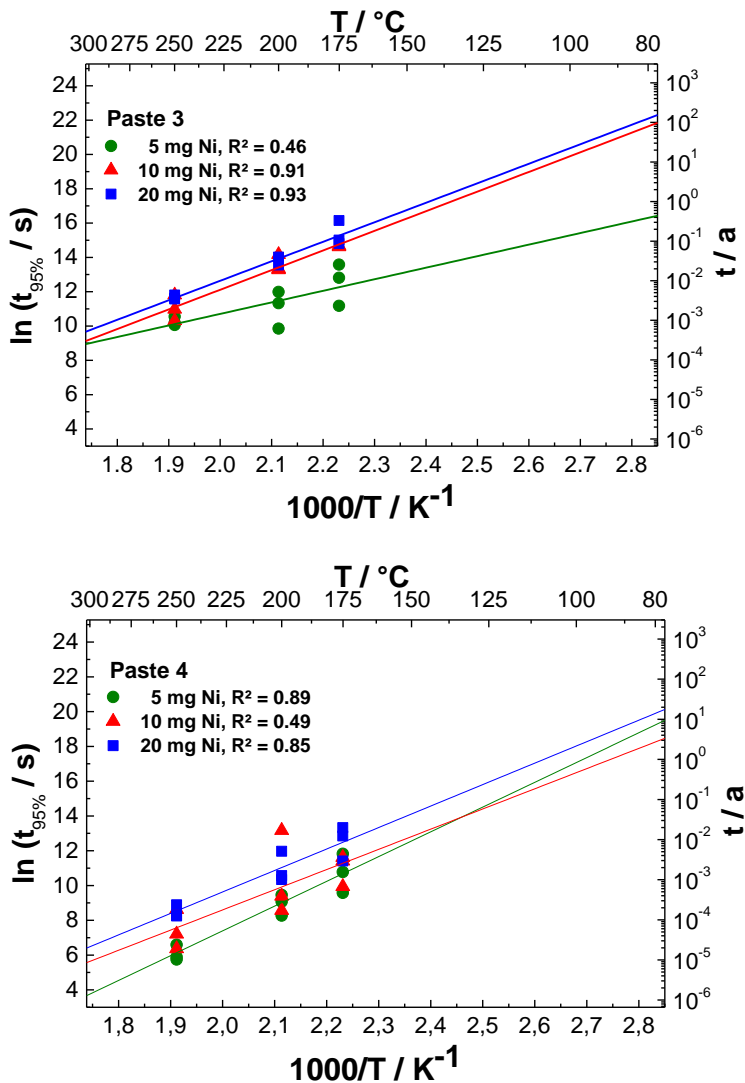


Fig. 8.17: Arrhenius plot for temperature/time pairs leading to a *pFF* degradation of 5%_{rel.} for cells with seed-layer paste 2 (upper diagram) and paste 3 (lower diagram), plated with 5 mg nickel (green circles), 10 mg nickel (red triangles) and 20 mg nickel (blue squares). Copper and silver plating were constant. The three data points for each measurement represent cells fired at different temperatures.

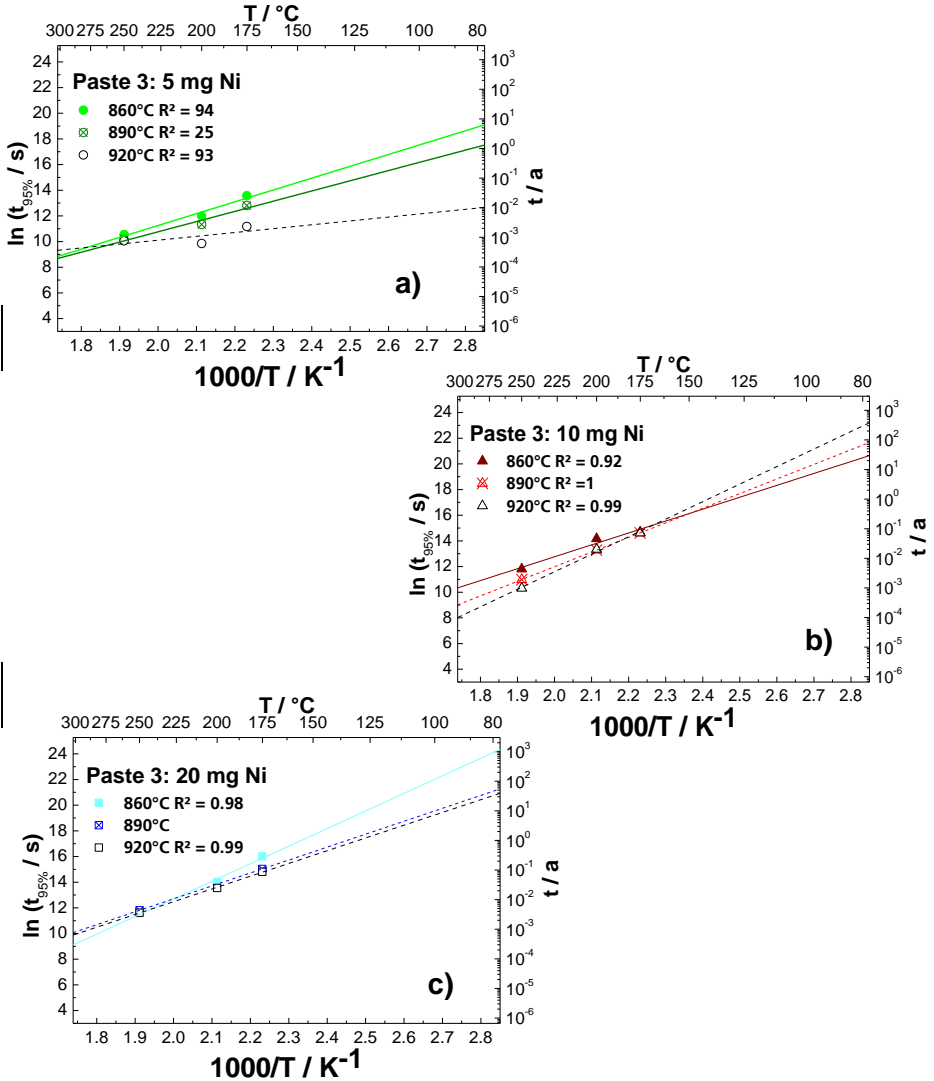


Fig. 8.18: Arrhenius plots for temperature/time pairs at a pFF degradation of 5%_{rel.} for cells with seed-layer paste 2 and different firing temperatures, plated with 5 mg nickel (a green data), 10 mg nickel (b red data) and 20 mg nickel (c blue data). The unfilled symbols correspond to the cells fired at 920°C, the diagonally crossed symbols represent the cells fired at 890°C and the filled symbols correspond to the cells fired at 860°C.

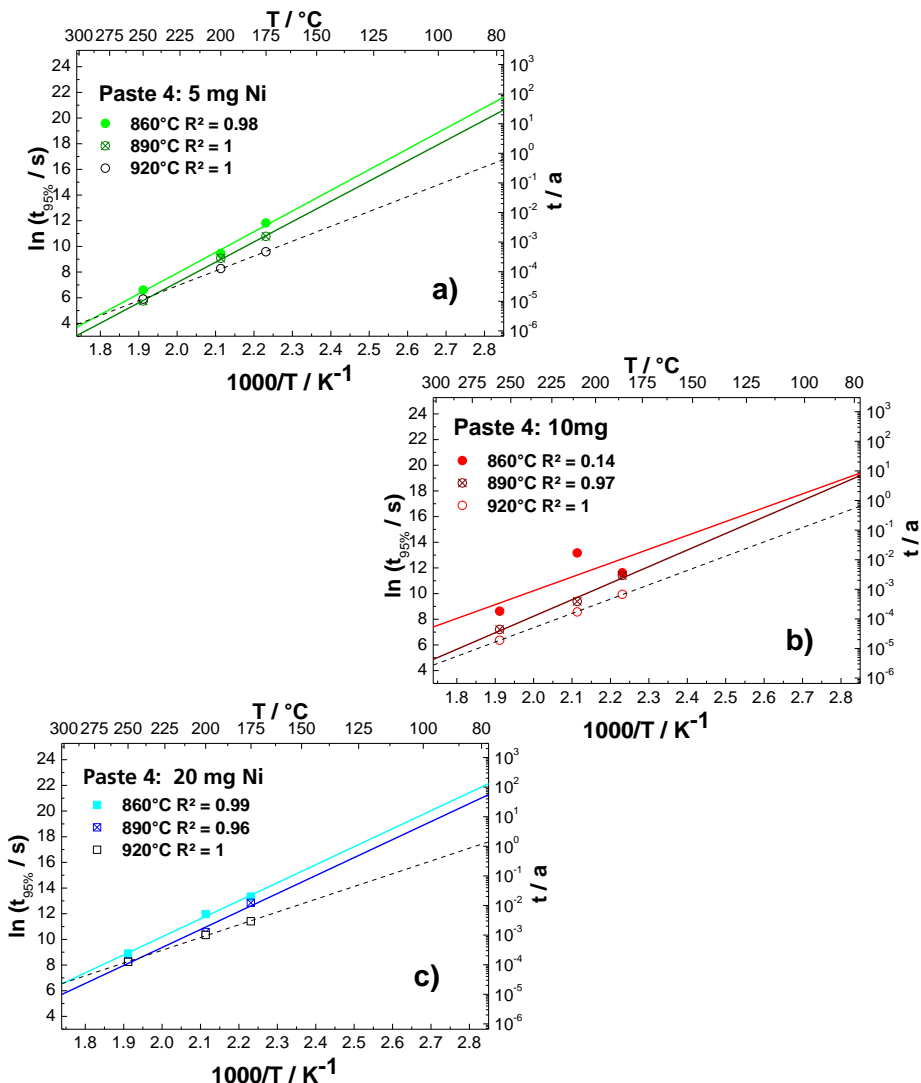


Fig. 8.19: Arrhenius plots for temperature/time pairs leading to a pFF degradation of 5%_{rel.} for cells with seed-layer paste 3 and different firing temperatures, plated with 5 mg nickel (a), 10 mg nickel (b) and 20 mg nickel (c). The unfilled symbols correspond to the cells fired at 920°C, the diagonally crossed symbols represent the cells fired at 890°C and the filled symbols correspond to the cells fired at 860°C.

Analysing the cell degradation of solar cells with a copper front side metallization based on different silver seed-layers the results indicate that besides the effectiveness of the nickel diffusion barrier the cell degradation depends on the used seed-layer and the firing temperature. Comparing cells with identical nickel masses, the seed-layer generating the largest metallized area shows the fastest degradation. This means aside from the effect on silver consumption and shading, fine seed-layers are also beneficial for long term stability. Despite reports about inhomogeneous plating on wide busbars [123], relatively thin diffusion barriers at this position do not necessarily lead to fast degradation. Possible explanations for this behaviour (paste 1 in this work) are a suitable paste composition, or a stronger effect of finger positions on long term stability as compared to the busbar. Comparing different firing temperatures the results show that high firing temperatures lead to faster cell degradation. Most probably this is due to a bigger opened silicon nitride fraction under the metallization.

8.5 Challenges for nickel plating on screen-printed silver seed-layers

The conditions for plated barrier layers to work effectively have been discussed in the last section. A more detailed analysis regarding the reasons for the observed behaviour is presented in the following section. The impact of the plated nickel mass on the performance durability under thermal stress was clearly demonstrated. As the nickel layer thickness obviously impacts the degradation behaviour, the nickel distribution on the cell with the used process becomes of great interest. A homogenous growth of nickel on the screen-printed silver seed-layer is important to achieve a dense diffusion barrier by depositing as less nickel as possible. To evaluate possible difficult spots where the deposition is hindered in the beginning of the plating process a SEM analysis of the contact microstructure following different nickel plating times were performed. The identification of potential weak spots for nickel deposition can give hints for the production of seed-layers, which can be plated homogeneously.

8.5.1 Distribution of plated nickel on screen-printed silver contacts

To evaluate the distribution of the nickel deposition on the screen-printed silver seed-layer, a nickel plating time variation was done using the Watts-type nickel

electrolyte introduced in table 5.1 and the single busbar precursors introduced in section 5.2.1. The light induced lab scale plating set up described in section 5.1.1 was used with a backside potential of -0.7 V between the cell backside and the nickel anode. The plating results were evaluated with SEM top-view and cross-section images to analyse which part of the contacts is plated preferential and to elucidate the lateral growth of the nickel layer. Fig. 8.20 shows top view SEM images of a screen-printed silver busbar before nickel plating (a), after 5 seconds of nickel plating (b), after 15 seconds of nickel plating (c) and after 60 seconds of nickel plating (d).

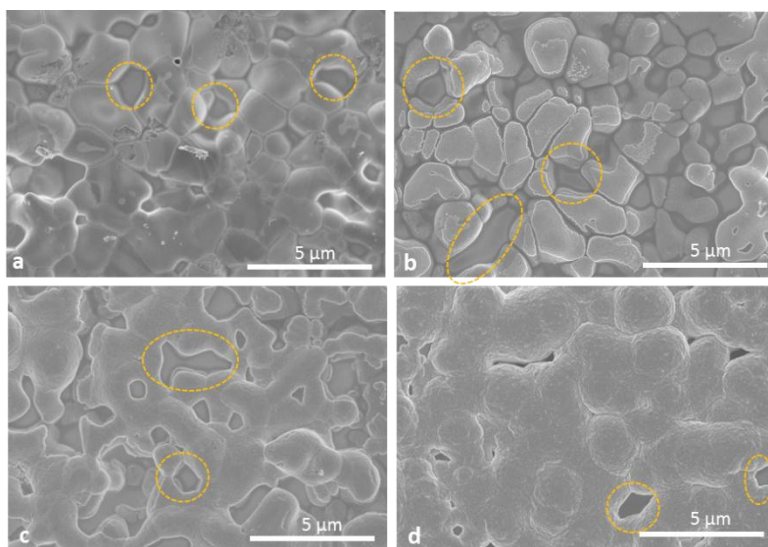


Fig. 8.20: SEM top view images of a busbar contact. Before nickel plating (a) after 5 seconds of nickel plating (b) after 15 seconds of nickel plating (c) and after 60 seconds of nickel plating (d). Areas covered with glass are marked with dashed circles.

Already after 5 seconds, the plated nickel layer is clearly visible as light coating on the silver surface (Fig. 8.20 a). After one minute the nickel layer grows in thickness and covers nearly the entire surface (Fig. 8.20 d). Besides the silver grains, glass areas can be observed at the contact surface with a diameter of 1 to 4 μm (marked with dashed circles). At the glass covered areas, no direct nickel growth can be observed due to the lower conductivity and therefore a lower current density compared to the adjacent silver surface. Additionally

adherence would probably be very poor if plating would be possible on these areas. These parts of the contacts have to be closed by lateral growth of the nickel layer. The bigger the diameter of these glass particles at the surface of the silver contacts the more nickel is needed to close the diffusion barrier at such spots. Even after one minute of plating (Fig. 8.20 d) some glass areas show openings in the nickel layer.

Fig. 8.21 shows SEM cross-section images of the nickel layer and the silver busbar underneath after one minute of nickel plating. Some small glass parts at the contact surface ($\sim 0.8 \mu\text{m}$) are already closed by lateral nickel growth (Fig. 8.21 b) but upon some big glass parts ($\sim 2 \mu\text{m}$) the nickel layer is not closed (Fig. 8.21 a).

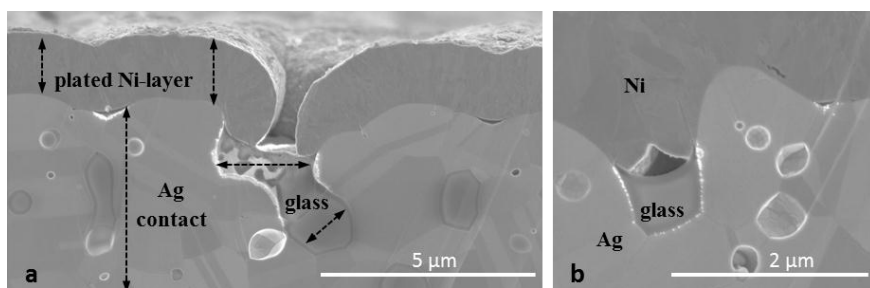


Fig. 8.21: SEM cross-section images of glass areas at the busbar surface after 60 seconds of nickel plating. The bigger ones are not closed by the lateral growth of the nickel layer (a), the smaller ones are closed by the nickel layer (b).

Also after 2 min. Ni plating none covered glass parts were observed. These parts represent potential weak points in the diffusion barrier because copper can be deposited in the openings in the direct vicinity to the glass surface and may migrate through the silver into the cell.

The development of seed-layer pastes should aim at the reduction of glass parts at the contact surface to reduce the appearance of such weak spots. Adding surfactants to the paste or using smaller glass particles might promote the melting and therefore the percolation of the glass to the silicon surface.

Fig. 8.22 shows the top-view SEM image of a contact plated with nickel for 20 seconds. Preferentially plated areas where the nickel layer is nearly closed (Fig. 8.22 middle) and less plated areas (marked with yellow dashed lines) can be observed. These differences in the early stages of the plating process were observed to correlate with height differences of the screen-printed contact.

Higher areas show more plating due to the higher current density than lower parts. Additionally lower laying parts of the metallization show a more comprehensive glass covering because the glass preferentially flows there during the firing process. This would intensify the inhomogeneous nickel distribution after plating. To reduce this difference more homogeneously printed contacts are beneficial.

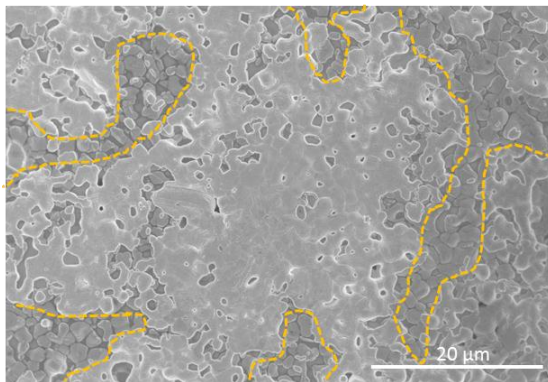


Fig. 8.22: SEM top view image of a silver contact plated with nickel for 20 seconds. Preferentially plated areas (middle of the image) and less plated areas (marked with yellow dashed lines) can be found.

8.5.2 Plating at the edge zones of screen-printed silver contacts

The edge zones of screen-printed silver contact fingers and busbars were analysed regarding the coverage of nickel. Standard solar cell precursors corresponding to section 5.5 with seed-layer paste 1 were used. Fig. 8.23 shows the edge zone of a contact finger after 2 minutes of nickel plating. The silver seed-layer is completely covered with the plated nickel diffusion barrier; no open positions can be observed where the subsequently plated copper would be plated directly on the seed-layer.

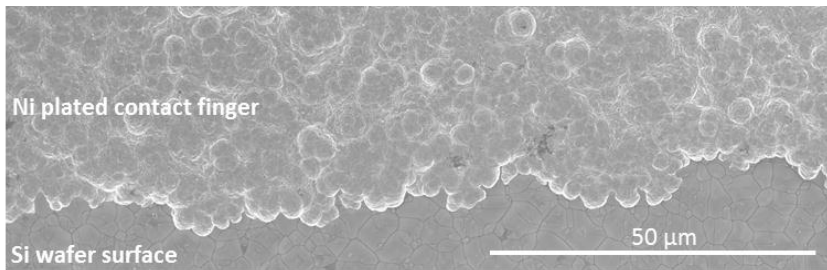


Fig. 8.23: SEM top view image of the edge zone of a Ni plated contact finger. No non-plated areas can be observed, the seed-layer is completely covered by the plated nickel layer.

Fig. 8.24 shows the edge zone of a busbar after 2 minutes of nickel plating (a). Due to less plating at the busbars (compare also section 8.6) non-plated pyramids can be observed (b). At these spots, glass has already etched the SiN_x layer partly or fully and copper could be plated directly on the possibly opened or aggrieved silicon nitride layer. This is another potential weak point in the metallization architecture. The printing of slightly higher busbars which cover the pyramids at the edges completely with improved edge definition would be beneficial.

The difference in the plated Ni mass between contact busbars (less plating) and contact fingers (pronounced plating) indicated by the microstructure analysis can potentially also be improved by adaptations of the nickel plating process. This is analysed in the following section based on an evaluation of the Ni distribution over the whole cell.

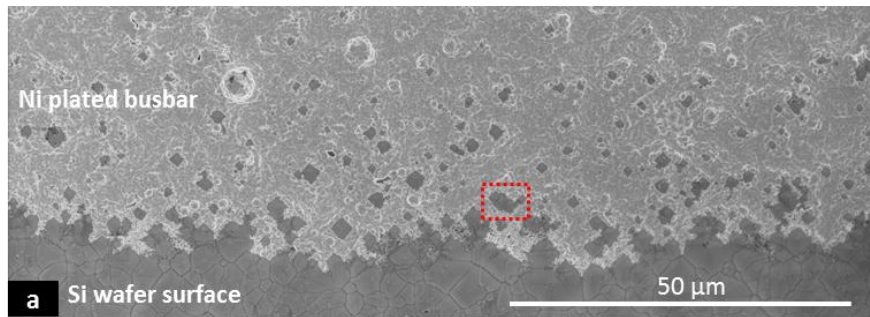
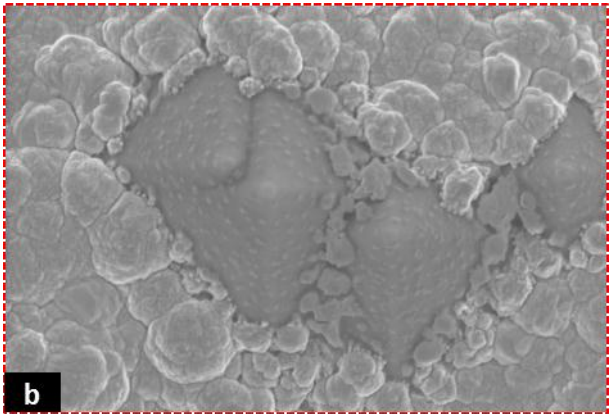


Fig. 8.24: SEM top-view image of the edge zone of a Ni plated busbar (a). Single non-plated pyramids, possibly wetted by glass, rise over the plated Ni layer, detail picture (b)



8.6 Homogeneity of the plated nickel diffusion barrier

The distribution of the electrochemical nickel deposition over the entire cell has a considerable influence of the tightness of the nickel diffusion barrier and therefore on the resulting long term stability of the cell. In this chapter the homogeneity of the plated nickel diffusion barrier is investigated using a confocal laser microscope (compare section 4.1.1) for analysis of deposition distribution of different nickel masses plated in the inline tool (compare section 5.1.2). The height of contact fingers and busbars was measured using average profiles evaluated by the microscope over a contact structure length of 640 μm . These measurements were done before and after Ni plating at identical selected positions on the cell. For this experiment cells with the 1 μm thin, screen-printed seed-layer of paste 1 (compare section 6) were used. Fig. 8.25 shows the measured positions at the contact fingers (1-12) and at the busbars (a-d) located in the upper left quarter of the cell.

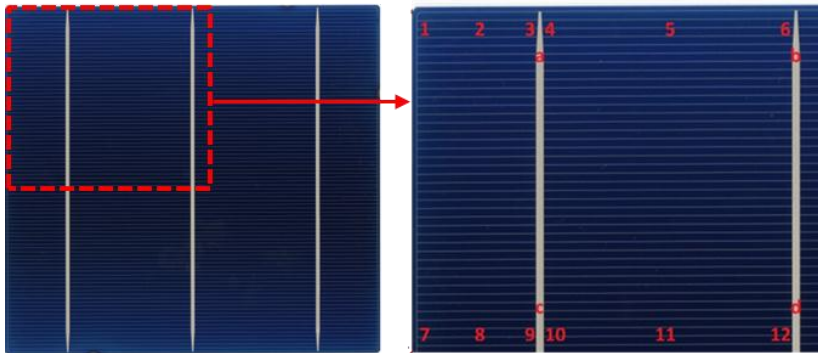


Fig. 8.25: Positions for thickness measurement of the plated nickel layer to evaluate the distribution of the nickel deposition achieved in the inline tools on the contact fingers (position 1-12) and the busbars (position a-d)

Due to the symmetrical geometry of the cell metallization the results of one quarter of the cell allow conclusions of the general nickel distribution. A similar experiment was done in [123] to investigate the distribution of silver plating on solar cells. Fig. 8.26 shows the measured height profiles at the contact finger positions 1 (a), 5 (b), 7 (c) and 11 (d). It becomes clear that the plated nickel layer thickness is the highest for position 1; $\sim 10 \mu\text{m}$ for 40 mg plated Ni due to the position near the wafer edges. The nickel layer thickness is slightly lower for

position 5 ($\sim 8 \mu\text{m}$ for 40 mg plated Ni) and 7 ($\sim 7 \mu\text{m}$ for 40 mg plated Ni) whereas position 11 in the middle of the cell shows the lowest nickel layer thickness ($5 \mu\text{m}$ for 40 mg plated Ni). This means for the contact fingers nickel deposition is pronounced at the edges of the wafer.

Fig. 8.27 shows the measured height profiles at the busbar positions a (a), and d (b). Compared with the contact fingers the busbar positions show considerably less plated nickel. The layer thickness for 40 mg plated Ni is around $0.6\text{--}0.8 \mu\text{m}$. Position a near the wafer edge shows a slightly higher plated nickel layer than position d in the middle of the wafer.

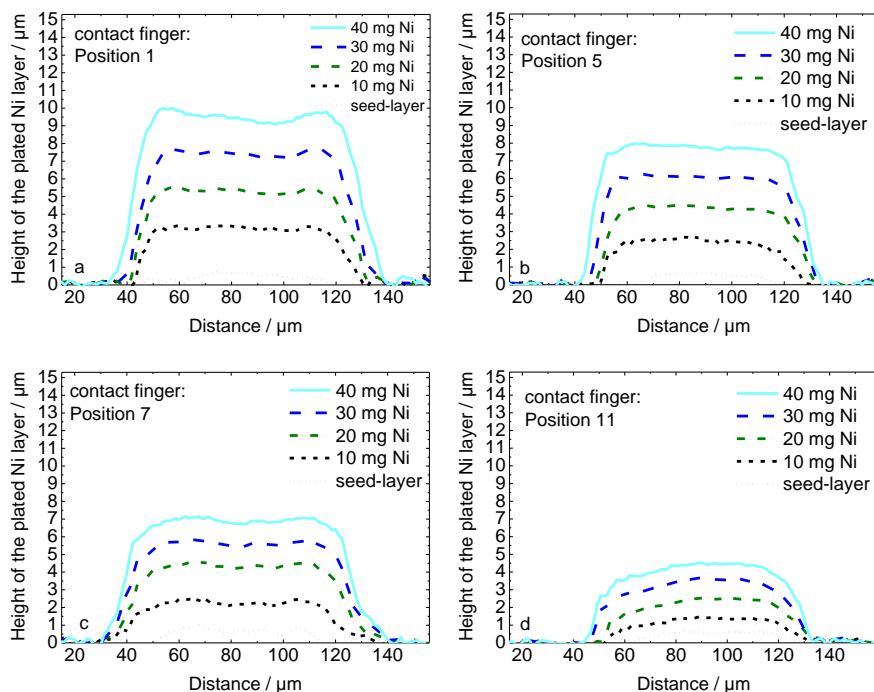


Fig. 8.26: Measured height profile of the contact finger at position 1 (a), at position 5 (b), at position 7 (c) and at position 11 (d) for the seed-layer (red dotted curve), 10 mg Ni (black short dashed curve), 20 mg Ni (green dashed and dotted curve), 30 mg Ni (blue long dashed curve) and 40 mg Ni (turquoise continuous curve) deposited in the inline tool

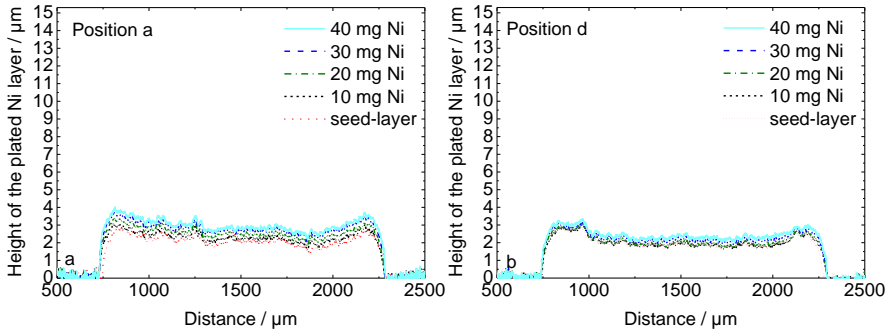


Fig. 8.27: Measured height profile of the busbar at position a (a) and position d (b) before nickel plating (seed-layer, red dotted curve), after 10 mg (black short dashed curve), 20 mg (green dashed and dotted curve), 30 mg (blue long dashed curve), and 40 mg (turquoise continuous curve) nickel deposition in the inline tool

The height evaluation of all measured positions on the cell without consideration of the seed-layer is shown in Fig. 8.28. A systematic difference in the distribution of the plated nickel height can be observed at the different cell areas. Less deposition can be observed in the middle of the cell. At position 5 the nickel layer after 40 mg nickel deposition is $\sim 2 \mu\text{m}$ higher than the nickel layer at position 11. The comparison of position 1 and 7 shows a difference of $2.7 \mu\text{m}$ in favour of position 1. At the finger positions in direct vicinity of the busbars ($\sim 600 \mu\text{m}$ distance, positions 3, 4, 6, 9, 10 and 12) the deposited nickel layer is $\sim 1.3 \mu\text{m}$ smaller than the total average of the contact fingers.

The most obvious effect is the difference between the nickel deposition at the busbar positions and the contact fingers. The average nickel thickness at the busbar after deposition of 40 mg nickel is $\sim 0.8 \mu\text{m}$, the average thickness at the contact fingers is $4.5 \mu\text{m}$ this represents a difference of $3.7 \mu\text{m}$.

Fig. 8.29 shows the nickel distribution by percentage at the measured positions on the cell relative to the average nickel distribution on the contact fingers. The plated nickel diffusion barrier at the busbars shows $\sim 10\%$ of the average contact finger height.

It becomes clear that the plated nickel mass is not homogeneously distributed over the wafer. Due to the bigger shading area under the busbars, which results in a lower current density during the plating process the Ni plating and therefore the plated nickel layer thickness at busbars is considerably smaller. In case of a

plated diffusion barrier this imbalance of the metal distribution bears the risk of weak spots in the nickel layer at the busbars.

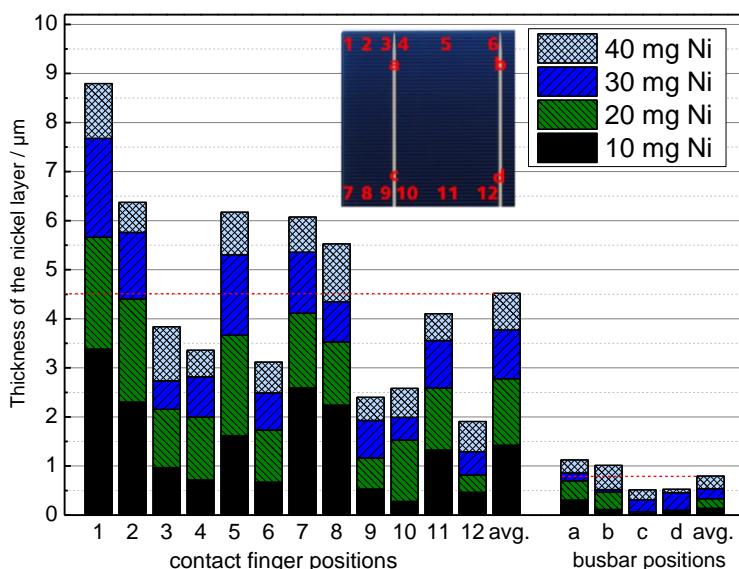


Fig. 8.28: Measured nickel layer thickness at the contact finger positions 1-12 and the busbar positions a-d for 10 mg, 20 mg, 30 mg, and 40 mg nickel deposition in the inline tool. The red horizontal lines represent average values for contact fingers (positions 1-12) or busbars (positions a-d) after 40 mg nickel deposition.

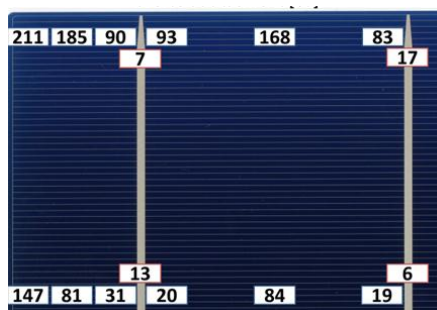


Fig. 8.29: Nickel distribution by percentage at the measured positions on the cell relative to the average nickel deposition on the contact fingers

To verify this result SEM top view images of contact finger position 11 and busbar position d were made and are shown in Fig. 8.30 for every plated nickel mass.

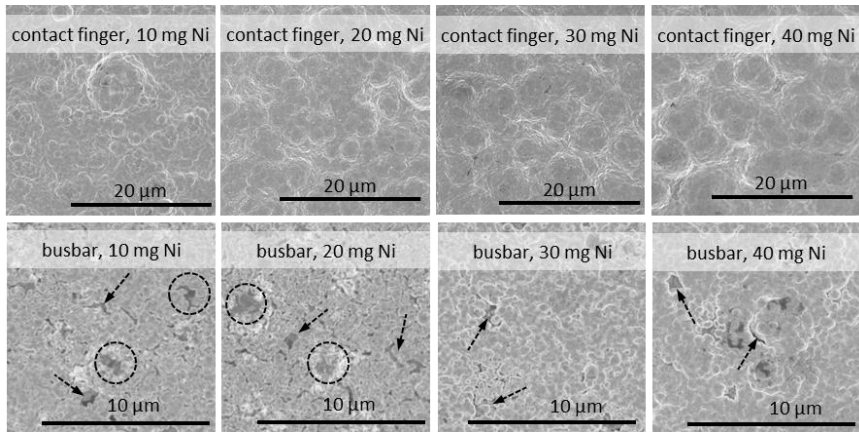


Fig. 8.30: SEM top view images of the contact finger position 11 (upper line) and the busbar position d (line below) for 10 mg, 20 mg, 30 mg, and 40 mg nickel. On the finger positions a dense and comprehensive nickel layer can be observed for every plated nickel mass whereas at the busbar positions none plated areas and gaps in the nickel layer can be observed (marked with dashed circles and arrows).

On the finger positions (upper line) a dense and comprehensive nickel layer can be observed for every plated nickel mass whereas at the busbar positions (line below), non-plated areas and gaps in the nickel layer can be observed (marked with dashed circles and arrows). This confirms that the thin measured nickel layers at the busbars corresponds to more frequent appearance of potential weak spots in the plated nickel diffusion barrier.

This is due to the current density, which is considerably smaller at the busbar than at the contact fingers in the plating process. Two effects play a role here: the bigger shading fraction of the busbars, and the unfavourable ratio of the current collecting area to deposition area. The unequal metal distribution for light induced plating is a known effect and was observed in the case of silver plating on printed seed-layers [123]. For silver plating this does not cause problems because silver is plated to improve the conductivity of the metallization. The insufficient conductivity due to less plating at the busbars is compensated by the soldered ribbon. However, the nickel layer works as diffusion barrier and is not deposited to enhance the conductivity of the metallization meaning that a dense

layer is crucial for good long term stability. The decreased deposition at the busbar compared to the contact fingers represents a potential weak spot in the metallization architecture regarding the long term stability. To improve deposition homogeneity of the plated nickel different adaptations of the plating process and adjustments of the plating tools were evaluated in the next chapter to check if the nickel distribution at the solar cell can be improved.

8.7 Improvement of the nickel homogeneity

For these general studies the experimental lab scale plating tool (compare section 5.1.1) and the Watts-type nickel electrolyte (compare table 5.1) were used. The nickel deposition on the cells was compared with the nickel deposition achieved in the inline plating tool (compare section 5.1.2). Precursor cells according to section 5.5 with a screen-printed seed-layer using paste 1 were used for the experiments.

The position and geometry of the nickel anodes in the process were varied, electrical shielding for the contact fingers and pulse-plating were evaluated.

Fig. 8.31 shows a schematic drawing of the installation of the standard plating setup in the lab scale tool with an anode basket filled with nickel pellets, located behind the solar cell (a) and the developed setup using three nickel wires as anode located in front of the cell, aligned to the busbars to avoid shading of the active cell area, with a distance of ~2 cm (b). With this setup an additional electrochemical shield of transparent acrylic glass (2 mm) covering the contact finger areas, with openings in the dimensions of the busbars, can be positioned between the anode and the cell. Cell, anode and shield were fixed with a holder (not shown in Fig. 8.31) and totally immersed in the nickel electrolyte. The illumination was realized from the front side using LEDs. Illumination and electrical parameters (700 mA for 80 seconds, light induced plating setup) were kept constant for all experiments to analyse the influence of the anode setup, the shielding and the pulse plating on the distribution of the nickel deposition. The wire anode modifies the direction and density of the electric field lines between the cathode (cell front side metallization) and the anode (nickel wire or basket with nickel pellets), indicated with red lines in Fig. 8.31 a and b.

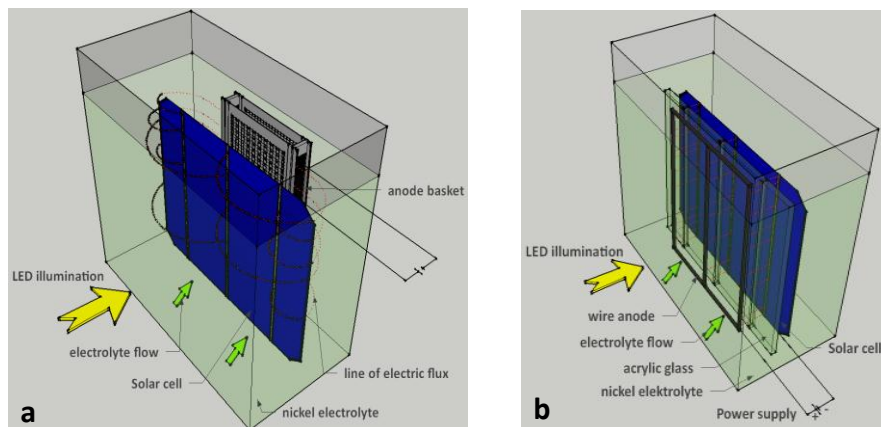


Fig. 8.31: Schematic drawing of the lab scale nickel plating setup with different anode geometries. Green arrows mark the approaching electrolyte flow on the cell the yellow arrows mark the direction of illumination. The standard adjustment using an anode basket with nickel pellets inside located behind the solar cell (a) and the developed anode setup using three nickel wires (1.5 mm diameter) as anode located before the cell aligned to the busbars (b) with additional option of electrochemical shielding with an acrylic glass plate (2 mm)

In the constellation with the anode basket behind the cell the electric field lines have to curve outward around the cell, to the anode. In the constellation with the anode wire in front of the cell the direct adverse location of anode and cathode leads to a more homogenous dispersion of the electric field lines with the smallest distance between anode and the busbars, which is the position where more nickel deposition is needed.

Fig. 8.32 shows the used pulse sequence for nickel pulse plating experiments. An anodic pulse with 700 mA and a duration of 10 ms was followed by a cathodic pulse of -700 mA and a duration of 60 ms. Between the pulses an off time of 200 ms was used. The light source was also pulsed delivering a constant illumination during the active parts of the voltage pulse and no illumination during the off time. 2000 repetitions of the pulse sequence were performed.

The electrochemical shield of acrylic glass can block or rather deflect the electric field lines at the contact fingers and redirect them closer to the busbars. This potentially leads to a better distribution of the nickel deposition in favour of the busbars.

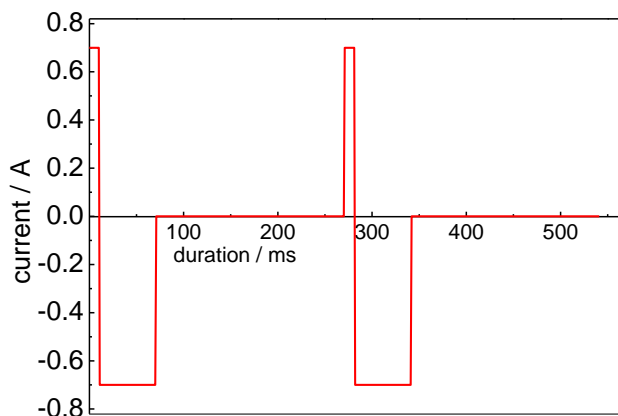


Fig. 8.32: Two full cycles of the used anodic and cathodic pulse sequence for nickel plating; anodic pulse: 10 ms/700 mA; cathodic pulse: 60 ms/-700 mA; off time 200 ms

Fig. 8.33 shows the relative nickel deposition achieved at the four measured busbar positions (a-d) relative to the respective average nickel deposition at the contact fingers for the different tested process adaptations. Two cells were processed for every experimental point and the nickel depositions were evaluated using the confocal laser microscope (compare section 4.1.1). Each mark in the diagram represents the measured relative nickel thickness for one cell at the respective position. The applied process adaptations show a rising relative nickel deposition at the busbars compared to the standard deposition in the inline tool (red stars) and the lab scale setup with anode basket (black circles), and therefore an improvement of the nickel distribution. The nickel deposition in the inline tools generates the thinnest nickel layer at the busbars. The nickel deposition in the lab scale set up using an anode basket is ~20% higher at the positions a, b and c and in the same range at position d. At position d in the middle of the cell, the nickel layer is less than 10% compared to the nickel layer at the contact fingers for all cases of conventional setups. The use of wire anodes raised the nickel deposition at position d to ~28%, which is more than a doubling. At the other positions also a deposition gain can be observed for the use of wire anodes. Using pulse plating and the electrochemical shielding in combination with the wire anode leads to an increase of nickel deposition of up to ~50% at position a, which is five times the nickel layer height deposited at the busbar in the inline tool under standard conditions.

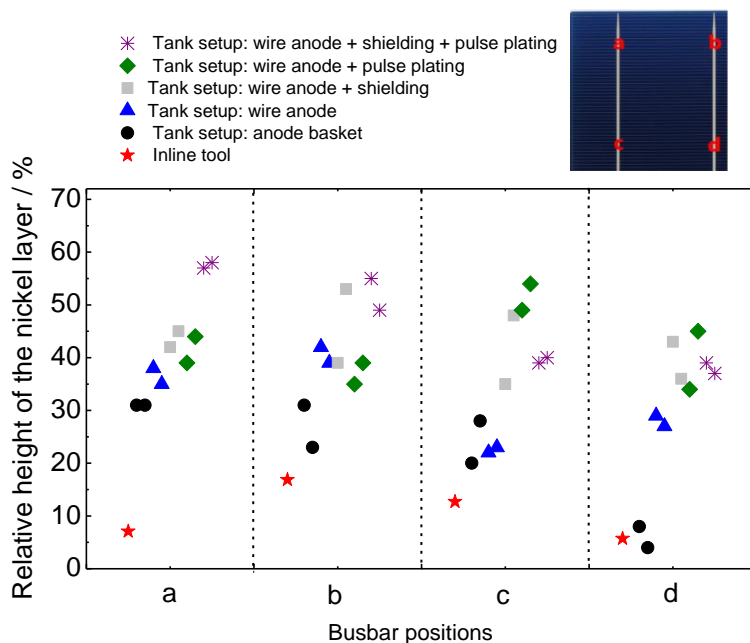


Fig. 8.33: Nickel deposition at the four busbar positions (a-d) relative to the average nickel deposition on the contact fingers for the deposition of 20 mg nickel in the inline tool (red stars) for the deposition in the lab scale setup with anode basket (black circles) with wire anodes (blue triangles) with wire anodes and shielding (grey foursquare), with wire anodes an pulse plating (grey diamonds) and with wire anodes shading and pulse plating (purple crosses)

At the other busbar positions the maximal nickel layer thickness increases due to the process adaption were ~40% (position b), ~45% (position c) and ~45% (position d) compared to the deposition in the inline tools. This means the tested adaptations: wire anode, pulsed plating and electrochemical shielding can improve nickel deposition homogeneity, which potentially improve long term stability and offers the possibility to reduce the nickel plating process duration. This will have positive influence on the resulting contact adhesion.

The tested variations from the standard plating conditions in the inline tool show the potential of homogeneity improvement over the cell, and ways to realize these in the inline tool are worthy to be considered. Further tests should be done for the pulse plating and the electrochemical shielding. In both cases the

conducted experiment was a proof of principle but not a complete evaluation of the methods. Shielding allows very sophisticated shaping of the field and has huge optimization potential. A bigger overlap of the shield at the edges of the cell, for example, may cause further suppression of the nickel deposition at the edges of the cell. In the case of pulse plating different pulse conditions offer the potential for even better results regarding the nickel distribution.

8.8 Chapter summary

In this chapter, a possible impact of copper diffusion on the electrical performance of silicon solar cells with a copper front side metallization based on screen-printed silver seed-layers was investigated.

The following key findings were achieved on p-type solar cells with 90 Ω phosphorus emitter. The findings expand the understanding of solar cell degradation due to copper migration:

- The cell degradation and thereby the copper migration was shown to depend on the *pFF*-measurement-frequency during thermal stress. More measurements and therefore more frequent cooling of the cell down to room temperature lead to significantly slower cell degradation (section 8.1). Measurement frequencies above 3.5 h do not show a significant influence of the degradation result. Probable mechanisms behind this phenomenon, such as copper out-diffusion to the surface, were discussed.
- Silicon nitride layers deposited by inline PECVD and inline sputtering avoid copper diffusion into the cell and act as diffusion barrier even after screen-printing or HF-dip pre-treatment (section 8.2).
- The investigation of the effectiveness of the nickel diffusion barrier on cell level revealed that 20 mg nickel (corresponding to a minimal nickel thickness of 0.2 μm) can be estimated to avoid long term stability issues in a normal module lifetime (section 8.3.1).
- The degradation of modules during damp heat test in the climate chamber (85°C, 85% r.h.) does not show significant degradation for cells with nickel diffusion barrier after 1500 h (section 8.3.2). Even the module without diffusion barrier passed the IEC criteria.
- The comparison of the slight degradation of the module without diffusion barrier with the related measured cell degradation showed good

accordance (section 8.3.3). This indicates that the used fast degradation method on cell level can predict module degradation at lower constant temperatures.

- Besides the effectiveness of the nickel diffusion barrier the cell degradation depends on the used seed-layer (section 8.4.1) and the firing temperatures (8.4.2).
- Challenges for nickel plating on screen-printed silver seed-layers regarding the aim of a homogenous and dense nickel diffusion barrier were identified (section 8.5). At glass areas on the contact surface (section 8.5.1) and at the edges of the busbar (section 8.5.2), nickel plating is severely limited which can cause weak spots in the plated nickel diffusion barrier. Small glass particles, an effective dissipation of the melted glass from the seed-layer surface and a defined busbar edge zone with less paste spreading are beneficial for a comprehensive plated nickel diffusion barrier.
- The homogeneity of the nickel distribution after plating on $156 \times 156 \text{ mm}^2$ cells showed considerable inhomogenities: about 80-90% less plating occurs at the busbars compared to the plating at the contact fingers (section 8.6). Changes in anode position and geometry, electrochemical shielding and pulsed plating were shown to be approaches with the potential to improve the nickel deposition homogeneity on solar cells significantly (section 8.7).

9 Acetic acid corrosion impact on printed solar cell contacts

The developed experimental procedures regarding contact corrosion by electrolytes obtained in chapter 7 and the resultant experiences were useful in the context of acetic acid corrosion of fully printed silver contacts. The results of the investigations are presented in this chapter.

Section 9.1 gives an introduction in the topic of damp heat induced degradation and shows what is published in literature regarding the corrosion phenomenon caused by acetic acid.

Different exposure experiments with fired solar cell contacts in acetic acid solutions with and without applied voltage were performed (section 9.2). The micro characteristics of the contact corrosion after acetic acid exposure were analysed by SEM (section 9.3), suspected electrochemical mechanisms were confirmed by chemical trace analysis (section 9.4), cyclic voltammetric stripping (section 9.5), an ethylene vinyl acetate incubation experiment (section 9.6) and the calculation of Pourbaix diagrams (section 9.7), which delivers insight in the underlying thermodynamics. Finally a model of the contact corrosion due to the interaction with acetic acid was elaborated based on the experimental findings (section 9.8). Section 9.9 gives a brief summary of the results presented in this chapter.

9.1 Introduction into damp heat induced degradation

The standard front side metallization of crystalline silicon solar cells, realized by screen-printing of silver containing pastes and high-temperature contact formation is known to exhibit weaknesses in long term stability tests. Especially after damp-heat testing in the climate chamber (85°C, 85% r. h.) according to IEC 61215 [54] a particular failure mechanism of the front side metallisation is described in literature [158], [159], [160], [161], [162]. Power loss of the modules, visible in electro-luminescence images as black regions spreading from the cell edges to the middle, is observed.

Fig. 9.1 a-b shows a electroluminescence image of encapsulated cell before (a) and after (b) 2500 h of damp heat test in the climate chamber published by Peike *et al.* in 2013 [162]. They further showed that this failure mechanism is due to a loss of the electrical contact between emitter and front side metallization

and suggested that the so called “Damp Heat Induced Degradation” (DHID) originates presumably from an attack of acetic acid on the glass frit inside the front side contact [162].

Fig. 9.1 c-e shows electroluminescence images of a full-size module after 1000 h (c), 2000 h (d) and 3000 h (e) of damp heat test published by Bogdanski *et al.* in 2011 [161]. They measured a decrease of the module output power due to climate chamber exposition of 1% (c), 4% (d) and 28% (e).

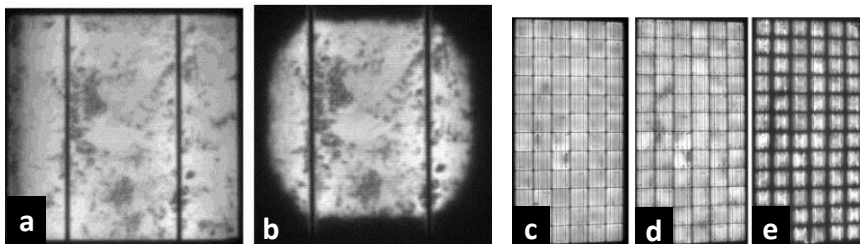


Fig. 9.1: Electroluminescence images of a laminated cell before (a) and after (b) 2500 h of damp heat test (85°C 85% r. h.) [162]. Electroluminescence images of a module after 1000 h (c), 2000 h (d) and 3000 h (e) of damp heat test (85°C, 85% r. h.) [161]

The standard module encapsulation material of crystalline silicon solar cells, ethylene-vinyl acetate (EVA), is known to degrade under acetic acid formation in the presence of humidity [163]. In the following sections the corrosion effects of screen-printed silver front side contacts induced by acetic acid are investigated in detail to clarify the exact region of failure in the contact, possible influencing factors and to elucidate the mechanism behind this behaviour.

9.2 Corrosion of screen-printed silver contacts due to the interaction with acetic acid

Solar cell samples were exposed to acetic acid solutions without applied voltage using concentrations of 1, 5, 10 and 50%. The pH ranged between 1.4 (for 50% acetic acid) and 2.75 (for 1% acetic acid). The exposure was executed for a duration was 45 minutes at 50°C using the procedure according to 5.2.2.

Exposure experiments with applied voltage were done with acetic acid concentrations of 0.1, 0.5, 1 and 5% for five minutes, while shining light on the cells and applying a potential of -0.7 V between the solar cell rear side and a nickel anode (light induced plating setup) according to section 5.2.3.

Subsequently the samples were soldered and peel-force tests were conducted (procedure compare section 5.3). Fig. 9.2 shows the contact adhesion results after solder and peel-test for the contacts exposed to acetic acid without applied voltage. Each mark in the diagram in Fig. 9.2 a represents the average contact adhesion along one busbar. The diagram in Fig. 9.2 b shows one representative peel-force curve for each experimental point.

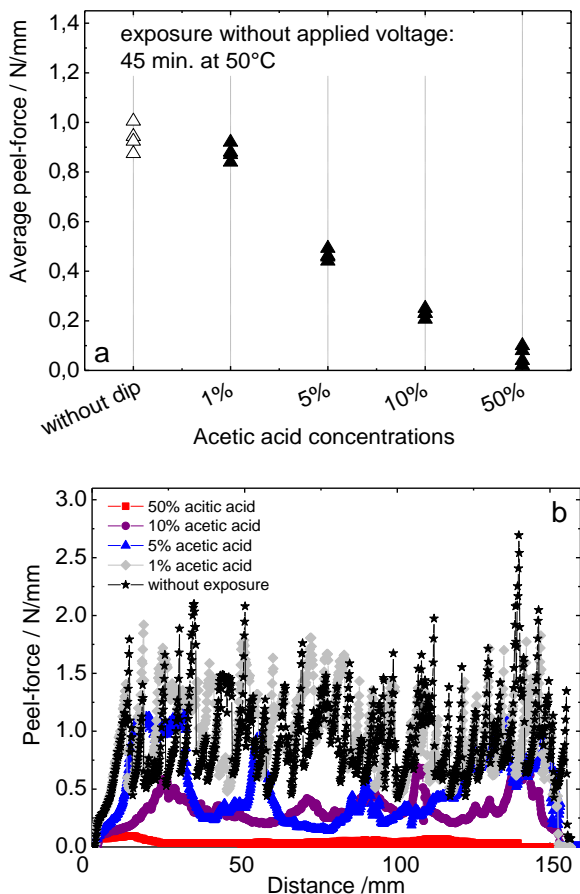


Fig. 9.2: Average peel-force results for soldered busbars, dipped in different concentrations of acetic acid (a) and corresponding adhesion curves of an exemplary busbar for every experimental point (b)

For 1% acetic acid no significant adhesion drop compared to the non-dipped reference could be found (grey curve and diamond symbols). For a concentration of 5% a drop of 0.5 N/mm, which is half of the original adhesion, could be observed (blue curve and triangles). For a 50% acetic acid solution the adhesion was zero after 45 minutes (red curve and squares). This means that acetic acid corrodes the contact and causes a clearly measurable contact adhesion loss depending on concentration.

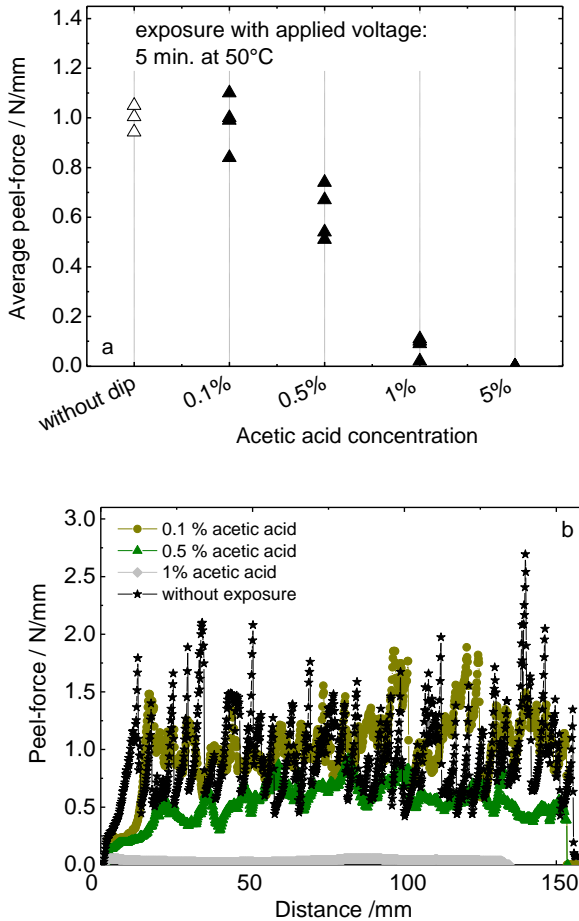


Fig. 9.3 Average peel-force results for soldered busbars, exposed in different concentrations of acetic acid with applied voltage (a) and corresponding adhesion curves of an exemplary busbar for every experimental point (b)

Fig. 9.3 shows the peel-force results for exposure with applied voltage. The contact adhesion fails a lot faster as without applied voltage. After 5 minutes of exposure even the one percent acetic acid solution corrodes the contacts resulting in a total adhesion loss (grey curve and diamond symbols). The 0.5% acetic acid solution causes an adhesion drop of 0.3 N/mm, only the 0.1% solution does not show significant influences on the measured adhesion. The applied voltage and cell illumination accelerate the corrosion mechanism induced by acetic acid considerably.

9.3 SEM cross-section analysis

To identify the weak point in the fired metallization SEM cross section images of screen-printed silver front side contacts (busbar) were done before and after acetic acid exposure. Fig. 9.4 a shows the cross section of an unaffected contact after the firing process. A glass-layer can be observed between silicon and bulk silver. The contact is interspersed with pores and cavities. Fig. 9.4 b shows the cross section of a contact after exposure to an acetic acid solution of 1% for 5 minutes with applied voltage. The measured contact adhesion was zero for this configuration (see Fig. 9.3 grey curve). A gap can be observed between bulk-silver and glass-layer inside the contact. This gap shows the same micro-characteristic as it was observed in section 7.3 due to contact corrosion after nickel plating. The detachment of glass and silver due to dissolution of the glass can be concluded to be the microstructural reason for bad contact adhesion after acetic acid exposure. A similar mechanism of lead oxide dissolution, as discussed in chapter 7 and as proposed in [162] appears to be very probable regarding the DHID phenomenon considering this result.

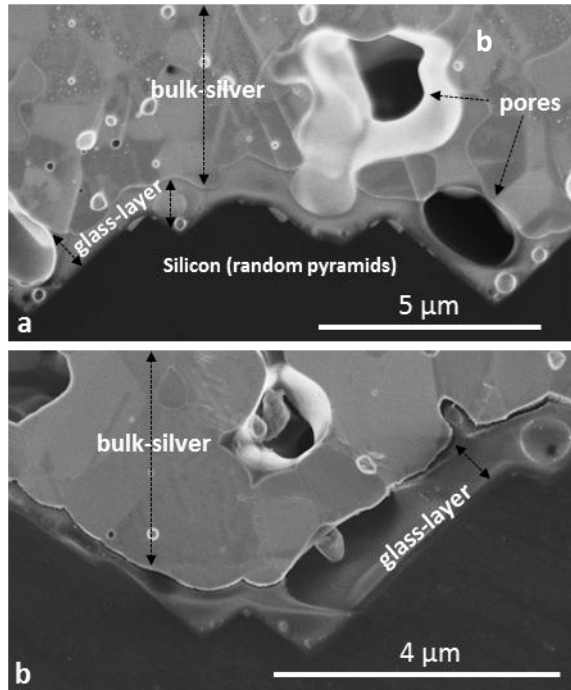


Fig. 9.4: SEM cross-section image of a screen-printed Ag front side metallization without acetic acid treatment (a) and SEM cross-section image of a screen-printed Ag front side contact exposed to 1% acetic acid for 5 minutes with applied voltage (b). A gap can be observed between the glass and the silver due to corrosion of the glass.

9.4 Chemical trace analysis

The acceleration of the glass-layer corrosion by an applied negative voltage has also been observed for plating electrolytes in chapter 7. The cause of this phenomenon has been suggested to be reduction of dissolved metal ions from the glass. While it is difficult to measure trace metal concentrations in plating electrolytes with inherently high metal concentrations to disturb the measurement, this is easily possible for acetic acid. If the suggested reduction mechanism occurs and is also true for exposure with applied voltage in acetic acid, less dissolved lead and silver out of the glass-layer should be found in the acetic acid solutions in the case of contact exposure with applied voltage.

To measure the amount of dissolved lead and silver in the solution after contact exposure, chemical trace analysis (ICP-OES) was conducted (for method description compare section 4.4.1). Fig. 9.5 shows the measured amounts of lead and silver for contact exposure without applied voltage (a) and for contact exposure with applied voltage (b) for different exposure durations and acetic acid concentrations.

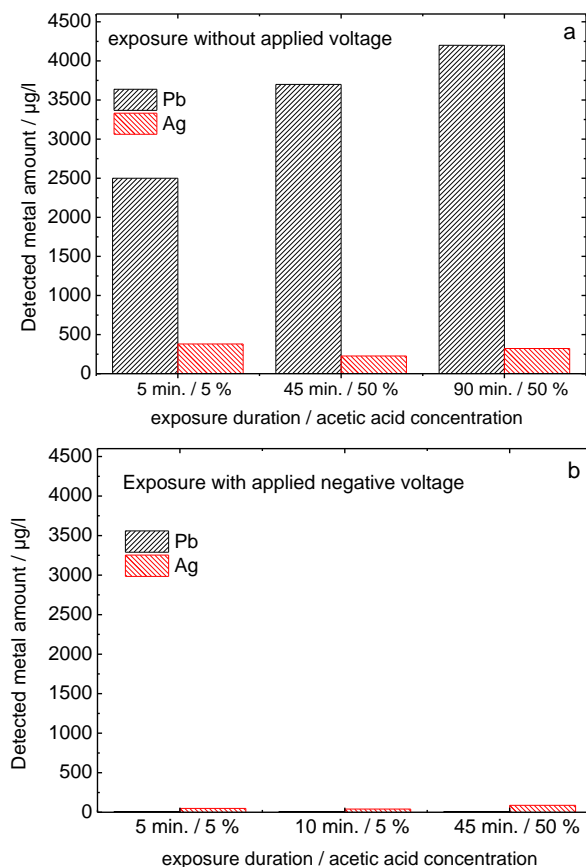


Fig. 9.5: Detected amounts of silver and lead in the chemical trace analysis (ICP-OES) of acetic acid solutions following contact exposure without applied voltage (a) and after contact exposure with applied voltage (b) for different acetic acid concentrations and exposure durations

It can be observed that after contact exposure without applied voltage the detected amount of lead and silver in the solutions is significantly higher than after exposure with applied voltage for every acetic acid concentration and for every tested exposure duration. Comparing same concentration and duration (5 minutes, 5% and 45 minutes, 50%) no lead and ~87% less silver was found after exposure with applied voltage compared to exposure without applied voltage. This is despite the fact that adhesion fails a lot faster after exposure with applied voltage (compare Fig. 9.2 b blue curve and triangles for exposure without applied voltage and 9.3 b, grey curve and diamonds for exposure with applied negative voltage).

These results support the conclusion that the postulated reduction of lead and silver and the related acceleration of the contact corrosion mechanism occurs.

9.5 Cyclic voltammetry measurements

The amount of dissolved lead and silver was shown to be significantly higher in the acetic acid solutions for contact exposure without applied voltage than with applied voltage. It was concluded that this difference is due to a reduction effect, in the case of an applied voltage, as has already been proposed for plating electrolytes in chapter 7. The dissolved species will be reduced and cannot be found in the solution by chemical trace analysis. To verify if lead dissolved out of the contact can be reduced, cyclic voltammetry measurements were performed with acetic acid solutions after the exposure of a contact without applied voltage (for detailed description of the set up and the measurement procedure compare section 4.4.2). Fig. 9.6 shows the results for a 1% (a) and 10% (b) acetic acid solution after 45 minutes of contact exposure at 50 °C (compare section 9.2). A clear reduction/oxidation peak pair at the potential of -0.3 mV (reduction) and -0.255 mV (oxidation) can be observed.

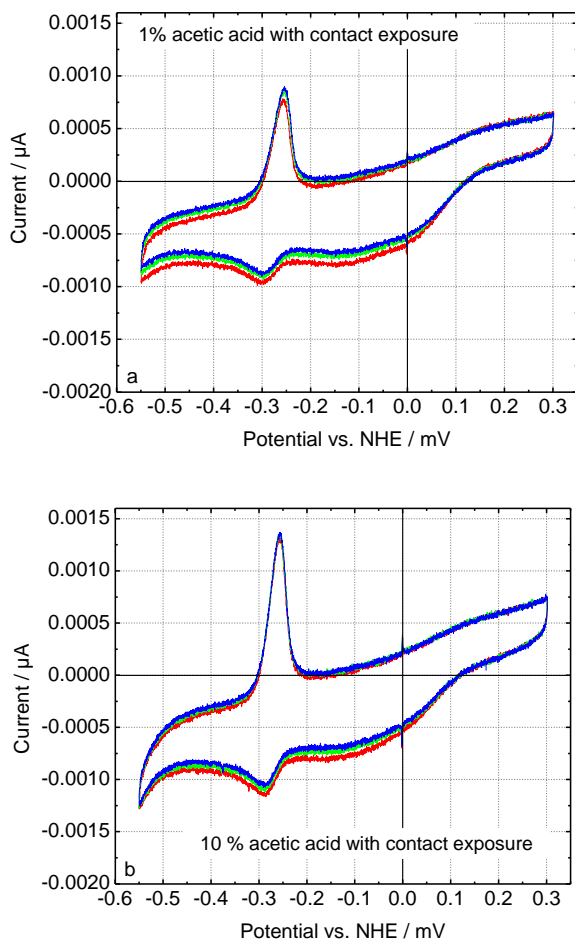


Fig. 9.6: CVS measurements (3 cycles) of a 1% (a) and a 10% (b) acetic acid solution where a contact was immersed for 45 minutes. A reduction/oxidation peak of lead can be observed.

Without exposed contact no oxidation and reduction peak pair can be observed. This is shown by the reference measurement in Fig. 9.7 a. The positive control in Fig. 9.7 b was realized by the addition of commercially available PbO powder to the 10% acetic acid solution ending up in a concentration of 500 μM . The result shows an oxidation and reduction peak pair at the same position as for

acetic acid solutions with exposed contact (Fig. 9.6 a and b). This proves that the observed reduction and oxidation peak in Fig. 9.6 originates from the reduction and oxidation of lead oxide dissolved in acetic acid.

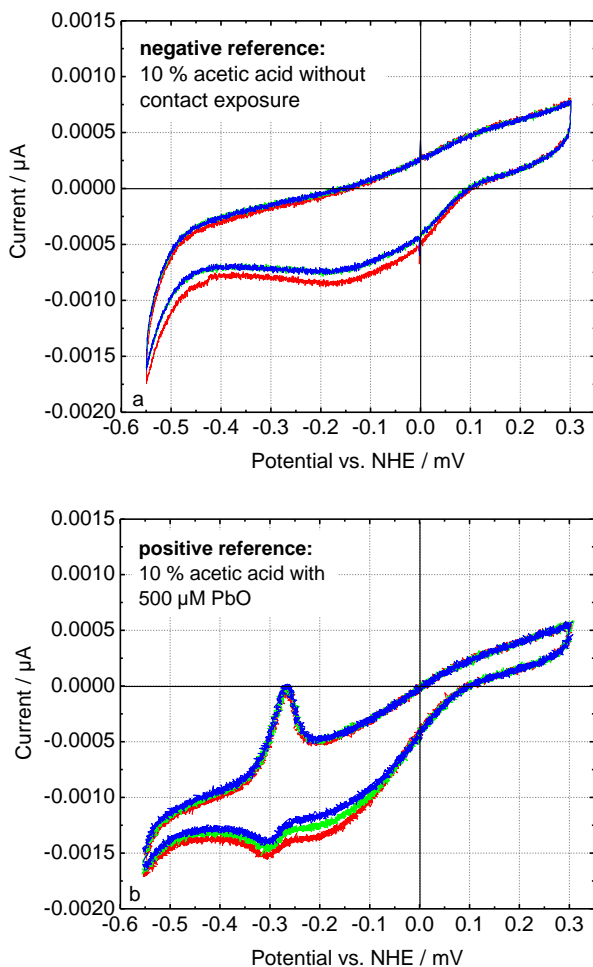


Fig. 9.7: CVS measurements (3 cycles) with a reference solution of 10% acetic acid without exposed contact (a) and a blank solution of 10% acetic acid intentional contaminated with a PbO concentration of 500 μM (b)

To confirm this with a different method, the metal deposition at the observed reduction peak on a platinum electrode was evaluated with EDX measurements. Fig. 9.8 a shows an SEM top view image of the platinum electrode surface with deposited metal particles. The EDX measurement of position 1 and position 2 reveals that lead was reduced on the platinum electrode. This confirms that the observed peaks represent the reduction and oxidation of lead and shows that lead dissolved from the contacts by acetic acid can be reduced if a suitable voltage is applied.

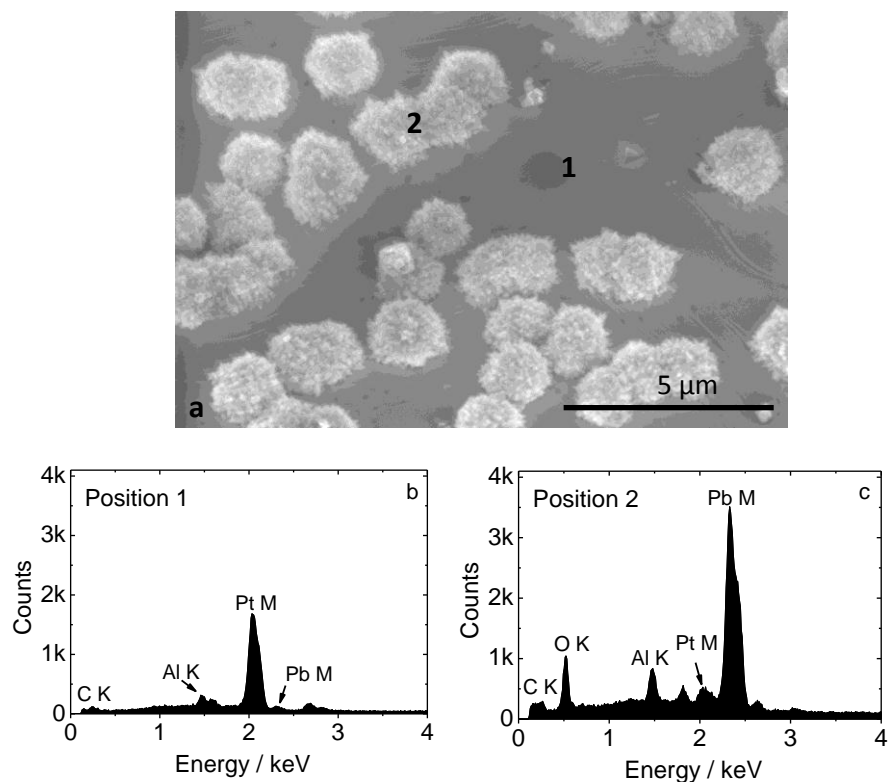


Fig. 9.8: SEM top-view image of the platinum electrode with deposited metal particles (a) and marked EDX measurement positions at the electrode surface (1) and at a deposited metal particle (2). EDX profiles measured at position 1 (b) and at position 2 (c)

9.6 Incubation experiment with ethylene-vinyl acetate

In an incubation experiment two $20 \times 20 \text{ cm}^2$ laminated EVA double layers from different suppliers were fragmented, wetted with 100 ml deionized water and introduced into a climate chamber (85°C , 85% r. h.). Depending on the EVA, pH-values of 3.8-5.2 were measured after an exposure of 1000 h (compare Fig. 9.9).

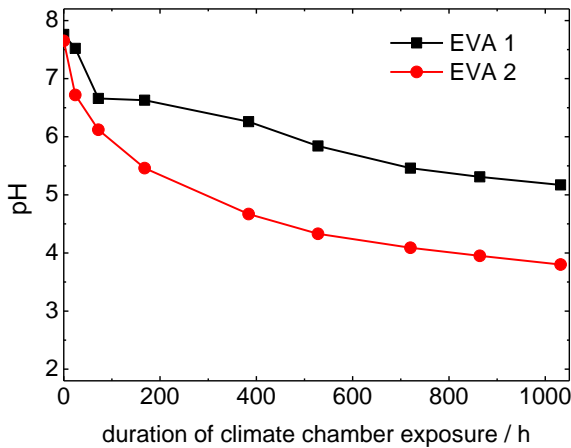


Fig. 9.9: Measured pH of two different EVA samples exposed to the climate chamber (85°C , 85% r. h.) for more than 1000 h

This shows that EVA encapsulations generate an acidic environment for solar cell contacts in the module depending on time and used EVA if humidity is present ($\text{pH} < 7$). While this experiment does not allow any conclusion about the local pH inside the porous front side contact of an encapsulated solar cell, the experiment offers an estimation of the at least possible pH-range present in the module, which is acidic. This pH region is in the focus of interest for further considerations.

9.7 Pourbaix diagrams

To complement the experimental results, to clarify the thermodynamics and to show possible reaction paths for lead in the presence of acetic acid, Pourbaix diagrams were calculated. For the generation the free simulation software

“Chemical equilibrium diagrams” was used. The software is based on the algorithms of Eriksson [164] and Haltafall [165]. The calculations were done by L. Labusch from the department of microsystems engineering at the university Freiburg, where input parameters were jointly discussed and results were published together.

Different acetic acid concentrations (0.1%, 0.5%, 5% and 10%) were calculated with a Pb^{2+} concentration of $1\text{ }\mu\text{M}$ at 25°C and a Bi^{3+} concentration of $1\text{ }\mu\text{M}$. Fig. 9.10 shows the Pourbaix diagrams for a 0.1% (a), a 0.5% (b), a 1% (c) and a 5% (d) acetic acid solutions and a Pb^{2+} concentration of $1\text{ }\mu\text{M}$ at 25°C . The ICP-OES measurement in Fig. 9.5 shows a Pb content of $2500\text{ }\mu\text{g/l}$ in an acetic acid solution of 5%, which corresponds to a concentration of $\sim 10\text{ }\mu\text{M}$. Even if a lot of lead is reduced the estimation of $1\text{ }\mu\text{M}$ Pb^{2+} represents a realistic dimension. The Pourbaix diagrams show that even at low acetic acid concentrations of 0.1%, lead oxide or lead hydroxide is dissolved to form aceto-complexes or even Pb^{2+} under acidic conditions, depending on pH. The EVA incubation experiment in section 9.6 suggests a pH-range of 3.8 to 5.2. In this pH-range the dissolved lead can be reduced to elemental lead at a suitable potential, especially if an over potential for hydrogen evolution is taken into account. Locally in the contact directly at the silver glass interface even higher concentrations of lead than the simulated $1\text{ }\mu\text{M}$ are probable, allowing the reduction of Pb^{2+} to elemental lead even within the electrochemical window of water.

Solar cell contacts are usually applied by screen-printing a silver paste containing silver particles, glass frits, organic solvents, cellulose resin, inorganic additives and surfactant agents. The paste of the investigated solar cell contacts contains a lead glass frit. In general bismuth glass can be used as alternative to lead glass in solar cell metallization [131]. To show if this can be beneficial in terms of corrosion, the Pourbaix diagram generation was additionally done using acetic acid (5%) and a Bi^{3+} concentration of $1\text{ }\mu\text{M}$. Fig. 9.11 shows the resulting Pourbaix diagram. Due to the higher reduction potential of bismuth, compared to lead, bismuth is reduced at lower negative voltages. In an acidic environment bismuth appears dissolved as bismuth-hydroxy-complex starting with a pH of ~ 4.9 . Due to this thermodynamically higher stability the driving force for dissolution is slower compared to lead, even if more acidic conditions are reached. In the module it would take longer until pH ranges are reached at which bismuth appears as dissolved species, and even then, dissolution would take place slower. Regarding the results of the EVA incubation experiment bismuth

would be dissolved for EVA 2 (pH = 3.8 after 1000 h in the climate chamber) but not for EVA 1 (pH = 5.2 after 1000 h climate chamber), assuming the measured pH represents the pH at the glass – silver interface. This means that ethylene-vinyl acetate encapsulations with a lower vinyl acetate fraction like EVA 1 in combination with contacts realized using bismuth glass could help to reduce the damp heat induced degradation phenomena.

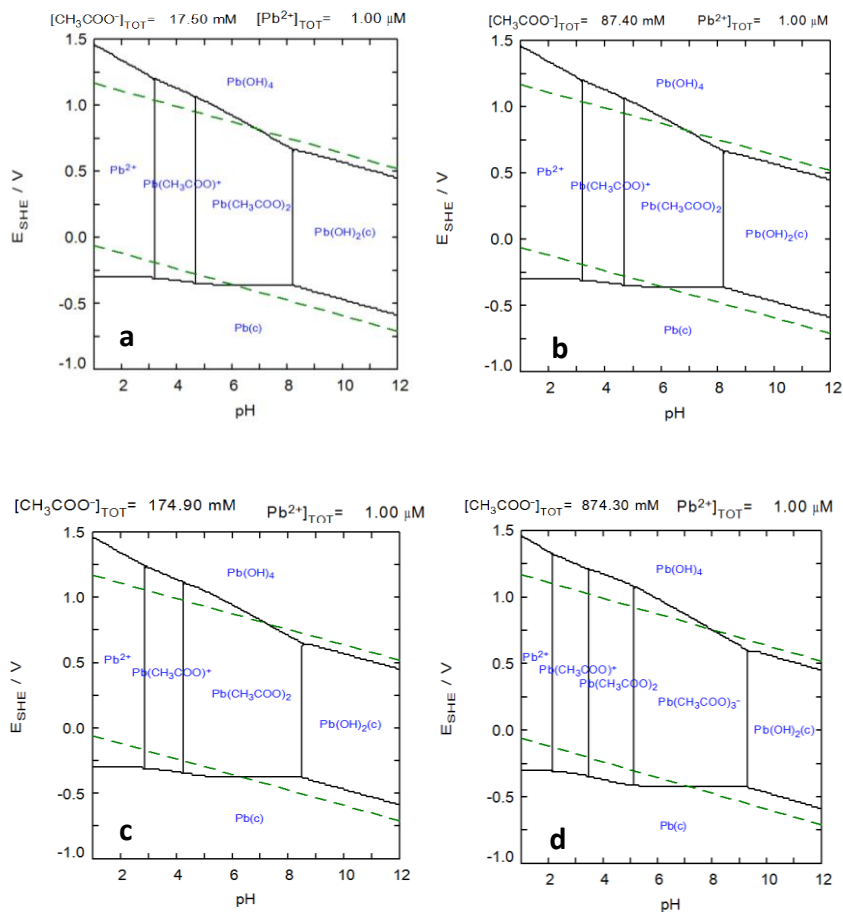


Fig. 9.10: Pourbaix diagrams of a (0.1%), b (0.5%), c (1%) and d (5%) acetic acid and $1 \text{ }\mu\text{M Pb}^{2+}$ at 25°C

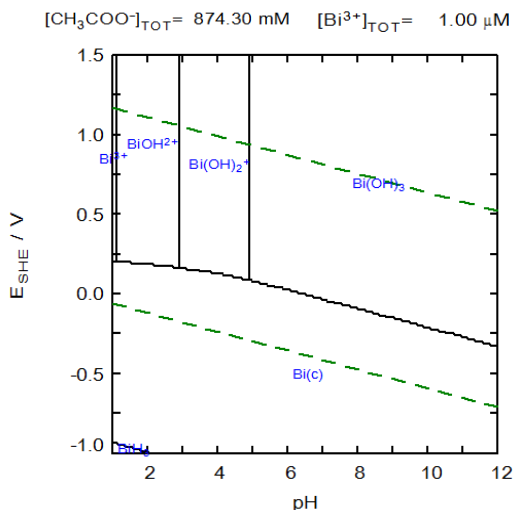
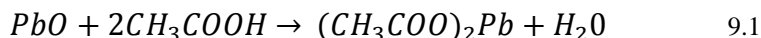


Fig. 9.11: Pourbaix diagram of acetic acid (5%) and 1 μM Bi³⁺ at 25°C

9.8 Model of the solar cell contact corrosion by acetic acid

In the standard lead glass, lead oxide is present, which is observed to corrode in the presence of acetic acid. According to the Pourbaix diagrams, the following reaction occurs:



Lead oxide reacts in the presence of acetic acid to lead acetate. Lead acetate is highly soluble in water (221 g / 100 g at 50°C [166]). Without applied voltage the amount of lead oxide that can be dissolved depends on the acetic acid concentration. Total contact adhesion loss was observed after 45 minutes using an acetic acid concentration of 50%. Solutions with lower acetic acid concentration will cause the same effect at longer exposure durations. The driving force for dissolution is generally high; much dissolution is possible especially for high acetic acid concentrations. For lower acetic acid concentrations the dissolution process will slow down considerably after little dissolution if the reaction equilibrium is reached locally. The time until such a

quasi-steady-state is reached at the contact interface is influenced by the time constants of diffusion processes within the pore system of the contact, transporting fresh acetic acid into the vicinity of the glass-silver interface and removing the lead acetate compound. However, with applied voltage the adhesion was observed to fail in 5 minutes even with a concentration of 1% acetic acid. This behaviour can be explained by reduction of the dissolved lead in presence of electrons at a suitable potential, which will take the lead out of the system and release the acetic acid for further dissolution. The ICP-OES results show no lead in acetic acid solutions after exposure with an applied negative voltage despite the fact that contact adhesion is destroyed more effective. Additionally the CVS measurements prove the possibility of lead reduction and the Pourbaix diagrams of lead in acetic acid show that the reduction is thermodynamically favoured in acidic environment. These findings support the suggested mechanism. This mechanism keeps dissolved lead concentration down and hydronium- and acetate ion concentration high, which will accelerate the reaction towards further corrosion of lead oxide and result in further dissolution of the glass layer. This electrochemically driven dissolution cycle is shown in Fig. 9.12 as a schematic drawing at the contact interface.

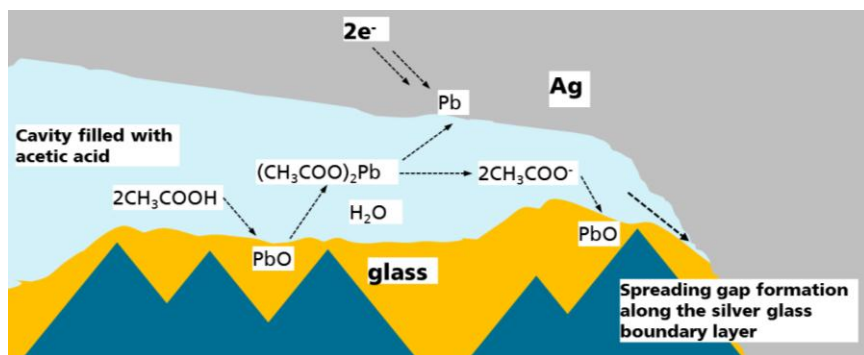


Fig. 9.12: Schematic drawing of the dissolution mechanism at the glass silver boundary layer in the contact, which causes poor contact adhesion and works especially efficient if a voltage is applied to the contacts, due to the reduction of the dissolved species

The reaction is particularly strong where the transport distance between the place of lead dissolution (glass layer) and the place of lead reduction (bulk silver) is very short. This leads to a very fast spreading gap formation between glass and silver inside the contact, which is the origin of the observed adhesion

loss due to the presence of acetic acid. The corresponding oxidation reaction can occur at any position in the module electrically or electrochemically connected to the front side metallization. The oxidation of the aluminium backside metallization of the cell is one possibility.

It has been known that humidity penetrates the modules through the back sheet, diffuses at the cell front side from the edges to the centre of the cell and takes the acetic acid, present in the EVA encapsulation, to the contacts. Then, the corrosion of the glass first described in detail in this work starts. Temperature, light and long exposure durations that are typical for modules in the field promote this reaction. Most importantly, reductive potentials at the solar cell front electrode, such as the cell voltage or possibly even more pronounced, a negative module voltage (if relevant to the contact in terms of resistance), support the dissolution process, as shown in section 9.2. As a consequence contact adhesion fails and the affected area does no longer contribute to energy conversion, which results in a power loss of the cell.

In a standard not grounded solar plant installation half of the modules work at a negative voltage with respect to ground and half of the modules work at a positive voltage with respect to ground (floating voltage). The voltage level depends on the number of modules. The experiments in this work show that a negative voltage accelerates the contact corrosion considerably. Applied to the situation in the field, it should be investigated if modules working at a negative voltage show damp heat induced degradation faster than modules working at a positive voltage. Also the position of the cell in the module may play a role. Cells located at the module edges could show DHID earlier than cells in the middle of the module because of the physical proximity to the module frame.

With a grounding of the negative pole of the solar plant all cells/modules work at a positive voltage towards ground. This could slow down the DHID in the field. This grounding is also beneficial to avoid the well-known potential induced degradation (PID) mechanism which only occurs at negative voltages [167]. Performing a damp heat test in the climate chamber the DHID is reported to occur at ~2000-3000 h depending on the cells and the encapsulation [161], [162]. In the standard procedure, test modules are aged without applied voltage. The use of a negative voltage has the potential to accelerate the visible corrosion due to DHID and can reduce the time needed to check different material combinations for sensibility to this corrosion mechanism. Of course, the time scale of humidity diffusion in the EVA, which is one critical factor in this system, cannot be influenced.

Several approaches can be derived to be promising to avoid the described degradation acceleration of silver front side contacts:

- Module architectures that do not permit humidity into the vicinity of the front contacts (e.g. glass-glass modules).
- Use of alternative encapsulation materials which are not based on network formers that decompose to acetic acid like EVA.
- Development of an Ag-paste which enables a less porous Ag-metallization after printing and firing to avoid the access of the acetic acid to the glass silver interface (compare section 7.3)
- Use of alternative glasses in the front side paste for contact formation, which are less easily dissolved by acetic acid (e.g. bismuth glass).
- Implementation of a sacrificial anode electrochemically connected to the front side metallization, consisting of a material that is less noble than lead oxide to avoid lead oxide dissolution.
- The operation of modules in the field at a positive voltage might avoid the acceleration of the DHID corrosion mechanism which appears for negative voltages as shown in this work. This can extend module lifetime.

9.9 Chapter summary

In this chapter the corrosion of silver front side contacts due to interaction with acetic acid which is a decomposition product of the most common module encapsulation material ethylene-vinyl acetate is investigated in detail. The results in this chapter reveal that:

- acetic acid leads to poor adhesion of the front side contacts (section 9.2) by corrosion of the glass-layer which leads to a gap formation between glass-layer and bulk silver (section 9.3). This proves that the contact loss between front side metallization and cell, which is the reason for power loss and the appearance of the damp heat induced degradation phenomenon in many modules including EVA after ~2000 h of damp heat treatment observed in literature [161], [162], originates from the corrosion of the glass layer inside the contacts by acetic acid as had already been suggested before.
- This corrosion is shown to be accelerated by an applied negative voltage (section 9.2).

- The analysis of the acetic acid exposure solutions by chemical trace analysis (ICP-OES) revealed that lead and silver are dissolved out of the contacts during exposure without applied voltage (section 9.4). With applied negative voltage the contact adhesion was shown to fail faster and at lower acetic acid concentrations which indicates corrosion acceleration. However, nearly now lead and silver were found in the chemical trace analysis (section 9.4). This suggests the conclusion that in the case of an applied voltage the dissolved lead and silver can be reduced which shifts the equilibrium of the dissolution reaction (equation 9.1) towards further dissolution and explains why no lead and nearly no silver could be found in the solutions.
- CVS measurements confirm that the suggested lead reduction out of acetic acid solutions after contact exposure is possible (section 9.5).
- An incubation experiment with two different laminated EVA's showed that EVA and humidity create an acidic environment for the contacts in the module (section 9.6).
- The generation of Pourbaix diagrams of Pb^{2+} and acetic acid reveals that lead appears as dissolved species in the acidic environment and can be reduced at suitable potentials which further supports the suggested conclusions (section 9.7). The calculated Pourbaix diagrams show that the suggested reduction mechanism is thermodynamically possible and indicate that a substitution of the used lead glass by bismuth glass can help to slow down DHID.
- In section 9.8 a model of the contact corrosion mechanism was elaborated based on the experimental results, which suggests that the corrosion appears as a repetitive cycle of dissolution and reduction, which accelerates the dissolution of the glass layer inside the contact and thereby the spreading gap formation along the glass silver boundary layer. Preventing this mechanism has the potential to extend module lifetime in the field because in a standard symmetric solar plant interconnection half of the modules work under negative voltages against ground. For such modules the DHID can be expected to be accelerated based on the results in this section.

10 Cost effects of solar cell front side metallization

To evaluate the process costs of the solar cell front side metallization production, investigated in this work, and to compare it with the process costs of the standard screen-printed metallization (introduced in section 3.2) and the direct plated Ni-Cu metallization (introduced in section 3.5), a Total Cost of Ownership¹⁰ (TCO) calculation was performed. This calculation method considers the overall life cycle costs generated by a product and is described in detail in [168]. The global trade association “Semiconductor Equipment and Materials International” (SEMI) defined a Cost of Ownership¹¹ (CoO) standard formulated to calculate the costs of production in the semiconductor industry [169]. The cost calculation using the CoO standard includes every manufacturing step of a solar cell production starting with the silicon wafer ending up with the measured cell and is therefore suited to calculate the total cell production costs [170]. The process cost calculation assumes that the production of solar cells can be divided into single production steps. The total costs of the entire solar cell production were calculated by adding the costs of the single production steps.

Fig. 10.1 shows the process sequences which were taken as basis for the cost calculation. The standard screen-printing process (left), the Ni-Cu-Ag metallization on screen-printed seed-layer (middle) and the direct Ni-Cu-Sn plating sequence (right). The three processes differ only in the back-end where the front side metallization is realized.

To compare the different solar cell production processes regarding the front side metallization and to expose the cost effects which influence the total costs, identical cell efficiency for the resulting solar cells, irrespective of the different metallization techniques was assumed. As result the process costs per wafer were calculated. These considerations were worked out in the context of a bachelor and a master thesis co-supervised within the present work [171],[172]. Details on the assumptions made for the presented calculations are given in the referenced works. As general principle, conservative assumptions were made with respect to uncertainties for the novel process routes, when in doubt. For long durations in

¹⁰ The Total Cost of Ownership calculation was developed by Bill Kirwin, research director of the consulting company Gartner Inc. in 1987.

¹¹ Cost of Ownership is the description of the TCO cost model standard E35-0312 by SEMI and is frequently used in the photovoltaic and semiconductor industry.

industrial application, a considerable learning rate is believed to offer a cost reduction potential for the novel techniques.

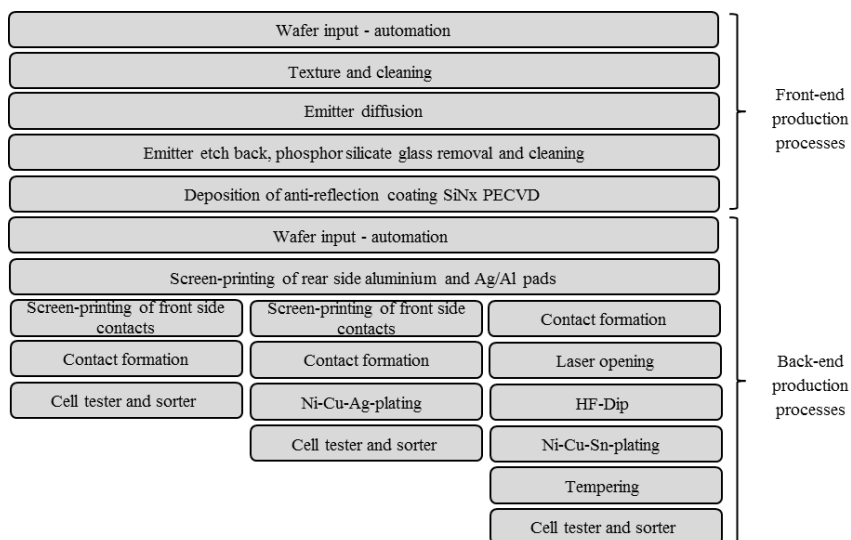


Fig. 10.1: Process sequences as basis for the process cost calculation using the SEMI CoO-standard. The standard screen-printed solar cell metallization (left), the Ni-Cu-Ag metallization on screen-printed seed-layer (middle) and Ni-Cu-Sn metallization by direct plating (right) were compared. The process routes differ in the back-end production processes.

Fig 10.2 shows the calculated solar cell process costs of the three metallization possibilities divided into the categories: equipment, facilities, labor, parts, utilities, process consumables, waste disposal, and yield loss.

The price for the silver paste, was researched in discussions with different paste suppliers, based on a silver market price of 490 €/kg (which is the most important contributing factor). For the screen-printed standard solar cells, a conservative silver paste consumption for the front side metallization of 110 mg/wafer was used, which corresponds to a total silver consumption of 105 mg/cell. For the seed- and plate metallization a paste consumption of 20 mg/wafer was assumed, which corresponds together with the plated silver capping to a total silver consumption for the front side metallization of 15 mg/cell as it was demonstrated using a screen-printed seed-layer (compare chapter 6).

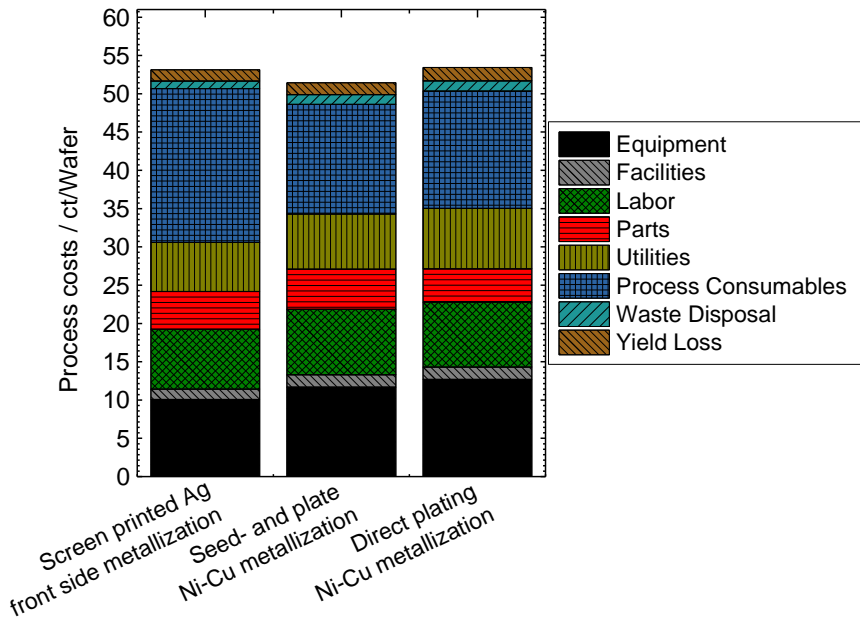


Fig. 10.2: Process costs for silicon solar cells with three different front side metallizations, divided in the costs for equipment (black), facilities (grey), labor (green), parts (red), utilities (yellow), process consumables (blue), waste disposal (turquoise) and yield loss (brown)

The standard screen-printing process causes total process costs of 53.13 €/wafer, the seed- and plate metallization is the most cost effective process and causes total process costs of 51.43 €/wafer. The direct plating process causes process costs of 53.44 €/wafer. The calculated differences are very small. The process cost savings due to the partial or total substitution of silver for the plating processes are compensated by additional costs in the other sectors, especially equipment, labour and waste disposal. The additional plating processes generate labour costs and plating tools are currently more expensive than screen-printing machines. To analyse the sensitivity of the calculated process costs to the silver price, which was subject to fluctuations in the last years (compare Fig. 1.1), and is most relevant for the investigated techniques, the calculation was done for silver prices between 500 €/kg and 1500 €/kg. Fig. 10.3 shows the results of the sensitivity analysis of the silver price on the process

costs for the different metallization methods. Due to the differences in silver consumption the increase of the process costs differs considerably with an increasing silver price. With the current silver price (~520 €/kg, December 2014) the cost advantage for the Ni-Cu-Ag seed- and plate metallization (red dashed line) compared to the standard screen-printed metallization (continuous black line) is ~2 €/wafer. Considering the silver price at its highest range (~1220 €/kg, April 2011) the cost advantage is ~10 €/wafer. This reveals that the cost-benefit analysis of the different metallization processes differs considerably with the silver price. In any cases the investigated seed- and plate metallization is the cheapest process because it offers the optimal balance between reduction of the needed silver amount compared to the standard screen-printing metallization and a reduced process complexity compared to the direct plating of Ni-Cu-Sn. The process chain is defined, and the needed tools are available in industrial scale.

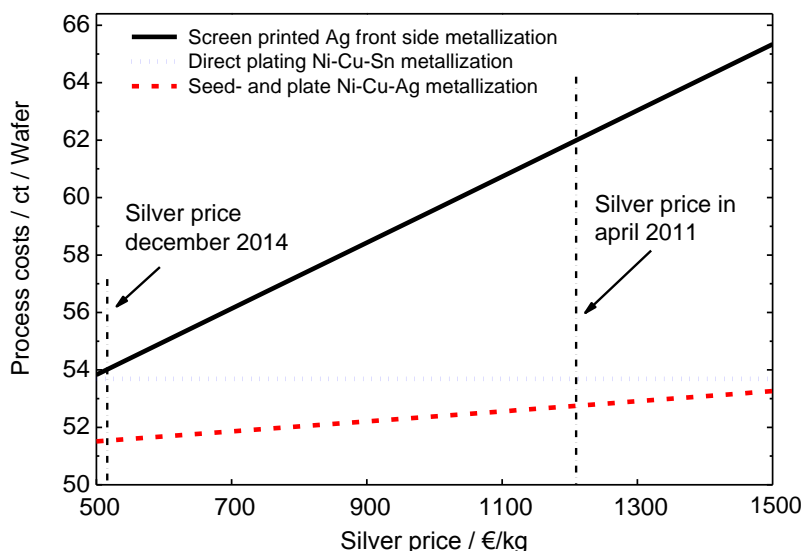


Fig. 10.3: Process costs for silver prices between 500 €/kg and 1500 €/kg for the standard screen-printed silver metallization (black continuous line), the Ni-Cu-Ag seed- and plate metallization based on a screen-printed silver seed-layer (red dashed line) and the Ni-Cu-Sn direct metallization process (blue dotted line)

The calculated results are valid for the assumption that equal cell efficiency can be reached with the three compared process routes. Regarding the seed-and-plate approach based on a screen-printed seed-layer optimization of the seed-layer paste is needed especially to improve the contact resistance as shown in chapter 6. In the last years considerable reductions of the paste consumption for the standard screen-printed metallization were reached by the implementation of segmented busbar designs and new silver pastes. This volume of reduction in paste consumption can most probably not be continued in the next years. Additionally rising silver prices can be expected due to the rising silver demand, not only driven by expanded solar cell production but by the rising silver demand of the electric industry. This means that on the long term view significant cost advantages for plated copper metallizations compared to screen-printed silver metallizations can be expected.

11 Summary and outlook

In the present work, a copper front side metallization for silicon solar cells based on a printed seed-layer, a plated nickel diffusion barrier, a plated copper conductive layer and a plated silver capping is investigated. The work was inspired by the proof of concept with high efficiency potential for this metallization architecture and the possibility to enable the substitution of a large part of the usually exclusively used silver for the front side metallization of silicon solar cells by copper. This can be realized by small process variations compared to the standard solar cell production while using inline capable techniques, feasible for implementation in mass production and available in industrial scale. Scientific understanding and development of solutions to challenges that are not necessarily an obstacle for lab scale demonstration but with the potential to hinder the implementation in industrial mass production are addressed in this work:

- The reproducible printability of fine seed-layers with very little silver consumption using industrial scale screen-printing.
- The corrosion of the printed seed-layers due to interaction with the electrolyte solutions during the electrochemical deposition, resulting in poor contact adhesion.
- The long term stability of the cells due to copper diffusion.
- The corrosion of the printed contacts on module level due to the interaction with the module encapsulation material.
- Cost effects of the investigated metallization compared to the standard screen-printed silver front side metallization.

In the first key task of this work, the correlation between the rheological parameters viscosity and yield stress of experimental and commercial silver pastes and the resulting seed-layer geometry as well as the needed wet-paste consumption after screen-printing and firing was investigated. The viscosity of the used paste was found to correlate with the resulting contact finger width: the higher the viscosity the smaller the resulting contact finger width. A reduction of the particle size increases the paste viscosity (at a constant solid content) and therefore reduces the printed contact finger width. The analysis of the silver paste yield stress revealed that it correlates with both key parameters the wet-

paste consumption and the contact finger width. Yield stress values >400 Pa lead to narrower contact fingers and simultaneously to less wet-paste consumption. With a silver paste set to the yield stress of 800 Pa, 30 μm fine contact fingers were reproducibly achieved by screen-printing with a wet-paste consumption of ~ 35 mg/cell. Using a commercial fine line paste, containing silver particles in the nanometre scale a wet-paste consumption of ~ 20 mg/cell was achieved corresponding to a silver consumption for the seed-layer of ~ 8 mg/cell.

Industrial scale $156 \times 156 \text{ mm}^2$ standard back surface field solar cells with plated Ni-Cu-Ag front side metallisation based on seed-layers printed with ink-jet printing, aerosol-jet printing, flexographic printing and screen-printing were produced and compared with cells featuring a standard fully screen-printed front side metallization, regarding the silver consumption for the entire front side metallization, the contact geometry and the electrical parameters. For the cells based on the ink-jet printed seed-layer the same efficiency level as for the screen-printed reference cells of 19.2% were obtained. For the cells with aerosol-jet and screen-printed seed-layers, need for contact resistance improvement was shown. With all four seed-layer printing technologies a total silver consumption of ≤ 18 mg/cell for the front side metallization (seed-layer + silver capping) was achieved using a grid pattern with three busbars and 90 contact fingers. This represents a reduction of the silver consumption of at least 80% compared to cells with fully screen-printed silver metallization.

The second key objective of the thesis was to understand and model the corrosion mechanism behind observed poor contact adhesion after electrochemical metal deposition. The interactions between screen-printed solar cell contacts and electrolyte solutions were investigated in detail by SEM, TEM, AFM and XRD analysis supported by exposure experiments with and without applied voltage to characterise the contact peel-force as a measure for the degree of contact corrosion. It was shown that exclusively the nickel plating affects adhesion significantly due to the corrosion of the glass layer inside the contacts. Material analysis revealed that the acidic electrolyte dissolves the glass layer that mainly consists of silicon oxide and lead oxide, but also contains silver or silver oxide after firing, which can also be detected. This glass dissolution results in a site specific gap formation along the glass silver interface in the contact. TEM measurements at that interface indicate that no specific weak glass composition

at that position is responsible for this behaviour¹². The dissolution of the glass layer is promoted by sulphates and chlorides in the electrolyte, which were shown to form lead sulphate and silver chloride with the dissolved species. This shifts the equilibrium towards further dissolution. Additionally an applied cathodic voltage accelerates the corrosion of the glass layer considerably, depending on the nobility of the metal ions in the solution. In solutions containing relatively noble ions like copper ions or iron (III) ions, the corrosion was observed to be avoided. In solutions containing less noble nickel ions or sodium ions, corrosion results in poor contact adhesion. This leads to the conclusion model conception that in the presence of cations with a higher reduction potential than lead, the reduction of these cations is preferred and the dissolution equilibrium of the lead oxide out of the glass is not shifted. In the presence of cations less noble or similarly noble than lead, the dissolved lead is reduced if a sufficiently cathodic voltage is applied. This takes the dissolved lead out of the system and shifts the equilibrium strongly towards further dissolution. This mechanism is particularly strong where the distance between the location of dissolution (glass layer) and the location of reduction (silver contact) is very small. It explains the site specific and fast expanding gap formation and is the reason for why only the nickel electrolyte causes significant contact adhesion losses during the plating process. The combination of these findings allowed the derivation of a full model of solar cell contact corrosion that gives a coherent explanation for all observed phenomena¹³.

The third major question was on a possible impact of copper diffusion on the electrical performance of silicon solar cells with the investigated copper front side metallization. It was shown that silicon nitride layers deposited by inline

¹² The analysis of the electrolyte impact on the contact microstructure was published in the **Electrochemical Society Journal of Solid State Materials and Technology**: A. Kraft, Y. Pernia, L. Ni, A. Filipovic, A. Hähnel, A. Graff, J. Bartsch, M. Glatthaar, *Microstructure analysis of the interaction between Watts-type nickel electrolyte and screen-printed solar cell contacts*, vol. 3: pp. Q55-Q60, **2014**.

¹³ The corrosion mechanism of the glass layer inside the printed solar cell contacts was published in the **Journal of applied electrochemistry**: A. Kraft, Y. Pernia, A. Kalio, A. Gautrein, L. Ni, J. Bartsch, S. W. Glunz, H. Reinecke, *Origin of corrosion effects in solar cell contacts during electrochemical nickel deposition*, vol. 45, Issue 1, pp. 95-104, **2015**.

PECVD and inline sputtering act as diffusion barrier and avoid copper diffusion into the underlying silicon wafer effectively even after a pre-treatment with hydro fluoric acid or the mechanical load induced by screen-printing. This is generally important for plated solar cell front side metallization including copper because the plated copper layer usually overlaps the nickel diffusion barrier plated before at the edges of the contact structures and is in direct contact with the silicon nitride layer. Additionally, the result is relevant to other copper metallization techniques (e.g. copper paste printing).

The investigations of the effectiveness of the nickel diffusion barrier on cell level revealed that 20 mg of nickel (corresponding to a minimal nickel layer thickness of 0.2 μm) can be estimated to avoid long term stability issues in normal module lifetimes¹⁴. Besides the effectiveness of the nickel diffusion barrier the cell degradation was shown to depend on the used seed-layer and the firing temperature. The degradation of modules during damp heat test in the climate chamber (85°C, 85% r.h.) does not show significant degradation for cells with nickel diffusion barrier due to copper diffusion after 1500 h (equivalent to $1.5 \times \text{IEC}$ standard test). Even the module without diffusion barrier passed the IEC criteria of < 5% output power loss. The comparison of the slight degradation of the module with the corresponding measured degradation on cell level showed good accordance in the degradation state. This is a first hint that the used method for rapid degradation at elevated temperatures on cell level is able to predict module degradation at lower constant temperatures. However, the methods for quick determination of copper-induced degradation of solar cells and modules still need to be refined and standardised, as none of the currently used procedures from IEC 61215 addresses the degradation of solar cells induced by copper migration.

Challenges for nickel plating on screen-printed silver seed-layers regarding the aim of a homogenous and dense nickel diffusion barrier, were identified at the glass areas on the printed contact surface and at the edges of the busbars. At these spots nickel plating was observed to be severely limited. This can cause

¹⁴ The long term stability results were published in the **Journal of Solar Energy Materials & Solar Cells**: A. Kraft, C. Wolf, J. Bartsch, M. Glatthaar, S. W. Glunz, *Long Term Stability of Copper front side Contacts for Crystalline Silicon Solar Cells*, vol. 136, pp. 25-31, **2015**

weak spots in the plated nickel diffusion barrier. The analysis of the nickel distribution homogeneity after plating on $156 \times 156 \text{ mm}^2$ cells showed considerable inhomogenities: about 80-90% less plating occurs at the busbars compared to the deposition at the contact fingers. Changes in anode position and geometry as well as electrochemical shielding and pulsed plating were shown to be approaches with the potential to improve the nickel distribution on solar cells. The corrosion of silver front side contacts on module level due to interaction with acetic acid, which is a decomposition product of the most common module encapsulation material EVA, is investigated as a fourth topic in this work. The investigation was motivated by the findings of paste corrosion by electrolytes, which obviously appeared to be similar to the effects described for damp heat induced degradation (DHID) in literature. Indeed a site specific gap formation at the glass-silver interface, as already observed for contact corrosion due to the interaction with electrolytes, was revealed by SEM investigations. This shows that the contact loss between front side metallization and cell, which is the reason for power loss and the appearance of the damp heat induced degradation phenomenon in modules including EVA and often described in literature, originates from the corrosion of the glass layer inside the contacts by acetic acid. This corrosion is shown to be accelerated by an applied negative voltage, underlining the parallels to the findings of interaction of pastes with plating electrolytes. It was successfully proven by CVS, EDXS and ICP-OES measurements that this traces back to the reduction of the dissolved lead at the contact, which additionally supports the model derived for electrolyte-paste interaction. Complemented by generated Pourbaix diagrams of lead in acetic acid solutions a model of the corrosion mechanism was developed.¹⁵

As a fifth task, a cost of ownership calculation shows a production cost advantage for the investigated copper front side metallization of 2-10 €/wafer compared to the standard silver screen-printed solar cell metallization depending on the silver price.

¹⁵ The corrosion of printed solar cell contacts due to the interaction with acetic acid is accepted for publication in the **Journal of Photovoltaics**: A. Kraft, L. Labusch, T. Ensslen, I. Dürr, J. Bartsch, M. Glatthaar, S.W. Glunz, H. Reinecke, *Investigation of Acetic Acid Corrosion Impact on Printed Solar Cell Contacts*, vol. 5 Issue 3, pp. 736-743, **2015**

The results obtained in this work give impulses for further investigations regarding the copper front side metallization for silicon solar cells based on printed seed-layers and beyond this topic.

The mechanical behaviour of the plated contacts was investigated during this work with large number of solder and peel-tests. It was noticed that the metal interfaces between silver seed-layer and plated nickel and between plated copper and silver capping layer never failed independent of the experimental conditions. The failure of the interface between printed seed-layer and silicon wafer was subject of detailed investigations. The only interface which additionally was observed to fail sometimes was the interface between nickel and copper. The practical experiences show that tempering of the plated metal stack at $\sim 275^{\circ}\text{C}$ for a few minutes or acidic pre-treatment of the plated nickel before copper plating reduce this effect. But still this offers room for further systematic studies to determine the reason for this phenomenon and to understand the differences between samples that were similarly processed at first glance.

Another important factor to allow the industrial implementation of the investigated metallization technique is the paste formulation. The rheological boundary conditions for fine screen-printed silver seed-layers were investigated in this work. Fine seed-layers with small wet-paste consumption were reproducibly achieved with screen-printing. To complement the results and to close the gap to the current industrial standard, further investigations of the seed-layer paste regarding the contact formation to the emitter are necessary. The example of the ink-jet-printed cells revealed that a contact formation comparable to standard screen-printed solar cells is possible. The further paste optimization to bring contact formation properties to the same level as the fully printed reference paste offers possibilities for even higher cell efficiencies with the seed-and plate approach using screen-printing in the future. As the most advanced contact formation system generally first employed for the standard printing paste and experimental fine line pastes for subsequent plating have less priority for paste manufacturers, it is likely that quick progress can be made in that respect.

The nickel distribution on the solar cell, which is important for the long term stability, has also been found to offer room for further improvement. It was shown on lab scale that adaptations of the anode position and geometry as well as electrochemical shielding and pulse plating offer the potential to improve the nickel homogeneity on the cell by improving the deposition conditions at the busbars considerably. The possible parameter range was not exhausted in this work, which offers the potential for further improvement. These improvements

should be adapted to the inline plating tools. A more homogenous nickel deposition leads to lower needed nickel masses, or even more important regarding contact adhesion, to reduced process times for nickel plating.

If solar cells with copper metallization become a standard industrial product, a rapid aging test on cell level should be developed that allows to check the effectiveness of the nickel diffusion barrier and to estimate if long term stability issues due to copper diffusion will arise in a typical module lifetime. The damp heat test, already established on module level, is not qualified to show possible problems due to copper migration. First key factors for the design of such a test procedure can be derived from this work. In general, the measurement of the pFF is well suited as characterisation procedure for copper diffusion in solar cells. The measurement equipment is cheap and the procedure is fast and simple. Temperatures between 150°C and 250°C should be used in order to create a rapid response and simultaneously avoid nickel diffusion which can distort the test results at higher temperatures. Further, a constant measurement frequency should be chosen. For the cell configuration tested in this work a frequency > 3.5 h will exclude the influence of copper diffusion deceleration by frequent cooling cycles. If these boundary conditions are considered the results in this work indicate that a prediction of the degradation behaviour at lower constant temperatures is possible.

In this work several technical obstacles for plated copper front side metallization on printed seed-layers for silicon solar cells were investigated. Although further investigation is needed at some points none of investigated issues was found to be a criterion of exclusion for industrial realization of this metallization architecture. Seed-layers can be reproducibly printed using the wide spread screen-printing technique which enables a total silver consumption of less than 15 mg/cell for the front side metallization. Sufficient contact adhesion of 1.5 N/mm after nickel plating can be realized by process times ≤ 1 minute and a dilution of the electrolyte. Copper diffusion cannot be stopped in general but decelerated by the use of a plated nickel diffusion barrier to a tolerable level, which makes the degradation impact during a normal module lifetime of 40 years very improbable.

Whether the investigated metallization architecture will be used for solar cell mass production in the future or not depends on the successful development of a seed-layer paste with excellent contacting ability and of economic factors like the silver market price and the price development of the plating tools. For special

solar cell concepts like bifacial cells, where both sides of the solar cell feature a screen-printed silver contact grid, the investigated contact architecture is particularly suited because the silver savings are twice as high as for the standard BSF solar cell concept, and the plating can be done simultaneously on both sides. This niche application can for example offer the possibility that the plated copper metallization on screen-printed seed-layers can show its potential to the market and the PV-community.

Deutsche Zusammenfassung

In der vorliegenden Arbeit wurde eine neuartige Vorderseitenmetallisierung für Silizium Solarzellen auf der Basis einer gedruckten Saatschicht, die mit Nickel, Kupfer und Silber galvanisch verstärkt wird, wissenschaftlich erforscht. Die Kontaktstruktur wurde entwickelt, um einen großen Teil des üblicherweise ausschließlich eingesetzten und wesentlich teureren Silbers für die Vorderseitenmetallisierung von Silizium Solarzellen durch Kupfer zu ersetzen. Zudem können unterschiedliche Anforderungen an das Kontaktierungssystem der Solarzelle durch Trennung der Funktionen „Kontaktbildung“ und „Leitfähigkeit“ flexibler optimiert werden. Motiviert durch technologische Herausforderungen bei der industriellen Umsetzung dieser Metallisierungsstruktur, die durch experimentelle Arbeiten gezielt adressiert wurden, konnte das wissenschaftliche Verständnis zu dieser speziellen Solarzellen-Kontaktstruktur und darüber hinaus erweitert werden.

Bei der Herstellung der Kontakte wird zunächst eine sehr dünne Saatschicht aus Silber auf die Solarzellen-Vorderseite aufgedruckt und anschließend galvanisch verstärkt. Die feine Silberschicht ermöglicht die Kontaktbildung zum Emitter und dient als Saatschicht für die elektrochemische Abscheidung von $\sim 1 \mu\text{m}$ Nickel als Diffusionsbarriere, gefolgt von einer $\sim 8\text{--}10 \mu\text{m}$ dicken Kupferschicht, die als Leitschicht dient und einer feinen $\sim 0,5 \mu\text{m}$ dicken Silber-Deckschicht. Diese dient sowohl dem Schutz gegen Kupferoxidation als auch zur besseren Lötbarkeit der Kontakte. Im Rahmen der Arbeit wurde grundlegendes Verständnis zum Druck feiner Saatschichten mit möglichst geringem Silberverbrauch, zur Korrosion der gedruckten Kontakte durch Interaktion mit Elektrolytlösungen und Chemikalien und durch Essigsäure im Modul, sowie zur Degradation von Solarzellen durch Kupfermigration, erarbeitet.

Im Bereich des Saatschichtdruckes wurden verschiedene, gezielt in ihrer Rheologie variierte experimentelle Siebdruck-Silberpasten auf ihre Druckeigenschaften, auf die erreichbare Kontakt-geometrie und den Silberübertrag der damit gedruckten und gefeuerten Kontakte analysiert. Dabei konnte gezeigt werden, dass kleine Silberpartikel in der Paste und eine Fließgrenze von $>400 \text{ Pa}$ sowohl für schmale gedruckte Kontaktstrukturen, als auch für einen geringen Silberübertrag vorteilhaft sind. Mit einer anhand dieser Ergebnisse bezüglich der Rheologie optimierten Feinlinienpaste konnten minimale Kontaktfingerbreiten von $30 \mu\text{m}$ im Siebdruckverfahren realisiert werden. Hinsichtlich der benötigten

Silbermenge wurden siebgedruckte Saatschichten mit Saatschichten, die in alternativen, für den Saatschichtdruck besonders geeigneten, Verfahren (Ink-jet-Druck, Aerosol-jet-Druck und Flexodruck) hergestellt wurden, verglichen. Für alle Verfahren konnte ein Gesamtsilberverbrauch (Silbersaatschicht + Silberdeckschicht) für die Vorderseitenmetallisierung von $156 \times 156 \text{ mm}^2$ Solarzellen von $<15 \text{ mg/Zelle}$ für ein Standard-Grid mit drei Busbars erreicht werden. Dies entspricht einer Silberreduzierung gegenüber der üblicherweise verwendeten Silber-metallisierung von $>80\%$. Hinsichtlich der elektrischen Parameter wurde auf den Zellen mit gedruckten Saatschichten im Tintenstrahl-Verfahren das Wirkungsgradniveau der Referenzzellen mit Siebdruck-Vollaufbau-Metallisierung von 19.2% auf industriellen Standard Back-Surface-Field Solarzellen erreicht. Für die Saatschichten, die mit Aerosoldruck und im Siebdruckverfahren hergestellt wurden, konnte ein Optimierungsbedarf der Pasten Zusammensetzung hinsichtlich verbesserter Kontaktbildungs-eigenschaften aufgedeckt werden.

Die reduzierte Kontakthaftung infolge der Interaktion der gedruckten Saatschicht mit Elektrolytlösungen stellt ein massives Hindernis für die industrielle Verschaltung von Solarzellen mit der untersuchten Metallisierungsstruktur dar. Um die Ursache der Kontaktkorrosion zu analysieren wurde ein Expositions-Schnelltest für Solarzellen-Kontakte mit anschließender quantitativer Kontakthaftungscharakterisierung entwickelt. Damit konnte der direkte Einfluss verschiedener Elektrolytlösungen und der darin verwendeten Chemikalien auf die Kontakthaftung gedruckter Solarzellen-Kontakte gezielt untersucht werden. Ergänzt durch eine ausführliche Analyse der Kontaktmikrostruktur mittels Rasterelektronenmikroskop, Transmissionselektronenmikroskop, Rasterkraftmikroskop, chemischer Spurenanalyse der Lösungen nach Exposition der Kontakte sowie Materialuntersuchungen mit Röntgenbeugung, ermöglichten die Ergebnisse die Entwicklung eines Modells des zugrundeliegenden Korrosionsmechanismus. Es konnte gezeigt werden, dass der Kontakthaftungsrückgang auf die Korrosion der Glasschicht innerhalb des gedruckten Kontaktes zurückgeht. Durch die Lösung des Bleioxids und der Silberbestandteile, des in Solarzellen-Kontakten üblicherweise verwendeten Bleiglasses, durch den sauren Elektrolyten, kommt es zu einer Spaltbildung entlang der Glas-Silber Grenzfläche im Kontakt, welche dem großflächigen Haftungsverlust ursächlich zugrunde liegt. Beschleunigend für diese Spaltbildung wirken Bestandteile wie Sulfate und Chloride im Elektrolyten, die mit dem gelösten Blei und Silber Bleisulfat und Silberchlorid bilden. Dies verschiebt die Gleichgewichtsreaktionen, die der Glaskorrosion zugrunde liegen und die im

Verlauf der Arbeit identifiziert werden konnten in Richtung weiterer Glasauflösung. Einen noch stärker beschleunigenden Effekt auf die Korrosion hat die während der elektrochemischen Metallabscheidung an die Solarzelle angelegte negative Spannung. Hierdurch werden das gelöste Blei und Silber aus der Lösung am Kontakt direkt wieder reduziert, was starken Einfluss auf das Lösungsgleichgewicht hat. Je mehr des gelösten Bleis und Silbers durch Reduktion aus dem Elektrolytssystem entfernt wird, desto größer wird die Triebkraft für eine weitere Auflösung der Glasschicht. Die Reduktion gelöster Bestandteile ist dort besonders effektiv wo die Distanz zwischen dem Ort der Auflösung (Glasschicht) und dem Ort der Reduktion (Silberschicht) im Kontakt besonders klein ist. Dies führt zu der in der Mikrostruktur-analyse beobachteten schnell fortschreitenden ortsspezifischen Spaltbildung entlang der Silber-Glas Grenzfläche im Kontakt. Die Effektivität der Reduktion vor allem des Bleis ist zudem stark vom Reduktionspotential der weiteren in der Lösung befindlichen Kationen abhängig. Befinden sich wie im Kupferelektrolyt wesentlich edlere Kupfer-Ionen in der Lösung, so läuft deren Reduktion gegenüber der des gelösten Bleis stark bevorzugt ab. Auf diese Weise wird die Bleireduktion blockiert und es kommt zu keiner signifikanten Kontaktkorrosion innerhalb des Zeitfensters des entsprechenden Galvanik Prozesses. Befinden sich jedoch Nickel-Ionen in der Lösung, die ein leicht unedleres Reduktionspotential als Blei aufweisen, so ist die Reduktion des gelösten Bleis bevorzugt bzw. läuft parallel zur Nickelreduktion ab. Dies erklärt, warum ausschließlich der Nিকেlelektrolyt eine starke Kontakt-korrosion verursacht, während die Kontakthaftung durch Interaktion mit dem Kupferelektrolyt trotz längerer Prozessdauer und niedrigerem pH-Wert kaum beeinträchtigt wird.

Im Themenbereich der Kupfermigration wurde durch eine Experimentreihe mit Lebensdauerproben gezeigt, dass industriell mit dem PECVD oder dem Sputter-Verfahren abgeschiedene Siliziumnitrid-schichten, selbst nach vorheriger HF-Exposition (1%, 30 Sekunden) oder mechanischer Belastung durch Siebdruck, die Kupferdiffusion wirksam verhindern. Dem kommt eine besondere Bedeutung zu, da die elektrochemisch abgeschiedene Kupferschicht die zuvor abgeschiedene Nickeldiffusions-barriere an den Rändern der Metallisierungsstruktur zwangsläufig überragt und damit dauerhaft direkt mit der Siliziumnitridschicht in Kontakt steht. Die Effektivität der abgeschiedenen Nickeldiffusionsbarriere gegen Kupferdiffusion wurde anhand von prozessierten Solarzellen mit unterschiedlicher Nickel Diffusionsbarrierendicke analysiert. Zur Charakterisierung des Degradationszustandes wurde der Pseudo-Füllfaktor der

Solarzellen nach thermischem Stress auf Heizplatten bei Temperaturen zwischen 175°C und 275°C bestimmt und mittels Arrheniusplots ausgewertet. Dies erlaubt sowohl die Bestimmung der Aktivierungsenergie aus der Steigung der linearen Regression, als auch die Extrapolation auf die maximalen Betriebsbedingungen von Solarzellen, die bei 80°C angenommen wurden. Es konnte gezeigt werden, dass 20 mg abgeschiedenes Nickel pro Zelle, was für die gewählte Abscheidekonfiguration an der dünnsten Stelle einer Schichtdicke von $\sim 0.2 \mu\text{m}$ entspricht, ausreichen, um während der Lebensdauer von Modulen ($\gg 20$ Jahre) eine Degradation durch Kupfermigration zu verhindern, die über 5% der ursprünglichen Leistungsfähigkeit der Zelle hinausgeht. Des Weiteren wurde die Homogenität der Nickelabscheidung über die gesamte Zellfläche analysiert. Dabei wurden Inhomogenitäten zu Ungunsten der Nickelabscheidung am Busbar gezeigt. Dort kommt es zu einer um 80-90% geringeren Abscheidung als an den Kontaktfingern. Durch Veränderung der Anoden-geometrie, durch gepulste Nickelabscheidung und durch Einbringung einer elektrochemischen Abschirmung konnte die Nickelabscheidung am Busbar um bis zu 50% gesteigert werden. Dies verbessert die Gesamthomogenität der Nickelschicht auf der Zellfläche erheblich und kann genutzt werden, um die abzuschcheidende Nickelmenge zu reduzieren, bzw. kürzere Prozesszeiten zu ermöglichen.

Auf Modulebene kommt es zur Interaktion von gedruckten Silber-Vorderseitenkontakten mit Essigsäure, die in Zusammenhang mit Feuchtigkeit aus dem Einkapselungsmaterial EVA freigesetzt wird. Mit Hilfe chemischer Spurenanalyse, Pourbaix-Diagrammen, einer Mikrostrukturanalyse und zyklischer Voltammetrie konnte die Ursache des in der Literatur als „Damp heat induced degradation (DHID)“ bezeichneten Degradationsphänomens von Solarmodulen ermittelt werden. Der Korrosion der Vorderseitenkontakte durch Essigsäure liegt ein sehr ähnliches Reaktionsmodell wie bei der Korrosion durch Elektrolytlösungen zugrunde. Es wird ebenfalls die Glasschicht im Kontakt durch die Essigsäure angegriffen, wobei angelegte negative Spannungen beschleunigend wirken. Es konnte experimentell bewiesen werden, dass dieser Beschleunigungseffekt auf die Reduktion des aus der Glasschicht gelösten Bleis zurückgeht, die nur bei angelegter negativer Spannung in erhöhtem Maße auftritt. Dieses Verständnis des Korrosionsmechanismus ermöglicht dessen Verminderung z.B. durch den Betrieb von Solarmodulen auf positivem Potential, und damit eine Lebensdauerverlängerung für Solarmodule, die Solarzellen mit gedruckten Silber-Vorderseitenmetallisierungen enthalten.

In einer Betriebskostenrechnung wurden die Herstellungskosten von Solarzellen mit Standard-Silbermetallisierung mit den Herstellungskosten von Zellen mit der untersuchten Kupfermetallisierung verglichen und hinsichtlich der Sensitivität gegenüber dem Silberpreis analysiert. Unter Einbeziehung aller bei den verschiedenen Herstellungsprozessen beteiligten Kosten wurde ein Kostenvorteil für die Kupfermetallisierung berechnet, der je nach Silberpreis zwischen ~2 und ~10 ¢/Zelle schwankt.

Appendix A

Pourbaix diagrams show the thermodynamics of aqueous corrosion reactions assembled from the Gibbs energy of the formation of the ionic species [173].

A.1 Pourbaix diagrams of silver in aqueous solution

In this section Pourbaix diagrams of silver found in literature are shown. With the Pourbaix diagrams it can be pointed out that the reactions (equation 7.4 and 7.5) suggested in section 7.4.2 and concluded to happen with dissolved silver out of the solar cell contact due to exposure in the nickel electrolyte, are probable regarding the under laying thermodynamics.

Fig. A 1 shows the Pourbaix diagram of silver with concentration dependency of the aqueous species ranging for 1 to 10^{-6} mol/l. The nickel electrolyte works at a pH of ~ 4 (marked in the diagram with a red dashed line). In the acidic area silver is dissolved from its oxide form. The driving force for this dissolution is stronger the smaller the Ag^+ concentration in the solution. This means that for high Ag^+ concentrations the reaction slows down. This is exactly the reaction suggested in equation 7.5.

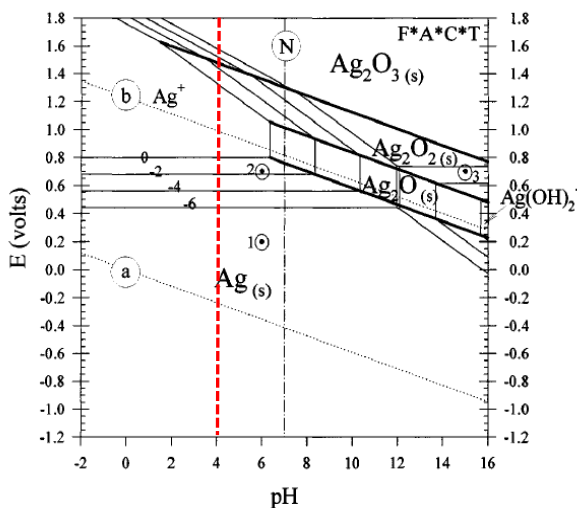


Fig. A 1: Pourbaix diagram of silver at 25°C. The calculation of the aqueous species range from 1 to 10^{-6} mol/l [133].

The formation of hardly soluble species like silver chloride promote the further dissolution of silver oxide out of the glass layer in the contact because it shifts the dissolution equilibrium by taking Ag^+ ions out of the system. This reaction is suggested by equation 7.4 and the related thermodynamics can be seen in the Pourbaix diagram of silver in chloride solution in Fig. A 2. The Pourbaix diagram shows additionally that with applied cathodic voltage, the parallel reduction of the dissolved species is possible, which offers another possibility to shift the reaction equilibrium. The reduction reaction is part of the corrosion model worked out in section 7.6.

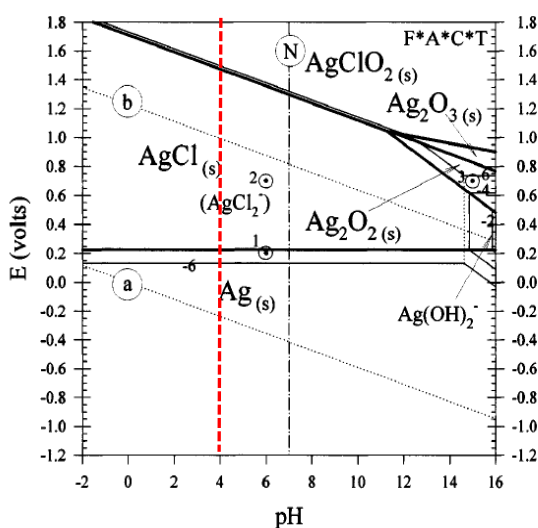


Fig. A 2: Pourbaix diagram of silver at 25°C in chloride solution at a Cl^- concentration of 1 mol [133]

A.2 Pourbaix diagrams of lead in aqueous solution

In this section Pourbaix diagrams of lead found in literature are shown. With the Pourbaix diagrams it can be pointed out that the reactions (equation 7.1 - 7.3) suggested in section 7.4.2 and concluded to happen with dissolved lead out of the solar cell contact due to exposure in the nickel electrolyte, are probable regarding the under laying thermodynamics.

Fig. A 3 shows the Pourbaix diagram of lead in aqueous solution. The nickel electrolyte works at a pH of ~ 4 (marked in the diagram with a red dashed line).

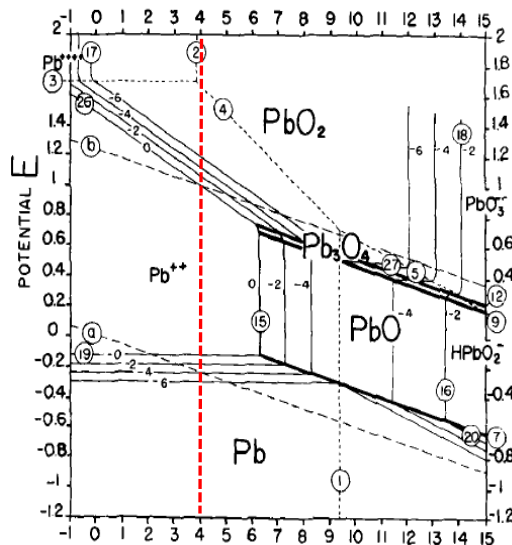


Fig. A 3: Pourbaix diagram of lead in aqueous solution at 25°C [142]

In acidic environment lead oxide, which is a compound in the glass layer, is dissolved to Pb^{2+} . The driving force for this dissolution is stronger the smaller the Pb^{2+} concentration in the solution. This means that for high Pb^{2+} concentrations the reaction slows down. This is exactly the reaction suggested in equation 7.3.

Fig. A 4 show the Pourbaix diagram of lead in the presence of sulphate ions. It becomes clear that the reaction suggested in equation 7.1 and 7.2 where lead and lead oxide reacts to lead sulphate are thermodynamically favoured in acidic environment.

Both Pourbaix diagrams of lead show that taking an over potential for hydrogen evolution into account the reduction of lead at a suitable potential is possible. This reduction possibility is part of the corrosion model worked out in section 7.6.

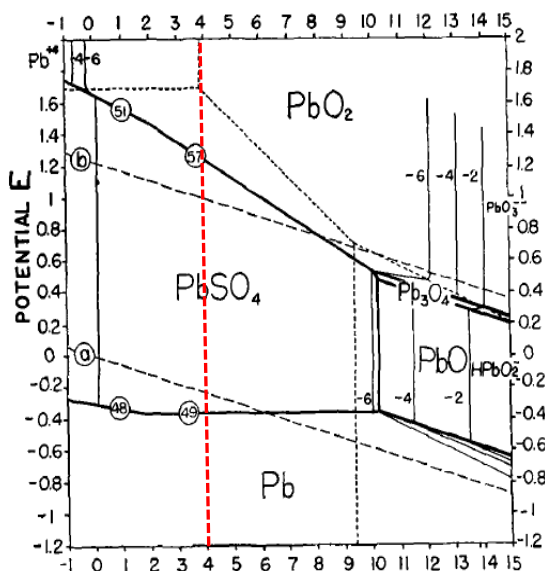


Fig. A 4: Pourbaix diagram of lead in the presence of sulphate ions at 25°C [142]

Appendix B

B.1 Diffractograms of powder XRD measurements

To investigate the material change in the fired seed-layer front side contact due to exposure in the Watts-type nickel electrolyte powder XRD measurements with different compounds and compound combinations of solid materials contained in the silver front side metallization of silicon solar cells were performed (for detailed experiment description compare section 7.4.2). A summary of the findings for each compound is given in Table 7.3. In this section the diffractograms of each compound before and after electrolyte exposure, are presented.

Diffractogram of lead powder (compound no. 1) before (black curve) and after electrolyte exposure (red curve).

Result: Lead sulphate peaks can be observed in the pattern after exposure (red line).

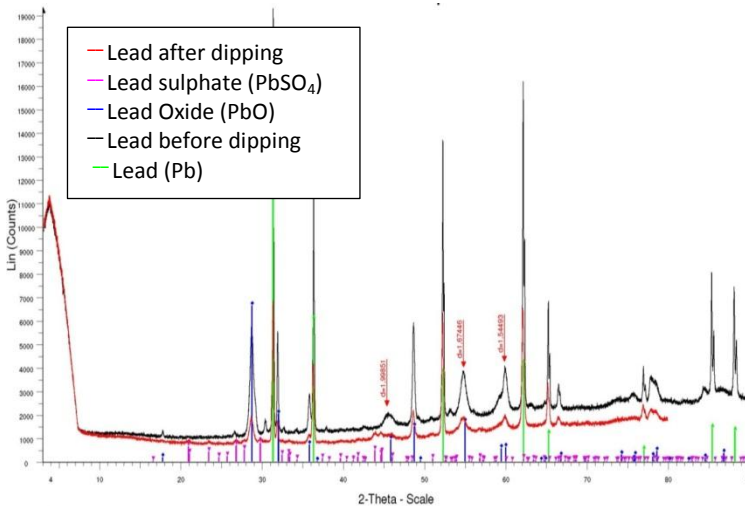


Fig. A 5: Diffractogram from lead powder before (black curve) and after (red curve) nickel electrolyte exposure

Diffractograms of lead oxide powder (compound no. 2) before and after electrolyte exposure.

Result: different variations of lead oxide are found in both patterns. After electrolyte exposure additional, lead sulphate peaks can be observed.

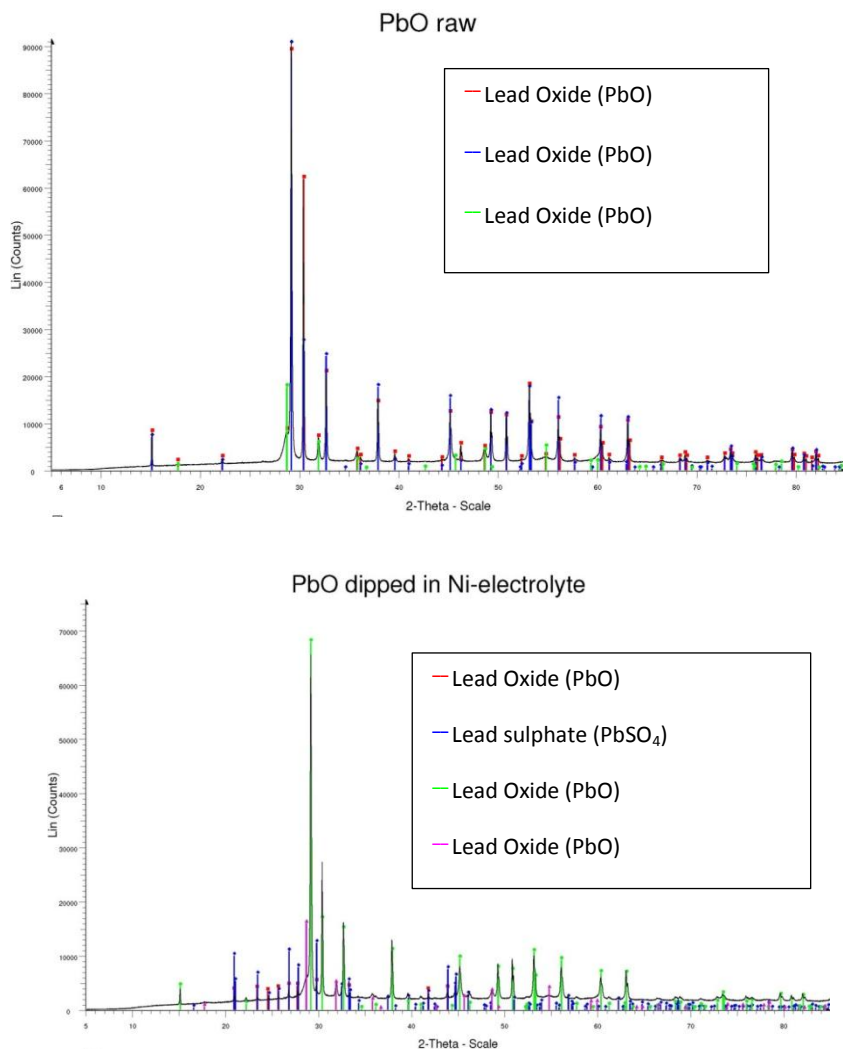


Fig. A 6: Diffractograms of lead oxide powder before (upper diagram) and after (lower diagram) nickel electrolyte exposure

Diffractograms of silver powder (compound no. 3) before and after electrolyte exposure.

Result: silver powder remains unaltered after exposure to the Watts-type nickel electrolyte.

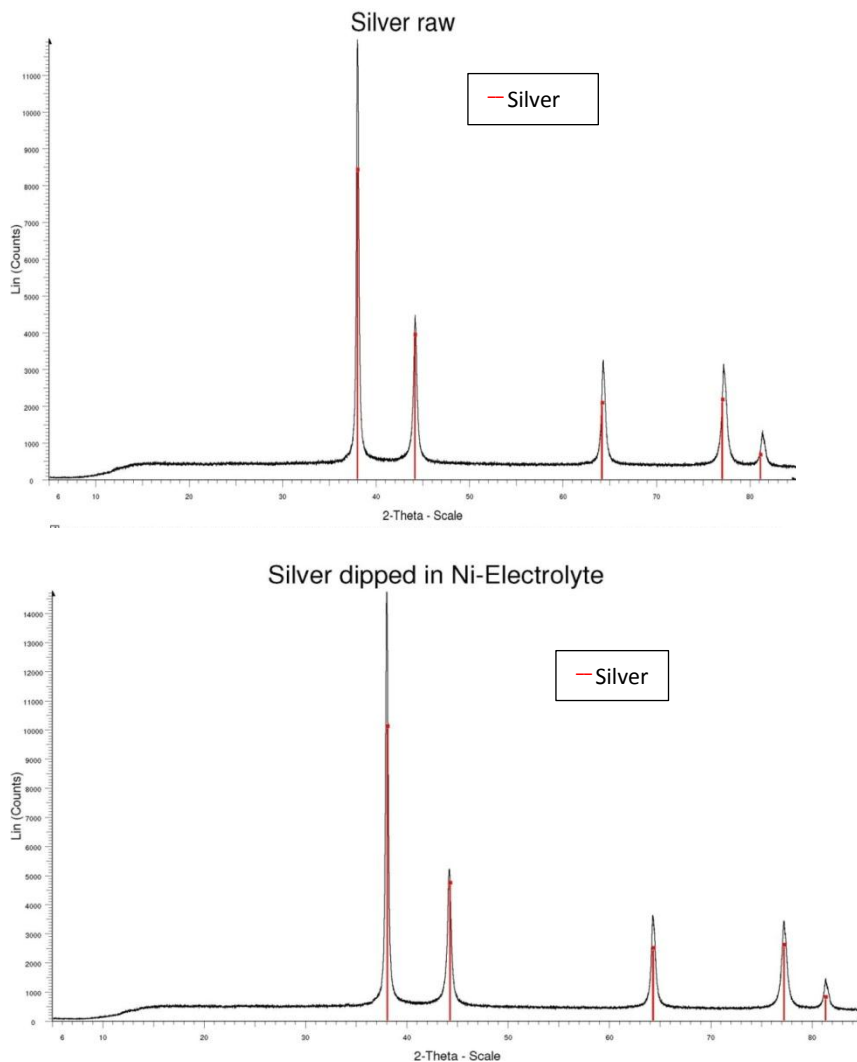


Fig. A 7: Diffractograms from silver powder before (upper diagram) and after (lower diagram) electrolyte exposure

Diffractograms of silver oxide powder (compound no. 4) before and after electrolyte exposure.

Result: after electrolyte exposure silver chloride peaks instead of silver oxide peaks can be observed.

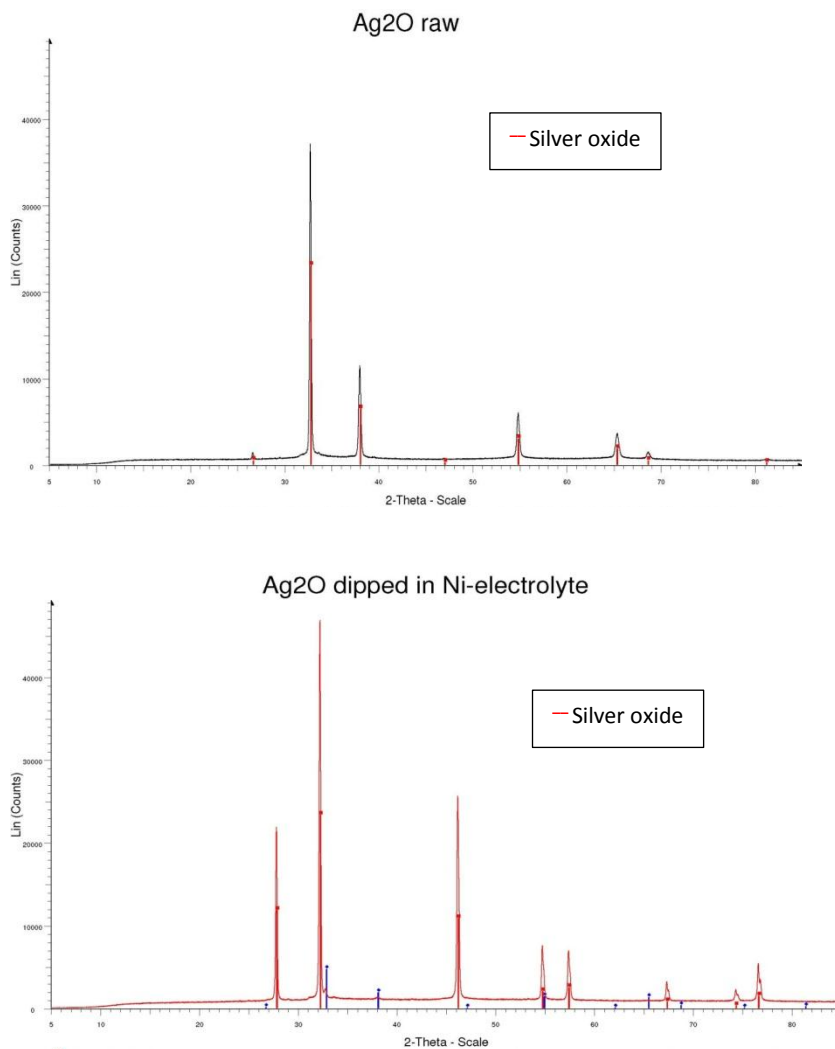


Fig. A 8: Diffractograms of silver oxide powder before (upper diagram) and after (lower diagram) electrolyte exposure

Diffractiongrams of silver (5%) + lead (95%) powder (compound no. 5) before and after electrolyte exposure. Result: most of the lead was oxidized by air, and the silver formed an alloy with the lead; after electrolyte exposure lead sulphate peaks can be observed clearly.

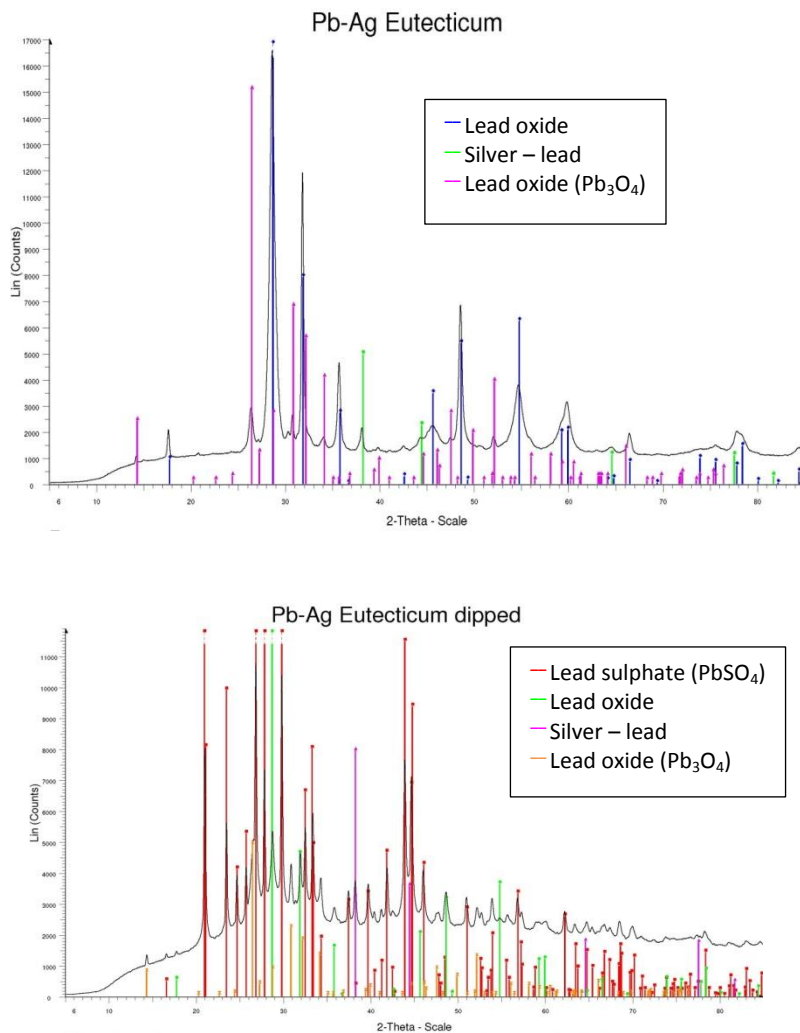
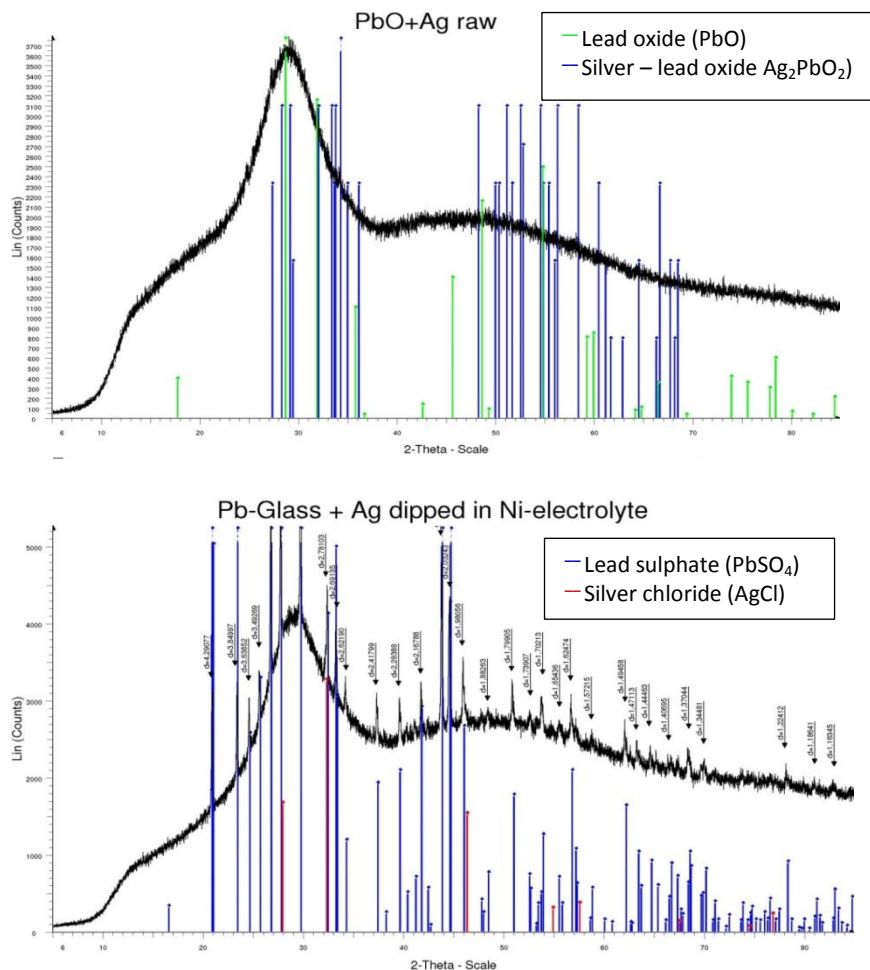


Fig. A 9: Diffractiongrams fo silver – lead powder before (upper diagram) and after (lower diagram) electrolyte exposure

Diffractograms of silver (30%) + lead glass (70%) powder (compound no. 6) before and after electrolyte exposure. Result: These diffractograms are uncertain, because glass is amorphous, therefore not suitable for XRD characterization. The lead sulphate peaks after dipping are visible, but the silver presence in both diffractograms cannot be assure. Most of the silver separated from the glass phase after cooling, so the amount of silver in this sample is probably very little.



Diffractograms of lead glass (50%) + silver (25%) + silicon (25%) powder (compound no. 7) before and after electrolyte exposure. Result: the presence of silicon dioxide and elemental lead agree with the contact formation theory. After electrolyte exposure, lead oxide is not present anymore, but lead sulphate can be observed. Elemental silver is unaffected.

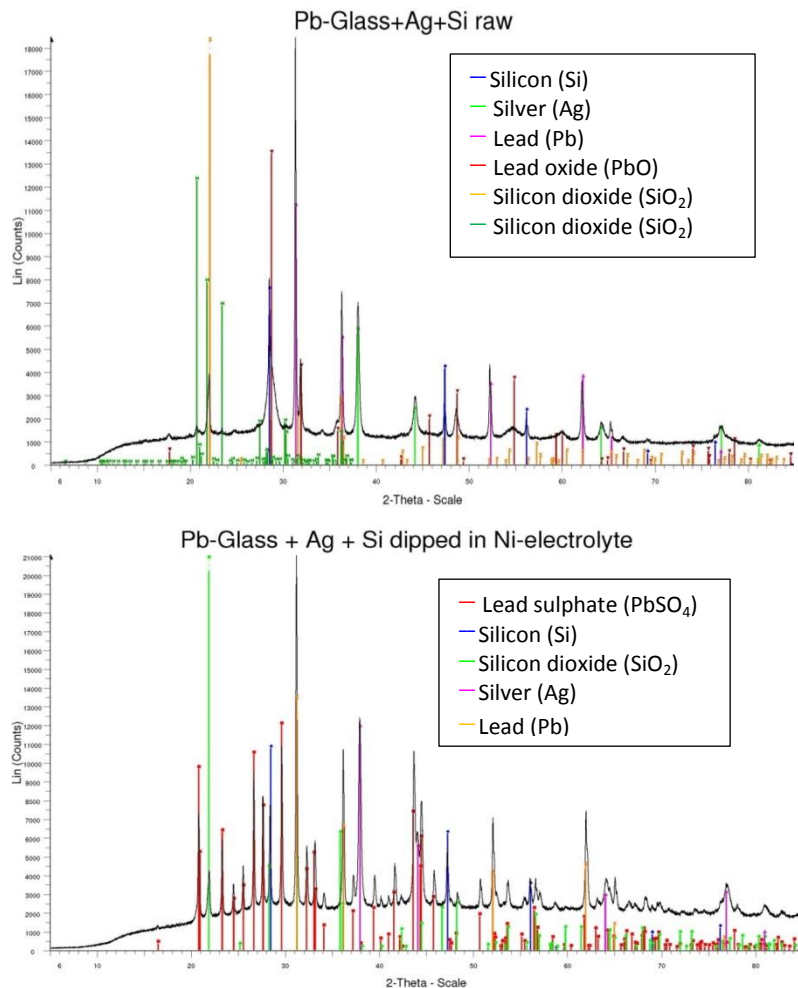


Fig. A 11: Diffractograms of silver + lead glass and silicon powder before (upper diagram) and after (lower diagram) electrolyte exposure

Diffractograms of lead glass (40%) + silver (20%) + silicon (20%) + silicon nitride (20%) powder (compound no. 8) before and after electrolyte exposure.
 Result: The addition of silicon nitride cannot be spotted, since the silicon nitride interacts with lead glass, producing silicon dioxide and nitrogen gas. After electrolyte exposure lead sulphate peaks can be observed.

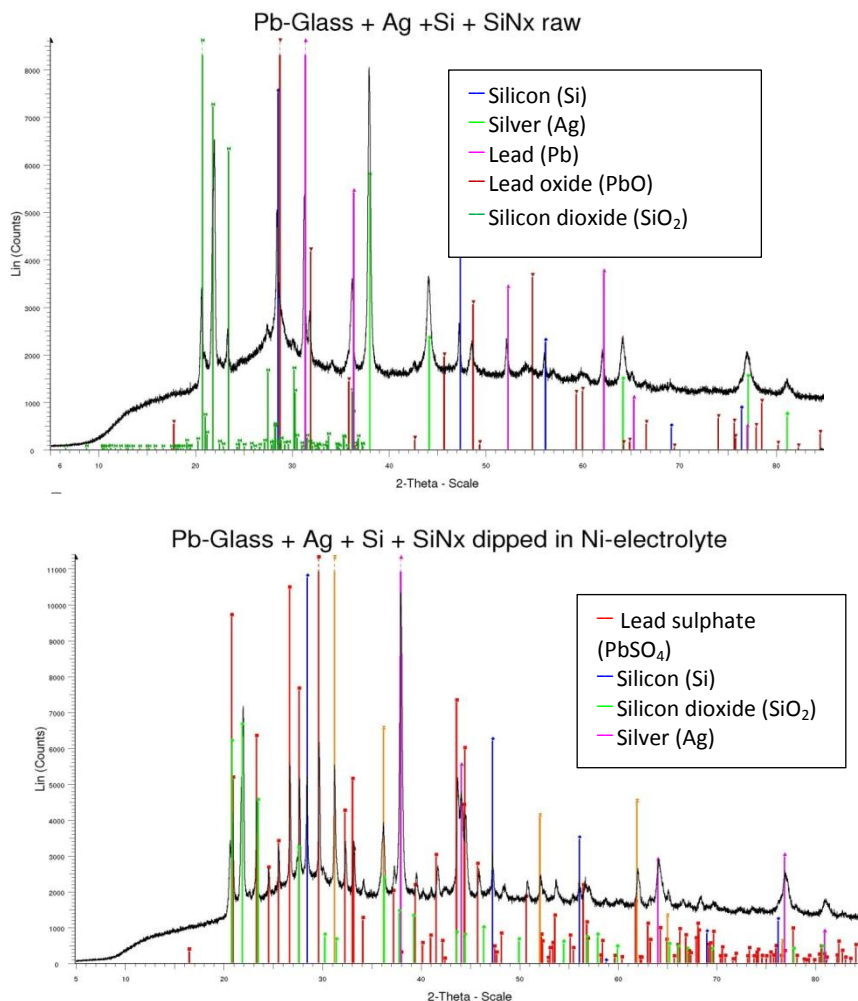


Fig. A 12: Diffractograms of silver + lead glass + silicon and silicon nitride powder before (upper diagram) and after (lower diagram) electrolyte exposure

List of Publications

Articles in peer reviewed journals

A. Kraft, Y. Pernia, L. Ni, A. Filipovic, A. Hähnel, A. Graff, J. Bartsch, M. Glatthaar, *Microstructure analysis of the interaction between Watts-type nickel electrolyte and screen-printed solar cell contacts*, Electrochemical Society Journal of Solid State Materials and Technology, vol. 3: pp. Q55-Q60, **2014**.

A. Kraft, Y. Pernia, A. Kalio, A. Gautrein, L. Ni, J. Bartsch, S. W. Glunz, H. Reinecke, *Origin of corrosion effects in solar cell contacts during electrochemical nickel deposition*, Journal of Applied Electrochemistry, Volume 45, Issue 1, Page 95-104, **2015**.

A. Kraft, C. Wolf, J. Bartsch, M. Glatthaar, S. W. Glunz, *Long Term Stability of Copper front side Contacts for Crystalline Silicon Solar Cells*, Journal of Solar Energy Materials & Solar Cells, vol. 136, pp. 25-31, **2015**.

A. Kraft, L. Labusch, T. Ensslen, I. Dürr, J. Bartsch, M. Glatthaar, S.W. Glunz, H. Reinecke, *Investigation of Acetic Acid Corrosion Impact on Printed Solar Cell Contacts*, Journal of Photovoltaics, vol. 5 Issue 3, pp. 736-743, **2015**.

A. Lorenz, A. Kalio, T. Barnes Hofmeister, A. Kraft, J. Bartsch, F. Clement, H. Reinecke, D. Biro, *Developing a High Throughput Printing Technology for Silicon Solar Cell Front Side Metallisation using Flexography* Journal of Print and Media Technology Research, vol. 47, pp. 1408-1426, **2014**.

Contributions to national and international conferences

M. Wendling, A. Mondon, A. Kraft, J. Bartsch, M. Glatthaar, S. W. Glunz, *Analysis of Chemical Stability of Printing Pastes in Electrochemical Plating Solutions*, in: Proceedings of the 2nd International Conference on Silicon Photovoltaics, Leuven, Belgium, **2012**.

Poster presentation by the first author, scientific publication in conference proceedings

J. Bartsch, A. Mondon, M. Kamp, A. Kraft, M. Wendling, M. Mehling, N. Wehkamp, M.N. Jawaide, A. Lorenz, F. Clement, C. Schetter, M. Glatthaar, S.W. Glunz, *Progress with Multi-Step Metallization Processes Featuring Copper as Conducting Layer at Fraunhofer ISE*, in: Proceedings of the 26th European PV Solar Energy Conference and Exhibition, Frankfurt, Germany, **2012**.

Oral presentation by the first author, scientific publication in conference proceedings

S. Olweya, A. Kalio, A. Kraft, E. Deront, A. Filipovic, J. Bartsch, M. Glatthaar, *Fine-line Silver Pastes for Seed-layer Screen-printing with Varied Glass Content*, in: Proceedings of the 4th Workshop on Metallization of Crystalline Silicon solar Cells, Konstanz, Germany, **2013**

Oral presentation by the first author, scientific publication in conference proceedings

A. Lorenz, A. Kalio, G.T. Hofmeister, S. Nold, A. Kraft, J. Bartsch, D. Wolf, M. Dreher, F. Clement, D. Biro, *Flexographic Printing- High Throughput Technology for Fine Line Seed-layer Printing on Silicon Solar Cells*, in: Proceedings of the 27th European PV Solar Energy Conference and Exhibition, Paris, France, **2013**.

Oral presentation by the first author, scientific publication in conference proceedings

A. Kraft, L. Ni, A. Kalio, A. Moldovan, J. Bartsch, M. Glatthaar, S. W. Glunz, *Influence of the chemicals used in nickel and copper plating solutions on the adhesion of screen-printed silver contacts*, in: Proceedings of the 3rd International Conference on Silicon Photovoltaics, Hamelin, Germany, **2013**.

Poster presentation by the first author, scientific publication in conference proceedings

A. Kraft, C. Wolf, A. Lorenz, J. Bartsch, M. Glatthaar, S. W. Glunz, *Long term stability analysis of copper front side metallization for silicon solar cells*, in: Proceedings of the 4th International Conference on Silicon Photovoltaics, 's-Hertogenbosch, the Netherlands, **2014**.

Poster presentation by the first author, scientific publication in conference proceedings

A. Kraft,

Chemische und elektrochemische Korrosionseffekte an siebgedruckten Ag-Vorderseiten-Kontakten von Silizium Solarzellen, Silicon Forest Workshop, Falkau, Germany, **2014**.

Oral presentation

A. Kraft, C. Wolf, J. Bartsch, M. Glatthaar,

Characterization of copper diffusion in silicon solar cells, in: Proceedings of the 5th Workshop on Metallization of Crystalline Silicon solar Cells, Konstanz, Germany, **2014**.

Oral presentation by the first author, scientific publication in conference proceedings

I. Dürr, S. Hoffmann, A. Kraft, J. Bartsch, C. Schmiga, D. Eberlein, K. A. Weiß, U. Eitner, H. Wirth,

Metallization Material Qualification in Terms of Damp Heat induced Degradation, in: Proceedings of the 5th Workshop on Metallization of Crystalline Silicon solar Cells, Konstanz, Germany, **2014**.

Oral presentation by the first author

G. Cimiotti, J. Bartsch, A. Kraft, A. Mondon, M. Glatthaar,

Design Rules for Solar Cells with plated Metallization, in: Proceedings of the 5th Workshop on Metallization of Crystalline Silicon solar Cells, Konstanz, Germany, **2014**.

Poster presentation by the first author, scientific publication in conference proceedings

M. Heinrich, A. Kraft, M. Lieder, B. Hoex, A.G. Aberle, M. Glatthaar,

Removal and Quantification of Background Plating on Silicon Wafer Solar Cells, accepted for presentation at the 5th International Conference on Silicon Photovoltaics, Konstanz, Germany, **2015**.

Poster presentation by the first author, scientific publication in conference proceedings

Other publications

J. Bartsch, M. Glatthaar, A. Kraft, M. Mondon, A. Lorenz, L. Sutor, S. Nold, S.W. Glunz,
Current trends in c-Si PV front side metallization, Photovoltaics International
20th Edition page 41-47, **2013**.

Patents

A. Kraft, J. Bartsch, M. Glatthaar, H. Nagel, H. Reinecke, *Solarmodul mit erhöhter Lebensdauer*
Ap. Nr. 10 2014 211 707.0

M. Heinrich, M. Lieder, M. Kamp, M. Glatthaar, A. Kraft, *Verfahren zur selektiven Entfernung von Background plating auf Siliziumsolarzellen*
Ap. Nr.: 10 2014 106140.3

Abbreviations and symbols

Abbreviation	Description
AFM	Atomic force microscopy
AM	Air mass
AR	Aspect ratio
ARC	Anti-reflection-coating
BSE	Back scattered electrons
BSF	Back surface field
CCD	Charge coupled detector
CE	Counter electrode
CHL	Compact Helmholtz pane
CoO	Cost of Ownership
CSS	Controlled shear stress
CVS	Cyclic voltammetric stripping
Cz-silicon	Czochralski grown silicon
DH	Damp heat
DHID	Damp heat induced degradation
DIN	Deutsches Institut für Normung
EDXS	Energy dispersive X-ray spectroscopy
EHT	Extreme high tension
ELI	Electroluminescence imaging
EN	European norm
EU PVSEC	European photovoltaic solar energy conference
EVA	Ethylene-vinyl acetate
FF	Fill factor
FIB	Focussed ion beam
FZ-silicon	Float zone silicon
HV	High voltage
HF	Hydrogen fluoride

ICP-OES	Inductively coupled optical emission spectroscopy
IEA	International energy agency
IEC	International Electrotechnical Commission
IHP	Inner Helmholtz pane
ISE	Institute for Solar Energy Systems (Fraunhofer)
IPCC	Intergovernmental Panel on Climate Change
ITRPV	International technology roadmap for photovoltaic
LC	Inductor Capacitor
LCOE	Levelized cost of electricity
LED	Light emitting diode
Mag	Magnification
MPI	Max Planck institute
MSA	Methane sulphuric acid
NDL	Nernst diffusion layer
NHE	Normal hydrogen electrode
OHP	Outer Helmholtz pane
PECVD	Plasma enhanced chemical vapour deposition
PID-controller	Proportional–integral–derivative controller
PID	Potential induced degradation
PLI	Photoluminescence imaging
PMMA	Polymethyl methacrylate
PP	Polypropylene
PSG	Phosphorous glass
PV	Photovoltaic
QSSPC	Quasi steady state photo conductance
RE	Reference Electrode
SCR	Space charge region
SE	Seconder electrons
SEM	Scanning electron microscopy
SEMI	Semiconductor equipment and materialinternational
STEM	Scanning Transmission electron microscopy

TCO	Total cost of ownership
TU	Technische Universität
TÜV	Technischer Überwachungsverein
UV	Ultra violet
WD	Working distance
WE	Working electrode

Symbol	Description	Unit
a	gap width at the rotational rheometer	m
a_O	screen opening fraction	%
c	cross section diameter of the screen wire	m
d	distance between atomic layers / wire separation distance	m
D	diffusion coefficient	$m^2 s^{-1}$
D_0	species specific diffusion factor	$m^2 s^{-1}$
D_1, D_2	Diodes	-
D_{it}	density of defects	$cm^{-3} eV^{-1}$
D_s	thickness of the screen mesh	m
D_{sc}	total screen thickness	m
E	electrode potential	V
E^o	reduction potential	V
E_A	activation energy	eV
E_C	energy level of conduction band edge	eV
E_F	Fermi-energy level	eV
E_g	band gap energy for silicon	eV
E_T	energy level of an impurity state in the bandgap of silicon	eV
E_V	energy level of valence band edge	eV
F	Force	N
FF	Fill factor	-
G_A	adhesive fracture energy	$J m^{-2}$
h	Planck constant	Js
I	electric current	A

j	current density	A m^{-2}
j_0	dark saturation current density	A m^{-2}
j_{01}	saturation current density in emitter and base	A m^{-2}
j_{02}	saturation current density in space charge region	A m^{-2}
j_{mpp}	current density at maximum power point	A m^{-2}
j_{PH}	photo generated current density	A m^{-2}
j_{rp}	current density at the parallel resistance	A m^{-2}
j_{SC}	short circuit current density	A m^{-2}
k	Boltzmann constant	eV K^{-1}
L	diffusion length	m
M	torque	Nm
mpp	maximum power point	-
n	electron concentration	cm^{-3}
n_A	integer	-
n_p	power law index	-
n_0	electron concentration in thermal equilibrium	cm^{-3}
n_a, n_b	diode ideality factors	-
n_l	SRH-density for electrons	cm^{-3}
n_i	intrinsic carrier concentration	cm^{-3}
n_s	electron concentration at the surface	cm^{-3}
N_C	effective density of states at the conductance band edge	cm^{-3}
N_V	effective density of states at the valence band edge	cm^{-3}
N_T	defect concentration	cm^{-3}
p	hole concentration	cm^{-3}
p_l	SRH-density for holes	cm^{-3}
p_0	hole concentration in thermal equilibrium	cm^{-3}
pFF	pseudo fill factor	-
p_s	hole concentration at the surface	cm^{-3}
q	elementary charge	C
\dot{Q}	rate of heat flow	J s^{-1}
R	cone radius	m

R^2	regression indicator	-
r_1	resistance of the base to metal contact	Ω
r_2	resistance of the semiconductor base	Ω
r_3	resistance of the semiconductor emitter	Ω
r_4	resistance of the emitter to metal contact	Ω
r_5	resistance of the contact fingers	Ω
r_6	resistance of the busbars	Ω
r_p	shunt (or parallel) resistance	Ω
r_s	series resistance	Ω
S	surface recombination velocity	$\text{cm}^3 \text{s}^{-1}$
t	time	s
T	temperature	K
U_i	recombination rate for recombination process I	$\text{cm}^3 \text{s}$
V	voltage	V
\dot{V}	volumetric flow rate	$\text{m}^3 \text{s}^{-1}$
V_a	voltage of the active cell area	V
V_{mpp}	voltage at maximum power point	V
V_{oc}	open circuit voltage	V
V_{rs}	voltage drop at series resistance	V
v_{th}	thermal velocity	cm s^{-1}
w	width	m
w_{min}	theoretical minimum contact finger width	m
α	cone angle	°
Δ	path difference of reflected wave fronts	m
Δ_n	excess charge carrier / excess electron concentration	cm^{-3}
Δ_p	excess hole concentration	cm^{-3}
Δ_{st}	thickness of the emulsion layer (emulsion over mesh)	m
λ	wave length of light	m
η	energy conversion efficiency	-
η_v	viscosity	Pas

ν	frequency	Hz
τ	shear stress	Pa
$\tau_{\theta\theta}$	shear stress at $\theta = \text{const.}$ and a given angle of twist θ	Pa
$\tau_{\text{Auger},n}$	carrier life time of Auger recombination in n-type Si	s
$\tau_{\text{Auger},p}$	carrier life time of Auger recombination in p-type Si	s
τ_i	carrier life time for recombination process i	s
τ_{eff}	effective excess carrier life time	s
τ_{rad}	carrier life time for radiative recombination	s
τ_y	yield stress	Pa
γ	deformation	%
$\dot{\gamma}$	shear strain rate	s^{-1}
μ_n	electron mobility	$\text{cm}^2 \text{V}^{-1} \text{s}^{-1}$
μ_p	hole mobility	$\text{cm}^2 \text{V}^{-1} \text{s}^{-1}$
σ_L	photo conductance	S m^{-1}
σ_n	capture cross-section of electrons	cm^2
σ_p	capture cross-section of holes	cm^2
τ_{SRH}	carrier life time due to Shockley-Read-Hall recombination	s
θ	angle of diffraction	°
Φ	incident power density	W/m^2
ϕ	angle of twist, peel angle	°

Danksagung

An dieser Stelle möchte ich den vielen Menschen danken, die zum Gelingen der Arbeit beigetragen haben und ohne deren Unterstützung die Fertigstellung nicht möglich gewesen wäre.

Meinen Betreuern Prof. Dr. Holger Reinecke und Prof. Dr. Eicke Weber danke ich für die Bereitschaft diese Arbeit zu betreuen. Die vielen Diskussionen und Gespräche mit wertvollen Anregungen haben mir immer wieder neue Impulse gegeben.

Ich danke Ansgar Mette und dem Team „Metallization“ bei Hanwha Q Cells für die super Betreuung meiner Master Arbeit, die eine sehr gute Vorbereitung für diese Arbeit war.

Meinen Kolleginnen und Kollegen am Fraunhofer ISE danke ich für die wunderbare Arbeitsatmosphäre, die vielen gemeinsamen Erlebnisse und allem voran natürlich für die fachlichen Gespräche. Ohne Euch hätte ich höchstens halb so viel gelernt. Einigen von Euch möchte ich namentlich danken:

Der größte Dank geht an Jonas Bartsch unseren Teamleiter in der Galvanik, der meine Arbeit am Fraunhofer ISE exzellent inhaltlich betreut und auch in schwierigen Phasen immer rückhaltlos unterstützt hat. Vielen Dank, lieber Jonas, für Dein großes Engagement und Deine stets positive Sicht auf Ergebnisse, Experimentideen und aufgestellte Theorien, die mich immer wieder aufs Neue motiviert hat. Dein Durchhaltevermögen beim Korrekturlesen verdient außerdem eine extra Auszeichnung.

Ich danke Stefan Glunz für die Möglichkeit der Promotion im Bereich Solarzellen Entwicklung und Charakterisierung am Fraunhofer ISE.

Meinen Doktorandenkollegen Andrew Mondon, Mathias Kamp, Martin Lieder, Christian Geisler, Andreas Lorenz, Andreas Büchler, Ralf Müller, Sebastian Binder, Maximilian Pospischil, Aline Gautrein, Sven Kluska, Michael Rauer, Milan Padilla, Kurt-Ulrich Ritzau, Frank Feldmann, und Anamaria Moldovan danke ich für die ausdauernde Unterstützung in den verschiedensten

Themengebieten und die vielen bereichernden Diskussionen, Korrekturen und Feed-backs zu Präsentationen und Papern, sowie für die kurzweiligen Konferenzaufenthalte.

Meinen Studenten Melinda Mehling, Yutriz Pernia, Limeng Ni, Bernhard Zahner, Christian Wolf, Franziska Geyer und Laura Sutor, deren Abschlussarbeiten ich während meiner Dissertation betreuen durfte, danke ich für den stetigen Strom an neuen Ideen, die vielen Fragen, deren Beantwortung mich selbst oft erheblich weiter gebracht hat, den großen Einsatz und die tollen Arbeitsergebnisse die wesentlich zum Gelingen dieser Arbeit beigetragen haben.

Meinen HiWis Julian Scherer, Johannes Spannagel Markus Wichmann, Limeng Ni, Bernhard Zahner, Christian Wolf, Alexander Maier, Carolin Wittich und Isabella Straub danke ich für den hartnäckigen Einsatz, die unzähligen Suns Voc Messungen (teilweise nachts und am Wochenende...), die Plating- und Dipping Experimente, sowie die unglaubliche Zahl an Abrisstests. Ohne Eure fleißigen Hände säße ich heute noch im Labor und an den Messgeräten.

Ich danke Giesela Cimiotti für den Rat und die praktische Hilfe bei allen Fragen rund um die elektrochemische Metallabscheidung.

Elisabeth Schäffer danke ich für das Messen von sehr vielen Solarzellen. Ich danke Aleksander Filipovic fürs Korrekturlesen, für viele Stunden am REM und die tollen Bilder, die dabei entstanden sind, sowie für die Hilfe am Ionenpolisher und mit der Chipsäge. Lieber Aleks, in der aufregenden Zeit der letzten drei Jahre hat mir Deine ruhige Art manchmal sehr gut getan.

Meinen Bürokollegen in wechselnder Besetzung Christian Geisler, Wilhelm Hördt, Franziska Geyer, Carolin Wittich, Frieder Junginger und Thomas Dietrich, danke ich für ein stets entspanntes und sehr unterhaltsames Arbeitsklima.

Den Kollegen Matthieu Ebert, Sybille Hopman, Ingrid Hädrich, Christoph Fleischmann, Katja Krüger, Ulrich Eitner, Christian Schmiga, Annika Raugewitz, Andreas Büchler, Florian Clement, und Henning Nagel danke ich für ein stets offenes Ohr für meine Fragen und die unkomplizierte Hilfe bei den alltäglichen Schwierigkeiten der experimentellen Arbeit.

Ein großer Dank geht an Birgit Stadel und Stefanie Vieler vom Bereichssekretariat der SEC. Ohne Eure tadellose Organisation von Konferenzaufenthalten und Hotelübernachtungen sowie Eure Unterstützung beim Ausfüllen von Formularen aller Art hätte ich mich im Instituts-Bürokratie-Dschungel mit Sicherheit mehrfach verlaufen.

Ich danke Dirk Eberlein, Peter Schmitt und Marco Tranitz für die fachkundige und praktische Unterstützung zum Thema Löten, Abrisstests und Modulintegration.

Ich danke Angelika Hähnel und Andreas Graff für die Zusammenarbeit bei der TEM-Charakterisierung von gedruckten Solarzellenkontakten.

Ich danke Lutz Labusch für die Erstellung von Pourbaix Diagrammen, Tobias Ensslen für die Durchführung von CVS Messungen sowie Ines Dürr für die Beratung und Unterstützung zu allen Fragen der Essigsäurekorrosion und der Modulalterung.

Dem Team Siebdruck aus dem Bereich PTQ Dennis Erath, Marc Retzlaff, Vanessa Krumm, Michael Linse sowie Andreas Lorenz, danke ich für die Erstellung von Sieblayouts, die Bestellung der Feinlinien Siebe und natürlich die unzähligen Druckversuche und die Geduld bei der Findung der richtigen Druckparameter. Lieber Andreas, dass die experimentelle Arbeit mit Metallpasten und einem Kapillarrheometer derart Spaß machen kann hat uns wohl beide positiv überrascht....

Ich danke meinen Eltern Volker und Theresia sowie meinem Bruder Ralf und meiner Schwester Anna-Katharina für die bedingungslose Unterstützung auf dem langen Weg zur Dissertation und in den letzten drei Jahren.

Mein größter Dank geht an Friederike und Sophia, Eure Liebe und Euer Rückhalt hat mich Tag für Tag motiviert. Ihr habt mir stets gezeigt, dass eine Doktorarbeit, so wichtig sie auch sein mag, nicht im entferntesten an das heranreicht worauf es im Leben wirklich ankommt...

Bibliography

- [1] IEA, "Key World Energy Statistics," International Energy Agency, Paris, 2014.
- [2] IPCC, "Intergovernmental Panel on Climate change, working group 1: Climate change 2013: The Physical Science Basis - Summary for Policymakers," 2013.
- [3] D. D. Hsu, P. O'Donoghue, V. Fthenakis, G. A. Heath, H. C. Kim, P. Sawyer, J.-K. Choi and D. E. Turney, "Life Cycle Greenhouse Gas Emissions of Crystalline Silicon Photovoltaic Electricity Generation," *Journal of Industrial Ecology*, vol. 16, pp. 122-135, 2012.
- [4] W. Moomaw, P. Burgherr, G. Heath, M. Lenzen, J. Nyboer and A. Verbruggen, "Annex II: Methodology," *IPCC Special Report on Renewable Energy Sources and Climate Change Mitigation: 10*, 2011.
- [5] P. Würfel, *Physik der Solarzellen*. Heidelberg, Berlin, Oxford: Spektrum, Akad. Verlag, 1995.
- [6] IEA, "Technology Roadmap, Solar Photovoltaic Energy " International Energy Agency, Paris, Edition 2014
- [7] C. Kost, J. N. Mayer, J. Thomsen, N. Hartmann, C. Senkpiel, S. Philipps, S. Nold, S. Lude, N. Saad and T. Schlegl, "Levelized Cost of Electricity Renewable Energy Technologies Study, Edition November 2013," *Fraunhofer Insitue for Solar Energy systems (ISE)*, 2013.
- [8] P. Verlinden, "Cost analysis of current PV production and strategy for future silicon PV modules," *presented at the 28th European Photovoltaic Conference and Exhibition, Paris*, 2013.
- [9] M. A. Green, *Solar cells: operating principles, technology and system applications*. Kensington: The University of New South Wales, 1998.
- [10] M. A. Green, *Silicon solar cells: advanced principles and practice*. Sydney, Australia: Centre for Photovoltaic Devises and Systems UNSW, 1995.
- [11] A. Goetzberger, B. Voß and J. Knobloch, *Sonnenenergie: Photovoltaik: Physik und Technologie der Solarzelle*: Teubner, 1994.
- [12] S. W. Glunz, R. Preu and D. Biro, "1.16 - Crystalline Silicon Solar Cells: State-of-the-Art and Future Developments," in *Comprehensive Renewable Energy*, A. Sayigh, Ed., ed Oxford: Elsevier, 2012, pp. 353-387.
- [13] D. S. H. Chan and J. C. H. Phang, "Analytical methods for the extraction of solar-cell single- and double-diode model parameters from I-V characteristics," *IEEE Transactions on Electron Devices*, vol. 34, pp. 286-293, 1987.
- [14] T. Tiedje, E. Yablonovitch, G. D. Cody and B. G. Brooks, "Limiting efficiency of silicon solar cells," *IEEE Transactions on Electron Devices*, vol. 31, pp. 711-6, 1984.
- [15] R. M. Swanson, "Approaching the 29% limit efficiency of silicon solar cells," in *Proceedings of the 31st IEEE Photovoltaic Specialists Conference*, Orlando, USA, 2005, pp. 889-94.
- [16] N. Matsubara, K. Masuko, K. Fujishima, M. Kai, T. Tsunomura, T. Yamanishi, T. Takahama, M. Taguchi, E. Maruyama and S. Okamoto, "Development of 25.6% Record Efficiency Silicon Heterojunction Solar Cell," in *The 6 th World Conference on Photovoltaic Energy Conversion*, Kyoto, Tokio, 2014.

- [17] P.J. Verlinden, W. Deng, X. Zhang, Y. Yang, J. Xu, Y. Shu, P. Quan, J. Sheng, S. Zhang, J. Bao, F. Ping, Y. Zhang and Z. Feng, " Strategy, Development and Mass Production of High-Efficiency Crystalline Si PV Modules," in *The 6th World Conference on Photovoltaic Energy Conversion*, Kyoto, Japan, 2014.
- [18] I. E. Comission, "International Standard, IEC 60904-3, Photovoltaic devices part-3: Measurement principles for terrestrial photovoltaic (PV) solar devices with refernece spectral irradiance data Edition 2," ed, 2008.
- [19] A. Mette, "New concepts for front side metallization of industrial silicon solar cells," Universitätsbibliothek Freiburg, 2007.
- [20] O. Hardouin Duparc, "Pierre Auger – Lise Meitner: Comparative contributions to the Auger effect," *International Journal of Materials Research*, vol. 100, pp. 1162-1166, 2009.
- [21] W. Shockley and W. Read, "Statistics of the Recombinations of Holes and Electrons," *Physical Review*, vol. 87, pp. 835-842, 1952.
- [22] R. Hall, "Electron-Hole Recombination in Germanium," *Physical Review*, vol. 87, pp. 387-387, 1952.
- [23] S. W. Glunz, "Ladungsträgerrekombination in Silicium und Siliciumsolarzellen," Dissertation, Fakultät für Physik, Universität Freiburg, Freiburg, 1995.
- [24] B. Stegemann, "Kapitel 8- Die optimale Silizium-Solarzelle," *Vorlesungsfolien zur Vorlesung Photoelektrische Prozesse M2, Fachbereich 1, Hochschule für Technik und Wirtschaft Berlin, Deutschland, Sommersemester 2010*.
- [25] R. Preu, "Innovative Produktionstechnologien für kristalline Silicium-Solarzellen," Dissertation, Fachbereich Elektrotechnik, FernUniversität Hagen, Freiburg, 2000.
- [26] J. Czochralski, "A new method for the measurement of the crystallization rate of metals," *Zeitschrift für Physikalische Chemie*, vol. 92, pp. 219–221, 1918.
- [27] H. C. Theuerer, "Method of preparing silicon," ed: Patent, 1959.
- [28] A. J. Bard and L. L. Faulkner, *Electrochemical methods second Edition*: Wiley Verlag, 2001.
- [29] Carl H. Hamann and W. Vielstich, *Elektrochemie 4. Auflage*: Wiley-VCH Verlag, 2004.
- [30] N. Kanani, *Galvanotechnik, Grundlagen, Verfahren und Praxis einer Schlüsseltechnologie 2. Auflage*. München, Wien: HANSER Verlag, 2009.
- [31] W. Nernst, *Zeitschrift für physikalische Chemie*, vol. 47, p. 52, 1907.
- [32] H. Helmholtz, "Ueber einige Gesetze der Verteilung elektrischer Ströme in körperlichen Leitern, mit Anwendung auf die thierisch elektrischen Versuche. ," in *Annalen der Physik und Chemie. Dritte Reihe*. 89, J. C. Poggendorff, Ed., ed Leipzig: Verlag von Johann Ambrosius Barth, 1853, pp. 211-233.
- [33] H. Helmholtz, "Studien über electrische Grenzschichten. In: G. Wiedemann (Hrsg.)," in *Annalen der Physik und Chemie*, ed Leipzig: Verlag von Johann Ambrosius Barth, 1879, pp. 337–382.
- [34] W. Späth, "Verfahren zur galvanischen Abscheidung einer Metallschicht auf Oberflächen eines Halbleiterkörpers," 1975.
- [35] L. Durkee, "Method of plating by means of light," 1979.
- [36] L. Grenon, "Electroplating method," 1981.
- [37] A. Fick, *Über Diffusion*: Annalen der Physik, volume 170(1), pp. 59-86, 1855.

- [38] L. Grenon, N. Sakiotis and M. Coleman, "Reliability of silicon solar cells with a plated Ni-Cu metallization system," in *Proceedings of the 15th IEEE Photovoltaic Specialists Conference*, Kissimmee, USA, 1981, pp. 522-526.
- [39] J. Bartsch, A. Mondon, K. Bayer, C. Schetter, M. Hörteis and S. W. Glunz, "Quick determination of copper-metallization long-term impact on silicon solar cells," *Journal of The Electrochemical Society*, vol. 157, pp. H942-H946, 2010.
- [40] C. J. Gallagher, "Electrolysis of copper in solid silicon," *Journal of Physics and Chemistry of Solids*, vol. 3, pp. 82-86, 1957.
- [41] R. N. Hall and J. H. Racette, "Diffusion and Solubility of Copper in Extrinsic and Intrinsic Germanium, Silicon, and Gallium Arsenide," *Journal of Applied Physics*, vol. 35, pp. 379-397, 1964.
- [42] E. Weber, "Transition metals in silicon," *Appl. Phys. A*, vol. 30, pp. 1-22, 1983.
- [43] J. D. Struthers, "Solubility and Diffusivity of Gold, Iron, and Copper in Silicon," *Journal of Applied Physics*, vol. 27, pp. 1560-1560, 1956.
- [44] A. A. Istratov, C. Flink, H. Hieslmair, E. R. Weber and T. Heiser, "Intrinsic Diffusion Coefficient of Interstitial Copper in Silicon," *Physical Review Letters*, vol. 81, pp. 1243-1246, 1998.
- [45] S. K. Estreicher, "Copper, lithium, and hydrogen passivation of boron in c-Si," *Physical Review B*, vol. 41, pp. 5447-5450, 1990.
- [46] M. S. Anand, S. P. Murarka and R. P. Agarwala, "Diffusion of Copper in Nickel and Aluminum," *Journal of Applied Physics*, vol. 36, pp. 3860-3862, 1965.
- [47] A. A. Istratov, C. Flink, H. Hieslmair, S. A. McHugo and E. R. Weber, "Diffusion, solubility and gettering of copper in silicon," *Materials Science and Engineering: B*, vol. 72, pp. 99-104, 2000.
- [48] A. A. Istratov and E. R. Weber, "Electrical properties and recombination activity of copper, nickel and cobalt in silicon," *Appl. Phys. A*, vol. 66, pp. 123-136, 1998.
- [49] R. H. Hopkins and A. Rohatgi, "Impurity effects in silicon for high efficiency solar cells," *Journal of Crystal Growth*, vol. 75, pp. 67-79, 1986.
- [50] "International Technology Roadmap for Photovoltaic (ITRPV)," *fifth Edition*, 2014.
- [51] *DIN EN 50461: 2007-03; Solar cells - Datasheet information and product data for crystalline silicon solar cells*. Berlin: Beuth Verlag, 2007.
- [52] *DIN EN 28510-1: Adhesives –Peel test for a flexible-bonded-to-rigid test specimen assembly –Part 1: 90° peel*. Berlin: Beuth Verlag, 2014.
- [53] *IEC 61189-2: Test methods for electrical materials, printed boards and other interconnection structures and assemblies – Part 2: Test methods for materials for terconnection structures* Berlin: Beuth Verlag, 2007.
- [54] *DIN EN 61215:2006-02; Crystalline silicon terrestrial photovoltaic (PV) modules - Design qualification and type approval* Berlin: Beuth Verlag, 2005.
- [55] N. Bogdanski and W. Herrmann, "Weighting of Climatic Impacts on PV-Module Degradation – Comparison of Outdoor Weathering Data and Indoor Weathering Data," *Proceedings of the 26th European Photovoltaic Solar Energy Conference and Exhibition, Hamburg, Germany, 2011*, pp. 3093 - 3096, 2011.

- [56] D. Pysch, P. Karl and S. Vaun, "Detailed analysis of fine line printed and plated solar cell contacts," *Presented at the 2nd European Photovoltaic Conference and Exhibition, Milan, Italy, 2007*.
- [57] M. Hörteis, J. Bartsch, S. Binder, A. Filipovic, J. Merkel, V. Radtke and S. W. Glunz, "Electrical properties of fine line printed and light-induced plated contacts on silicon solar cells," *Progress in Photovoltaics: Research and Applications*, vol. 18, pp. 240-248, 2010.
- [58] E. Ralph, "Recent advancements in low cost solar cell processing," in *11th Photovoltaic Specialists Conference*, 1975, p. 315.
- [59] R. P. Mertens, R. J. Van Overstraeten and K. U. Leuven, "Solar Cell Fabrication Techniques for Single and Semicrystalline Silicon Substrates," *International Journal of Solar Energy*, vol. 2, pp. 121-140, 1984.
- [60] G. C. Cheek, R. P. Mertens, R. Van Overstraeten and L. Frisson, "Thick-film metallization for solar cell applications," *IEEE Transactions on Electron Devices*, vol. 31, pp. 602-609, 1984.
- [61] H. J. Homann, *Lehrbuch Siebdruck. Druckformherstellung*. Emmendingen: Verlag Ursula Homann, 1995.
- [62] H. G. Scheer, *Siebdruck Handbuch*. Lübeck: Verlag Der Siebdruck, 1999.
- [63] P. Hahne, *Innovative Drucktechnologien Siebdruck - Tampondruck*: Verlag Der Siebdruck Lübeck, 2001.
- [64] M. Nakayama, N. Ochiai, K. Harigae, K. Honda, S. Kitada, H. Hayashi, K. Nakamura, M. Aoki, I. Sumita and Y. Ohshita, "Lead-free Silver-paste for Fine-line Printing with Ultra-fine Mesh Screen," presented at the 4th Metallization Workshop, Constance, Germany, 2013.
- [65] F. Huster, "Investigation of the alloying process of screen-printed aluminium pastes for the BSF formation on silicon solar cells," in *Proceedings of the 20th European Photovoltaic Solar Energy Conference*, Spain, Barcelona, 2005, pp. 1466-1469.
- [66] S. Narasimha, A. Rohatgi and A. W. Weeber, "An optimized rapid aluminum back surface field technique for silicon solar cells," *IEEE Transactions on Electron Devices*, vol. 46, pp. 1363-1370, 1999.
- [67] B. L. Sopori, X. Deng, J. P. Benner, A. Rohatgi, P. Sana, S. K. Estreicher, Y. K. Park and M. A. Roberson, "Hydrogen in silicon: A discussion of diffusion and passivation mechanisms," *Solar Energy Materials and Solar Cells*, vol. 41-42, pp. 159-169, 1996.
- [68] G. Schubert, "Thick Film Metallisation of Crystalline Silcion Solar Cells Mechanisms, Models and Applications," Dissertation, Universität Konstanz Fachbereich Physik, 2006.
- [69] K.-K. Hong, S.-B. Cho, J. S. You, J.-W. Jeong, S.-M. Bea and J.-Y. Huh, "Mechanism for the formation of Ag crystallites in the Ag thick-film contacts of crystalline Si solar cells," *Solar Energy Materials and Solar Cells*, vol. 93, pp. 898-904, 2009.
- [70] H. H. Kühnlein, N. Kösterke, G. Cimiotti, E. Hartmannsgruber, N. Bürger, H. Nussbaumer, D. Luetke-Notarp and M. Becker, ">0.4% Absolut Efficiency Gain by Fast Ni-Cu-Sn Electroplating of Solar Cells with Fine Line Printed Contacts by a Single Side Wet Treatment Technology," in *Proceedings of the*

- 24th European Photovoltaic Solar Energy Conference and Exhibition, Hamburg, Germany, 2009, pp. 282 - 284.
- [71] J. Bartsch, A. Mondon, C. Schetter, M. Hörteis and S. W. Glunz, "Copper as conducting layer in advanced front side metallization processes for crystalline silicon solar cells, exceeding 20% on printed seed-layers," in *Proceedings of the 35th IEEE Photovoltaic Specialists Conference*, 2010, pp. 1299-1303.
- [72] S. Binder, J. Bartsch, M. Glatthaar and S. W. Glunz, "Printed contact on emitter with low dopant surface concentration," *Energy Procedia*, vol. 21, pp. 32-38, 2012.
- [73] A. Mette, F. Stenzel, A. Hofmann, S. Hörnlein, T. Florian, I. Hoschek, A. Kraft, M. Schaper, M. Fischer and P. Wawer, "Evaluation of fine-line printing and plating in pilot production at Q-Cells," *Presentation at the 3th Metallization Workshop, Constance, Germany 2011*.
- [74] S. Binder, M. Glatthaar and E. Rädlein, "Analytical Investigation of Aerosol Jet Printing," *Aerosol Science and Technology*, vol. 48, pp. 924-929, 2014.
- [75] M. Hörteis, T. Gutberlet, A. Reller and S. W. Glunz, "High-Temperature Contact Formation on n-Type Silicon: Basic Reactions and Contact Model for Seed-Layer Contacts," *Advanced Functional Materials*, vol. 20, pp. 476-484, 2010.
- [76] A. Kalio, A. Richter, M. Glatthaar and J. Wilde, "Study of Contact Formation of Printed Contacts through Different Passivation Layers on Lowly Doped Emitters," *Energy Procedia*, vol. 38, pp. 745-752, 2013.
- [77] S. Binder, C. Schmiga, M. Glatthaar and S. W. Glunz, "Optimized Aerosol Jet Printed Contacts on Lowly Doped Phosphorous and Boron Emitters," *Energy Procedia*, 2014.
- [78] A. Mette, P. L. Richter, M. Hörteis and S. W. Glunz, "Metal aerosol jet printing for solar cell metallization," *Progress in Photovoltaics: Research and Applications*, vol. 15, pp. 621-627, 2007.
- [79] M. Hörteis, J. Benick, J. Nekarda, A. Richter, R. Preu and S. W. Glunz, "Fundamental studies on the front contact formation resulting in a 21% efficiency silicon solar cell with printed rear and front contacts," in *Proceedings of the 35th IEEE Photovoltaic Specialists Conference*, 2010, pp. 672-677.
- [80] M. Hörteis and S. W. Glunz, "Fine line printed silicon solar cells exceeding 20% efficiency," *Progress in Photovoltaics: Research and Applications*, vol. 16, pp. 555-560, 2008.
- [81] M. Hörteis, *Fine-Line Printed Contacts on Crystalline Silicon Solar Cells*: Dr. Hut, 2009.
- [82] K. Teng and R. Vest, "Application of ink jet technology on photovoltaic metallization," *Electron Device Letters, IEEE*, vol. 9, pp. 591-593, 1988.
- [83] H. P. Le, "Progress and Trends in Ink-jet Printing Technology," *Journal of Imaging Science and Technology*, vol. 42, pp. 49-62, 1998.
- [84] J. Heinzl and C. Hertz, "Ink-jet printing," *Advances in electronics and electron physics*, vol. 65, pp. 91-171, 1985.
- [85] T. Lindemann, "Droplet generation-from the nanoliter to the femtoliter range," Universitätsbibliothek Freiburg, 2006.
- [86] A. Ebong, B. Rounsaville, I. Cooper, K. Tate, A. Rohatgi, S. Glunz, M. Hörteis, A. Mette and M. Gundermann, "High efficiency silicon solar cells with ink

- jetted seed and plated grid on high sheet resistance emitter," in *Proceedings of the 35th IEEE Photovoltaic Specialists Conference*, 2010, pp. 1363-1367.
- [87] A. Lorenz, A. Senne, J. Rohde, S. Kroh, M. Wittenberg, K. Krüger, F. Clement and D. Biro, "Evaluation of flexographic printing technology for multi busbar solar cells," presented at the 5th Workshop on Metallization of Crystalline Silicon Solar Cells, Constance, Germany, 2014.
- [88] A. Lorenz, A. Kalio, G. T. Hofmeister, S. Nold, A. Kraft, J. Bartsch, D. Wolf, M. Dreher, F. Clement and D. Biro, "Flexographic printing – High throughput technology for fine line seed-layer printing on silicon solar cells," in *Proceedings of the 28th European Photovoltaic Solar Energy Conference and Exhibition*, Paris, France, 2013, pp. 1017-1023.
- [89] A. Lorenz, A. Kalio, T. Barnes Hofmeister, A. Kraft, J. Bartsch, F. Clement, H. Reinecke and D. Biro, "Developing a High Throughput Printing Technology for Silicon Solar Cell Front Side Metallisation using Flexography " *Accepted for publication in the Journal of Print and Media Technology Research*, 2015.
- [90] M. Frey, F. Clement, S. Dilfer, D. Erath and D. Biro, "Front side metalization by means of flexographic printing," *Energy Procedia*, vol. 8, pp. 581-586, 2011.
- [91] S. Thibert, D. Chaussy, D. Beneventi, N. Reverdy-Bruas, J. Jourdan, B. Bechevet and S. Mialon, "Silver ink experiments for silicon solar cell metallization by flexographic process," in the *38th IEEE Photovoltaic Specialists Conference* 2012, pp. 2266-2270.
- [92] N. Mason, D. Jordan and J. G. Summers, "A high efficiency silicon solar cell production technology," in *Proceedings of the 10th EU PV Solar Energy Conference*, Lisbon, Portugal, 1991, pp. 280–283.
- [93] Z. Shi, S. Wenham and J. Ji, "Mass production of the innovative PLUTO solar cell technology," in *Proceedings of the 34th IEEE Photovolt. Specialists Conference*, 2009, pp. 1922–1926.
- [94] R. Russell, L. Tous, H. Philipsen, J. Horzel, E. Cornagliotti, M. Ngamo, P. Choulal, R. Labie, J. Beckers, J. Bertens, M. Fujii, J. John, J. Poortmans and R. Mertens, "A Simple Copper Metallisation Process for High Cell Efficiencies and Reliable Modules," *Proceedings of the 27th European Photovoltaic Solar Energy Conference and Exhibition, Frankfurt, Germany*, pp. 538 - 543, 2012.
- [95] A. Mondon, M. N. Jawaïd, J. Bartsch, M. Glatthaar and S. W. Glunz, "Microstructure analysis of the interface situation and adhesion of thermally formed nickel silicide for plated nickel–copper contacts on silicon solar cells," *Solar Energy Materials and Solar Cells*, vol. 117, pp. 209-213, 2013.
- [96] J. Horzel, N. Bay, M. Passig, M. Sieber, J. Burschik, H. Kühnlein, A. Brand, A. Letize, B. Lee, D. Weber and R. Böhme, "Low Cost Metallization based on Ni/Cu Plating enabling high Efficiency industrial Solar Cells," in *Proceedings of the 29th European Photovoltaic Solar Energy Conference and Exhibition*, Amsterdam, The Netherlands, 2014.
- [97] A. Büchler, S. Kluska, A. Brand, C. Geisler, S. Hopman and M. Glatthaar, "Micro Characterization and Imaging of Spikes in Nickel Plated Solar Cells," *Energy Procedia*, vol. 55, pp. 624-632, 2014.
- [98] A. Mondon, "Nickel silicide from plated nickel for high adhesion of fully plated silicon solar cell metallization," Dissertation, Universität Freiburg im Breisgau, 2015.

- [99] A. u. Rehman and S. H. Lee, "Review of the Potential of the Ni/Cu Plating Technique for Crystalline Silicon Solar Cells," *Materials*, vol. 7, pp. 1318-1341, 2014.
- [100] *Brochure for Hitachi Ion Milling System IM 4000*. Tokyo: Hitachi High Tech, 2012.
- [101] M. Knoll and E. Ruska, "Das Elektronenmikroskop," *Zeitschrift für Physik*, vol. 78, pp. 318-339, 1932.
- [102] J. I. Goldstein, D. E. Newbury, P. Echlin, D. C. Joy, C. Fiori and E. Lifshin, *Scanning electron microscopy and X-ray microanalysis. A text for biologists, materials scientists, and geologists*: Plenum Publishing Corporation, 1981.
- [103] "Instruction Manual for Model SU-70 Scanning Electron Microscope ", ed. Tokyo: Hitachi High Tech, 2008.
- [104] E. D. R. Committee, *Microelectronics Failure Analysis: Desk Reference*: ASM International, 2011.
- [105] D. B. Williams and C. B. Carter, *The Transmission Electron Microscope*: Springer, 1996.
- [106] A. J. Kinloch, C. C. Lau and J. G. Williams, "The peeling of flexible laminates," *International Journal of Fracture*, vol. 66, pp. 45-70, 1994.
- [107] U. Eitner and L. C. Rendler, "The mechanical theory behind the peel-test," in *Proceedings of the 4th International Conference on Silicon Photovoltaics*, s-Hertogenbosch, The Netherlands, 2014.
- [108] G. Binnig, C. F. Quate and C. Gerber, "Atomic Force Microscope," *Physical Review Letters*, vol. 56, pp. 930-933, 1986.
- [109] P. J. Eaton and P. West, *Atomic force microscopy* vol. 10: Oxford University Press, 2010.
- [110] R. A. Sinton and A. Cuevas, "A quasi-steady-state open-circuit voltage method for solar cell characterization," in *Proc. 16th EC PVSEC*, Glasgow, UK, 2000, pp. 1152-5.
- [111] T. Trupke, R. A. Bardos, M. C. Schubert and W. Warta, "Photoluminescence imaging of silicon wafers," *Applied Physics Letters*, vol. 89, p. 044107 2006.
- [112] T. Fuyuki, H. Kondo, T. Yamazaki, Y. Takahashi and Y. Uraoka, "Photographic surveying of minority carrier diffusion length in polycrystalline silicon solar cells by electroluminescence," *Applied Physics Letters*, vol. 86, p. 262108, 2005.
- [113] R. A. Sinton, A. Cuevas and M. Stuckings, "Quasi-steady-state photoconductance, a new method for solar cell material and device characterization," in *Photovoltaic Specialists Conference, 1996., Conference Record of the Twenty Fifth IEEE*, 1996, pp. 457-460.
- [114] J. Nölte, *ICP Emissionsspektrometrie für Praktiker*. Weinheim: Wiley-VCH, 2002.
- [115] C. B. Boss and K. J. Fredeen, *Concepts, Instrumentation and Techniques in Inductively Coupled Plasma Optical Emission Spectrometry*: Perkin Elmer, 1997.
- [116] B. E. H. Saxberg and B. R. Kowalski, "Generalized standard addition method," *Analytical Chemistry*, vol. 51, pp. 1031-1038, 1979.

- [117] R. S. Nicholson, "Theory and Application of Cyclic Voltammetry for Measurement of Electrode Reaction Kinetics," *Analytical Chemistry*, vol. 37, pp. 1351-1355, 1965.
- [118] W. Vielstich, *Cyclic voltammetry*: Wiley Online Library, 2010.
- [119] V. Pecharsky and P. Zavaliy, *Fundamentals of powder diffraction and structural characterization of materials*: Springer, 2008.
- [120] W. H. Herschel and R. Bulkley, "Konsistenzmessungen von gummi-benzollösungen," *Kolloid-Zeitschrift*, vol. 39, pp. 291-300, 1926.
- [121] C. W. Makosko, "Rheology principles, measurements, and applications," *VCH, New York*, 1994.
- [122] T. Mezger, "Das Rheologie Handbuch," *Vincentz-Verlag, Hannover*, 2000.
- [123] J. M. Bartsch, *Advanced Front Side Metallization for Crystalline Silicon Solar Cells with Electrochemical Techniques*: Verlag Dr. Hut, 2012.
- [124] N. Bay, J. Horzel, M. Passig, M. Sieber, J. Burschik, H. Kühnlein, J. Bartsch, A. Brand, A. Mondon, D. Eberlein, C. Völker, S. Gutscher, A. Letize, B. Lee, D. Weber and R. Böhme, "Reliable Contact Formation for Industrial Solar Cells by Laser Ablation and Ni/Cu Plating," in *Proceedings of the 29th European Photovoltaic Solar Energy Conference and Exhibition*, Amsterdam, The Netherlands, 2014, pp. 1272 - 1276.
- [125] "Betriebsanleitung/Benutzerhandbuch: InCellPlate Labtool 120962/13697," *RENA GmbH*, 2013.
- [126] J. Unruh, "Tabellenbuch Galvanotechnik, 7. Aufl., Eugen G," ed: Leuze Verlag, Bad Saulgau, 2001.
- [127] S. Kurtz, K. Whitfield, G. TamizhMani, M. Koehl, D. Miller, J. Joyce, J. Wohlgemuth, N. Bosco, M. Kempe and T. Zgonena, "Evaluation of high-temperature exposure of photovoltaic modules," *Progress in Photovoltaics: Research and Applications*, vol. 19, pp. 954-965, 2011.
- [128] M. Pospischil, J. Specht, M. König, M. Horteis, C. Mohr, F. Clement and D. Biro, "Paste Rheology Correlating With Dispensed Finger Geometry," *IEEE Journal of Photovoltaics*, vol. 4, pp. 498-503, 2014.
- [129] M. Pospischil, M. Klawitter, M. Kuchler, J. Specht, H. Gentischer, R. Efinger, C. Kroner, M. Luegmair, M. König, M. Hörteis, C. Mohr, L. Wende, J. Lossen, M. Weiß, O. Doll, I. Koehler, R. Zengerle, F. Clement and D. Biro, "Process Development for a High-throughput Fine Line Metallization Approach Based on Dispensing Technology," *Energy Procedia*, vol. 43, pp. 111-116, 2013.
- [130] M. D. Wendling, A. Mondon, A. Kraft, J. Bartscha, M. Glatthaar and S. W. Glunz, "Analysis of Chemical Stability of Printing Pastes in Electrochemical Plating Solutions," *Energy Procedia*, vol. 27, pp. 497-502, 2012.
- [131] A. Kalio, M. Leibinger, A. Filipovic, K. Krüger, M. Glatthaar and J. Wilde, "Development of lead-free silver ink for front contact metallization," *Solar Energy Materials and Solar Cells*, vol. 106, pp. 51-54, 2012.
- [132] J. A. Pask and R. M. Fulrath, "Fundamentals of Glass-to-Metal Bonding: VIII, Nature of Wetting and Adherence," *Journal of the American Ceramic Society*, vol. 45, pp. 592-596, 1962.
- [133] R. W. Revie, Ed., *Uhlig's Corrosion Handbook* (Pourbaix diagrams of multielement systems. W.T. Thompson, M.H. Kaye, C.W. Bale, A.D. Pelton, 2011, p.^pp. Pages.

- [134] S. Olweya, A. Kalio, A. Kraft, E. Deront, A. Filipovic, J. Bartsch and M. Glatthaar, "Fine-line Silver Pastes for Seed-layer Screen-printing with Varied Glass Content," *Energy Procedia*, vol. 43, pp. 37-43, 2013.
- [135] S. B. Rane, P. K. Khanna, T. Seth, G. J. Phatak, D. P. Amalnerkar and B. K. Das, "Firing and processing effects on microstructure of fritted silver thick film electrode materials for solar cells," *Materials Chemistry and Physics*, vol. 82, pp. 237-245, 2003.
- [136] K.-I. Yajima and T. Yamaguchi, "Sintering and microstructure development of glass-bonded silver thick films," *Journal of Materials Science*, vol. 19, pp. 777-784, 1984.
- [137] K. Yajima and T. Yamaguchi, "A further study on the microstructure of glass-bonded Ag thick-film conductors," *Components, Hybrids, and Manufacturing Technology, IEEE Transactions on*, vol. 7, pp. 281-285, 1984.
- [138] S. B. Rane, T. Seth, G. J. Phatak, D. P. Amalnerkar and B. K. Das, "Influence of surfactants treatment on silver powder and its thick films," *Materials Letters*, vol. 57, pp. 3096-3100, 2003.
- [139] J. C. Lin and C. Y. Wang, "Effects of surfactant treatment of silver powder on the rheology of its thick-film paste," *Materials Chemistry and Physics*, vol. 45, pp. 136-144, 1996.
- [140] V. K. Nagesh, A. P. Tomsia and J. A. Pask, "Wetting and reactions in the lead borosilicate glass-precious metal systems," *Journal of Materials Science*, vol. 18, pp. 2173-2180, 1983.
- [141] J. Burbank, "The Anodic Oxides of Lead," *Journal of The Electrochemical Society*, vol. 106, pp. 369-376, 1959.
- [142] P. Delahay, M. Pourbaix and P. V. Rysselberghe, "Potential pH Diagram of Lead and its Applications to the Study of Lead Corrosion and to the Lead Storage Battery," *Journal of The Electrochemical Society*, vol. 98, pp. 57-64, 1951.
- [143] R. Hönig, "Evaluation and microstructure analysis of thick film contacts for industrial silicon solar cells," Dissertation, Universität Freiburg im Breisgau, 2015.
- [144] G. Tünker and H. Paulus, "DE 195 02 653 A1," *Deutsche Patent*, 1995.
- [145] A. Istratov, H. Hedemann, M. Seibt, O. Vyvenko, W. Schröter, T. Heiser, C. Flink, H. Hieslmair and E. Weber, "Electrical and Recombination Properties of Copper-Silicide Precipitates in Silicon," *Journal of The Electrochemical Society*, vol. 145, pp. 3889-3898, 1998.
- [146] A. A. Istratov, O.F. Vyvenko, C. Fink, T. Heiser, H. Hieslmair and E. R. Weber, *Defect and impurity engineered semiconductors II*. Warrendale, PA: Material research Society, 1998, P. 313.
- [147] M. B. Shabani, T. Yoshimi and H. Abe, "Low-Temperature Out-Diffusion of Cu from Silicon Wafers," *Journal of The Electrochemical Society*, vol. 143, pp. 2025-2029, 1996.
- [148] C. Mc Carthy, M. Miyazaki, H. Horie, S. Okamoto and H. Tsuya, "Semiconductor Silicon," *The Electrochemical society*, p. 629, 1998.
- [149] D. Wood, I. Kuzma-Filipek, R. Russell, F. Duerinckx, N. Powell, A. Zambova, B. Chislea, P. Chevalier, C. Boulord and A. Beucher, "Passivated Busbars from

- Screen-printed Low-temperature Copper Paste," *Energy Procedia*, vol. 55, pp. 724-732, 2014.
- [150] M. Vogt, M. Kachel and K. Drescher, "Dielectric barriers for Cu metallization systems," in *Materials for Advanced Metallization, 1997. MAM '97 Abstracts Booklet., European Workshop*, 1997, pp. 51-52.
- [151] Y. Shacham-Diamond, A. Dedhia, D. Hoffstetter and W. G. Oldham, "Reliability of copper metallization on silicon-dioxide," in *Proceedings of the 8th International IEEE Multilevel Interconnection Conference 1991*, pp. 109-115.
- [152] P. L. Pai and C. H. Ting, "Copper as the future interconnection material," in *Proceedings of the 6th International IEEE Multilevel Interconnection Conference*, 1989, pp. 258-264.
- [153] J. D. McBrayer, R. Swanson and T. Sigmon, "Diffusion of metals in silicon dioxide," *Journal of The Electrochemical Society*, vol. 133, pp. 1242-1246, 1986.
- [154] M. Vogt and R. Hauptmann, "Plasma-deposited passivation layers for moisture and water protection," *Surface and Coatings Technology*, vol. 74-75, Part 2, pp. 676-681, 1995.
- [155] R. Labie, J. L. Hernandez, J. Govaerts, C. Allebe, L. Tous, A. U. D. Castro, R. Russel, I. Gordon and K. Baert, "Cu plated I-Perl cells: Aging and humidity reliability tests," in *Proceedings of the 26th European Photovoltaic Energy Conference*, Leuven, Belgium, 2012.
- [156] J. Bartsch, A. Mondon, B.J. Godejohann, M. Hörteis and S. W. Glunz, "Advanced front side metallization for crystalline silicon solar cells based on a fully plated contact," in *Proceedings of the 25th European PV Solar Energy Conference and Exhibition, Valencia, Spain*, 2010, pp. 6-10.
- [157] P. Gas and F. d'Heurle, "Kinetics of Formation of TM Silicide thin films: Self diffusion in Properties of metal silicides, edited by K. Maex and M.V. Rossum, Chapter 7, Institution of Electrical Engineers London, United Kingdom, 1995."
- [158] U. Weber, R. Eiden, C. Strubel, T. Sögding, M. Heiss, P. Zachmann, K. Nattermann, H. Engelmann, A. Dethlefsen and N. Lenck, "Acetic Acid Production, Migration and Corrosion Effects in Ethylene-Vinyl-Acetate- (EVA-) Based PV Modules," *Proceedings of the 27th European Photovoltaic Solar Energy Conference and Exhibition, Frankfurt, Germany*, 2012, pp. 2992 - 2995.
- [159] H. Gong, G. Wang and M. Gao, "Degradation Mechanism Analysis of Damp Heat Aged PV Modules," in *Proceedings of the 27th European Photovoltaic Solar Energy Conference and Exhibition, Frankfurt, Germany*, 2012, pp. 3518 - 3522.
- [160] B. Ketola and A. Norris, "Degradation Mechanism Investigation of Extended Damp Heat Aged PV Modules," in *Proceedings of the 26th European Photovoltaic Solar Energy Conference and Exhibition, , Germany, Hamburg*, 2011, pp. 3523 - 3528.
- [161] N. Bogdanski and W. Herrmann, "Weighting of Climatic Impacts on PV-Module Degradation – Comparison of Outdoor Weathering Data and Indoor Weathering Data," in *Proceedings of the 26th European Photovoltaic Solar Energy Conference and Exhibition, Hamburg, Germany*, 2011, pp. 3093 - 3096.

- [162] C. Peike, S. Hoffmann, P. Hülsmann, B. Thaidigsmann, K. A. Weiß, M. Koehl and P. Bentz, "Origin of damp-heat induced cell degradation," *Solar Energy Materials and Solar Cells*, vol. 116, pp. 49-54, 2013.
- [163] M. D. Kempe, G. J. Jorgensen, K. M. Terwilliger, T. J. McMahon, C. E. Kennedy and T. T. Borek, "Acetic acid production and glass transition concerns with ethylene-vinyl acetate used in photovoltaic devices," *Solar Energy Materials and Solar Cells*, vol. 91, pp. 315-329, 2007.
- [164] G. Eriksson, "An algorithm for the computation of aqueous multi-component, multiphase equilibria," *Analytica Chimica Acta*, vol. 112, pp. 375-383, 1979.
- [165] N. Ingri, W. Kakolowicz, L. G. Sillén and B. Warnqvist, "High-speed computers as a supplement to graphical methods—V: Haltafall, a general program for calculating the composition of equilibrium mixtures," *Talanta*, vol. 14, pp. 1261-1286, 1967.
- [166] P. Patnaik, *Handbook of inorganic chemicals*. Burlington: McGraw-Hill Professional, 2002.
- [167] S. Pingel, O. Frank, M. Winkler, S. Daryan, T. Geipel, H. Hoehne and J. Berghold, "Potential Induced Degradation of solar cells and panels," in *Proceedings of the 35th IEEE Photovoltaic Specialists Conference* 2010, pp. 2817-2822.
- [168] K. Geißdörfer, *Total cost of ownership (TCO) und life cycle costing (LCC): Einsatz und Modelle: ein Vergleich zwischen Deutschland und USA* vol. 7: LIT Verlag Münster, 2009.
- [169] "SEMI E35-0312 Guide to Calculate Cost of Ownership (COO) Metrics for Semiconductor Manufacturing Equipment," 2007.
- [170] S. Nold, N. Voigt, L. Friedrich, D. Weber, I. Hädrich, M. Mittag, H. Wirth, B. Thaidigsmann, I. Brucker, M. Hofmann, J. Rentsch and R. Preu, "Cost Modelling of Silicon Solar Cell Production Innovation along the PV Value Chain," in *Proceedings of the 27th European Photovoltaic Solar Energy Conference and Exhibition*, Frankfurt, Germany, 2012.
- [171] L. Sutor, "Galvanische Kupfermetallisierung für Kristalline Silicium solarzellen - Wirtschaftlichkeit und Leistungsfähigkeit," *Bachelor Thesis, Karlsruher Institut für Technologie (KIT)*, 2013.
- [172] F. Geyer, "Einzel- und Gesamtprozesskosten der Direktgalvanischen Metallisierung für Kristalline Silicium Solarzellen," *Master Thesis, Karlsruher Institut für Technologie (KIT)*, 2014.
- [173] M. Pourbaix, "Atlas of electrochemical equilibria in aqueous solutions," 1974.

A novel copper front side metallization architecture for silicon solar cells based on a fine printed silver seed-layer, plated with nickel, copper and silver, is investigated. The work focuses on the printing of fine seed-layers with low silver consumption, the corrosion of the printed seed-layers by the interaction with electrolyte solutions and the encapsulation material on module level and on the long term stability of the cells due to copper migration. The investigation of the correlation between fine contact finger geometry and rheological parameters of the printing pastes enabled the reduction of the total silver consumption to < 15 mg/cell front side.

The analysis of the contact corrosion revealed that site specific dissolution of the glass layer inside the contacts by electrolyte solutions is responsible for contact adhesion loss. A model of the underlying reaction mechanism is developed. These results were successfully transferred to improve the understanding of the damp heat induced degradation phenomenon which occurs on module level. The investigations of the copper migration showed that silicon nitride anti reflection coatings prevent copper diffusion into the silicon wafer and that ~ 20 mg plated nickel per cell, is sufficient to avoid long term stability issues due to copper migration during a module lifetime.



ISBN 978-3-8396-0939-2



9 783839 609392